Modelling Tremie Concrete Placement in Deep Foundations

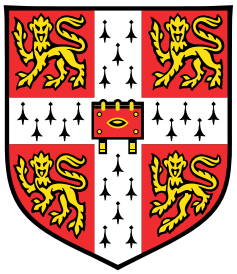

Christopher Wilkes

Department of Engineering
University of Cambridge

This dissertation is submitted for the degree of
Doctor of Philosophy

Darwin College

January 2021

Declaration

I hereby declare that except where specific reference is made to the work of others, the contents of this dissertation are original and have not been submitted in whole or in part for consideration for any other degree or qualification in this, or any other university. This dissertation is my own work and contains nothing which is the outcome of work done in collaboration with others, except as specified in the text and Acknowledgements. This dissertation contains fewer than 65,000 words including appendices, bibliography, footnotes, tables and equations and has fewer than 150 figures.

Christopher Wilkes
January 2021

Abstract

Modelling Tremie Concrete Placement in Deep Foundations

Christopher Wilkes

Cast-in-place foundations are typically constructed using the Tremie Method of concrete emplacement. A pipe and hopper system is used to fill an excavation from the base up with a specialised, highly workable concrete called Tremie Concrete.

In this thesis, numerical modelling and experimental analysis are employed to define what conditions encourage the occurrence of defects in cast-in-place foundations. Two numerical methods were chosen to simulate concrete: Computational Fluid Dynamics (CFD) and the Material Point Method (MPM).

A new thixotropic model integrating the Papanastasiou-Bingham model with thixotropy equations was developed, enabling the simulation of thixotropic behaviour of Tremie Concrete in the Material Point Method framework. The novel model revealed a decline in concrete workability during simulations of the Slump-flow and L-box tests after a period of rest which the physical version of the test fails to capture.

A classification system of flow behaviours which relies on a scale of flow restriction was developed based on CFD simulations of concrete flow in a novel apparatus designed to represent conditions closer to those found in cast-in-place foundations. Additional simulations of the same apparatus in MPM found the effect of thixotropy and the addition of a support fluid represent further restrictions to flow that can lead to defective foundations.

In summary, defects within deep foundations associated with the flow behaviour of concrete during the Tremie Method can be predicted based on the level of restriction to flow the concrete will experience.

Acknowledgements

First and foremost, I would like to extend my sincerest gratitude to my supervisor, Dr Giovanna Biscontin. This work would not have been possible if not for her steadfast belief in me along every step of my PhD journey. For this, I am honoured and forever grateful. I must also thank Dr Krishna Kumar; his numerical expertise, continued mentoring, and friendship throughout my PhD have been a constant source of inspiration for which my thanks cannot be overstated.

Many thanks are given also to: Duncan Nicholson, Aidan Thorp, Chris Barker, and Shahid Padhani of ARUP for their insightful discussions and guidance on the project. This work was made possible with the generous funding of the EPSRC ICASE (ref: 1769998) which I am grateful to have been given. I also thank CEMEX UK and BASF for the provision of materials. I would also like to thank the hard work of the MEng students I had the pleasure of advising: David, Jin, and Irina. To the CB-Geo community, Professor Kenichi Soga and Ezra Setiasabda, I extend my warmest thanks for all the advice and discussions, of which I have certainly benefited. To my colleague and friend, Charalambos Konstantinou, thank you for four years of camaraderie.

On a different note, I also extend thanks to all my friends in the Darwin College community and the Darwin College Boat Club. James, Felipe, Charles, and Sarah - thanks for making Cambridge life all the more richer. To my friends at Queens, Andrej and Piet, thank you for the long lunches and longer discussions on our work. My heartfelt thanks also go to the love and support of family, my brother Robert, my sister Laura, and my Parents: Tracey and David. For our lockdown family FaceTimes, my sanity thanks you.

To James, Robert, William, Richard, Tucker, and George: For the memories we have shared along the way, for the personal growth you have afforded me, and for all the motivation you have given me to succeed, I am indebted to you.

Finally, to Isabelle: Had it not been for you, a year of lockdowns may have bested me. Thank you for all you have done for me.

Table of contents

List of figures

List of tables

Nomenclature

Roman Symbols

$\dot{\varepsilon}$	Strain rate tensor
η	Apparent viscosity
$\mathbf{B}$	Strain-displacement B-matrix
$\mathbf{D}_{ij}$	Rate of deformation tensor
$\mathbf{L}_{ij}$	Velocity Gradient
$\mathbf{S}$	Vector of the surface of the Control Volume
$\mathbf{U}$	Three dimensional mixture velocity field shared by all phases
$\mathbf{U}_f$	Surface velocity
T	Traction
^{T}	Transposed (superscript)
A_{thix}	Restructuring rate at rest
c_p	Compression wave velocity in an isotropic elastic continuum
E	Young's modulus
E_c	Constrained modulus
F	Surface tenstion force

G	Shear modulus
h	Height
J	Jacobian
K	Bulk Modulus
L_e	Element Length
m	Papanastasiou regularisation parameter
P	Pressure
p_0	Initial thermodynamic pressure
r	Radius
T	Torque
t	Time
u	Velocity
v	Poisson ratio
W_{ij}	Spin tensor
$\mathbf{a}$	Acceleration
$\mathbf{b}$	Body force
$\mathbf{v}$	Velocity
N	Shape function
n	Number of nodes or points
p	Position of a material point / node
w	Weight function / test function
SF_0	Slump-flow spread 0 s

SF_{240} Slump-flow spread 240 s

Greek Symbols

α Destruction parameter

$\alpha\prime$ Volume of fraction marker

δ_{ij} Dirac Delta function

$\dot{\gamma}$ Shear rate

ε Strain

κ Curvature

λ Flocculation state

λ_0 Previous or Original Flocculation state

μ_0 Pre-yield viscosity

Ω Domain under consideration

ρ Mass Density

σ^s Surface tension coefficient

σ_{ij} Total Stress

τ Shear Stress

$\tau_{0_{dynamic}}$ Yield Stress no rest

$\tau_{0_{static}}$ Yield Stress after rest

τ_0 Yield Stress

$\tau_{apparent}$ Apparent Shear Stress

$d\varepsilon_v$ Volumetric strain

τ_{ij} Deviatoric stress tensor

σ Cauchy's stress tensor

Acronyms / Abbreviations

rt Rest Time

A240 Mix A at 240 s

A60 Mix A at 60 s

B240 Mix B at 240 s

B60 Mix B at 60 s

C240 Mix C at 240 s

C60 Mix C at 60 s

CFD Computational Fluid Dynamics

CFL Courant-Friedrichs-Levy

CSF Continuum surface force

CV Control Volume

DEM Discrete Element Method

DFE Distance From End of flow in L-box

DFI Deep Foundation Institute

EFFC European Federation of Foundation Contractors

FC Friction Coefficient

FEM Finite Element Method

FT L-box Flow-time 0 s

FT_{240} L-box Flow-time 240 s

FT_{60} L-box Flow-time 60 s

FVM Finite Volume Method

GFB Gravity Flow Box

GIMP Generalised Interpolation Material Point Method

GUI Graphical User Interface

H1 Concrete depth, vertical L-box Chamber

H2 Concrete depth, horizontal L-box Chamber

$H2_0$ Concrete depth, horizontal L-box Chamber 0 s

$H2_{240}$ Concrete depth, horizontal L-box Chamber 240 s

$H2_{60}$ Concrete depth, horizontal L-box Chamber 60 s

HB Herschel and Bulkley

HPC High Performance Computing

ICE Institution of Civil Engineers

MPM Material Point Method

MUSL Modified Update Stress Last

NSE Incompressible Navier-Stokes equation

PIMPLE The Pressure Implicit with Splitting of Operators

PPC Points Per Cell

PR-Bingham Papanastasiou-Roussel Bingham

SCC Self Compacting Concrete

SF Slump-flow Spread

SIMPLE Semi-Implicit Method for Pressure-Linked Equations

SPERWall Specification for Piling and Embedded Retaining Walls

TC Tremie Concrete

UML Unified Modelling Language

USF Update Stress First

USL Update Stress Last

VOF Volume of Fluid

VSI Visual Stability Index

Chapter 1

Introduction

The process of constructing reinforced concrete piles and diaphragm walls relies upon the Tremie Method. The Tremie Method utilises a pipe and hopper system to fill an excavation from the base up with a specialised, highly workable concrete called Tremie Concrete. Stability of the shaft is maintained by a support fluid exerting over-pressure on the excavation walls to prevent collapse. Although the method is conceptually simple, the behaviour of the fresh concrete once it leaves the tremie pipe is not well understood.

A growing number of projects within the UK and worldwide are incurring time and cost delays upon discovering defects within finished foundations and wall panels. Defects typically present as superficial channels forming a crosshatch pattern called matressing (due to the visual similarity between the resulting pattern and the indentations on a spring matress) where concrete flow around reinforcement bars has been inadequate, foreign material inclusions, or changes to a concrete's degree of homogeneity; all of which will affect durability at best, and structural performance at worst.

Increasingly, the behaviour of concrete is examined through numerical analysis of the construction operation [47, 101, 52, 125, 104]. This is undertaken with the expectation that knowledge of concrete flow behaviour will allow the development of simplified methods of assessment to ensure successful construction.

1.1 Background

The typical process of casting a deep foundation pile begins with the initial excavation of a shaft, fig. 1.1a. This can be done by a multitude of different methods like drilling auger or

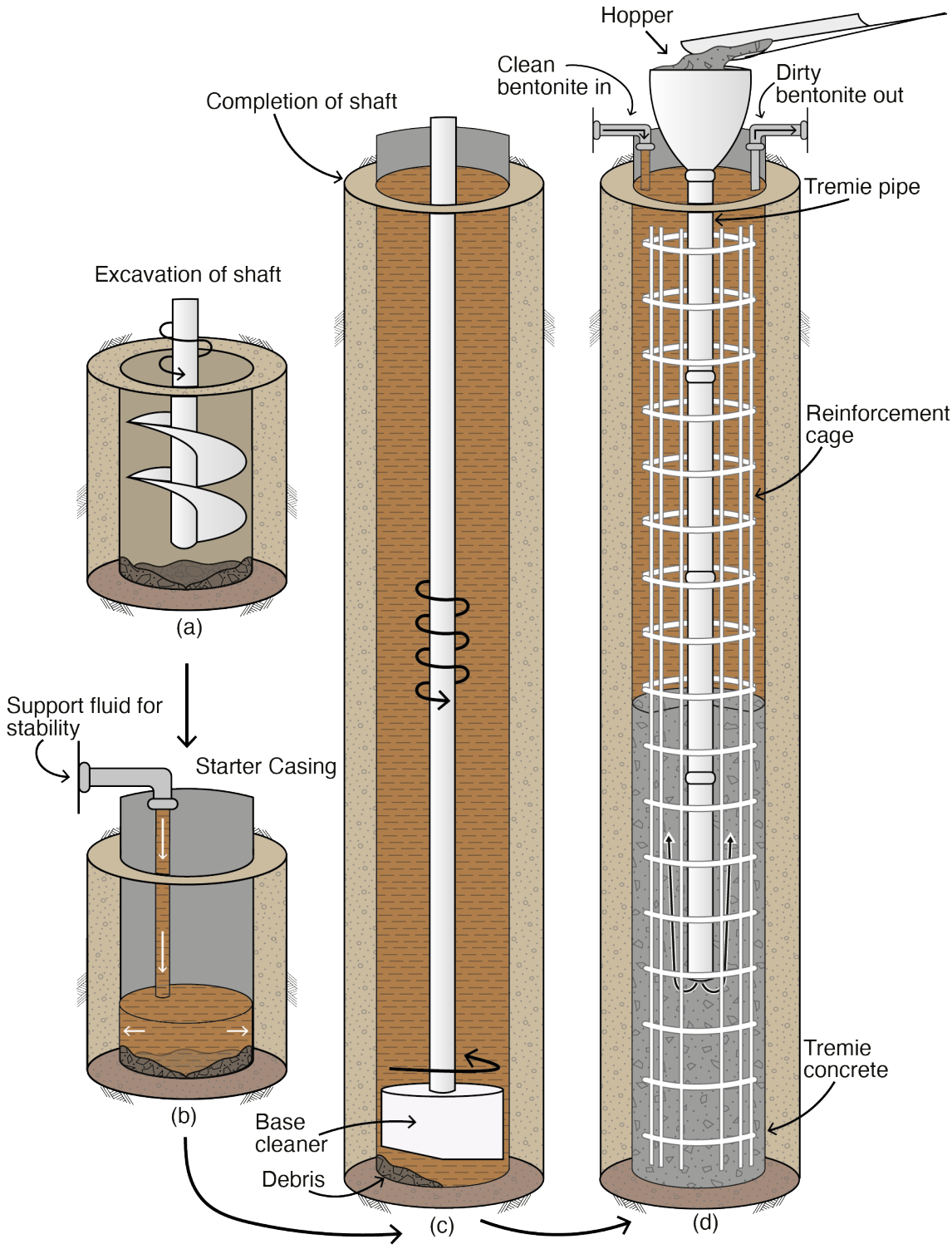

Fig. 1.1 Schematic diagram of the tremie method used to cast a bored pile under support fluid.

grab excavation. Support fluid is added to stabilise the excavation and prevent the collapse of the shaft by maintaining an over-pressure, fig. 1.1b. A bentonite slurry is typically used but the use of polymer support fluids is steadily increasing. A casing may also be used for part of an excavation if the upper soils are weak and need additional support. With the addition of the support fluid, the excavation can be completed to the target depth, fig. 1.1c. The base must be cleaned upon completion of the shaft excavation as end bearing capacity often represents the majority of the axial resistance in many cases, [24]. With the excavation complete, the Tremie Method can begin, fig. 1.1d.

Depending on the function of the pile, it may be necessary to use a reinforcement cage. This is typically done before concreting although some variations of the Tremie Method that still use Tremie Concrete, like the continuous flight auger method, may plunge the cage into fresh concrete. Once the cage is in place, the concreting commences. Concrete is poured into a hopper that is connected to a system of pipes extending to the base of the shaft. It is required that the Tremie Pipe is charged (full of concrete) at all times [66], thus, to prevent the intermixing of concrete and support fluid a 'plug' (often a bag of vermiculite) is used to maintain separation before the flow begins. The pipe can be raised from the base no more than the diameter of the pipe (around 250 mm) to initiate flow and to allow the plug to flow to the surface. The Tremie pipe is periodically raised as the concrete level rises so long as the base of the pipe remains embedded no less than 3 m into the concrete. As the concrete rises it will displace the bentonite support fluid which is continuously cycled and cleaned throughout the casting process to maintain a clean solution.

Unless in a specific set of circumstances, such as a basement excavation or retaining wall, the finished foundations are rarely exposed. Nevertheless, walls that are exposed are routinely found to contain defects. Any defects present in un-excavated foundations are concealed until testing is undertaken. Even then, it may not be possible to test every foundation on a site. When a defect is detected, however, it it can prohibitively expensive to remedy and may require the casting of additional foundations. Using numerical models to predict the performance of concrete can help to understand the problem and reduce the occurrence of defects.

Continuous and discrete numerical methods have been modified to be able to model Concrete behaviour, though they are not without limitations. These include scalability concerns, sub-optimal descriptions of the material, and performance hindering levels of mesh distortion occurring to due large scale deformation of the continuum. Continuous methods are suitable for large scale problems but may struggle simulating less workable concrete where inter-granular relationships become more important. Discrete particle methods that represent

concrete as individual particles capture the micro-scale behaviour accurately, however, these methods are computationally intensive and cannot always be scaled to the full field-scale required. Concrete properties are demonstrably time and stress dependent, in both short term (thixotropy) and long-term (hydration), however, the simulation of time-dependent concrete behaviour has been hindered due to a combination of method limitations or complexity of implementation. Therefore, the absence of this functionality is a fundamental barrier to accurately simulating the flow behaviour of concrete.

Hybrid methods that seek to combine the benefits of multiple methods to reduce the overall limitations are growing in popularity but many remain in the developmental stage. The Material Point Method (MPM) [111, 112] is an emerging numerical method capable of simulating large scale deformations in addition to the previously discussed time/stress-dependent properties of concrete. The Material Point Method combines the benefits of mesh based and mesh-less approaches to provide a unique framework to simulate concrete. This method will be used extensively to simulate different concrete testing methods and concrete behaviours throughout this work.

Computational Fluid Dynamics, a continuous and typically mesh-based method, represents the most popular method of simulating concrete flow behaviour. The most common CFD method of simulating concrete uses the finite volume method (FVM) of domain discretisation and the volume of fluid (VoF) method to determine the boundary of the concrete. However, there are two notable limitations to consider: First, the simulation of time/stress-dependent behaviours may not be possible. Second, modifiable frictional boundary conditions are not possible in many software packages, if at all. Despite these limitations, CFD simulations remain the standard of which other numerical methods must meet. Thus, simulations in MPM that do not consider the time dependent nature of concrete properties should be compared with CFD simulations of similar conditions to validate their performance.

1.2 Objectives of Research

The main objective of this work is to use numerical modelling to define what conditions encourage the occurrence of defects in cast-in-place foundations. Specifically, the objectives were to:

- Determine the effect stress/time-dependent concrete behaviour has on the flow behaviour of Tremie Concrete by using the CB-Geo MPM code.

- Use the OpenFOAM® Computational Fluid Dynamics package to determine the controlling factors on concrete flow within deep foundation conditions.

Accurate simulation of Tremie Concrete within the CB-Geo MPM code required three developments: Implementation of the Generalised Interpolation Material Point Method, an improved 3D friction algorithm, and the creation of a constitutive model capable of representing the time/stress-dependent behaviour of Tremie Concrete.

1.3 Thesis Organisation

This thesis is organised into seven chapters, including the present introductory chapter, Chapter 1, and is organised as follows:

Chapter 2 provides an overview of the Tremie process, including a review of the literature on the current state of investigations into flow behaviour of Tremie Concrete. A review of both concrete testing methods and concrete rheology is also provided.

Chapter 3 presents the methodology used in this research, beginning with a summary of current techniques in numerical modelling of concrete, together with their advantages and disadvantages. The selection criteria for a numerical model capable of simulating Tremie Concrete is presented and the chosen numerical models discussed. The Material Point Method framework is reviewed in detail with context given to necessary developments and modifications made to the CB-Geo MPM code in order to successfully simulate concrete. The numerical framework of the OpenFOAM® Computational Fluid Dynamics package is also given.

Chapter 4 presents a novel testing apparatus capable of capturing the early flow behaviour of concrete flow in a deep foundation. The experimental apparatus is also simulated using OpenFOAM® so that the physical and experimental results can be compared and contrasted. A new classification method of concrete flow behaviour is given as a result of the work performed in this chapter.

Chapter 5 begins with the development of a new constitutive model that allows for the simulation of time-dependent concrete behaviour in MPM. This model is subsequently used to simulate the behaviour of concrete in the Slump-flow test. A rest period is added into the simulated concrete to measure the influence of time-dependent behaviour on the test results. Physical and numerical results are compared to ascertain the viability of the Material Point Method and the effect of thixotropy on concrete behaviour.

Chapter 6 combines simulations of the L-box test with the novel apparatus discussed in Chapter 4 to allow for an assessment to be made on the effect stress/time-dependent behaviour has on the ability of concrete to flow adequately in a deep foundation.

Chapter 7 concludes this work with a review of the findings and makes recommendations for future researchers.

Chapter 2

Literature Review

2.1 Introduction

An in-depth review of appropriate literature is conducted to assess the current understanding of Tremie concrete behaviour and how numerical modelling can help identify the conditions likely to cause foundations defects. A detailed overview of the tremie process, concrete rheology, and concrete testing methods is presented.

It is worth noting that within this chapter, concrete as a viable construction material is not considered. Mix design and the resulting impact on strength and durability are also not considered. This work focuses mainly on the mechanical behaviour of tremie concrete as a flowable medium.

2.2 Tremie Process

2.2.1 Stages of the Tremie Process

Whilst the material properties of concrete may lead to defects arising during the casting process of deep foundations, they are not the only factor to consider. The tremie method itself is known to have direct influence, hence the stringent process recommendations made by [66].

There are three distinct phases to the tremie method: flow initiation, during flow, and post placement. Within each phase, the concrete behaves differently. For example, during the flow initiation phase, the rapid onset of flow may cause tremie concrete to come into contact

with debris or mix with the support fluid. Whereas, when a steady flow has been established the concrete will be moving slowly and encountering the reinforcement cage. During the post placement phase, concrete will be subject to low shearing forces allowing for gravity driven processes like static segregation to occur, where the sinking of denser elements of the concrete mix could cause a reduction in concrete homogeneity.

The top row of fig. 2.1 introduces each of the the three stage of the tremie process, whilst the second row indicates how an improved understanding of the stage above might translate into practical applications.

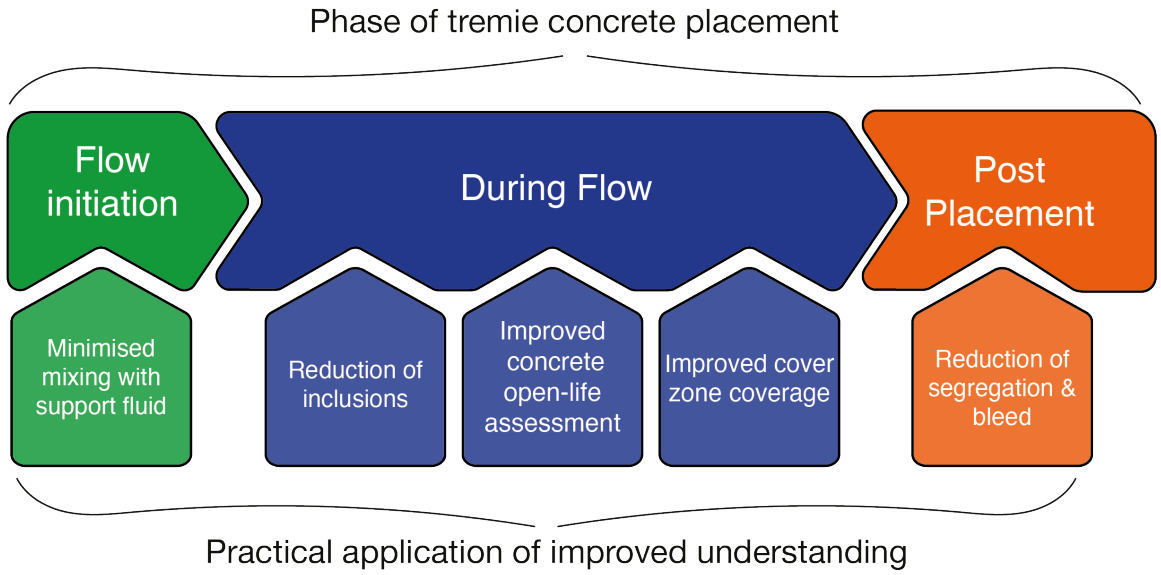

Fig. 2.1 Top row: Phases of tremie concrete process. Bottom Row: Practical applications of an improved understanding of the above phase.

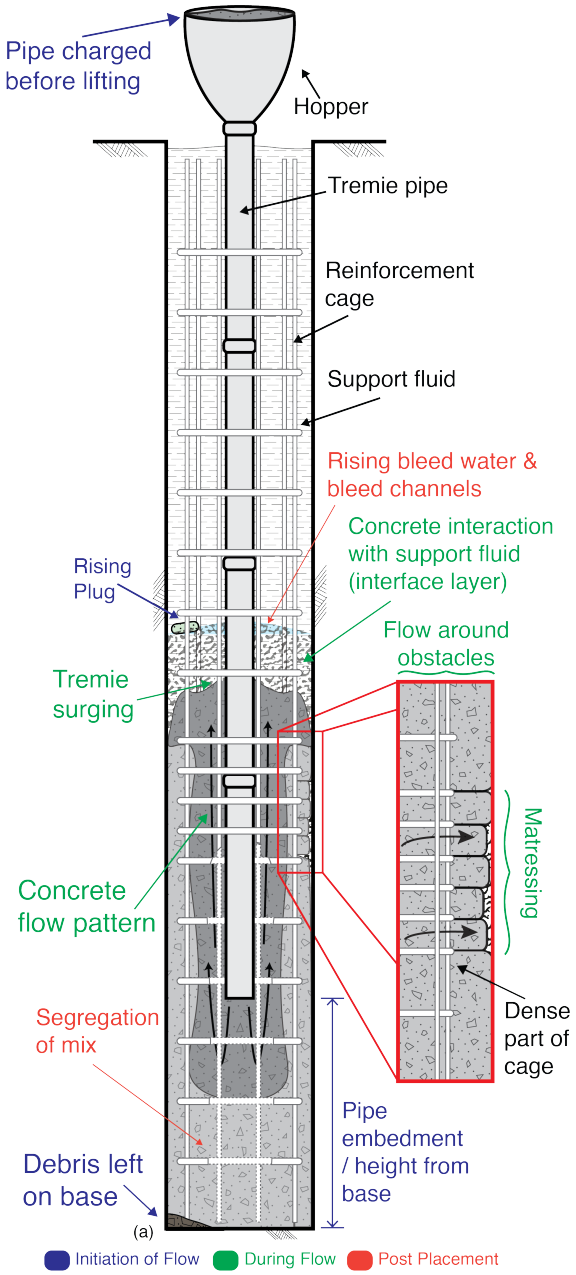

Fig. 2.2 (a) Schematic diagram of a bored pile cast using tremie method, with areas of investigation highlighted and colour coded.

Figure 2.2 is a schematic diagram of a bored pile in which specific areas of investigation and how they relate to the stages of the tremie process are highlighted. Attention is also drawn to the impact of insufficient flow around obstacles causing a matressing effect.

Table 2.1 combines the different areas of investigation within each phase, with the associated improvement that a greater understanding could provide to the industry. The possible

causes of issues within the flow initiation phase are more equipment and process oriented. Conversely, during the flow phase it is the material properties that appear to have the greatest impact.

Table 2.1 Comparison of phase, area of investigation and impact of understanding for the tremie process.

Phase of Tremie concrete placement	Area of investigation	Practical impact of understanding
Flow Initiation	Pipe charged before lifting Using a plug to initiate constant flow Tremie pipe height from base	Minimise mixing with support fluid, reducing inclusions
	Debris left on base	Improved end-bearing capacity
During Flow	Dominant flow pattern of concrete	Reduced open-life requirements Improved casting process
	Concrete interaction with support fluid interface layer	Reduced Inclusions
	Concrete flow around obstacles	Improved Cover-zone coverage
	Dynamic segregation	Improved homogeneity
Post placement	Bleed water and bleed channels	Reduced dewatering
	Static Segregation	Improved homogeneity

As discussed in Chapter 1, the present study seeks to utilise numerical modelling techniques to further the understanding of the tremie process and tremie concrete and determine the conditions likely to cause foundation defects. The "During Flow" phase of the tremie process appears to be the period where most serious defects occur. Thus, the focus of this work should be on how the concrete behaves during the filling of the excavation.

2.2.2 During Flow of Tremie Concrete

In the tremie method, Tremie Concrete (TC) is emplaced into the foundation in batches with the time between concrete loads spanning from minutes to hours. The bulk flow behaviour of newer TC entering a part-cast foundation with TC already in-place is commonly described as a concrete *flow pattern*.

The European Federation of Foundation Contractors and The Deep Foundation Institute (EFFC and DFI) [47] identify two flow patterns of concrete that can occur during the tremie process: Plug-flow and Bulging-flow, fig. 2.3. Plug-flow, fig. 2.3a, takes its name from the occurrence of a rising plug of older concrete atop the concrete column. This plug rises upwards on top of the new flow front while it ascends and older concrete is displaced by newer batches exiting the pipe below. At its most extreme, this plug could represent a non sheared and resting unit of concrete that can struggle to flow adequately. Many contractors will artificially increase the setting-time of concrete using superplasticizers to prevent Plug-flow from occurring. Unfortunately, it was recently recognised by Thorp et al. [118] that an extended setting time will increase static and dynamic segregation. Letting the plug of old concrete rise through the pile is not always desirable as the low level of workability will prevent adequate flow of the concrete and increase the force needed to displace the concrete. If plug flow is occurring where reinforcement is present there is a higher chance of poor flow around reinforcement bars and the defects associate with such behaviour. However, some consider plug flow to be the more favourable flow behaviour as it could minimise concrete interaction with support fluid if the plug can adequately displace the interface layer upwards as the flow rises [76].

A concrete which has undergone segregation will see a notable decrease in structural integrity and strength through shrinkage, as well as the development of nonuniform compressive strength profiles [27]. Identifying the conditions that cause Plug-flow may help to reduce the need for superplasticisers in some situations.

Bulging-flow, considered to be the most likely flow behaviour, is a vertical, laminar flow of concrete following the path of least resistance, which is broadly confined to the area surrounding the tremie pipe, fig. 2.3b, [47]. Although it is expected that concrete will breach the head of the flow at some point during the process, during venting the path of least resistance becomes confined to the area immediately surrounding the tremie pipe, rather than extending to a broader area. High velocity venting concrete can breach the interface layer (a mixture of support fluid and concrete) sitting atop the concrete head causing inclusions of un-cemented interface material. Repeated head breaches during the course of normal bulging flow, or the presence of a concrete vent could increase the likelihood of interface material becoming included in the finished product. Inclusions of the interface layer within the foundation can lead to durability issues or the potential for reduced bearing capacity [47].

Another consideration to make when identifying the risks associated with bulging flow is the occurrence of a flow-front differential: The height difference between the concrete inside the cover zone and that closest to the pipe. A front-differential can cause a trough to form in

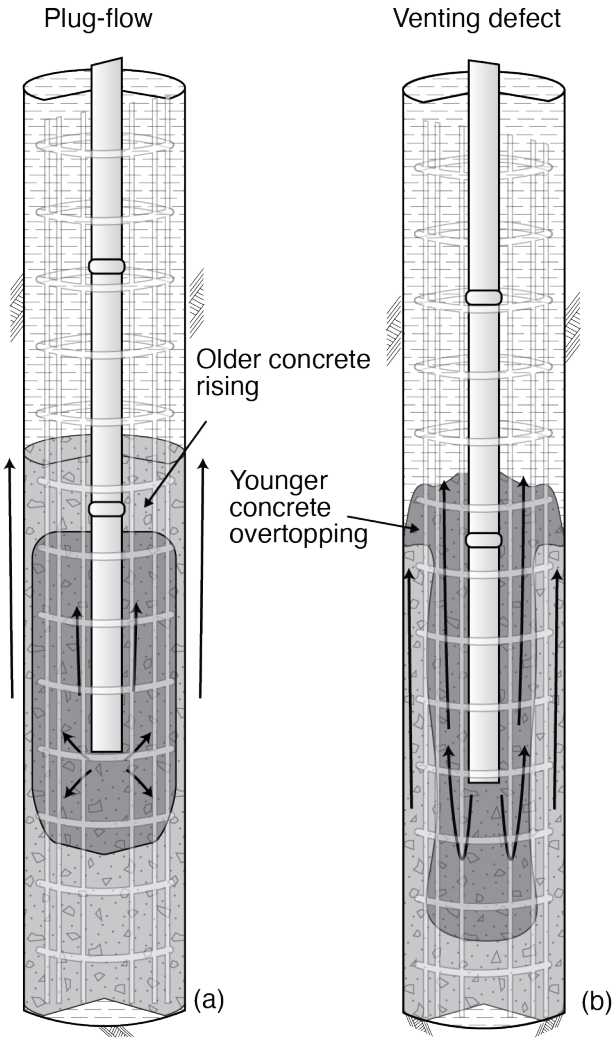

Fig. 2.3 Schematic diagram of the to ultimate state flow patterns, a) Plug flow, b) Venting defect at the ultimate state of bulging flow.

the cover zone where material can easily become trapped. This material can originate from the excavation walls, the filter cake (mixture of support fluid and excavation walls) or the interface layer that is becoming enveloped as the concrete flows around the reinforcement bars horizontally (as apposed to rising vertically) [86].

EFFC and DFI [47] propose that resistance to flow in the form of a dense reinforcement cage or high frictional boundary conditions may cause the realisation of one style over another. However there are few field or laboratory studies available to support their hypothesis.

Fierenkothen and Pulsfort [53] combined numerical modelling with laboratory experiments in order to identify which flow style is the most likely to occur in a given set of circumstances. For a reinforced pile, shell-shaped behaviour similar to bulging-flow was proposed as the dominant flow style. However, [53] did not have access to real-time experimental footage, instead relying on back-calculations from the finished product. Bohle and Pulsfort [18] also attempt to determine flow-styles post curing, opting to excavate and bisect pile-scale samples to expose multiple concrete influxes. A shell-like behaviour of rising concrete was also offered as the main filling pattern in [18].

The numerical simulations discussed correlate well with cured samples, however, they remain partially invalidated as no footage of the tremie process exists for comparison. If real-time physical and validated numerical evidence of concrete flow patterns supports the boundary condition hypothesis of [47], foundations can be designed in such a way as to avoid flow-pattern related defects. The following section details a novel experimental apparatus capable of providing flow conditions similar to those found in a cast in situ pile.

2.3 Tremie Concrete

Tremie concrete is similar to traditional self compacting concrete (SCC), thus, has similar durability and strength requirements which often lead to the specification of higher strength classes and lower water/cement ratios. Additional requirements are placed on workability and stability to prevent defects occurring during the placement of concrete. ICE [66] like many other British and European standards refer to concrete in terms of workability, consistence, and stability: qualitative terms used to empirically describe the behavioural properties of concrete. It is, however, accepted that although these terms are long-standing [116], they may not be the most appropriate due to their subjectiveness. It is beneficial to describe concrete using some other metric that can quantify the target behaviours, such that concretes of differing mix designs can be compared with relative ease. The most appropriate method

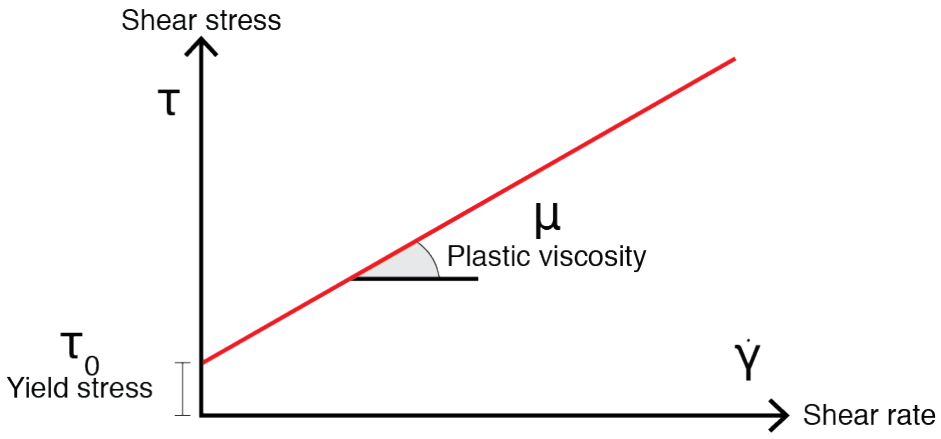

Fig. 2.4 Relationship of Bingham parameters.

for doing this is to quantify concrete in terms of its flow behaviour, or as it is more commonly known, its rheology.

2.3.1 Rheology

Tattersall [115] first presented the possibility of using a more quantitative approach to analysing concrete by using a simple model to describe two key functionalities of concrete; the stress required for it to flow, and the rate at which the flow propagates. This can be expressed using the Bingham model, eq. (2.1):

$$\tau = \mu\dot{\gamma} + \tau_0\,, \tag{2.1}$$

where τ represents the shear stress, τ_0 the yield stress, μ the plastic viscosity and $\dot{\gamma}$ the shear rate. The yield stress, τ_0, represents the initiation force needed to commence flow. In the Bingham model, materials experiencing stresses below critical yield stress behave akin to rigid bodies with viscoelastic effects, whilst stresses that exceed the yield criterion cause the material to behave as a viscous liquid [98]. The relationship of shear stress and shear rate is demonstrated in fig. 2.4. The two-fold nature of a Bingham material is a form of viscoplastic behaviour.

A balance must be struck when designing a tremie concrete mix to account for all of the desired behavioural traits of the concrete. It must be workable enough to flow easily and self level without the need for vibration, but it must also be able to withstand shearing forces that could cause segregation of concrete into its constituent elements. Often, this means that the yield stress must be low enough to allow for workability constraints, but not so low as the

material cannot support itself and begins to segregate. Similarly with plastic viscosity, the slope of fig. 2.4, if it is too high the concrete will not flow with ease. Conversely, if it is too low, stability concerns will arise.

Even with the tight controls on Tremie concrete rheology, there is still a considerable degree of variability of acceptable concrete properties. This is largely because concrete is approved for use by means of empirical testing rather than rheology.

In general, Tremie Concrete has a yield stress of 50-150 Pa and a plastic viscosity of approximately 20-50 $\mathrm{Pa\,s^{-1}}$ [74, 50, 118]. However, the rheological properties of concrete are stress and time dependent, thus, they are not constant. Left undisturbed, tremie concrete yield stress will increase during the dormant period of the hydration reaction [96, 103], leading to a reduction in the ease with which it can flow. Fortunately, the loss of mobility due to stiffening can be partially recovered with an application of stress, so long as the applied stress is significant enough to break down the hydration byproducts causing the elevated strength [103]. The temporary reduction in concrete mobility that can be alleviated by stress application is referred to as thixotropy, discussed in the following section.

2.3.2 Thixotropy

The yield stress of a cement-based material like concrete originates from the micro-structure of cement particle-particle networks through colloidal interactions or direct contact between cement particles [93]. This micro-structure can sustain a certain amount of stress before it is broken down and starts to flow. In concrete, the resistance to flow due to the micro-structure is defined as the Bingham yield stress [96]. At rest, this micro-structure will continue to build up due to colloidal flocculation and calcium silicate hydrate (CSH) bridges forming between particles as a result of partial hydration of cement [103], resulting in increased yield stress [78], and therefore, is the origin of thixotropy. When sufficient shear force is applied, the micro-structure will begin to break down, causing the elevated yield stress to dissipate to a constant yield stress upon which no further breakdown of the structure is possible. The temporary increase in yield stress after a period of rest is referred to as the '*static*' yield stress, while the constant yield stress observed once the elevated level has dissipated is referred to as the '*dynamic*' yield stress [93]. Figure 2.5 is a schematic of how yield stress may increase over time. Generally, short-term increases in yield stress are assumed to be linear. A time-dependent A_{thix} may be appropriate for longer rest times, however, for the purposes of this work only short-term (minutes, rather than hours) thixotropy is considered, thus, a linear assumption is acceptable.

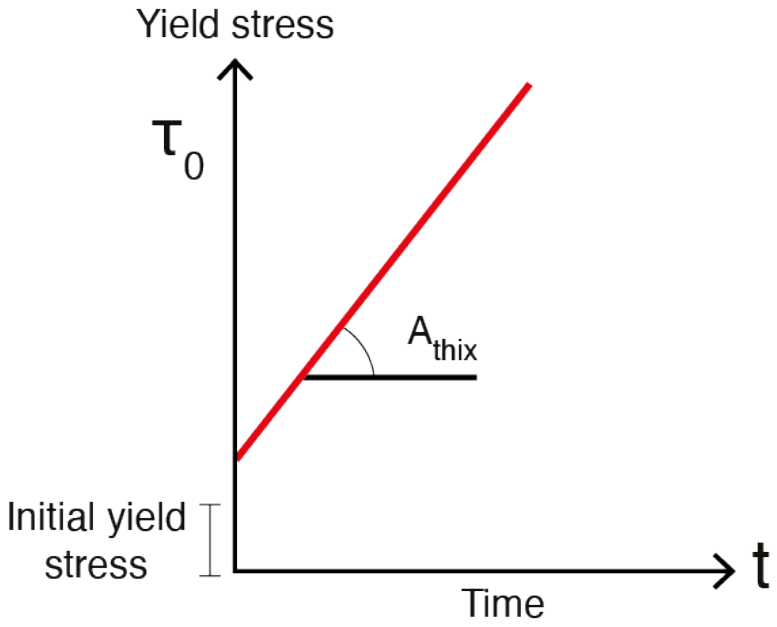

Fig. 2.5 Relationship of Thixotropy parameters.

Roussel [96] proposed a series of equations to characterise the influence of thixotropy on yield stress. Incorporating a flocculation state λ in eq. (2.1) gives:

$$\tau = \mu\dot{\gamma} + (1+\lambda)\tau_0, \tag{2.2}$$

$$\frac{\partial\lambda}{\partial t} = \frac{1}{\tau_0/A_{thix}} - \alpha\lambda\dot{\gamma}, \tag{2.3}$$

where A_{thix} is the restructuring rate at rest and α is the destruction parameter (typically of the order 0.01) [100]. Considering the rate of build-up of the micro-structure is relatively long compared to the rate of destructuration, as reported by [91, 96], eq. (2.3) becomes:

$$\frac{\partial\lambda}{\partial t} = -\alpha\lambda\dot{\gamma}. \tag{2.4}$$

integrating eq. (2.3), we get:

$$\lambda = \lambda_0 e^{-\alpha\dot{\gamma}t}, \tag{2.5}$$

where, t is time spent at a particular shear rate and λ_0 is the original flocculation state. A measurement of torque from a rested concrete can be used to obtain the three thixotropic parameters needed for eq. (2.2)-eq. (2.5)(λ, α and A_{thix}),

One potential way of obtaining torque measurements directly is by using a rotational rheometer. In a rotational rheometer, the material is sheared between two surfaces, one undergoing

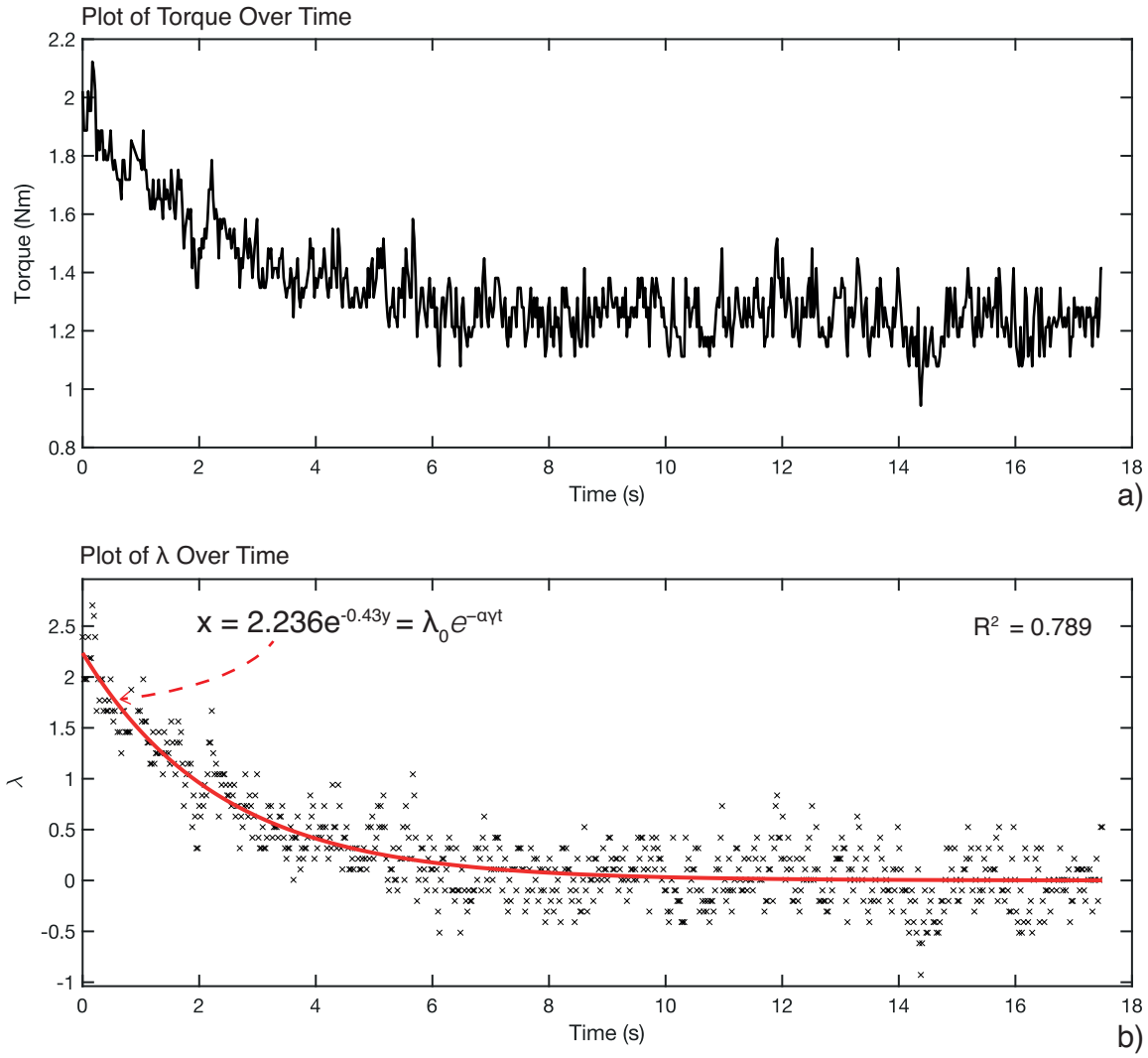

Fig. 2.6 a) Evolution of torque with time, measured by a rotating vane submerged in Tremie Concrete, with a shear rate of 12.43 s^{-1}. Torque decaying over time to a constant average. b) Evolution of λ over time with a fitted exponential curve. Data provided by internal communications with ARUP.

rotation. Both the speed and torque are recorded. Rheometers can be either stress-controlled where torque is controlled but speed measured or rate-controlled, where speed is regulated and torque monitored. Rotation speed can be converted into a shear rate while torque is converted into a shear stress [98]. Most commercially available concrete rotational rheometers are rate controlled. One shear surface rotates at a controlled speed and the resistance of the material is measured as torque. The test involves an increase and decrease in speed and a measurement of the response. There are however concerns an apparatus measuring rheological parameters may use calibration variables, of which the understanding is not fully known [46].

Vane rheometers are the most common rotational rheometers due, in part, to their relative simplicity and economical cost. However, they are sensitive to internal and external influences [16].

An impeller is submerged in a container filled with the material to be tested and rotated at various speeds. The resistance of the material to the rotation is measured on the impeller. Among the first to employ this technique to concrete were Tattersall and Bloomer [117] who developed the 'Two-Point Test' as a means to represent concrete by its Bingham properties. An advancement to this test is proposed by Koehler and Fowler [71] and Koehler et al. [73] in the form of the ICAR rheometer. Developed to be able to handle a material closer to tremie concrete. This rheometer consists of a four-blade vane rotating in a bucket with space between the vane and the bucket. The ICAR rheometer has been used in numerous studies since its inception and is now widely used throughout the industry to measure concrete rheology.

Figure 2.6a shows a gradual decay in observed torque with time for a Tremie Concrete using an ICAR [72] rheometer at a site within the United Kingdom. Bingham parameters are then derived from the torque and rotational velocity using the Reiner-Riwlin equations [129, 49].

For a thixotropic concrete, observed torque, T, will gradually decay from an elevated initial measurement to a stable average reading. In fig. 2.6a, torque reduces from approximately 2 N m to 1.25 N m during rotation of the vane (shearing), until a stable mean average is achieved after approximately 10 s. The reduction from 2 to 1.25 N m, assuming a constant rotational velocity of the vane, indicates the transition from static yield stress to dynamic yield stress. To relate torque to Bingham parameters, so that the thixotropic parameters may be calculated, the apparent shear stress (defined as a function of the observed torque T, radius r and height h of the vane) must be assessed first. The apparent shear stress is a direct measurement of the shear stress calculated from torque in a rheometer as shown below:

$$\tau_{apparent} = \frac{T}{2\pi r^2 h} = \mu\dot{\gamma} + (1+\lambda)\tau_0\,, \tag{2.6}$$

Following the RH side of eq. (2.6), $\tau_{apparent}$ can be used to calculate a flocculation state λ for any given apparent shear stress. Thus, by taking $\tau_{apparent}$ at different time intervals and using it to calculate the corresponding flocculation state of the concrete, a λ/time plot can be generated, fig. 2.6b. At the maximum λ, the elevated static yield stress can be calculated as:

$$(1+\lambda)\tau_{0_{dynamic}} = \tau_{0_{static}}\,. \tag{2.7}$$

Despite the level of noise measured by a rheometer, an exponential best-fit curve can be applied to the λ/time plot (fig. 2.6b) where the corresponding equation of the curve can be used to generate an approximation of α. To do this, the exponent, 0.43, from fig. 2.6b is divided by the known constant shear rate, 12.43 s^{-1}, as per eq. (2.5), to yield an approximate α of 0.0358 for this particular concrete.

Two out of the three thixotropic parameters are now identified. The remaining variable, A_{thix}, which represents the rate at which yield stress increases over time (Pa s^{-1}), can be calculated using the static yield stress obtained by eq. (2.7) to give:

$$A_{thix} = \left(\tau_{0_{static}} - \tau_{0_{dynamic}}\right)/rt\,. \tag{2.8}$$

A_{thix} is used as a single value representing the thixotropic propensity of concrete, where a value of $A_{thix} > 0.5$ is considered to be highly thixotropic [96].

2.3.3 Measurement of Fresh Concrete Rheology

Tests determining properties of concrete are used extensively on-site with much credit given to the results, potentially leading to concrete batches being discarded if they do not meet the required performance standards. Tests are designed to assess two key aspects of a concrete: consistence and stability. Consistence refers to the flowability of a concrete and stability refers to the ability of a concrete to resist segregation [66].

Segregation within concrete is defined by the measured ability of concrete to maintain uniformity against forces applied during emplacement (dynamic segregation) and when the concrete is at rest (static segregation) [123]. A concrete which has undergone segregation will see a dramatic decrease in structural integrity and strength, [85].

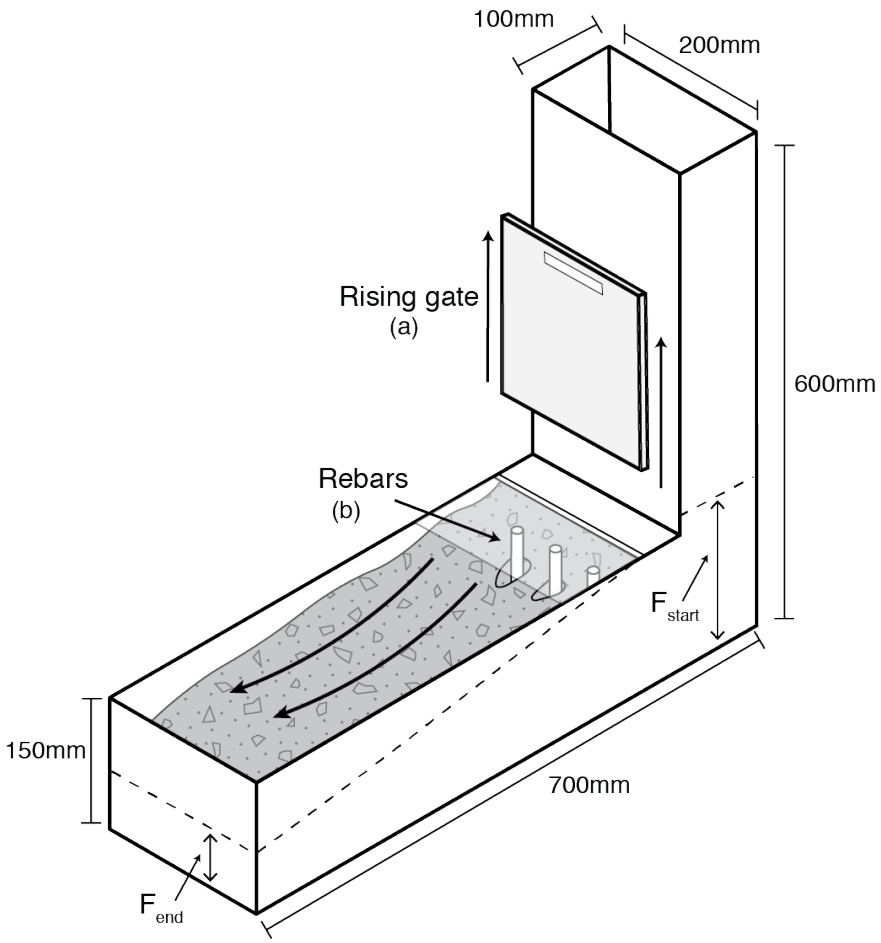

Fig. 2.7 L-box test apparatus. a) Rising gate to initiate concrete flow b) Rebars to test dynamic segregation and passing ability.

Obtaining rheological parameters from tests traditionally designed to provide a qualitative assessment is difficult. The popular L-box test [25] ,fig. 2.7, was originally developed for super workable concrete [31] to assess key aspects of tremie concrete: passing ability, free surface flow, and dynamic segregation [87].

Concrete is placed in the vertical portion of the apparatus and filled completely whilst a gate prevents flow between the vertical and horizontal chamber. Once opened, the gate allows concrete to flow freely into the horizontal segment, first passing around reinforcement bars spaced at a distance determined by the largest aggregate. The result of this test is therefore governed by both rheology and the ability to maintain homogeneity [3]. The passing of concrete through the bars offers an important dynamic segregation indicator, but little on the basis of static segregation [3].

According to ICE [66], if the concrete does not reach the end of the horizontal chamber the test is considered a failure and the concrete deemed unacceptable. Similarly, EFFC and DFI [46] consider the concrete taking longer than 12 seconds to reach the end of the chamber a test failure. Both are concerned with the concrete at least reaching the end. The British Standards Institution [25], however, considers the difference in height of the concrete at the end of the chamber and that left in the vertical segment to be the most important factor. This ratio of filling depth F_{end} and remaining depth F_{start} (fig. 2.7) is referred to as the 'passing ability'.

Nguyen et al. [87] and Chamani et al. [28] attempt to correlate L-box measurements with Bingham parameters by using the passing ability. By performing L-box tests on concretes with known rheological properties an attempt is made to correlate the two. Both determined that L-box filling ratios could be used as a measure for yield stress, provided there was a low degree of blocking or segregation.

The L-box test is useful from a qualitative perspective because it provides an assessment for many different concrete behaviours. However, this is also presents a problem. The L-box test does not measure a property or characteristic of the concrete, it measures a combination behaviours. Where some tests are largely governed by a single rheological property, like the Slump-flow test described in the following section, the L-box can be effected by issues not related to the rheology, as is the case with blocking.

Blocking occurs as a result of aggregate accumulating behind the bars, as it may be too large to pass the obstruction [58]. Gram [58] also suggests a higher percentage of coarse material compared to fines may also encourage blocking, as a reduction in the paste layer surrounding each particle may not be sufficiently thick. Where sufficient flow of concrete has been prevented, though, openings or grooves in the concrete flow can be observed. Therefore, although the L-box test should not be used to validate a numerical model's ability to simulate concrete, is is a useful test to simulate once the model has been validated to determine additional controls on concrete behaviours.

For concrete placement by tremie in submerged condition under support fluid, ICE [66] recommends the use of the 'slump-flow' test in accordance with [26] as a way to measure the consistence of a concrete, ensuring it is workable enough for the tremie process. Figure 2.7a demonstrates how a slump-flow test is designed. Widely attributed to have originated from Abrams [57], the test has maintained its position as one of the most important throughout the industry [14] in part due it its repeatability and practicality. In slump-flow testing, a flat-topped cone mould is filled with concrete to be tested and allowed to rest. The mould is then raised at a constant velocity taking between 1-3 s. The slump is defined as the difference

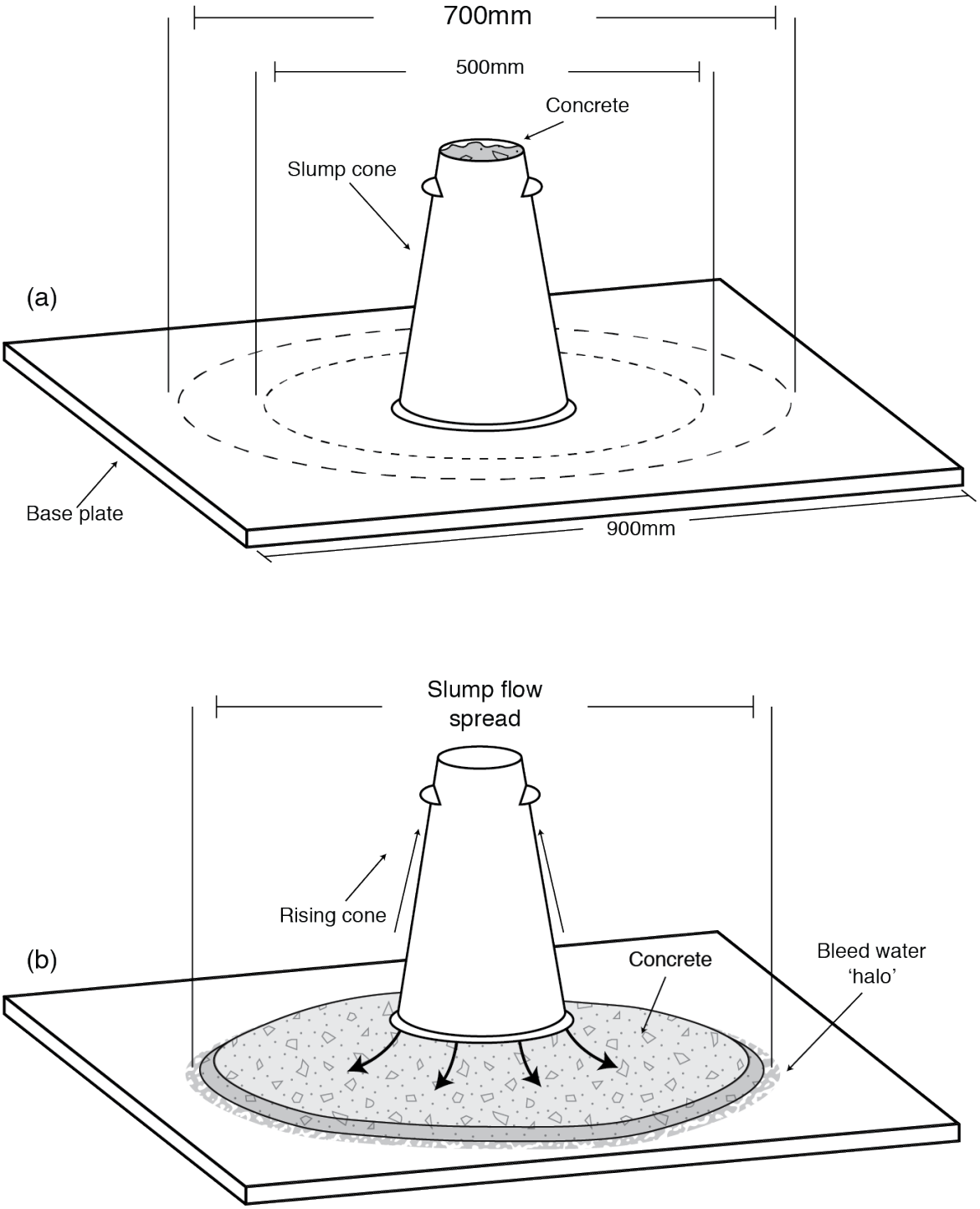

Fig. 2.8 a) Slump-flow test apparatus in accordance with BS EN 12350-8. b) Visualisation of slump spread and segregation halo.

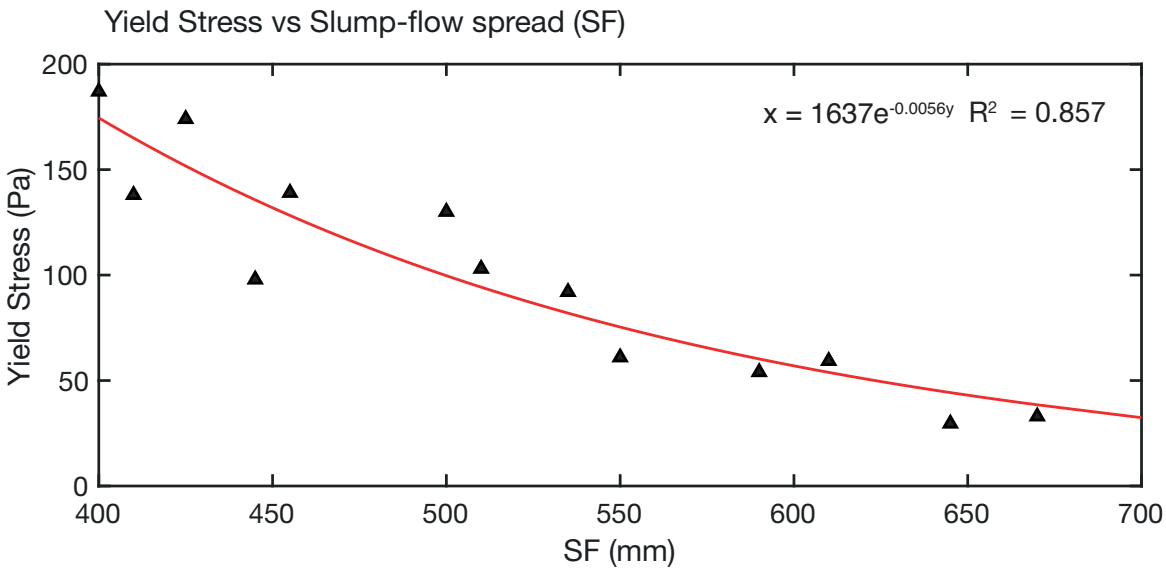

Fig. 2.9 Experimental correlation between dynamic yield stress and slump flow (reproduced after [74, 50]).

between the height of the mould and the height of the slumped material after flow of concrete stops. An alternative, but more common measurement for tremie concrete is a measure of the final spread diameter of the material, the Slump flow spread (SF) fig. 2.8a [55].

The Slump flow spread is used as a quantitative indicator of workability. As such, it is bound by lower and upper limits. The SF of a Tremie Concrete is typically in the range of 500 mm to 600 mm [66], although concretes with a SF as low as 450 mm or as high as 650 mm are also considered acceptable [47].

Figure 2.9 shows the experimental correlation between yield stress derived from rheometer and SF. The SF is observed to increase exponentially as the yield stress decreases [128, 99, 105]. When the shear stresses generated during the slump flow test are lower than the yield stress of the concrete, the flow stops [101]. Thus, any change in yield stress will inherently influence the point at which the flow stops, creating the yield stress and SF relationship demonstrated in Figure 2.9.

Plastic viscosity also impacts the flowability, however, its influence is considered less significant than that of the yield stress as it does not appear to control the stopping of the concrete flow, only the rate at which it spreads [98, 51]. This is supported by [101, 74, 50], who did not report any strong correlations between plastic viscosity and SF, but did observe an increase in the time taken for concrete to stop spreading, referred to as SF-Time, with increasing plastic viscosity as specified in EFFC and DFI [47]. However, it is worth noting

that Deeb et al. [41], Roussel and Gram [101] showed that the speed at which the cone is raised influences the spreading rate, without influencing the final SF [88, 114]. Thus, SF-Time/plastic viscosity relationships may be subject to user-variance as different operators may raise the cone at different speeds, within the Slump-Flow test standard [26].

The accuracy of a Slump-Flow simulation can, therefore, be judged largely by considering how well the final SF measurements match, as the yield stress/ SF relationship is subject to less controversy and user-variance. That is not to say the spreading time should be discounted, however, it should not be used solely to confirm if a numerical model is reliable.

Owing to the central role of segregation in concrete performance, one popular method used in conjunction with a slump-flow test is based on the visual stability index (VSI) of the slump-spread [6]. By identifying the presence of a mortar halo around the slump-spread and rating it visually from 0 to 3, an assessment of the stability can be quantified [67]. A 0 rating represents no segregation and a rating of 3 represents severe segregation. However, visual evaluation of bleeding and aggregate segregation according to the VSI test may be misleading, as only dynamic stability evaluations can be made.

Dynamic segregation occurs in both horizontal and vertical directions. Vertical segregation results in less aggregate within top layers of the flowing concrete and horizontal results in loss of aggregate at the flow front [65]. Tregger et al. [122] demonstrated the slump-flow test to be only capable of indicating horizontal dynamic segregation resistances. Mixtures that segregate during slump-flow testing would likely segregate after placement, but the lack of segregation during a slump-flow test does not necessarily imply that the mixture is resistant to static segregation [20].

One method for obtaining an indication of static segregation is the Static Segregation Test [7]. The test involves a cylindrical sample of the test concrete allowed to cure over time. It is then sawn in half and an assessment of the level of segregation rated form 0-3, similar to a VSI scale; referred to as the Hardened Visual Stability Index (HVSI) fig. 2.10. Although this test does not provide instant feedback prior to a mix being used on-site, it highlights the susceptibility of a mix to undergo static segregation in laboratory based mix designing. Segregation of any kind can cause the reduction of strength properties of concrete [46]

Bleed is often discussed in association with segregation. Whilst both segregation and bleed result in the loss of homogeneity, bleed refers to the loss of water or paste of a concrete whereas segregation is commonly used to describe the sinking of heavier elements. The most common bleed test is in accordance with [5], where a sample of concrete is allowed to rest and surface water content measured, to assess the level of water-loss or 'bleed' of the

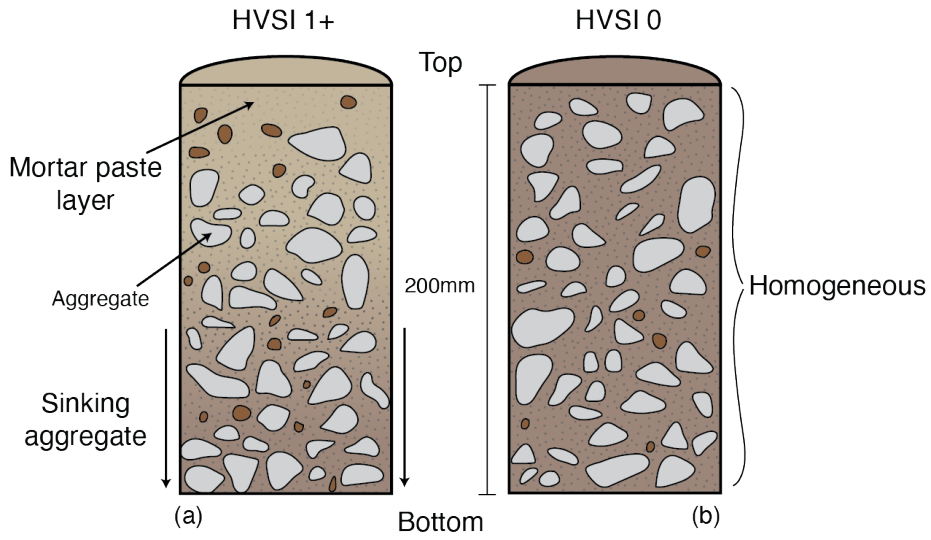

Fig. 2.10 Demonstration of static segregation within a Hardened Visual Stability Index test. a) segregation occurring, b) no segregation.

concrete. Bleed is often seen to be analogous to segregation, in that they both represent a separation of the concrete into constitutive elements with a detrimental effect on concrete strength properties. However, bleed may cause channels to form on the surface of a pile allowing an ingress of water after curing while segregation will lead to a loss of internal strength.

Chapter 3

Numerical Modelling

3.1 Background

The behaviour of fresh concrete is typically modelled as a continuum using Lagrangian methods [41, 81] or Eulerian Computational Fluid Dynamics (CFD) [47, 99, 101, 100, 126, 52, 70]. De Schryver et al. [40] modified OpenFOAM® (Open Source Field Operation and Manipulation), a popular CFD solver, to incorporate time-dependent thixotropic concrete behaviour. However, thixotropic concrete in CFD remains unvalidated. Continuum methods are suitable for large scale problems but may struggle simulating less workable concrete where inter-granular relationships become more important. Discrete particle methods [81] that represent concrete as individual particles capture the particle-scale behaviour accurately, however, these methods are computationally intensive and cannot always be scaled to the full field-scale. A comprehensive review of numerical methods used in the modelling of concrete flow is presented by Roussel and Gram [101] with more recent model reviews presented by [125, 104].

Computational Fluid Dynamics (CFD) is the part of fluid mechanics that refers to the use of numerical methods and algorithms to solve fluid flow problems, typically Eulerian and single-phase in its approach. Using the most general description of a fluid flow, Navier Stokes Equations, mass conservation, conservation of momentum and conservation of energy are obtained [120]. CFD is characterised by a coordinate system that is either stationary or moving in order to accommodate the continually changing domain. The mass travels between computational cells even if the grid moves, because grid movements are not related to the motion of the mass. Gram et al. [60] consider the main issue with their chosen CFD model to be defining the optimum strategy for interference tracking.

Ostensibly, CFD appears to be an appropriate choice because of economic computational speed and ability to use pre-developed software capable of modelling concrete placement conditions with ease. Roussel and Gram [101] and Gram and Silfwerbrand [59] conclude CFD is appropriate for a general overview of concrete, and represents the behaviour well. However, due to the Eularian frame of reference, describing time-dependent properties within the simulated concrete may become problematic.

Using a single-phase Finite Element Method (FEM, or sometimes FEA) will incur the same pitfalls as with its singular fluid counterpart CFD [101] with the addition of element distortion. A pile-scale simulation will require simulated concrete to undergo large deformation, particularly with reference to contact with reinforcement bars. Due to the nature of FEM, when the material represented becomes distorted, elongation of elements can occur. Cell elongation is known to cause inefficiency and inaccuracies in the results [82]. Adaptive re-meshing approaches aim to reduce this issue but a high computational cost redues the scale at which this method can be used.

Particle based methods, like the Discrete Element Method (DEM), offer a solution to reduce element based problems, simulating the material as a granular medium, rather than a continuum body. Depending on mix design, concrete is potentially governed by granular like behaviour, which could be described well by DEM. The calculations performed in DEM alternate between the application of Newton's second law with respect to the particles and a force-displacement law at the contact point between particles. The force-displacement law is used to update the contact forces arising from the relative motion at each contact, while the Newton's second law is used to determine the motion of each particle arising from the contact and body forces acting upon it. The contacts between two neighbouring particles occur only at a point [113]. According to [100] this offers a disadvantage, as the true nature of these contacts can never truly be known. Despite Roussel et al. [102] advising that slump-flow results from DEM are comparable to CFD and FEM, Roussel [96] advises that due to both computational time and scaling issues, DEM may not be viable in pile-scale simulations.

Alyhya et al. [4] offers a promising review of a particle method in the form of SPH (smoothed particle hydrodynamics), with early results indicating there may be a potential for future work to produce compelling results. Dhaheer et al. [42], however, discovered similar pitfalls to DEM within SPH due to the high computational time attributed to the search for neighbouring particles. Although SPH has been successfully used there are additional drawbacks. Bonet and Kulasegaram [21] identified that SPH exhibits spatial instabilities, as a consequence of the point-wise integration. Bandara [10] also argued insufficient neighbouring particles cause

Table 3.1 Comparison of numerical method capabilities.

Capability	Method			
	OpenFOAM®(CFD)	Abaqus FEA	Particle Based	Hybrid
Single phase	✓	✓	✓	✓
Granular representation			✓	
Pile-scale simulations	✓			✓
Low computational time	✓	✓		-
No remeshing				✓
Range of material models	✓	✓		✓
Handle high deformation	✓		✓	✓

inconsistencies. Thus, SPH may not yet be ready for use in large-scale concrete simulations required by the present study.

Moresi et al. [82] used the Finite Element Method with Lagrangian Integration Points (FEMLIP), presented also by Roussel et al. [100], to simulate the Slump-flow test with very encouraging results [82, 44].

An extension of FEMLIP, The Material Point Method (MPM) [111, 112] has recently gained significant traction in the geotechnical community for its ability to accurately simulate high deformation material [48]. MPM offers a new hybrid Eulerian-Lagrangian approach that combines the Lagrangian benefits of point tracking with the Eulerian background grid for modelling complex flow problems with history-dependent materials, whilst maintaining good computational efficiency [110, 10]. The MPM uses a background grid on which Lagrangian material points could traverse, thereby avoiding the need for frequent re-meshing to avoid mesh distortion [109]. MPM has been used to successfully model large deformation [110], interaction [95], and history dependent materials [9] with a high degree of accuracy.

Roussel et al. [102] attempted to generate a benchmark test to compare the ability of differing numerical methods to simulate the same virtual concrete. The results from this test indicate that although each method may converge at a similar spread diameter, there are discrepancies in the depth of the concrete measured at the centre of the spread. The most likely cause of the depth discrepancy is the difference in compressibility of the different simulated materials. Nonetheless, this benchmark offers a method of validation for any new simulation method and is used to validate numerical models in later sections.

Table 3.1 summarises the capabilities of the discussed numerical models where a check-mark denotes that the method has the capacity to meet the capability. To determine which numerical

model is appropriate for the simulation of concrete, the key capability requirements must be addressed. For the present study, there are two key requirements:

1. The chosen model must be able to handle high deformation at both empirical test, and pile scale.
2. The chosen model must be able to simulate tremie concrete, ideally with thixotropy.

Based on the criteria mentioned above, there are two methods that could meet these requirements, CFD and Hybrid methods. CFD has significant potential, it is able to simulate a continuum at macro-scale whilst maintaining good computational efficiency. Unfortunately, simulating thixotropic concrete in CFD may be impractical, so the method would be best suited to general overviews of concrete, as [101] suggested.

The hybrid method, MPM, appears to match CFD in its ability to model large deformations with the addition of a proven track-record of simulating history dependent materials. The drawback with MPM could be issues regarding computational efficiency when compared to CFD, where multiple optimised software packages are available.

Thus, for the present study both CFD and MPM will be used to analyse behaviour of Tremie concrete in line with the objectives of the research outlined in previous sections. What follows is a review of both methods and the chosen software packages / open source projects from which simulations will be generated.

3.2 Single Phase Material Point Method

The Material Point Method [111, 112] involves taking a continuum body and discretising it into a finite set of points, as demonstrated by fig. 3.1. Similar to the process of finite element discretisation, where a body is divided into elements, in MPM the body is divided into a series of ‘material points’. The continuum of point properties like mass, velocity and position are tracked and stored at the point level, making up a Lagrangian computational stage, while the calculations for stress are computed on a Eulerian background grid. This transfer of properties from point to grid allows for the computation of of material forces, but requires an additional mapping of properties back to the points. The MPM is hybrid in the sense that it combines both Lagrangian and Eulerian computational stages, however, unlike other Eulerian methods where the background grid changes as the simulation progresses, the background grid in MPM does not deform.

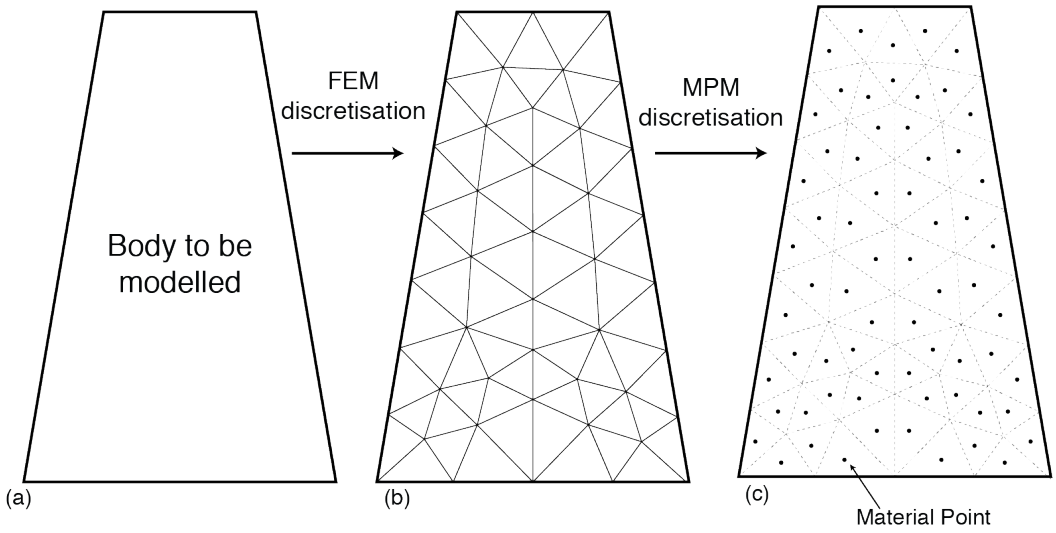

Fig. 3.1 a) Body to be modelled b) the finite element method of discretising a body, c) the material point method of discretisation, extending from the FEM style.

Typically, the MPM Eulerian background grid is a Cartesian domain of rectilinear elements. Each element is defined by nodes, usually at the vertices of the element unless otherwise specified. The material points carry the material properties, such as density, stresses, shear strength or any other variables as defined by the constitutive model. Typically, most material properties are specified at the start as an input, and later modified by the constitutive model. Figure 3.2 is a schematic diagram of the MPM solution process. The shape-functions, which are derived from the position of the material points within the element, are used to map material point properties to the nodes, fig. 3.2a-b, [110]. Therefore, no permanent information is stored at the nodes. The equation of motion is solved at the background mesh to find the current acceleration, with the element integration based on the material point locations [131], fig. 3.2c. The grid nodal acceleration and velocity values are mapped back to the points to update their velocities and positions using the same shape functions as before [133], fig. 3.2d. The stresses are computed at each material point using a constitutive model. Finally, the locations of the material points are updated based on the mapped velocity from the node as shown in fig. 3.2e.

What follows is an overview of governing equations and integration schemes used by the Material Point Method.

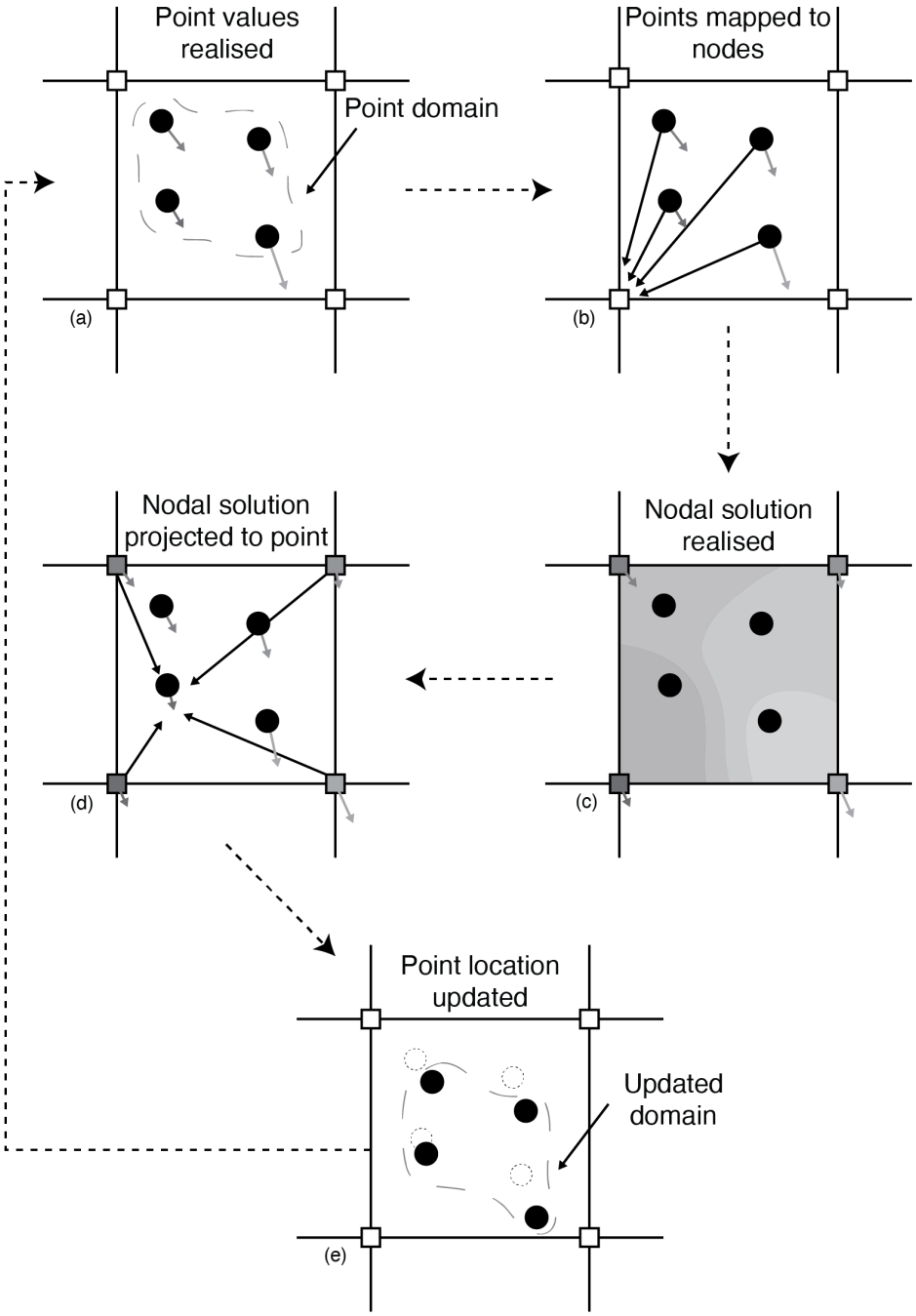

Fig. 3.2 Schematic diagram of the material point algorithm, arrows represent material point properties (velocity, mass, etc.) a) Point values are initialised b) Point values are mapped to nodes c) The equations of momentum are solved on the nodes d) Updated Nodal values are projected back to points e) Point locations and states are updated.

3.2.1 Governing Equations

Neglecting the thermal effects, the governing equations for the MPM are derived from the standard conservation equations for mass and momentum, eq. (3.1) and eq. (3.2) respectively. Derivations presented here are based on work conducted by [112, 10, 110, 133, 30].

$$\frac{d\rho}{dt} + \rho \nabla \cdot \mathbf{v} = 0\,, \tag{3.1}$$

$$\rho a = \nabla \cdot \sigma + \rho b\,. \tag{3.2}$$

A continuum body is discretised into a finite number of points n_p and let $\mathbf{x}_p^t$ represent the current position of point p at time t where $p = (1,2,...n_p)$. At any given time t, each point will have an associated mass m_p^t, density ρ_p^t, velocity $\mathbf{v}_p^t$, and stress and strain σ_p^t & ε_p^t, respectively, providing a Lagrangian description of the body. In addition it will also include parameters required by the chosen constitutive model. To obtain the discrete form of the equation, eq. (3.2) is multiplied by weight function w and integrated over domain Ω to give

$$\int_\Omega \rho w \cdot a \, d\Omega = \int_\Omega w \nabla \cdot \sigma \, d\Omega + \int_\Omega \rho w b \, d\Omega\,. \tag{3.3}$$

After integration by parts, the central term of eq. (3.3) becomes

$$\int_\Omega w \nabla \cdot \sigma \, d\Omega = \int_\Omega \nabla \cdot (w\sigma) \, d\Omega - \int_\Omega \nabla w \cdot \sigma \, d\Omega\,, \tag{3.4}$$

where the central term of eq. (3.4) becomes

$$\int_\Omega \nabla \cdot (w\sigma) \, d\Omega = \int_{\partial\Omega} w\sigma \cdot n \, dS \tag{3.5}$$

because of the divergence theorem, n represents the normal to the boundary.

The right hand side of eq. (3.5) represents the boundary term such that

$$\int_{\partial\Omega} w\sigma \cdot n \, dS = \int_{\partial\Omega_t} w\sigma \cdot n \, dS + \int_{\partial\Omega_u} w\sigma \cdot n \, dS\,, \tag{3.6}$$

but owing to Nueman boundary conditions

$$\sigma(x,t) \cdot n = \mathrm{T}(t) \text{ on } \partial\Omega_t \tag{3.7}$$

and test function w being zero on Direchlet boundary $\partial\Omega_u$, eq. (3.6) becomes

$$\int_{\partial\Omega} w\sigma n\, dS = \int_{\partial\Omega_t} w \cdot \mathrm{T}\, dS \tag{3.8}$$

where T represents surface traction.

Substituting eq. (3.8) into eq. (3.4) gives:

$$\int_{\Omega} w\nabla \cdot \sigma\, d\Omega = \int_{\partial\Omega_t} w \cdot \mathrm{T}\, dS - \int_{\Omega} \nabla w \cdot \sigma\, d\Omega \tag{3.9}$$

and substituting eq. (3.9) into eq. (3.3) gives the final weak form of the equation of motion:

$$\int_{\Omega} \rho w \cdot a\, d\Omega = \int_{\partial\Omega_t} w \cdot \mathrm{T}\, dS - \int_{\Omega} \nabla w \cdot \rho\sigma^s\, d\Omega + \int_{\Omega} \rho w b\, d\Omega\,. \tag{3.10}$$

Here, $\rho\sigma^s$ represents the the specific stress ($\sigma^s = \sigma/\rho$) necessary for the derivation of discrete equations, and dS and $d\Omega$ represent surface and volume differential respectively. Equation (3.1) is automatically satisfied as material points have a fixed mass at all times.

As the material is discretised into points, the mass density can be written as

$$\rho(\mathbf{x},t) = \sum_{p=1}^{n_p} m_p \delta(\mathbf{x} - \mathbf{x}_p^t) \tag{3.11}$$

where δ represents the Dirac delta function.

Substituting eq. (3.11) into eq. (3.10) converts integrals to sums of quantities evaluated at material points, giving

$$\begin{aligned} \sum_{p=1}^{n_p} m_p[w(\mathbf{x}_p^t,t) \cdot \mathbf{a}(\mathbf{x}_p^t,t)] = \sum_{p=1}^{n_p} m_p[-\sigma^s \cdot (\mathbf{x}_p^t,t)\nabla w|_{\mathbf{x}_p^t} \\ + w(\mathbf{x}_p^t,t) \cdot \mathrm{T}^s(\mathbf{x}_p^t,t)h^{-1} + w(\mathbf{x}_p^t,t) \cdot b(\mathbf{x}_p^t,t)] \end{aligned} \tag{3.12}$$

where h is the thickness of the boundary layer upon which the traction boundary conditions are enforced.

Continuing discretisation, the coordinates of any material point located within an element of the background mesh can be represented as

$$\mathbf{x}_p^t = \sum_{i=1}^{n_n} \mathbf{x}_i^t N_i(\mathbf{x}_p^t) \tag{3.13}$$

where spacial nodes are represented as $\mathbf{x}_i^t$ such that node number $i = (1,2...n_n)$ with n_n representing the number of nodes in the element. The element shape, determined by the background mesh, governs the applied basis function N_i similar to a finite element implementation. Velocity and acceleration also have a similar representation,

$$\mathbf{v}_p^t = \sum_{i=1}^{n_n} \mathbf{v}_i^t N_i(\mathbf{x}_p^t) \tag{3.14}$$

$$\mathbf{a}_p^t = \sum_{i=1}^{n_n} \mathbf{a}_i^t N_i(\mathbf{x}_p^t) \tag{3.15}$$

as does the weight function

$$\mathbf{w}_p^t = \sum_{i=1}^{n_n} \mathbf{w}_i^t N_i(\mathbf{x}_p^t)\,. \tag{3.16}$$

Substituting eq. (3.15) and eq. (3.16) into eq. (3.12) and evaluating at time t gives

$$\begin{aligned} \sum_{i=1}^{n_n} w_i^t \cdot \sum_{j=1}^{n_n} m_{ij}^t \mathbf{a}_j^t = -\sum_{i=1}^{n_n} w_i^t \cdot \sum_{p=1}^{n_p} m_p \sigma_p^{s,t} \cdot \nabla N_i(\mathbf{x})|_{\mathbf{x}=\mathbf{x}_p^t} \\ + \sum_{i=1}^{n_n} w_i^t \cdot \sum_{p=1}^{n_p} m_p N_i(\mathbf{x}_p^t) \mathrm{T}_p^{s,t} h^{-1} + \sum_{i=1}^{n_n} w_i^t \cdot \sum_{p=1}^{n_p} m_p \mathbf{b}_p^t N_i(\mathbf{x}_p^t)\,. \end{aligned} \tag{3.17}$$

eq. (3.12) includes the addition of nodal mass matrix m_{ij}^t,

$$m_{ij}^t = \sum_{p=1}^{n_p} m_p N_i(\mathbf{x}_p^t) N_j(\mathbf{x}_p^t) \tag{3.18}$$

and the specific stress at a point represented by

$$\sigma_p^{s,t} = \sigma^s(\mathbf{x}_p^t, t)\,. \tag{3.19}$$

eq. (3.17) can be further reduced to

$$\sum_{j=1}^{n_n} m_{ij}^t \mathbf{a}_j^t = \mathbf{f}_i^{int,t} + \mathbf{f}_i^{ext,t}\,. \tag{3.20}$$

Where internal force vector is written as

$$\mathbf{f}_i^{int,t} = -\sum_{p=1}^{n_p} m_p \sigma_p^{s,t} \cdot \nabla N_i(\mathbf{x})|_{\mathbf{x}=\mathbf{x}_p^t} \tag{3.21}$$

and external written as

$$\mathbf{f}_i^{ext,t} = \sum_{p=1}^{n_p} m_p N_i(\mathbf{x}_p^t) \mathrm{T}_p^{s,t} h^{-1} + \sum_{p=1}^{n_p} m_p \mathbf{b}_p^t N_i(\mathbf{x}_p^t)\,. \tag{3.22}$$

Boundary conditions are evoked when a point falls within a boundary cell, if multiple points are located within a boundary cell, they are treated as boundary points. Soundararajan [110] suggests maintaining a smaller mesh at boundaries may be beneficial. A modified frictional algorithm based on the work of Soundararajan [110] and Bandara [10] is presented later in this report. Integration and solution schemes are also detailed later in this report.

3.2.2 Explicit Material Point Method

The equation of momentum, eq. (3.2), is a second-order differential equation with respect to time and can be solved by using either an explicit integration scheme or an implicit integration scheme.

An implicit method involves finding the unknown displacement solution for the current time step by using information from both the current and previous time steps whereas explicit schemes do not consider the previous time-step. Unlike in the implicit scheme, the equilibrium of the internal forces is not enforced in the explicit scheme, which can cause errors to accumulate. Once the acceleration is known, this is used to explicitly advance the solutions for velocity and displacement. This procedure is the Euler method for numerical integration, a first-order explicit method. Its accuracy depends on the size of the step taken between solutions, hence the time step size influences the accuracy of the solution [89].

For a scenario involving a slowly applied and propagated stress [2] suggests the use of an implicit time integration scheme will reduce computational time. The high stability of an implicit time integration scheme is presented by [80], but owing to rapid application of forces required to simulate the tremie process, and explicit time integration scheme must be adopted.

The stresses in the MPM algorithm can be updated before or after computing the acceleration term and are commonly referred to as separate methods termed updating stress first (USF) or updating stresses last (USL). Bardenhagen [12] proposed USL performed better than USF, in addition, [2] recommends the use of USL over USF in a granular flow-like simulation as USL dissipates energy in flow problems. However, during simulations it was observed that USF offered greater numerical stability with the constitutive model used in the work. All simulations discussed in this thesis that utilise MPM, therefore, use USF.

Algorithm

A USF solution scheme is presented here based on the earlier work of [111] which is implemented into the CB-GEO MPM code [75] presented in the following section. The USF algorithm is also detailed in a simplified flow-chart by fig. 3.3.

Following the discretisation of a body as demonstrated by fig. 3.1, an arbitrary computational grid is initialised so as to describe the coordinates provided by the method of discretisation; typically a Cartesian grid for simplicity.

The point quantities such as mass, stress, and strain are initialised first. Following this, shape functions $N_{ip}^t(x_p)$ and the gradient of the shape function $\nabla N_i(\mathbf{x})|_{\mathbf{x}}$ for each material point is computed from the point position, similar in implementation to FEM shape functions. Using the shape functions, the point quantities are projected onto the background mesh.

The nodal mass matrix is obtained as

$$m_i^t = \sum_{p=1}^{n_P} N_i(\mathbf{x}_p^t) m_p \tag{3.23}$$

where m_i^t is the mass at note i and time t, m_p is the point mass, N_i is the shape function associated with node i and x_p^t is the location of the point at time t.

Similar to nodal mass, nodal momentum is solved by:

$$(m\mathbf{v})_i^t = \sum_{p=1}^{n_P} N_i(\mathbf{x}_p^t) m_p \mathbf{v}_p^t \,, \tag{3.24}$$

note the use of point velocity $\mathbf{v}_p^t$ here. The nodal velocities at each active node i can then be computed based on the momentum and the nodal mass (nodes that are active are considered to have at least one point in an associated cell) by

$$\mathbf{v}_i^t = \frac{(m\mathbf{v})_i^t}{m_i^t} \,. \tag{3.25}$$

As a USF algorithm is used in this work, the strain at each material point is computed at this stage by mapping the strain rate from the nodes:

$$\boldsymbol{\varepsilon}_p^t = \sum_{p=1}^{n_P} B_i(\mathbf{x}_p^t) \mathbf{v}_i^t \tag{3.26}$$

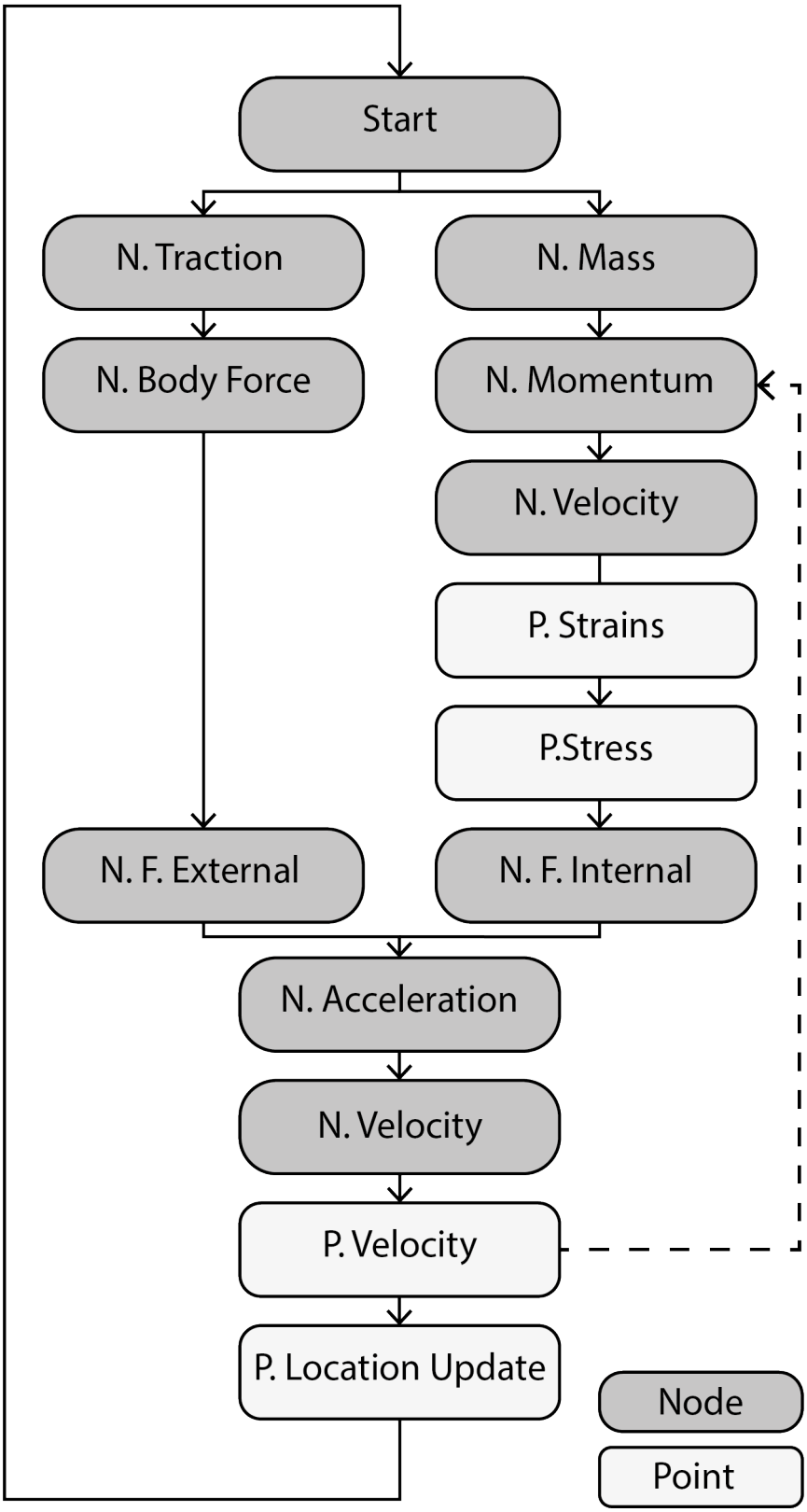

Fig. 3.3 Flow-chart of USF MPM algorithm.

by using the strain-displacement matrix

$$B = \begin{bmatrix} \frac{\partial N_i(\mathbf{x}_p^t)}{\partial x} & 0 & 0 \\ 0 & \frac{\partial N_i(\mathbf{x}_p^t)}{\partial y} & 0 \\ 0 & 0 & \frac{\partial N_i(\mathbf{x}_p^t)}{\partial z} \\ \frac{\partial N_i(\mathbf{x}_p^t)}{\partial y} & \frac{\partial N_i(\mathbf{x}_p^t)}{\partial x} & 0 \\ 0 & \frac{\partial N_i(\mathbf{x}_p^t)}{\partial z} & \frac{\partial N_i(\mathbf{x}_p^t)}{\partial y} \\ \frac{\partial N_i(\mathbf{x}_p^t)}{\partial z} & 0 & \frac{\partial N_i(\mathbf{x}_p^t)}{\partial x} \end{bmatrix} \tag{3.27}$$

in which derivatives of shape functions in respect to global coordinates are calculated as

$$\begin{Bmatrix} \frac{\partial N_i(\mathbf{x}_p^t)}{\partial x} \\ \frac{\partial N_i(\mathbf{x}_p^t)}{\partial y} \\ \frac{\partial N_i(\mathbf{x}_p^t)}{\partial z} \end{Bmatrix} = [J]^{-1} \begin{Bmatrix} \frac{\partial N_i(\mathbf{x}_p^t)}{\partial \xi} \\ \frac{\partial N_i(\mathbf{x}_p^t)}{\partial \eta} \\ \frac{\partial N_i(\mathbf{x}_p^t)}{\partial \zeta} \end{Bmatrix} \tag{3.28}$$

where the Jacobian J is

$$J = \begin{bmatrix} \frac{\partial x}{\partial \xi} & \frac{\partial y}{\partial \xi} & \frac{\partial z}{\partial \xi} \\ \frac{\partial x}{\partial \eta} & \frac{\partial y}{\partial \eta} & \frac{\partial z}{\partial \eta} \\ \frac{\partial x}{\partial \zeta} & \frac{\partial y}{\partial \zeta} & \frac{\partial z}{\partial \zeta} \end{bmatrix}. \tag{3.29}$$

The stress at each material point is can now be updated using $\Delta\sigma_p^t$ based on the constitutive model and the strain rate calculated in the previous steps by

$$\sigma_p^t = \sigma_p^{t-\Delta t} + \Delta\sigma_p^t \tag{3.30}$$

$$\Delta\sigma_p^t = \mathbf{D} : \Delta\varepsilon_p^t, \tag{3.31}$$

where $\mathbf{D}$ is the rate of deformation, described in chapter 5. Now, the nodal body force $\mathbf{b}_i^t$ can be computed as

$$\mathbf{b}_i^t = G \sum_{p=1}^{n_P} N_i(\mathbf{x}_p^t) m_p \tag{3.32}$$

in order to generate the nodal external force,

$$\mathbf{f}_i^{ext,t} = \mathbf{b}_i^t + \mathbf{t}_i^t, \tag{3.33}$$

while the internal force takes the mapped point stresses and point volume to give

$$\mathbf{f}_i^{int,t} = \sum_{p=1}^{n_P} V_p^t \nabla N_i(\mathbf{x}_p^t)\sigma_i^t. \tag{3.34}$$

The nodal acceleration and velocities of the next step $t + \Delta t$ are computed by

$$\mathbf{a}_i^{t+\Delta t} = \frac{\mathbf{f}_i^{int,t} + \mathbf{f}_i^{ext,t}}{m_i^t} \tag{3.35}$$

$$\mathbf{v}_i^{t+\Delta t} = \mathbf{v}_i^t + \mathbf{a}_i^{t+\Delta t} * \Delta t \tag{3.36}$$

where any velocity (with corresponding acceleration) constraints are applied at the nodes such as boundary walls. Point acceleration and velocities can now be updated by projecting the nodal values back to the points using the shape functions by

$$\mathbf{v}_p^{t+\Delta t} = \sum_{i=1}^{n_n} N_i(\mathbf{x}_p^t)\mathbf{v}_i^{t+\Delta t} \tag{3.37}$$

such that the material point position can be updated from the point velocity by

$$\mathbf{x}_p^{t+\Delta t} = \mathbf{x}_p^t + \mathbf{v}_p^{t+\Delta t} * \Delta t. \tag{3.38}$$

At the end of every time step, all the variables on the grid nodes are initialised to zero. The material points carry all the information about the solution, and the computational grid is re-initialised for the next step. At the end of each time step, all grid node values are reset to 0, and the computational grid is essentially re-set. The grid node positions are not considered to be updated in this algorithm.

3.2.3 Frictional Boundary

Prior to conducting any real-world simulations, correct boundary conditions need to be established. One boundary condition that may result in an inconsistency between expected and observed results, is the impact of friction. Without a set boundary friction, physically the

material should spread indefinitely until the material properties restrain it. Therefore, there is a need to include an accurate boundary friction algorithm.

A friction algorithm was implemented into CB-GEO by algorithm 1 below.

Algorithm 1: Modified 3*D* Friction Algorithm

if $a_N^{t+1} > 0.0$ *;* // Acceleration towards plane
then
  if $\left|v_T^{t+1}\right| \neq 0.0$ *;* // If velocity > 0 in any direction;
  then // Kinetic friction
    if $\left|v_T^{t+1}\right| \leq v_F^{t+1}$ // If velocity $\not>$ frictional force
    then
      $a_{T^i}^{t+1} = -v_{T^i}^{t+1}$ // No movement occurs, acceleration set to 0
    else
      $a_{T^i}^{t+1} = a_{T^i}^{t+1} - \mu_k \cdot \left|a_N^{t+1}\right| \cdot \frac{v_{T^i}^{t+1}}{\left|v_T^{t+1}\right|}$ // Friction opposite to movement
    end
  else // Static friction
    if $\left|a_T^{t+1}\right| \leq \mu_s \cdot \left|a_N^{t+1}\right|$ // Tangent acceleration < normal
    then
      $a_{T^i}^{t+1} = 0;$
    else
      $a_{T^i}^{t+1} = a_{T^i}^{t+1} - \mu_s \cdot \left|a_N^{t+1}\right| \cdot \frac{a_{T^i}^{t+1}}{\left|a_T^{t+1}\right|}$ // Friction opposite to T^i
    end
  end
end

The Coulomb frictional boundary from [10] has been modified for use in 3D by incorporating multiple tangential directions denoted by T^i where $i = (0..n)$ where n depends on direction of normal. This frictional boundary condition is applied on the background mesh nodes. The selection of nodal acceleration of nodal force allowed for easier manipulation of frictional constraints. Both static and kinetic friction are considered and only applied when points fall within boundary cells. The kinetic and static frictions are denoted by μ_k and μ_s respectively. A subscript N represents normal direction to the boundary. Kinetic friction is applied when the node has a velocity in any direction greater than $|0|$, if a nodal velocity is not greater than the frictional force v_F^{t+1} $(= \mu_s \cdot \left|a_N^{t+1}\right| \cdot \Delta t)$ its velocity is reduced to 0 using $-v_{T^i}^{t+1}$. If nodal velocity is greater than v_F^{t+1} then kinetic friction is applied opposite to the direction of movement.

If the node has a velocity of $|0|$ but hasn't gained velocity yet, tangential acceleration is checked against normal acceleration by the condition $\left|a_T^{t+1}\right| \leq \mu_s \cdot \left|a_N^{t+1}\right|$. If tangential acceleration is $\leq$ normal acceleration then it is reduced to 0. If there is a greater tangential acceleration then static friction reduces the acceleration in the direction opposite to the tangential.

3.2.4 GIMP method

Within MPM, when a point crosses from one cell to another, particularly if the cell it enters is empty, a sudden change to the stress profile is observed. This effect is commonly called cell crossing noise [13]. Multiple spurious stresses arising in a deforming continuum where cells are regularly crossing boundaries will give rise to incorrect accelerations and stresses. These sudden changes to the stress profile can often result in large, non-physical accelerations detaching points from the continuum [112]. The main cause of cell crossing noise is the use of piecewise linear shape functions used to interpolate information between nodes and points.

This issue is of particular importance in the work presented in the present study due to the way concrete deforms. It is likely that any simulation involving concrete will require the material to flow readily and easily, thus incurring multiple cell crossings - particularly into empty cells. Bardenhagen and Kober [13] proposed a modification to traditional linear shape functions with a smoother, continuous function that spans multiple cells. This method of multiple-cell shape functions is termed the Generalised Interpolation Material Point Method, or GIMP. The GIMP shape function [92], represented here as N_i is given by

$$N_i = \begin{cases} 0 & x_p - x_v \leq -L - l_p\,, \\ \frac{(L+l_p+(x_p-x_v))^2}{4Ll_p} & -L-l_p < x_p - x_v \leq -L+l_p\,, \\ 1+\frac{x_p-x_v}{L} & -L+l_p < x_p - x_v \leq -l_p\,, \\ 1-\frac{(x_p-x_v)^2+l_p^2}{2l_p} & -l_p < x_p - x_v \leq l+p\,, \\ 1-\frac{x_p-x_v}{L} & l_p < x_p - x_v \leq L-l_p\,, \\ \frac{(L+l_p-(x_p-x_v))^2}{4Ll_p} & L-l_p < x_p - x_v \leq L+l_p\,, \\ 0 & L+l_p < x_p - x_v\,. \end{cases} \tag{3.39}$$

where L represents the cell spacing, that is the length of one cell and x denotes the coordinates of point p and node v by x_p and x_v respectively. The initial point length l_p is determined by dividing the cell spacing by the number of points in the cell at the beginning of the simulation. For d dimensions and n points x_{pn}, this can be achieved by $L/x_{pn}^{1/d}$. The weighting function itself can be extended to two dimensions by substituting the second dimension into eq. (3.39) and multiplying the functions with respect to the two dimensions by

$$N_i(x,y) = N_i(x) \cdot N_i(y) \tag{3.40}$$

and three dimensions by

$$N_i(x,y,z) = N_i(x) \cdot N_i(y) \cdot N_i(z)\,. \tag{3.41}$$

The gradient of the shape function ∇N_i is calculated as

$$\nabla N_i() \begin{cases} 0 & x_p - x_v \leq -L - l_p\,, \\ \frac{l_p+(x_p-x_v)+L}{2Ll_p} & -L-l_p < x_p - x_v \leq -L+l_p\,, \\ \frac{1}{L} & -L+l_p < x_p - x_v \leq -l_p\,, \\ \frac{-x_p-x_v}{Ll_p} & -l_p < x_p - x_v \leq l+p\,, \\ -\frac{1}{L} & l_p < x_p - x_v \leq L-l_p\,, \\ \frac{l_p+(x_p-x_v)+L}{2Ll_p} & L-l_p < x_p - x_v \leq L+l_p\,, \\ 0 & L+l_p < x_p - x_v\,. \end{cases} \tag{3.42}$$

where the 2D gradient is given as

$$\nabla N_i(x,y) = [\nabla N_i(x) \cdot N_i(y), \nabla N_i(y) \cdot N_i(x)] \tag{3.43}$$

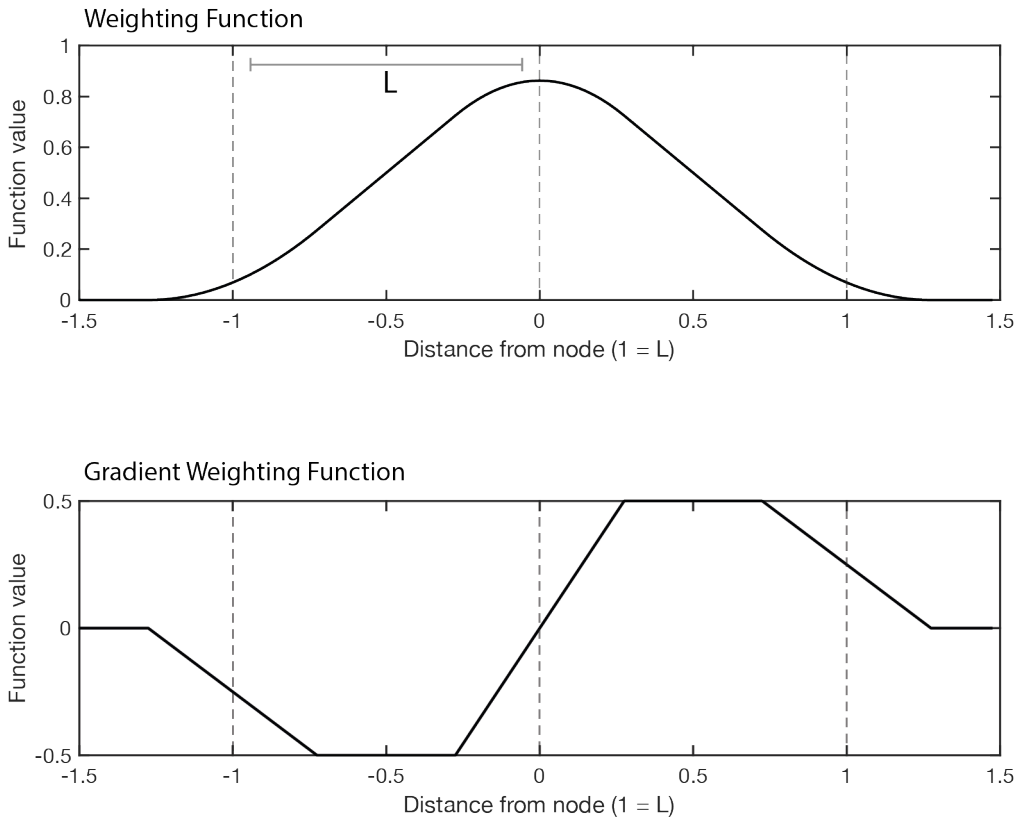

Fig. 3.4 Example of GIMP weighting function.

and the 3D gradient:

$$\nabla N_i(x,y) = [\nabla N_i(x) \cdot N_i(y) \cdot N_i(z), N_i(x) \cdot \nabla N_i(y) \cdot N_i(z), N_i(x) \cdot N_i(y) \cdot \nabla N_i(z)] \tag{3.44}$$

Standard linear shape functions have two characteristic elements, they have a constant gradient and hold a partition of unity. Conversely, GIMP functions as demonstrated by fig. 3.4 do not have a constant gradient and do not hold a partition of unity. Note in fig. 3.4 the non zero value of the shape-function past the cell boundary where the distance from the node is greater than 1. A standalone C++ code was developed to prepare fig. 3.4 [36], which represents 1D GIMP cell and the corresponding shape function value as a point traverses the cell starting at -1.5 and ending at 1.5. As a GIMP cell is comprised of multiple lower order cells, the starting point of -1.5 is outside the cell of interest (the centre cell) and also finishes outside the cell of interest. What can be seen is that at the cell boundaries of the cell of interest (-1 and 1) the value of the shape function is not 0 as it would be in the standard

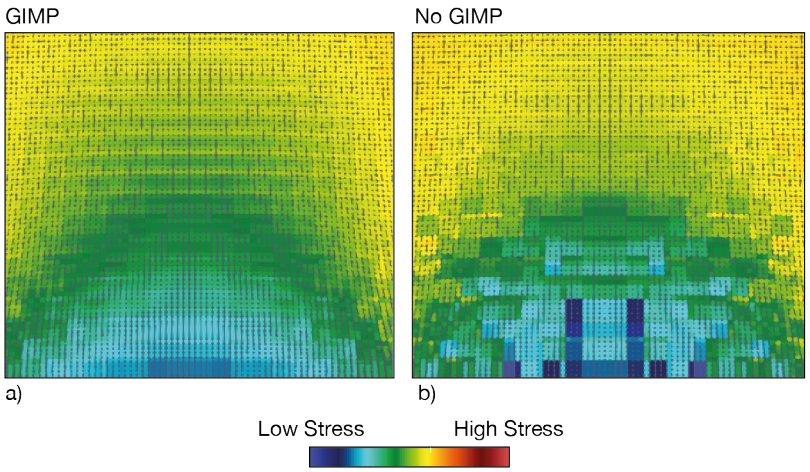

Fig. 3.5 Example of the smoothing effect achieved by applying GIMP to a simple linear-elastic column collapse.

MPM method. This code was used to validate the implemented GIMP model, in 2D and 3D by confirming that the shape function value was not 0 at cell boundaries.

The dramatic effect GIMP shape functions can have on the stress profile of a simulation is presented by fig. 3.5, where a clear smoothed stress profile is observed. For the present study, both 2D and 3D GIMP was implemented into the CB-GEO MPM code by the author.

There are multiple iterations of the GIMP that attempt improve computational accuracy. Many of these methods look to add in a way to include point deformation. Bardenhagen and Kober [13] presented uGIMP, or undeformed GIMP, where the point does not deform and Contiguous particle GIMP or cpGIMP [130] where the size (length in 1D) of a point changes based on its changing volume. In more recent work, Sadeghirad et al. [106] introduced CDPI, a form of GIMP where the rotation of a point is considered. uGIMP was implemented into the CB-GEO MPM code for the purposes of this work by the author with the functionality to add deformed point GIMP methods if the results from uGIMP were not sufficient at reducing cell crossing noise.

One practical consideration to make when building GIMP meshes is the lack of an available mesh-building package and the complexity, particularly in 3D, of creating a hexahedral based mesh where each cell is comprised of 9 individual cube elements. To do this, a GIMP-MESH code was written for the purpose of generating large GIMP MPM meshes, [35]. The GIMP mesh generator requires a specific node ordering scheme, fig. 3.6, as GIMP elements are derived from hexahedral elements within the CB-Geo code. Essentially, the numbering of the local cell (the cell with points of interest) is treated as a standard hexahedron element and the neighbouring nodes are added on. This specific numbering scheme is required by the

code due to the way elements are processed. Thus, to build a mesh comprising of 64 node elements that overlap and use this specific numbering sequence is a non-trivial task.

A second practical consideration to make is the slight modification to boundary conditions required for successful simulations. For the standard formulation of the MPM, a velocity boundary can be applied to a single layer of nodes to create a solid boundary or wall condition. In GIMP this is not strictly possible, as the lack of a partition of unity will allow points to pass through a solid boundary of only a single layer of nodes. Thus, all boundary conditions must contain two rows of nodes in order to prevent losing points outside of the domain.

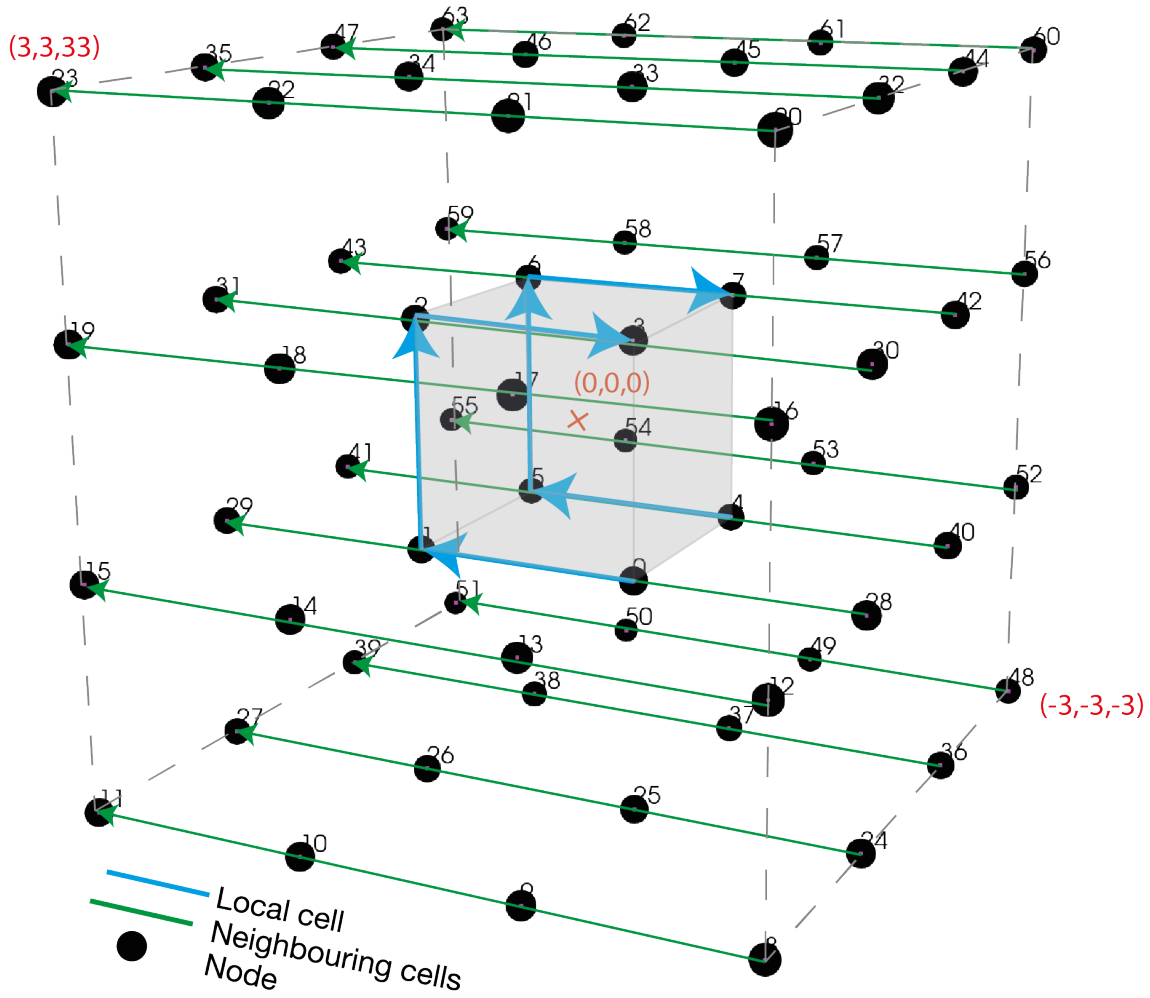

Fig. 3.6 Schematic of the order of node numbering used in [35], blue indicates node ordering of the local element (element with points of interest) and green the node ordering of neighbouring element.

3.2.5 Time-Step

As discussed previously, the explicit integration scheme uses a time-step to forward the simulation in time. The stability of the simulation is heavily dependent on a suitable time-step being chosen. This time step must be low enough to maintain stability, but high enough to maintain computational efficiency. According to the Courant-Friedrichs-Levy (CFL) [34] condition, the size of the time-step,∇t, must satisfy the condition

$$\nabla t \leq \frac{L_e}{c_p} \tag{3.45}$$

where L_e is the element length used in the background mesh and c_p is the compression wave velocity in an isotropic elastic continuum. The compression wave velocity can be written as:

$$c_p = \sqrt{\frac{E_c}{\rho_s}} \tag{3.46}$$

where E_c is the constrained modulus of the material,

$$E_c = K + \frac{4}{3}G \tag{3.47}$$

with K being the bulk modulus, often computed as

$$K = \frac{E}{3(1-2v)} \tag{3.48}$$

from E the Young's modulus and v the Poisson ratio. G in eq. (3.47) is the shear modulus also computed from the Young's modulus and Poisson ration by:

$$G = \frac{E}{2(1+v)} \tag{3.49}$$

3.2.6 Geometry

The geometry of an MPM simulation can be divided into two categories: mesh and points. The important consideration to make regarding the mesh is its coarseness, or simply the number of cells used to discretise the area of interest. For points, the key factor to consider is points per cell (PPC) used to define the geometry. Often PPC is referenced in terms of the starting geometry of the continuum to be modelled.

Guilkey et al. [62] recommended at least 4 points per cell, for large deformation problems as low numbers of points in cells can result in non-physical separation of points causing openings or fractures in the continuum. However, a higher value of point density affects the computational time. Soundararajan [110] presented a study on the PPC of a GIMP mesh, concluding that the run-out distance of a gravity driven flow is improved by increasing the number of material points per cell. However, it was noted that the duration of the run-out is independent of PPC.

The size of an MPM mesh and its relation to accuracy has been covered in the literature many times. Zhao and Liang [134] considered the effect of mesh size with PPC on an unconfined flow problem not unlike the behaviour of flowing concrete and concluded no significant influence from the refinement of either could be determined. However, Zhao and Liang [134] did conclude that a higher PPC should be used if a finer mesh is chosen to reduce pressure oscillations. Fern et al. [48] also noted for gravity driven flows that mesh size effects are often negligible. It is worth considering though, the observation of Bardenhagen and Kober [13] that if the mesh is too fine and the PPC to high, due to the relationship between point size and cell length described in section 3.2.4, the GIMP interpolation function will approach that of the standard MPM interpolation function. This will, in turn, reduce the added benefit of implementing GIMP, bringing with it the abundant cell crossing noise associated with traditional MPM.

An interesting observation by Abe et al. [1] where coarser meshes performed better with higher PPC and finer meshes with lower PPC supports the idea that finer meshes are subject to more cell crossing noise do to an increase in the frequency with which a point will cross a boundary, therefore reducing points is beneficial. Whereas in coarse meshes, increasing the PPC will improve accuracy as cell crossings are much more infrequent.

In summary, fine meshes generally perform better with lower PPC, but not so low that point tearing is possible and coarse meshes perform better with higher PPC but not so high that computational efficiency is compromised.

In terms of selecting an initial mesh coarseness, the general rule in numerical modelling is that a cell length should be no larger than the size of the smallest object to be modelled. For instance, in the case of concrete modelling this would likely be governed by the size of the obstacle to be modelled, like the diameter of a reinforcement bar. The PPC should, according to the previously described works, be no smaller than 4 to reduce any unwanted splitting but to prevent an increase in cell crossing noise due to reduced GIMP functionality by having too many PPC.

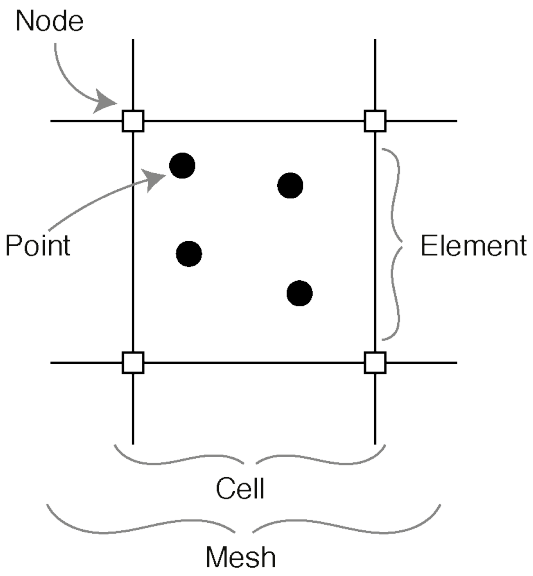

Fig. 3.7 Format of entities with the CB-GEO MPM code.

CB-GEO MPM

For simulations presented in this work that use the Material Point Method, the CB-GEO MPM [75] code is used. CB-Geo, the computational geomechanics research group, is an academic community with members from the University of Cambridge, University of Texas at Austin and California Berkeley. The original framework of the open source, C++ based CB-GEO MPM 3D code was primarily developed by Dr Krishna Kumar of the University of Texas at Austin, who also oversees and verifies further developments to the code. Developments to the existing framework were undertaken by the author as part of this thesis, including implementing 3D GIMP, frictional boundary modifications, and the creation of a concrete constitutive model.

Within any MPM code, there are multiple entities, such as element types, material models, point types amongst others. The nature of MPM means that several entities described are interconnected. In the case of CB-GEO MPM, there are Nodes, Points, Elements (which describe Shape functions and Quadratures) and Cells formed of nodes. There is also a mesh which is a collection of all the entities, as demonstrated by fig. 3.7.

An abstract factory based design is adopted to describe the different entities in the code, with a virtual base class for each entity followed by a derived class of a concrete type. For example, a virtual abstract base class Element has concrete derived types: Quadrilateral and Hexahedron elements. A simplified Unified Modelling Language (UML) diagram of the CB-

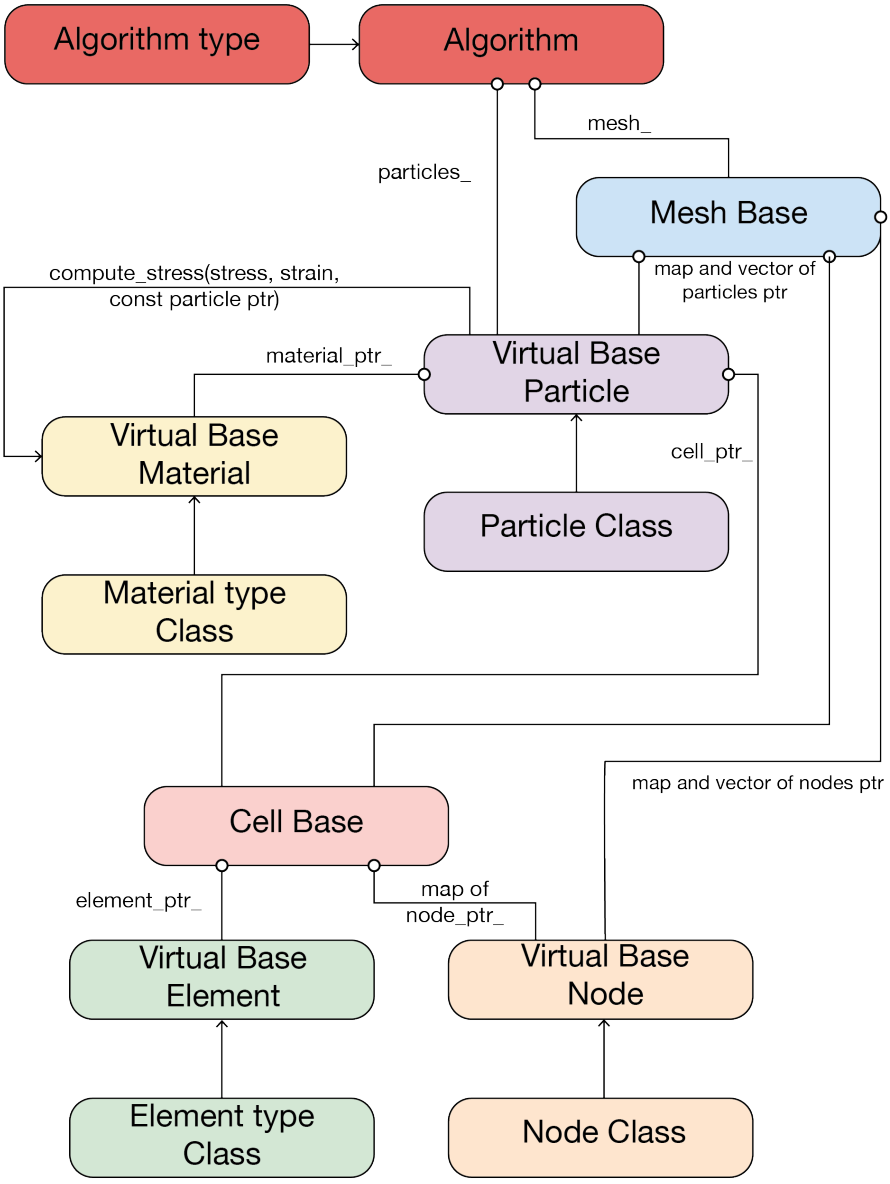

Fig. 3.8 Simplified UML diagram of the CB-GEO factory design.

Geo MPM code is shown in fig. 3.8 with annotations to demonstrate the interconnectedness of different entities.

High Performance Computing

A significant benefit of using the CB-GEO MPM code is the ability to utilise the power of parallel computing to reduce computational time of MPM simulations and increase the number of points or cells to be computed. The code can perform both distributed and shared memory prallelisation techniques [75].

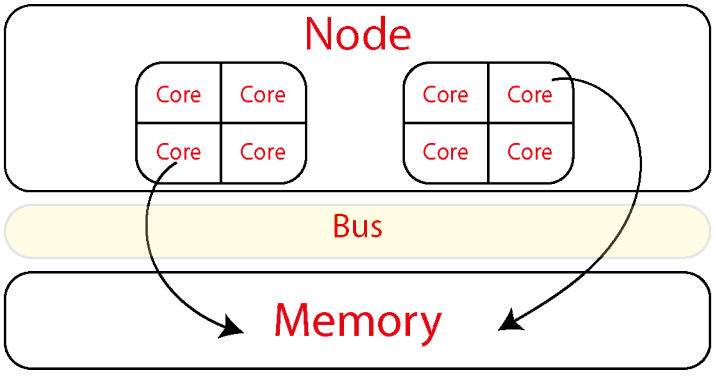

Fig. 3.9 Schematic of shared memory

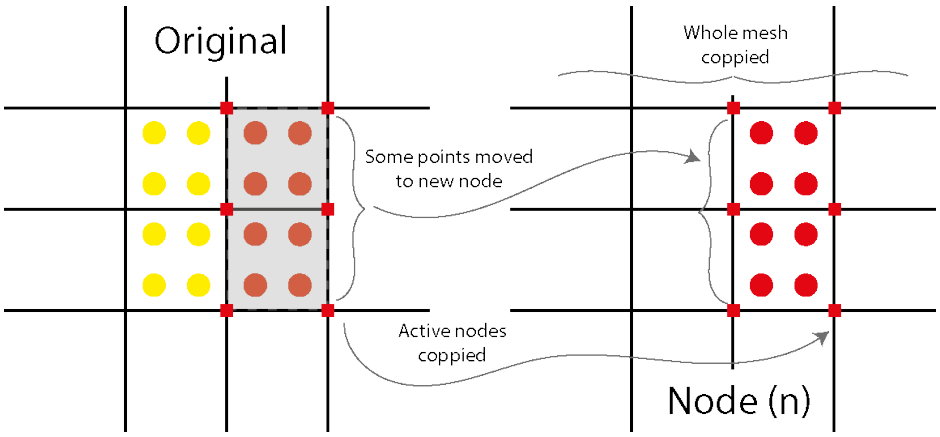

Fig. 3.10 Schematic of distributed memory

Figure 3.9 is a schematic of a two socket node with 4 cores in each socket. Code can be run in parallel on each core, utilising the same memory. This is referred to as shared memory parallelisation and is controlled using a Intel TBB (Threaded Building Block) task implementation.

Distributed parallelisation is where multiple compute nodes each with its own shared memory are strung together through a high-bandwidth network. Special messaging passing techniques have to be utilised to communicate between the nodes. Typically this is done using MPI and the mesh is divided and split across multiple compute nodes - this operation is called Domain Decomposition and a schematic is presented in fig. 3.10.

Due to its hybrid nature, MPM allows for an easy load balancing technique, where the whole mesh is copied to every compute node, along with a selection of material points. The benefit of this is that the domain is not redistributed, as the material points move through the mesh. This method will find out which are the active nodes, that is, nodes which belong to cells with material points, which in turn are updated at each time step - this is arguably not the most efficient way - but it is unique to MPM and makes the first step of MPI parallelisation simpler. The benefit is this method is much simpler for complex geometries as the mesh does not get divided into sub-domains.

The CB-Geo code described in this chapter was executed on the CSD3, the Cambridge Service for Data-Driven Discovery cluster, a general purpose compute cluster run by the University of Cambridge's High Performance Computing Service (HPCS).

CSD3 is a combination of three platform types:

- Intel Scalable processors (Intel Xeon Gold - Skylake)
- Intel Xeon Phi (KNL)
- Nvidia P100 GPUs

This is built with the Intel Omni-Path interconnect and Mellanox InfiniBand EDR, the latter forming the fabric used on the GPU component of CSD3. The three components are referred to as Peta4-Skylake, Peta4-KNL, and Wilkes2-GPU respectively.

Simulations on the CSD3 cluster are submitted based on compute power requirements. All simulations discussed in this study were submitted to Peta4-Skylake and used a minimum of 1 compute node running 32 tasks per node.

Each compute node contains:

- 2x16 cores, Intel Skylake 2.6 GHz32 CPUs
- 192GB RAM at 6GB per CPU
- 100 Gb/sec Omni-Path10 GB/sec (for MPI and storage)

3.2.7 Conclusion

The benefits of using the Material Point Method to simulate concrete are clearly demonstrated by its implementation. The separation of points and background mesh present a reliable and well conceived solution to the limitations of traditional numerical methods like the Finite Element Method. The recent and active developments within this method will only serve to increase its popularity and reliability. The following chapters examine a method for developing a MPM code suitable for use in simulating placement of concrete in deep foundations.

3.3 Computational Fluid Dynamics

In three dimensions, the Navier-Stokes equations become a set of four equations with for unknowns. They are: fluid pressure, and each component of fluid velocity (x, y, z). These equations are solved using a numerical model requiring a continuum body to undergo some aspect of discretisation.

To discretise the continuous partial differential equations, the finite volume method (FVM) is applied by using arbitrary polyhedral non-overlapping cells, or control volumes [132]. The domain is first divided into discrete nodal points. Cell boundaries (or faces) of the discrete control volumes are located at the midpoint of neighbouring nodes, such that each node lies entirely within a control volume (or mesh element) [69, 45]. The control volume, commonly called a CV, is a 3D element bounded on all sides by planar faces.

Pressure terms are present in the Navier-Stokes equations and this creates pressure-velocity coupling [32]. A pressure equation is determined from the requirement of mass conservation and the momentum equation gives a relation between the velocity field and pressure field within a flow. The pressure equation is derived by substituting the relationship between the velocity and pressure into the continuity equation.

As the simulation of concrete flow problems requires multiple fluids such as different concrete batches, a method must be defined that can identify the boundary between two fluids. The volume of fluid [64] (VOF) method is commonly used to simulate layered flows in which the phases have explicit boundaries, such as free surface flows [127]. The OpenFOAM® (Open Source Field Operation and Manipulation) multiphase solvers, *interfoam* and *multiphaseInterfoam*, used in this study simultaneously solve conservative forms of continuity and momentum equations for all available phases using a Pressure Implicit with Splitting Operators (PISO) algorithm.

3.3.1 OpenFOAM

OpenFOAM®, is a free, open source CFD software developed primarily by OpenCFD Ltd. It is a is a C++ based open-source library that contains many tools and methods capable of simulating a variety of problems. As such, it does not have a graphical user interface (GUI) and relies primarily on the use of a back-end source code and multiple input files defining all aspects of the problem, from geometry to solution scheme. Simulations of concrete flow by OpenFOAM® solvers have demonstrated a good degree of accuracy [52]. This makes it the obvious choice for use in this work, where it will be used to define concrete behaviour and as a comparison tool for assessing the performance of MPM.

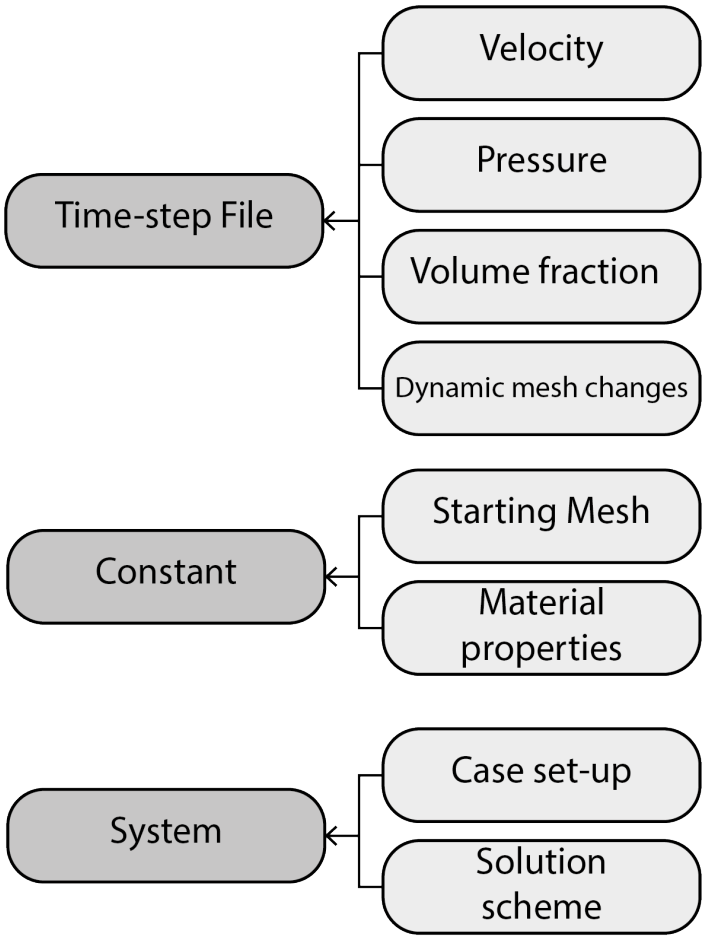

Fig. 3.11 Schematic of OpenFOAM® property distribution within the file structure.

As previously discussed, OpenFOAM® requires the use of multiple input files as no GUI is available. There are three main sections of input file, as demonstrated by fig. 3.11. The first series of input files is the *system* folder that contains all information related to the numerical

method employed. The second category of input files is the *Constant* folder. This folder contains information about the simulation that does not change. Typically, this contains the building blocks of the mesh, though time-dependent meshes may have some of their files located in the computational folders. The material properties are also contained in this folder. The final section is the section that pertains to the simulation output. At each time step, a folder named after the real-time at which it was output contains a series of files where the velocity, pressure and volume fraction fields are defined. The computational folders may also contain information about time-dependent mesh changes.

Within the system folder, the case-setup file *controlDict* controls the time-stepping method. The stability of a numerical simulation is often governed by the size of the time step used to advance the simulation through time. The time-step should be small enough such that a point does not cross more than one cell during a single time-step. This is represented in OpenFOAM® as the Courant number, which must be kept below 1 for stability. It is possible that a *runTimeModifiable* time-step is employed to maintain a suitable Courant number. An interface Courant number can also be set in the *controlDict* file to maintain a stable interface between the phases (such as concrete and air) reffered to as a *maxAlphaCo*. The present study used a Courant number of 0.2 and a run-time adjustable time-step condition to maintain stability for all simulations. Similar to the Courant number A *maxAlphaCo* of 0.5 was selected, with 4 *nalphaSubCycles* (cycles of the interface calculation) giving an effective interface Courant number of 0.125.

The *fvSchemes* file allows the user to set the various terms related to the governing equations and the solution scheme. The *ddtschemes* specifies how the time derivative is handled in the momentum equations. For the present study the first-order backward implicit Euler scheme is employed. The remaining options in the *fvschemes* file set the different schemes used for interface behaviour among others, many of which are designed to improve accuracy of the solution given a specific set of conditions. An excellent review of how these schemes can influence the result is given by Larsen et al. [77], where the multiphase damn-break problem is analysed. For the purposes of this study, the default solutions schemes are maintained from the damn-break tutorial found within the OpenFOAM® tutorials within the source code. The most common approach to using OpenFOAM® is to start with the most applicable tutorial, in this case the multiphase damn-break tutorial and modify the inputs such as mesh and material properties to solve the issue you are modelling, rather than starting anew. This preserves the optimal conditions for the chosen solver. One difficulty with using OpenFOAM® is the large number of solution schemes and types available, creating a steep learning curve for new users.

The final file within the systems folder is the *fvSolution* file, where the iterative solvers, solution tolerances and algorithm specific settings are determined. Again, many of the settings within this file are kept as default for the present study, however it is worth drawing attention to the use of the generalised geometric-algebraic multi-grid (GAMG) solver that is used in the predictor steps during the solving of the equations detailed in the following section. The GAMG generates a rapid solution on a coarse mesh comprised of agglomerated cells which is then used as the initial guess on during predictor stages of the algorithm [77].

3.3.2 Governing Equations

The equations presented in this section are based on work by Jasak [69] and are presented with reference to OpenFOAM® [32, 29, 45, 11].

The incompressible Navier-Stokes equation (NSE) for a multiphase system of incompressible immiscible fluids provides a mass conservation equation:

$$\frac{\partial \rho}{\partial t} + \nabla \cdot (\rho \mathbf{U}) = 0 \tag{3.50}$$

and momentum conservation equation:

$$\frac{\partial (\rho \mathbf{U})}{\partial t} + \nabla \cdot (\rho \mathbf{U}\mathbf{U}) = -\nabla P + \nabla \cdot (2\eta \mathbf{D}_{ij}) + \rho g + F \tag{3.51}$$

where ρ is density, $\mathbf{U}$ is the three dimensional mixture velocity field shared by all phases, g is the gravitational acceleration constant, P is the pressure, F is the the surface tension force and η is the apparent viscosity where $\mathbf{D}_{ij}$ is the is the rate of strain tensor

$$\mathbf{D}_{ij} = \frac{1}{2}(\nabla \mathbf{U} + \nabla \mathbf{U}^T)\,. \tag{3.52}$$

The VOF approach involves using a volume of fraction marker $\alpha\prime$ to determine the portion of each phase required using:

$$\frac{\partial \alpha\prime_i}{\partial t} + \nabla \cdot (\alpha\prime_i \mathbf{U}) = 0 \tag{3.53}$$

such that mixture properties like ρ are calculated as a weighted average according to the number of fluids N [83] to give:

$$\rho = \sum_{i=1}^{N} \alpha\prime_i \rho_i \,. \tag{3.54}$$

The continuum surface force (CSF) according to [23] is given by including the surface tension force, F, on the right-hand side of the momentum equation. Hence, the surface tension force for the interface between each phase pair according to [124] is

$$F = \sum_{i,j} \sigma_{ij}^{s} \kappa_{ij} \nabla \alpha\prime|_{ij} \tag{3.55}$$

where σ_{ij}^{s} is the surface tension coefficient, $\nabla \alpha\prime|_{ij}$ is a pair-averaged gradient of the phase fraction which also corresponds to an estimation of the unit interface normal vector given by:

$$\nabla \alpha\prime|_{ij} = \alpha\prime_j \nabla \alpha\prime_i - \alpha\prime_i \nabla \alpha\prime_j \tag{3.56}$$

for all phase pairs (i, j), the corresponding curvature κ_{ij} is calculated as:

$$\kappa ij = -\nabla \cdot \nabla \alpha\prime|_{ij} \,. \tag{3.57}$$

The volume of fraction markers $\alpha\prime$ for each phase must sum to 1 in any given cell, where 1 represents a cell filled by the reference fluid. Therefore, the VOF method does not achieve a strict boundary between fluids, instead creating a smoothed area between two fluids that represents the boundary.

Discretising terms in the momentum equation that are relevant to velocity and lumping them together yields:

$$\sum_{i} a_i \mathbf{U_i} - \frac{\mathbf{U}^0}{\delta t} = -\nabla P + F \tag{3.58}$$

where a_i denotes the entries of a matrix corresponding to the discretised momentum equation [29]. $\sum_i a_i \mathbf{U_i}$ includes the contributions from all the implicit velocity terms in a discretised momentum equation. $\mathbf{U}^0$ represents the velocity from the previous time step, or the predicted velocity if the option to do so is selected. $\frac{\mathbf{U}_0}{\delta t}$ arises from the discretisation of velocity with respect to time. To reduce the need for complex matrix manipulations, the diagonal terms a_p can be used to give

$$a_p \mathbf{U}_p = \mathbf{H}(\mathbf{U}) - \nabla P + F \tag{3.59}$$

where a subscript p indicates an association with the cell under consideration. The $\mathbf{H}(\mathbf{U})$ operator has two parts, the transport which contains the matrix of coefficient for neighbouring cells multiplied by correspondent velocity

$$\mathbf{H}(\mathbf{U}) = \sum_n a_n \mathbf{U}_n + \frac{\mathbf{U}^0}{\Delta t} \tag{3.60}$$

and the source part which contains the source terms. In eq. (3.60) the $\sum_n a_n \mathbf{U}_n$ denotes the contribution of neighbouring nodes.

The discretised form of the continuity equation for incompressible fluids is given as

$$\nabla \cdot U = \sum_f \mathbf{S} \cdot \mathbf{U}_f \tag{3.61}$$

where $\mathbf{U}_f$ denotes velocity on the surface and $\mathbf{S}$ the vector of the surface of the CV with directions normal to the surface.

Equation (3.59) can be used to express velocity at the centre of the cell by

$$\mathbf{U}_p = \frac{\mathbf{H}(\mathbf{U})}{a_p} - \frac{\nabla P}{a_p} + \frac{F}{a+p} \tag{3.62}$$

and the cell face through interpolation of velocities in the cell as

$$\mathbf{U}_f = \left(\frac{\mathbf{H}(\mathbf{U})}{a_p}\right)_f - \left(\frac{\nabla P}{a_p}\right)_f + \left(\frac{F}{a_p}\right)_f . \tag{3.63}$$

Combining eq. (3.61) with eq. (3.63) gives

$$\sum_f \mathbf{S} \cdot \left(\frac{1}{a_p} \nabla P\right)_f = \sum_f \mathbf{S} \cdot \left[\left(\frac{\mathbf{H}(\mathbf{U})}{a_p}\right)_f + \left(\frac{F}{a_p}\right)_f\right] \tag{3.64}$$

which is more commonly known as the pressure equation.

The system of equations defined above are difficult to solve and require a specific ordering of equations. There are two well-known methods to solving the system, they are the Semi-

Implicit Method for Pressure-Linked Equations (SIMPLE) and the The Pressure Implicit with Splitting of Operators (PISO):

The SIMPLE, as described by Morgan [84]:

1. Solve the momentum equation to calculate the velocity field using best-guess initial values. Under-relaxation is normally used. This step is sometimes referred to as the "Momentum Predictor" step.
2. Use the predicted velocities to solve the pressure equation.
3. Calculate a new set of mass-conservative fluxes for the cell faces.
4. Calculate the new best-guess velocity field from the new set of face fluxes. Once the process has converged, this velocity field will satisfy both mass and momentum conservation.

After each iteration has completed, additional equations, such as turbulence models or multi-phase models may be solved using the updated velocities and cell-face fluxes.

The PISO algorithm after Issa [68] described in Morgan [84] is solved as:

1. The momentum equations are solved using a best-guess pressure field to produce a best-guess velocity field
2. The best-guess velocities are used to solve the pressure equation.
3. The velocity field is corrected using the new pressures.

It is possible to combine the SIMPLE and PISO above methods into the PIMPLE (PISO-SIMPLE) method, which allows for a larger Courant number to be used in calculations to improve computational speed. However, this method defaults to the PISO algorithm unless otherwise specified within the code. For this study, the default to the PISO algorithm was adopted. Thus, the solution for the discretised equations is [11]:

1. Momentum Predictor: Solve eq. (3.59). However, since the exact pressure gradient is not known, the pressure field from the previous step is used.
2. Pressure solution: By using the velocities from the previous step, the pressure equation is used to generate an approximation of the pressure field.
3. Velocity Correction: The velocity can now be corrected using eq. (3.62) and new pressures.

4. For non-Newtonian fluid, update the viscosity from a generalized Newtonian constitutive equation using the corrected velocity.

3.3.3 Boundary Conditions

The conditions for boundaries in OpenFOAM® are defined in the *constant* folder, normally within the *polyMesh* subfolder and within the *boundary* file. Here, the option to define a geometric boundary as an impermeable layer is chosen. Some boundaries are defined as wedges for axisymmetric cases, as seen in later chapters of this study, to reduce computational time. Boundary conditions are applied to control volume faces, which are defined using the chosen meshing method discussed in the following section.

7The conditions of boundaries are further set in the individual folders related to specific time-steps. Here, conditions like *inletOutlet* are used to define atmosphere boundaries, where a fluid is allowed to pass through the wall freely. An atmosphere condition is usually applied to the top boundary to allow for the exchange of the background fluid, most commonly air. Inlet boundaries such as a boundary defining the outlet of a pipe are defined as a *fixedValue* boundary, where the velocity of the material flowing out is set, normally using a *uniform* condition, but it is possible to set non-uniform velocity profiles for outlets. The fixed value boundary is generally used in *interFoam* within the individual phase fraction files, to set the velocity of that phase faction as it exits the pipe. Other common boundary types for walls are slip and no-slip conditions. These conditions influence the velocity on the boundary. A no-slip condition implies that the velocity close to the wall is equal to the wall velocity, which for a fixed wall is zero, commonly represented as a fixed value boundary with a constant value of zero. A slip condition essentially implies a friction-less wall. Finally, when setting the pressure conditions for the boundaries, a *zeroGradient* boundary is commonly used, as there is no gradient of pressure on the boundary.

3.3.4 Mesh

OpenFOAM® meshes are defined in the *polyMesh* folder contained within the time-step output for dynamic meshes, or the constant folder for static meshes. Poly-meshes are a complex format specific to OpenFOAM®, meaning they cannot be easily created by commonly found tools and must be built using the toolboxes provided in the OpenFOAM® library. That is not to say that conventional meshing methods cannot be converted into usable meshes, as is the case with some of the meshes used in the present work, described at the point of use in the following chapters.

OpenFOAM® uses a mesh of arbitrary polyhedral cells in 3-D, bounded by arbitrary polygonal faces. Thus, it is possible for cells to have an large number of faces where, for each face, there is no limit on the number of edges nor any restriction on its alignment, allowing for a large degree of mesh manipulation [61]. Poly-meshes use a combination of points, a unique labelled location in 3D space defined by a vector in units of metres, and faces, an ordered list of points where a point is referred to by its label. Faces are compiled into a list and each face is referred to by its label, representing its position in the list [61]. As previously discussed, boundaries are applied to a set list of faces, beginning with *startFace* and continuing for the amount of faces representing the boundary, input as *nfaces*. Faces are also used to define *patches* in the *boundary* file of the poly-mesh, created using the chosen meshing tool.

The simplest meshing tool available for OpenFOAM® is the *blockMesh* meshing utility. The size, and cell type of the mesh are set in the *blockMeshDict* file within the system folder. The output mesh can be directly used in a simulation. An added benefit of using *blockMesh* to create a mesh, is the ability to subtract unwanted regions, refine additional parts and redefine boundaries creating a significantly more complex mesh by using the *snappyHexMesh* tool. By using *.stl* files to define boundaries, easily output from many conventional meshing tools, these boundaries can be applied to a simple block-mesh created in OpenFOAM®. Additional refinement can also be specified here. There is a great degree of freedom afforded to creating a mesh in this way, however, the process of generating meshes this way is can be time-consuming and tedious.

The process of subtracting cells and creating a new mesh from a block-mesh using the *snappyHexMesh* tool is simplified in fig. 3.12. Although only three steps are presented, multiple iterations will be performed to find the optimum mesh. Finally, the quality of the mesh can be obtained by using the *checkMesh* tool, which gives warnings or errors for low quality meshes or cells. All meshes used in the present work have been checked using this functionality and passed all necessary checks.

3.4 Post Processing

The Visualization Toolkit provides a number of source and writer objects to read and write popular data file formats, mainly the VTK file format. Visualisation of OpenFOAM® results can be converted to this format, to be readily readable by the open-source, multi-platform data analysis and visualization application developped by Kitware, ParaView. Additionally, the CB-GEO MPM code also offers the option for results to be output as VTK files. ParaView allows for data manipulation using qualitative and quantitative techniques. Where both point

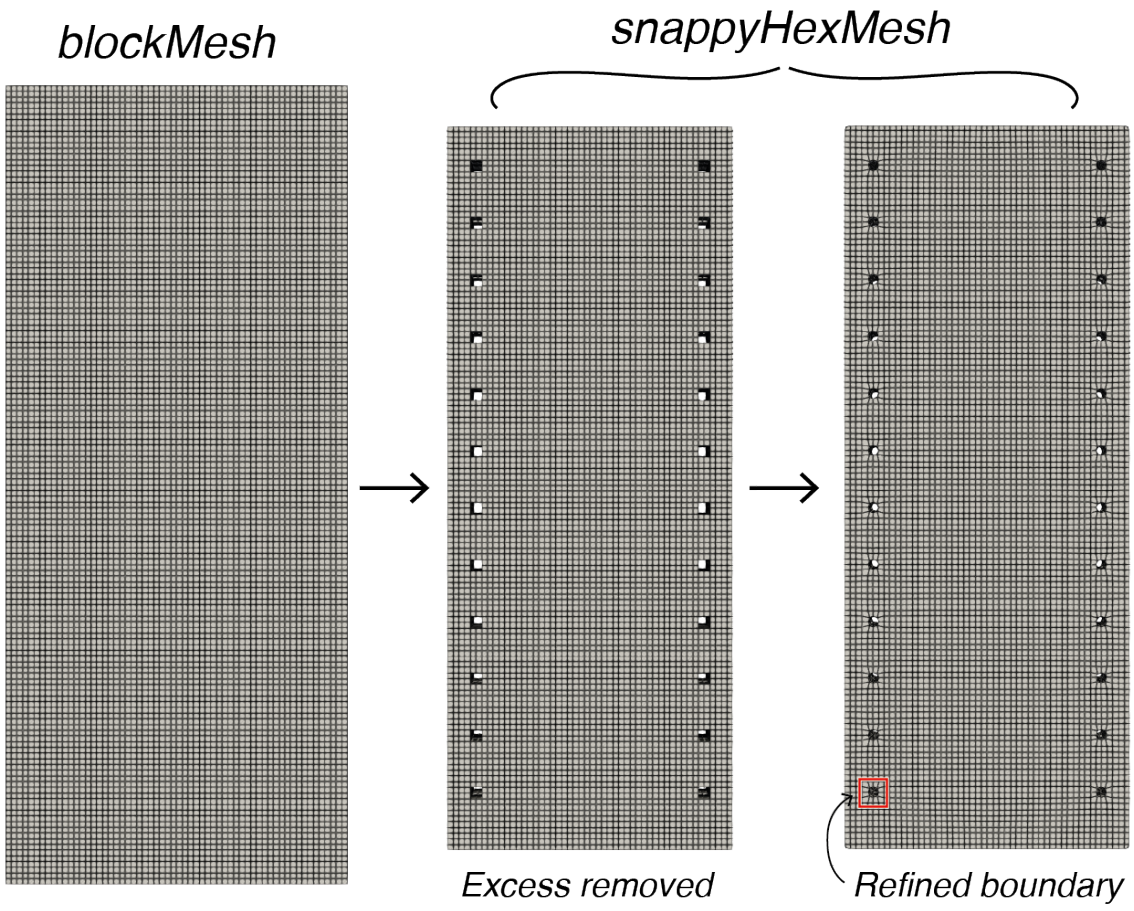

Fig. 3.12 A simplification of the blockMesh and snappyHexMesh tools of OpenFOAM®, where an original mesh has had excess cells subtracted and new boundaries refined.

data, and cell data can be explored. It is particularly useful for processing large data-sets, as is the case with MPM results in this work where more than a hundred thousand data points are regularly output at each step.

For additional MPM data manipulation, CB-GEO MPM results for each point can be output in the Hierarchical Data Format (HDF) HDF5. HDF5 data can be read using different programming languages, and for the purposes of this study, will be read and manipulated using a MATLAB® code capable of reading and plotting the desired data, developed for this work [37]. Many of the plotted graphs for MPM results in this work are created using this code.

3.5 Conclusion

Both the Material Point Method and Computational Fluid Dynamics have the ability to simulate Tremie Concrete, albeit with some caveats for each method. This chapter has discussed the software used for each numerical method, and presented the governing equations. The following chapters will implement each method and simulate concrete for a specific purpose, with a comparison made later in this work.

Chapter 4

CFD Simulation of Tremie Concrete in Deep Foundations

4.1 Introduction

In the Tremie Method, TC is emplaced into the foundation in batches with the time between concrete loads spanning from minutes to hours. The bulk flow behaviour of newer TC entering a partly cast foundation with TC already in place is commonly described as a concrete flow pattern. The dominant flow pattern of concrete within a deep foundation can cause a variety of construction issues, including: voids or exposed reinforcement bars if concrete is unable to flow easily around obstacles, indirect segregation of concrete, and the inclusion of low-strength material by way of concrete inter-mixing with support fluid. As such, investigating concrete flow behaviour can provide ways to avoid defects in the final structure.

Physical investigations of concrete flow patterns rely on excavations exposing defects, or the exhumation of test piles for dissection [53]. This is both time consuming and costly. To reduce the time and cost associated with physical experiments, numerical models have been employed to conduct back-analysis of exhumed piles to ascertain what behaviour the concrete exhibited to create the observed patterns [52, 53, 46, 70].

Whilst back-analysis has proven useful, a real-time analysis of concrete flow behaviour in deep-foundation like conditions has not been conducted. Thus, numerical models have only been validated by modelling final conditions in simple empirical tests [102], but are assumed to be valid for more complex flow behaviour.

This chapter presents a new physical experiment where concrete behaviour closely related to that found within a deep foundation can be captured in real-time. This presents a new validation opportunity for numerical models of concrete flow. OpenFOAM® is employed in this chapter to simulate the physical test, providing additional evidence of the ability of CFD models to capture complex concrete flow behaviours. The implementation of the CFD model is first validated validated using the Slump-Flow test before simulations of the novel experimental apparatus are conducted. The objective of this chapter is to combine numerical and physical data to define the controls on bulk flow behaviour of concrete within deep foundations.

The chapter is structured as follows: First, a novel experimental procedure aimed at capturing the early-stage flow behaviour of concrete for the first time, in real-time, is presented. This is followed by an overview of the constitutive model used in OpenFOAM® and the complex meshes used to represent the experimental apparatus. Finally, results of both the laboratory tests and simulations are presented, where validated numerical models and experimental analysis are combined to give a new classification system of flow behaviour in deep foundations.

4.2 Methods and Materials

4.2.1 Experimental Design

A 1 m x 0.2 m x 0.05 m gravity-driven concrete flow-box (GFB) was designed to represent a plane-strain cross-section through a 1:6 scale bored pile, figure 4.1a. The apparatus features a scaled tremie pipe that can be raised from the base to allow the outflow of concrete in accordance with the initiation height recommendations by the Institute of Civil Engineers [66]. Concrete is stored in the hopper and raised with the pipe to allow concrete to flow outwards once the pipe is raised, fig. 4.1b. The flow behaviour of the concrete as it exits the pipe and rises through the box can be observed through the clear perspex window on the front.

During the physical tremie process, a charged pipe should be maintained throughout the entire process to ensure the hydro-static pressure inside the pipe is greater than that of the outside to prevent inflow of the support fluid [46, 66]. Prior to the initiation of flow, a charged pipe is typically achieved by using an insert within the pipe to prevent an ingress of support fluid. The GFB achieves a similar effect by using a foam gasket on the base to allow the pipe to be charged (filled) without concrete escaping. The initial raise of the GFB pipe also

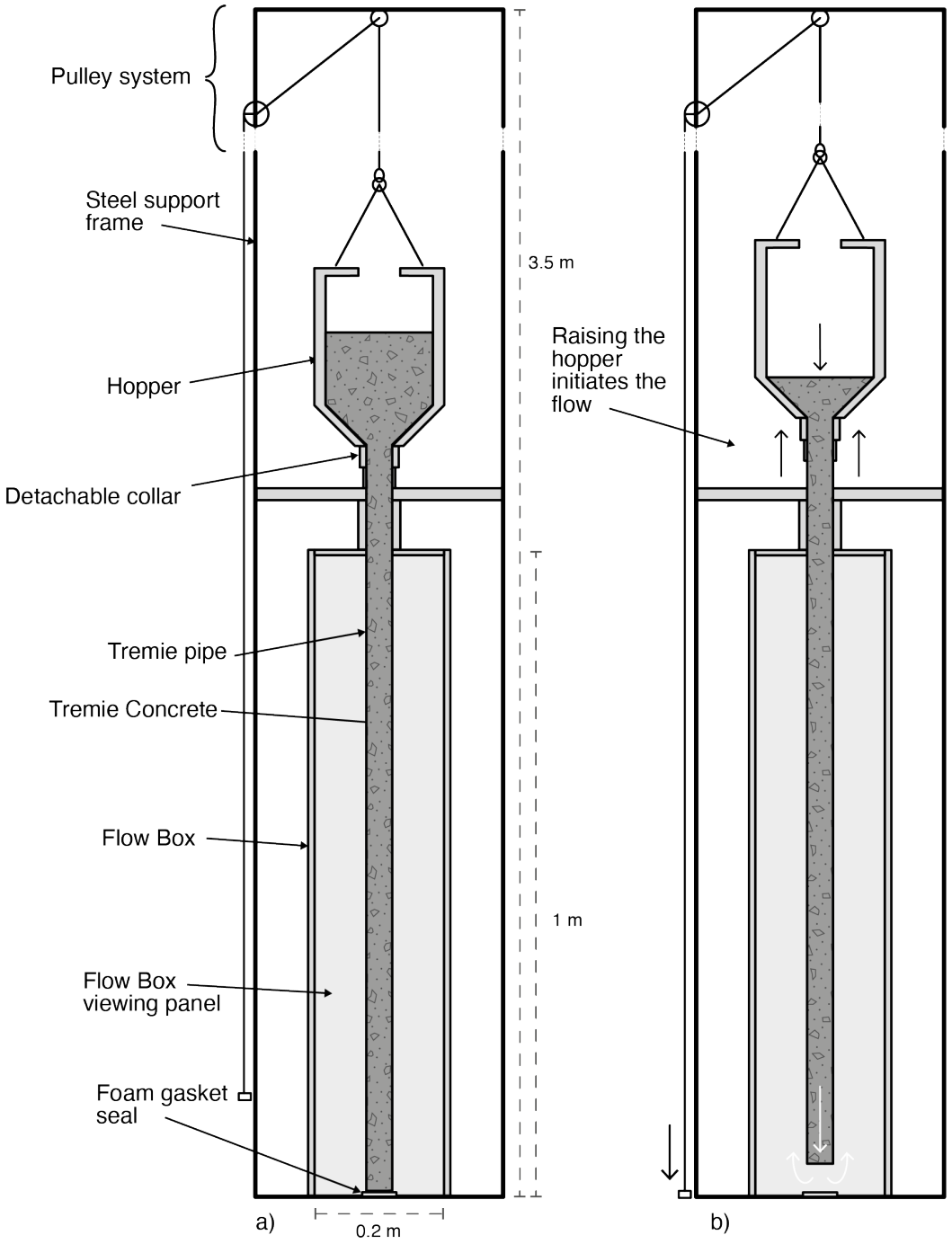

Fig. 4.1 a) Schematic diagram of experimental design, featuring the Flow-box and steel support frame with pulley system. Diagram is a slice through centre of apparatus. b) Demonstration of how raising the hopper initiates the flow

conforms to a scaled representation of the physical initiation height as specified in [66], which corresponds to the diameter of the tremie pipe, or 40 mm.

Reinforcement inserts can be used in the GFB, providing they are spaced horizontally and vertically within the GFB in accordance with best practice recommendations on concrete spacing and aggregate size [47]. The recommended spacing between horizontal bars is 4x the maximum aggregate size used in the concrete mix, while vertical spacing is recommended to be at least 0.1 m [47]. For tests using horizontal rebar inserts, spacing of at least 0.04 m is used in accordance with the mix design described in the following sections of this chapter. A nominal concrete cover (the distance between the excavation wall and the reinforcement bars) of 75 mm is recommended for industry use, thus, considering the 1:6 scale of the GFB, a concrete cover of 25 mm is sufficient for the experiment.

4.2.2 Experimental Procedure

The construction of reinforced concrete foundations does not always require the rebar cage to be present during the filling of the shaft. Depending on the contractor preference, the cage may be plunged post concrete emplacement. Additionally, some deep foundations do not require reinforcement at all, such as the production of secant-pile walls where reinforcement is often used in alternating piles. Therefore, it is important to model both scenarios to understand the effect this has on the bulk flow behaviour of concrete.

To monitor the flow behaviour, two batches of concrete are used for each test. First, an un-modified mix (the design of which is specified in the following section) is emplaced into the GFB. A second concrete mix with red pigment is then emplaced immediately after the first batch, fig. 4.2. Video footage of the flow behaviour of both concrete batches is captured through the perspex viewing window at 30fps and 1080p resolution using a Canon EOS 1200D DSLR camera with an EFS 18-55mm lens set up to minimise the impact of lens curvature. Initial tests presented in this chapter will have motion tracking markers present, however, they are removed in later tests as they obscured the viewing window.

Traditional flow tracking methods of flowing materials were unusable for concrete as many methods rely on granular colour changes across pixels that are not present in concrete. Therefore, the spreading behaviour of the second, dyed concrete batch is quantified using the *bwboundaries* [17] function of MATLAB®. For the present study, this function was implemented into a code capable of tracking the moving boundary of a body [38]. This function requires the conversion of coloured video stills into black and white images where the boundary between black and white pixels can be easily identified. The boundary between

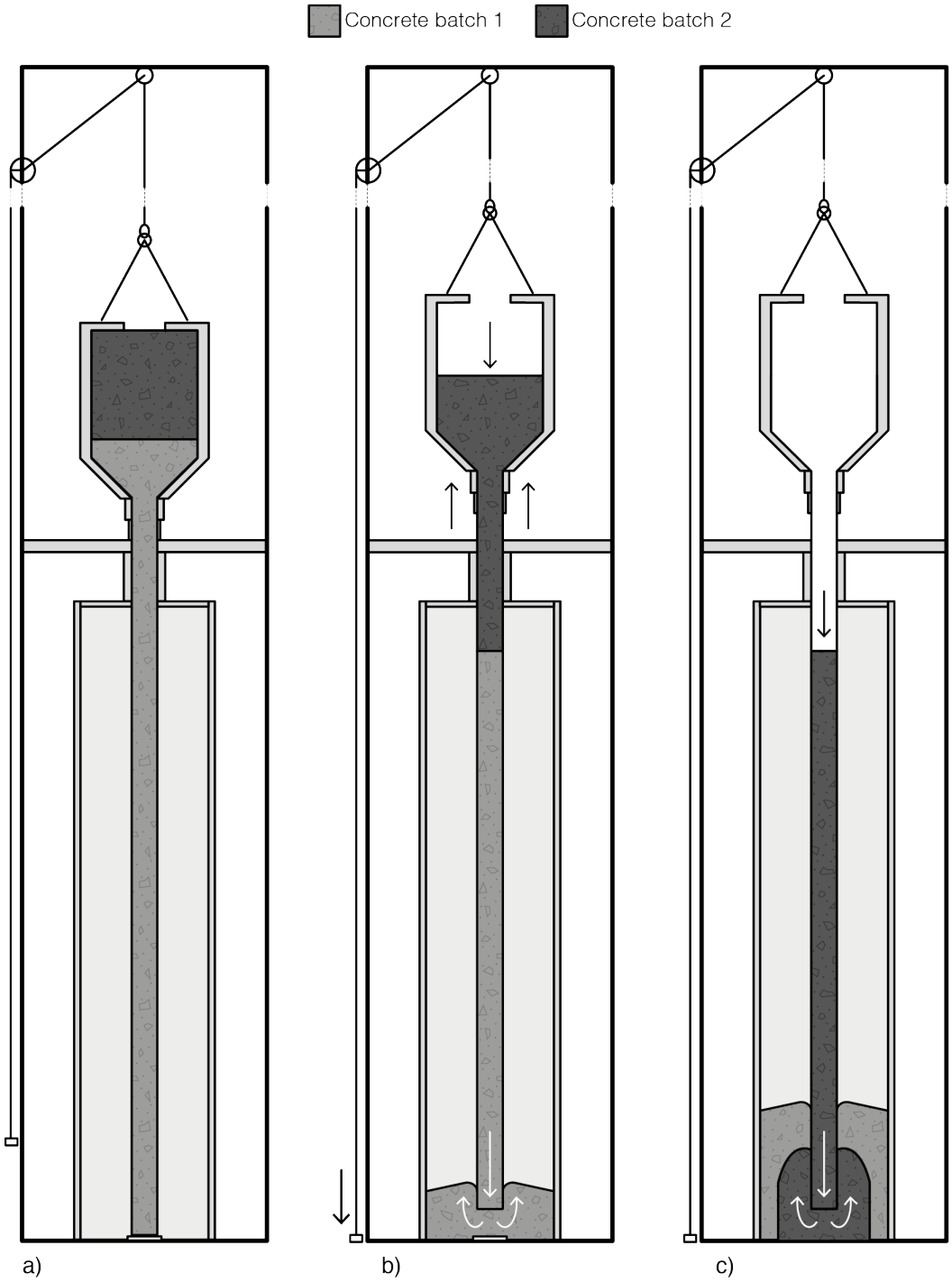

Fig. 4.2 a) Start of an experiment where two batches of different colours are in the hopper. b) Pipe raised and concrete begins to flow. c) Once all of batch one is emplaced, the second concrete of a different colour is emplaced, and the flow behaviour captured through the viewing panel.

the dyed concrete (batch 2) and the already in place concrete (batch 1) can be plotted using this method, presented in fig. 4.3. As the time step between each frame of a video is constant, the spreading velocity of the dyed concrete can be calculated.

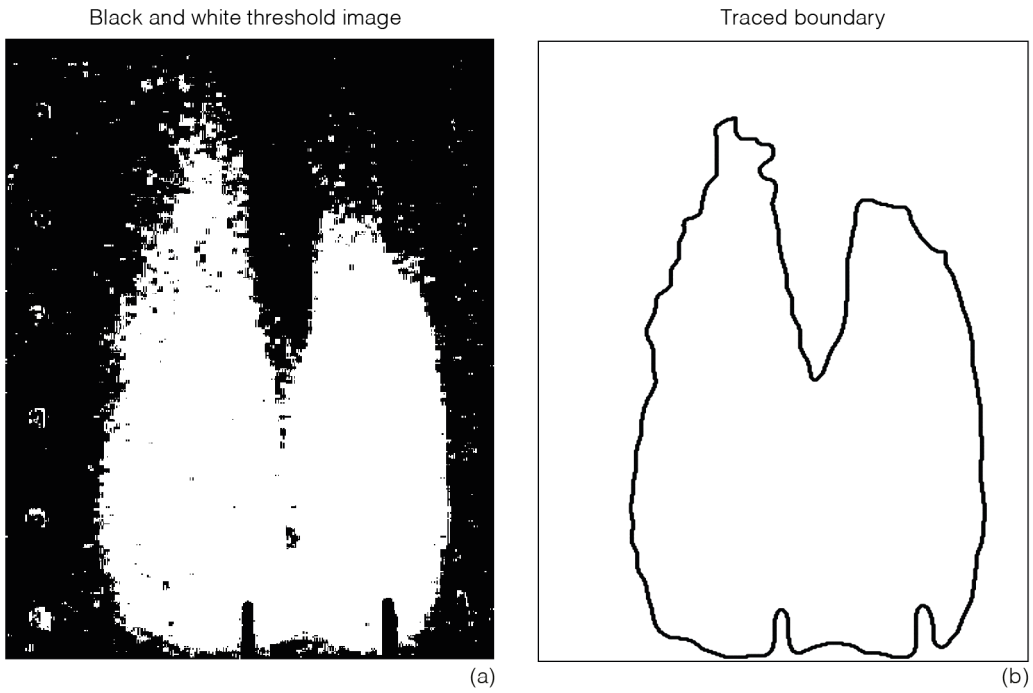

Fig. 4.3 a) Black and white threshold image of a photographic still taken from footage of a GFB experiment. b) The outline of the boundary of a), mapped using [38].

The experimental apparatus requires two persons to operate, as such, the collection of experimental data was completed with the assistance of Mr David Buglass.

4.2.3 Mix Design

ICE [66] recommends the maximum aggregate size used in a Tremie Concrete mix design should not exceed $1/6$ of the tremie pipe diameter, to maximise flowability. The GFB pipe is a 1:6 scale of the standard tremie pipe size, resulting in a 40 mm pipe opening. In order to maintain the correct material properties in conjunction with required workability, an 8 mm maximum aggregate size is used in the GFB.

A 0.55 cement-water ratio, CEM II/B-V based mix was designed following a similar mix design used by [52] with the cement provided by CEMEX UK. This is a Portland fly ash cement with a 65-79% Portland cement clinker content and 21-35% pulverised fly ash content. A polymer-based superplasticiser provided by BASF in the form of MasterGlenium SKY 920 was used at 400 ml per 100 kg of cement to provide additional workability and

Material		Mass per 8.3 kg batch
Water		880g
CEM II/B-V		1610g
Sands / Aggregates	0.15 - 0.30 mm	1900g
	0.40 - 1.40 mm	830g
	1.00 - 2.00 mm	780g
	2.00 - 3.00 mm	880g
	3.00 - 5.00 mm	430g
	5.00 - 8.00 mm	1030g
Air Volume (Assumption)		15 dm^3/m^3 [52]
MasterGlenium SKY 920		7g

Table 4.1 Tremie Concrete mix design for GFB with an 8.3kg batch size.

extended retention times. Aggregate and sand were sourced from local suppliers with grain size distribution detailed in table 4.1.

ICE [66] recommends the use of the 'slump-flow' test in accordance with [26] as a way to measure of the consistence of a concrete, ensuring it is workable enough for the tremie process. The experimental mix achieved a slump flow of 560 mm which places it well within the range of acceptability.

The GFB provides a means for capturing the flow behaviour of concrete in real-time, providing numerical models with a more comprehensive method of validation. The following section details the numerical model used in the present study.

4.2.4 Numerical Model

The apparent viscosity, η, in eq. (3.51) depends on the rheological model used to describe concrete. A rheological model provides a quantitative description of a materials flow properties. For Tremie Concrete, this model takes the form of a simple Bingham model. Applied to concrete by Tattersall [115], the Bingham model allows for a description of the minimum initiation force required for concrete to flow, known as the yield stress (τ_0), as well as the proceeding Newtonian behaviour. The 1D constitutive equation of the Bingham model is:

$$\tau = \mu\dot{\gamma} + \tau_0\,, \tag{4.1}$$

where τ represents the shear stress, μ represents plastic viscosity and $\dot{\gamma}$ represents the shear rate, which is $\dot{\gamma} = 2(\mathbf{D}_{ij}\mathbf{D}_{ij})^{1/2}$ in 3D. The shear stress is a linear function of shear rate, with

an intercept on the shear stress axis representing the yield stress. Materials with stress below the yield stress exhibit properties of a rigid body with viscoelastic effects. Materials that exceed the yield criteria behave as a viscous liquid [98]. A Bingham material is said to be viscoplastic in nature.

In OpenFOAM®, the Bingham model takes the form of a generalised Herschel and Bulkley [63] (HB) model:

$$\tau = k\dot{\gamma}^n + \tau_0\,, \tag{4.2}$$

where k is the consistency index and n is the power law index. If $n = 1$ the HB-model reduces to the Bingham model in eq. (4.1). The transition from rigid behaviour to viscous presents an issue as both the discontinuity and the simulation of rigid body behaviour through solid mechanics is not possible in OpenFOAM® [107]. To overcome this, the HB-model is regularized using the bi-viscosity technique presented in [15] which is implemented into OpenFOAM® as [107]:

$$\eta = min(\eta_0, \frac{\tau_0}{\dot{\gamma}} + k\dot{\gamma}^{n-1})\,. \tag{4.3}$$

where *min* represents a conditional statement to select the minimum of the two successive conditions separated by a comma, Equation (4.3) is equivalent to

$$\eta = \begin{cases} \eta_0 & \text{if } |\dot{\gamma}| \leq \dot{\gamma}_c \\ \frac{\tau_0}{\dot{\gamma}} + k\dot{\gamma}^{n-1} & \text{otherwise} \end{cases} \tag{4.4}$$

where $\dot{\gamma}_c$ is the critical shear rate at which the transition from viscous to rigid body behaviour occurs. This value is automatically calculated in OpenFOAM® depending on the chosen HB-model and η_0 values. Equations (4.3) and (4.4) prevent the occurrence of infinite apparent viscosity as the shear rate approaches 0 by including a maximum apparent viscosity value in the form of η_0. For the present study, $n = 1$ is adopted, reducing eq. (4.4) to the Bingham model such that

$$\eta = \begin{cases} \eta_0 & \text{if } |\dot{\gamma}| \leq \dot{\gamma}_c \\ \frac{\tau_0}{\dot{\gamma}} + \mu & \text{otherwise} \end{cases}. \tag{4.5}$$

4.2.5 Model Parameters

To validate a numerical model's ability to simulate concrete accurately, Roussel et al. [102] devised a benchmark comparison test where a virtual concrete with a yield stress of 50 Pa and plastic viscosity of 50 Pa · s is simulated and the result compared with analytical and experimental results. If the modelled concrete behaves in accordance with the analytical and physical expectations, the model is validated. The benchmark simulation concrete is input into the transport properties as:

```
{
    transportModel   HerschelBulkley;
    rho              rho [1 -3 0 0 0 0 0] 2300;
    HerschelBulkleyCoeffs
    {
        k               k [0 2 -1 0 0 0 0] 0.02173913;
    nu0             nu0 [0 2 -1 0 0 0 0] 10;
    tau0            tau0 [0 2 -2 0 0 0 0] 0.02173913;
    n                n [ 0 0 0 0 0 0 0 ] 1;
    }
}
```

The transport values, e.g. 'tau0', are input as kinematic values which require dividing the required value (in this case, 50 Pa) by the density, ρ, rho. This is also the case for all other OpenFOAM® input values presented within this chapter.

The benchmark test in [102] consisted of simulating a Slump-Flow test according to BS EN 12350-8:2019 [26]. An empirical test, the Slump-Flow test is used for measuring the consistency of Tremie Concretes on site, and in a laboratory setting. The test involves filling a flat-topped cone with concrete and allowing it to rest for no more than 30 s. The cone is then raised at a constant velocity in 1-3 s to allow the concrete to flow outwards. The Slump-flow spread or SF is the diameter of the resulting spread averaged over two perpendicular measurements.

Simulating the Slump-Flow test in OpenFOAM® requires the use of a moving boundary and a mesh capable of deformation in order to accurately represent the rising cone. For the present study, a dynamic mesh was created using a *dynamicMotionSolverFvMesh* where the moving boundary velocity is determined using the *velocityComponentLaplacian* option within the OpenFOAM® input files. Diffusivity, the distribution of deformation within each

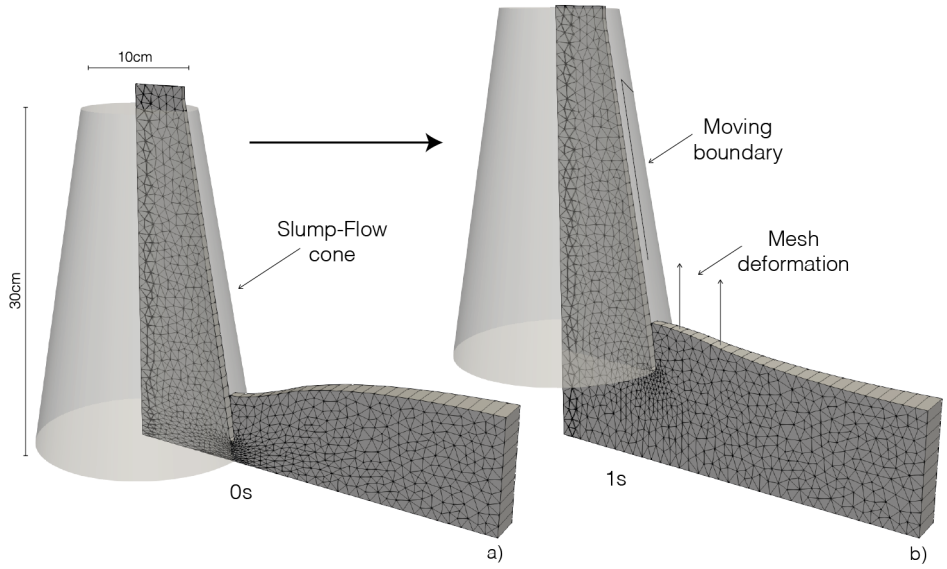

Fig. 4.4 Axisymmetric, wedge, dynamic mesh used for benchmark test validation. a) Initial mesh at 0 seconds of runtime. b) Mesh at 1 second of runtime. The moving boundary and areas of the mesh that deform are indicated by arrows.

cell as the boundary and mesh deform, was set using the *inverseDistance* from the cone boundary.

Figure 4.4 displays the mesh used for the benchmark case. It is an axisymmetric, wedge mesh, which is equivalent to simulating the whole 3D cone but requires significantly less computational effort. The wedge mesh was generated using the free mesh generator tool GMSH [56], and the OpenFOAM® meshing tool *gmshToFoam*. Fierenkothen [52] used a similar wedge meshing approach and reported that the Slump-flow test has a low degree of mesh sensitivity.

The slump flow test for the experimental mix design gave a result of 560 mm. According to [47] this would give an approximate yield stress of 75 Pa. Unfortunately, a rheometer was not available to measure viscosity. However, a viscosity of 28 $\mathrm{Pa} \cdot \mathrm{s}$ was chosen by assuming that the relationship between yield-stress and viscosity of tremie-concrete observed in [46] is true for the experimental mix (the relationship arises due to mix designers balancing low viscosity with high yield stress and vice versa). This is also in-line with the typical viscosity values observed in high SF tremie concretes. The results of a simulated Slump-flow test for the experimental mix is presented alongside the benchmark case in the results section of this paper. For the transport properties file, this is input as:

```
{
    transportModel   HerschelBulkley;
    rho              rho [1 -3 0 0 0 0 0] 2400;
    HerschelBulkleyCoeffs
    {
        k               k [0 2 -1 0 0 0 0] 0.011875;
    nu0             nu0 [0 2 -1 0 0 0 0] 10;
    tau0            tau0 [0 2 -2 0 0 0 0] 0.03125;
    n                n [ 0 0 0 0 0 0 0 ] 1;
    }
}
```

The results of a simulated Slump-flow test for the experimental mix is presented alongside the benchmark case in the results section of this chapter.

To simulate the GFB, a hexahedra cell, 3D mesh was constructed for the both the reinforced, see fig. 4.5, and un-reinforced cases. The mesh is 0.6 m tall, as opposed to the 1 m experimental GFB as all the necessary information can be captured in this region. The simulated GFB is also marginally wider, at 0.24 m rather than 0.2 m, to account for boundary effects from the pipe having a higher than desirable level of friction due to the assigned *noSlip* boundary condition. The rigid bodies of the tremie pipe and reinforcement inserts are included into the mesh as walls with a *noSlip* condition by creating holes through the mesh and applying boundary conditions.

A *noSlip* condition assumes that the velocity of the fluid in contact with the wall has the same velocity as the wall, which for a stationary wall will be zero. The *noSlip* condition could over estimate the frictional contact between the concrete and solid wall, but for the purposes of this study, is acceptable. Conversely, for the moving boundary of the benchmark simulation mesh, a *slip* condition is maintained to allow the concrete to flow down the sides of the mesh, as the *noSlip* condition prevented smooth out-flowing of concrete.

The GFB mesh was generated using the free meshing tool GMSH [56] and the OpenFOAM® meshing tool *snappyHexMesh* which generates a hexahedra mesh by subtracting the GMSH mesh from an existing, larger hexahedra mesh generated by the OpenFOAM® meshing tool *blockMesh*.

The Cell Reynolds Number, R_e, is the value of the Reynolds number within a cell. A dimensionless parameter, the Reynolds number provides a single value for the ratio of inertia forces to viscous forces. This is typically presented as:

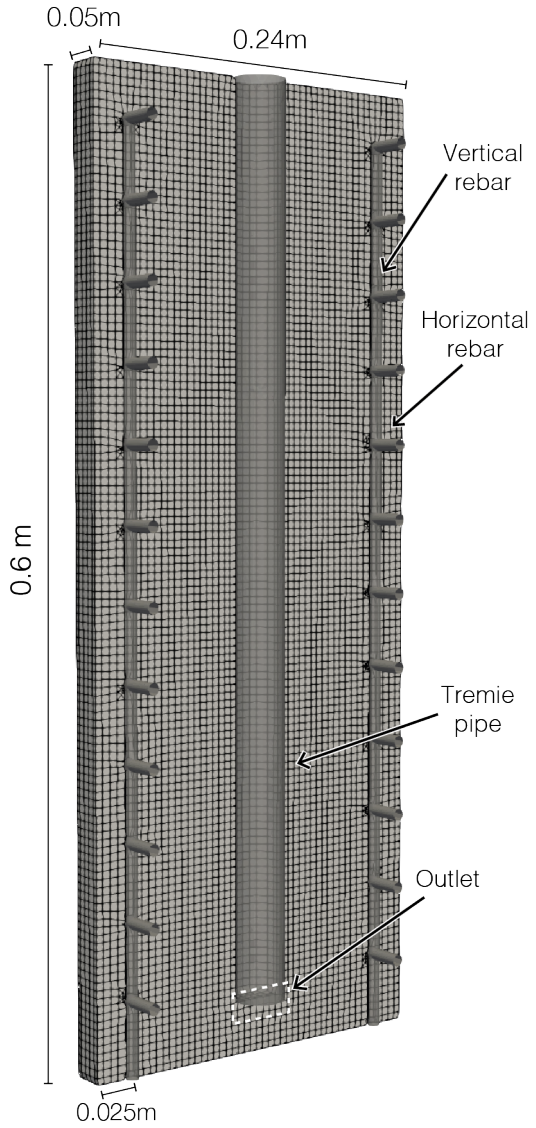

Fig. 4.5 Hexahedra mesh of GFB, featuring location of the wall used to represent the reinforcement inserts.

$$R_e = \frac{\rho V' D'}{\mu'}, \tag{4.6}$$

Where V' is the flowing velocity, D' the dimension of the cell (or flow domain) and μ' the viscosity. According to Roussel and Gram [101], the Reynolds number of a Bingham fluid can be expressed as:

$$R_e = \frac{\rho V'^2 D'}{D' \tau_0 + \mu V'} \tag{4.7}$$

where μ is now the plastic viscosity of eq. (2.1). With a cell length of 0.005 m and an maximum injection flow rate of $0.4\,\mathrm{m\,s^{-1}}$, the cell Reynolds number is approximately 0.1630 for the experimental concrete mix. Generally, a maximum cell Reynolds number of 1.0 should be maintained for stability.

The pressure boundaries of both meshes are set as *zeroGradient* for boundaries that are walls, and as an atmosphere with the type *inletOutlet* for those boundaries that require the exchange of fluid freely across the boundary, such as the top of the GFB that allows air to flow out of the box as the concrete rises. The front and back faces of the wedge mesh are set as a *wedge* boundary type as required by OpenFOAM® for reading axisymmetric meshes.

The outlet at the base of the pipe is the point of entry for the concrete into the mesh and velocity is set as a fixed value boundary of the *fixedValue* type. Material is injected at a steady, uniform velocity, set using the *uniform* parameter, over the entire inlet face in accordance with the velocity observed in the experimental analysis provided in the results section.

For the experimental GFB tests, no support fluid is used, leaving the concrete to displace air inside the box. For the simulated GFB tests, air is also used, represented as a Newtonian fluid with a viscosity of $0.0000148\,\mathrm{Pa\cdot s}$ and a density of $1\,\mathrm{kg/m^3}$. This is input into transport properties by:

```
{
    transportModel  Newtonian;
    nu              nu [ 0 2 -1 0 0 0 0 ] 1.48e-05;
    rho             rho [ 1 -3 0 0 0 0 0 ] 1;
    CrossPowerLawCoeffs
    {
        nu0             nu0 [ 0 2 -1 0 0 0 0 ] 1e-06;
        nuInf           nuInf [ 0 2 -1 0 0 0 0 ] 1e-06;
```

```
        m               m [ 0 0 1 0 0 0 0 ] 1;
        n               n [ 0 0 0 0 0 0 0 ] 0;
    }

    BirdCarreauCoeffs
    {
        nu0             nu0 [ 0 2 -1 0 0 0 0 ] 0.0142515;
        nuInf           nuInf [ 0 2 -1 0 0 0 0 ] 1e-06;
        k               k [ 0 0 1 0 0 0 0 ] 99.6;
        n               n [ 0 0 0 0 0 0 0 ] 0.1003;
    }
}
```

4.3 Results and Discussion

In this section, the results from two cases are presented:

- Case One: Without reinforcement inserts.
- Case Two: With reinforcement inserts.

Each case is modelled experimentally and numerically, with the results and discussion presented in this section.

4.3.1 Experimental

Case One

Figure 4.6 contains a series of images captured during a Case One GFB experiment. Figure 4.6a is the final state of the experiment, where all concrete in the hopper has flown freely through the Tremie pipe and into the lower box. In fig. 4.6a, the second batch of concrete has spread entirely out to the edge of the box. Batch 2 has effectively bisected batch 1 by splitting it into a small portion in the lower corners and a larger section at the head of the flow. The larger section of batch 1 appears to be uncontaminated by the red concrete of batch 2, suggesting a low level of mixing has occurred. According to the description of flow patterns outlined previously and in [47], the larger section of undisturbed batch 1 sitting atop batch 2 could be considered a concrete ‘plug’ if the shearing forces are low enough.

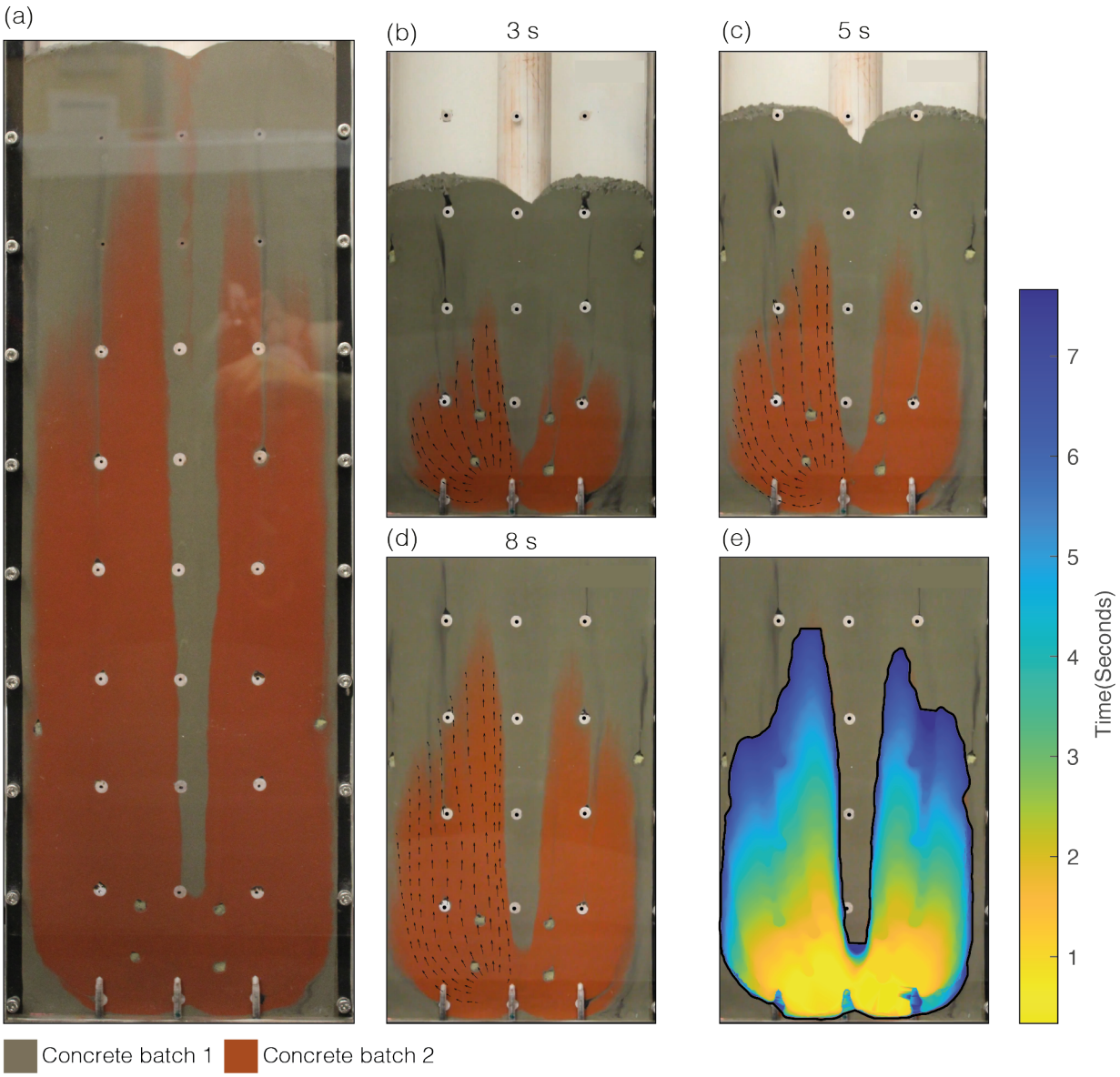

Fig. 4.6 a) Photograph of the GFB viewing panel at the end an experimental model of Case One. b-d) development of flow pattern of second concrete batch at 3, 5 and 8 s. e) Tracking of concrete flow head over time.

Figure 4.6b-d shows the spreading behaviour of batch 2 at three time intervals, 3, 5 and 8 s. At 3 s, the second batch is predominantly flowing horizontally from the pipe towards the outer boundary. By 5 s the dominant horizontal flow appears to have transitioned into vertical flow. At 8 s there is no more room to spread horizontally, so the flow is now predominantly vertical. Figure 4.6e is a visualisation of how the flow pattern in fig. 4.6d evolved over time, using the boundary trace method described in section 4.2.2. The closeness of horizontal colour changes compared to vertical suggests that upwards flow of the concrete is the dominant style at this point in time. However, as discussed, the dominant flow during the initial stages is predominantly horizontal.

With Reinforcement

Figure 4.7 is a set of images recorded from a GFB experiment of Case Two, where inserts are added at 60 mm intervals on the left side, oriented perpendicular to the visible plane to represent horizontal rebar. A single vertical insert placed 25 mm from the front, back, and right side is used to represent vertical rebar. It is possible to use different conditions on the left and right sides of the GFB as no visible interaction is observed between the two halves.

The final state of the experiment is shown in fig. 4.7a. The most notable difference between Case One and Two, is the increased thickness of Concrete batch 1 at the edges of the viewing window when inserts are present. Concrete between the excavation wall and the reinforcement cage is often described as the 'cover zone'. From fig. 4.7a, the cover zone appears to be almost completely formed of batch 1, rather than batch 2. The top of fig. 4.7a indicates that some mixing between batches has occurred, as the clear boundary between batches that can be observed in fig. 4.6a is not present. The lack of a clear boundary suggests there is no 'plug' of low shear concrete present in this case, either.

The early-stage flow behaviour of Batch 2 in Case One (fig. 4.6b-d) shows a large amount of horizontal flow, whereas, for Case Two, there is a limited amount of horizontal flow, fig. 4.7b-c. This can be observed by the rate of change between colours in the vertical direction compared to horizontal direction in fig. 4.7d, with vertical colour changes happening over larger distances than horizontal changes. Figure 4.7b-c are displayed as grey-scale to highlight batch 2 due to the reduction in definition between batches in Case Two.

One key difference the inclusion of rebar has on the flow properties, aside from the differing bulk flow patterns, is the flow velocity of the second concrete batch. For an un-reinforced case, the outflow velocity from the pipe, over the first 10 s is approximately $0.4\,\mathrm{m\,s^{-1}}$, based on the volume output and the diameter of the circular pipe. Interestingly, the calculated

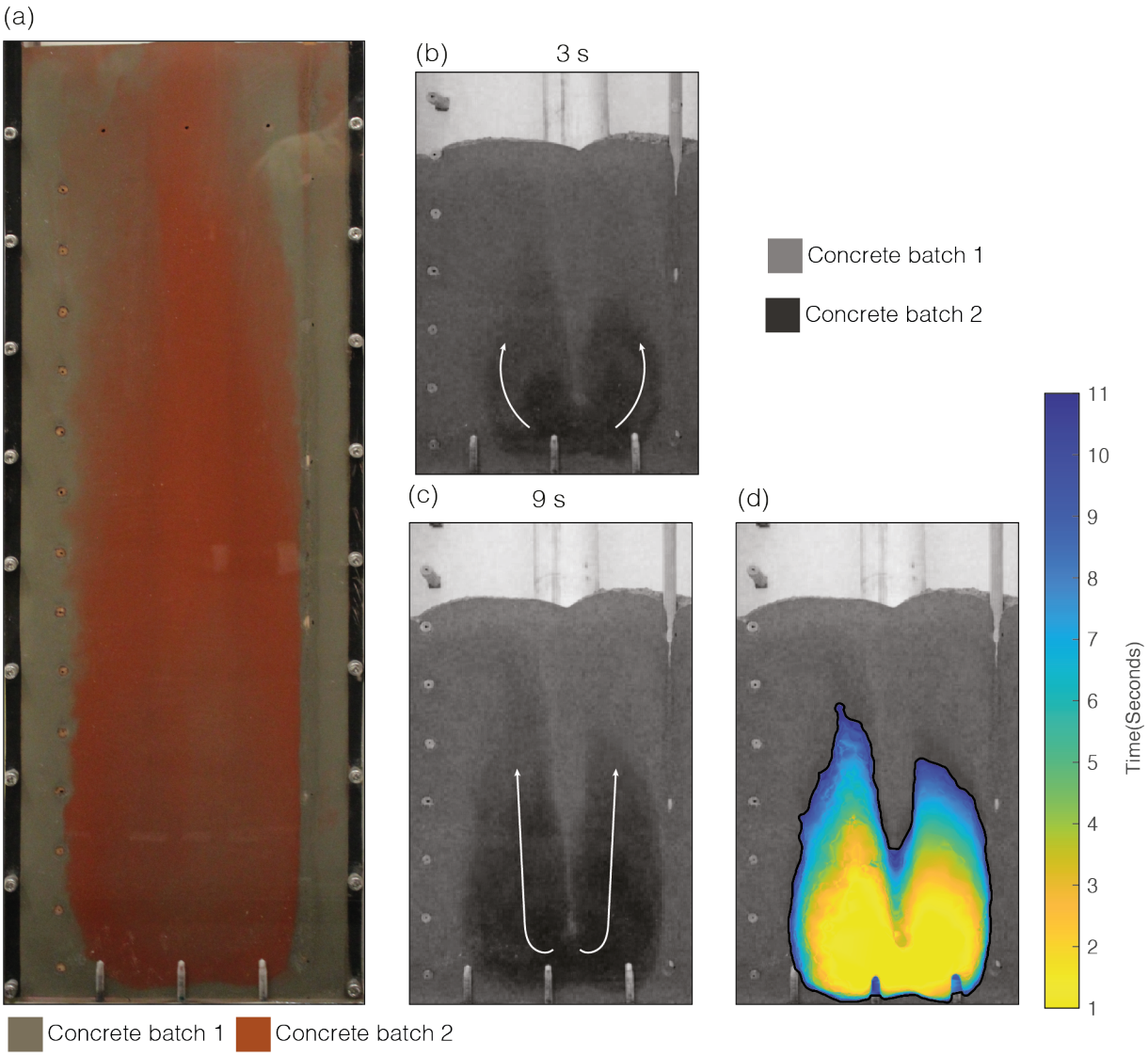

Fig. 4.7 a) Front view of flow pattern for a Case Two, first 10 seconds of the secondary batch (darker) are presented, scaled to time in seconds. b-c) development of flow pattern of second concrete load. e) Tracking of concrete flow head.

velocity of the reinforced case is approximately $0.2\,\mathrm{m\,s^{-1}}$, or roughly half. So for two concretes of the same properties, the outflow velocity is halved by the addition of rebar.

The confinement of the flow to within the area surrounding the pipe, rather than a broader area was theorised to be caused by a change in boundary conditions [47]. The results from experimental analysis of Case One and Two support this hypothesis, as evidenced by the significant difference between the two cases after the inclusion of reinforcement inserts. The increased likelihood of vertical flow in a secondary concrete batch when emplaced into a pre-existing fresh concrete encompassed in a reinforcement cage is an important observation when concerning concrete behaviour in a deep foundation and could impact how mixes are designed.

If the numerical model can capture the same behaviour observed in the experimental cases, then the model could feasibly be used with a higher degree of confidence for more complex problem analysis, leading to significant time and cost savings vs experimental operations.

4.3.2 Numerical simulations

Benchmark

The Roussel et al. [102] benchmark comparison test is performed first to validate the ability of CFD to simulate concrete accurately. The test takes the form of the a virtual Slump-flow test where the rheological input parameters should create a slump-spread of a known diameter. It is worth noting that the chosen rheological model for the simulations will always cause the simulations to exhibit a small degree of deformation even at low shear rates. For this reason, a cutoff time of 15 s is applied to the benchmark test as suggested by Roussel et al. [102].

Figure 4.8a shows the results from the benchmark test. It demonstrates the evolution of the Slump-flow spread of the virtual concrete. According to Roussel et al. [102], a target Slump-flow of 0.60 m is expected. This is highlighted as the dashed line for fig. 4.8a. Figure 4.8b is the final shape of the concrete spread as a slice of the asymmetric mesh.

Figure 4.8c shows the results from a Slump-flow simulation of the experimental mix design used for the experiments in the GFB. The yield stress and plastic viscosity for this simulation are derived from the experimental Slump-flow result of 0.560 m. The target slump-flow and the Slump-flow at the cutoff time differ due to the approximations made to obtain the rheology input parameters from the Slump-flow test and the correlation between yield stress/plastic viscosity and SF presented in Chapter 2. Figure 4.8d shows the shape of the concrete at 15 s.

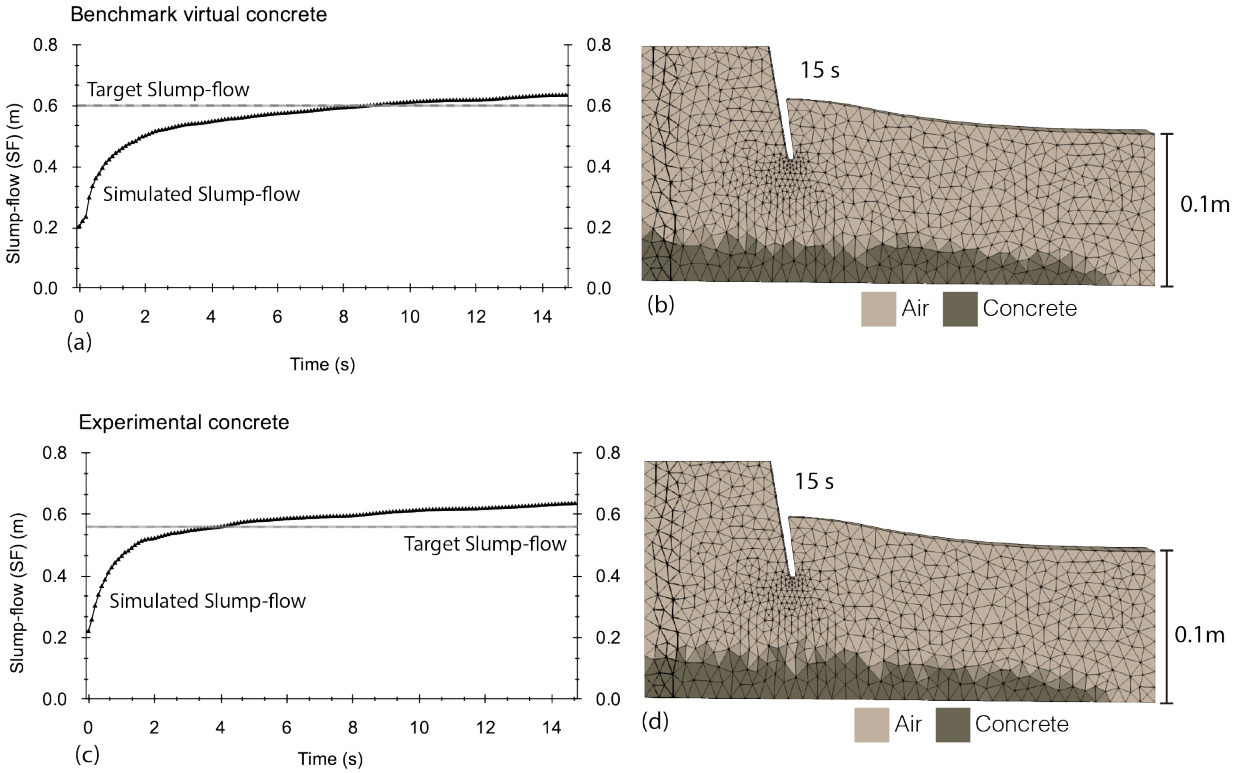

Fig. 4.8 a) Slump-flow spread (SF) over time for benchmark concrete. b) Final geometry for benchmark concrete. c) Slump-Flow spread evolution over time for simulated experimental concrete. d) Final geometry for simulated experimental concrete.

The simulated benchmark and experimental Slump-Flow tests demonstrate that OpenFOAM® is able to represent the macroscopic behaviour of Tremie Concrete. As with other authors [52, 101, 102], CFD simulations of the Slump-flow test were found to be in good agreement with the expected behaviour. However, both simulations were seen to spread slightly further than expected, suggesting the boundary conditions may need calibrating. Unfortunately, as with many CFD packages, OpenFOAM® does not have the ability to implement a friction coefficient. The only option is slip, or no slip. There are some CFD packages that offer increased frictional conditions, such as surface roughness, but these are not akin to the frictional boundary conditions available to discrete, or mesh-less methods. If a more detailed analysis is required, it may be necessary to opt for an alternative numerical method, particularly one where boundary conditions can be tightly controlled and calibrated. It is also possible the oversimplification of concrete as a continuous, homogeneous Bingham material removes some boundary effect attributed to aggregate contact with the plate that is usually accounted for by including an assumed boundary friction coefficient.

Simulated GFB

As with the experimental analysis, there are two simulated cases:

- Case One: Without reinforcement inserts.
- Case Two: With reinforcement inserts.

Figure 4.9 represents slices through the centre of the simulated box for both cases, at time intervals of $0, 2, 8$ and 14 s. Case one is filled with batch one for 8 s at a flow rate of $0.4\,\mathrm{m\,s^{-1}}$. Case Two is filled with batch one for 16 s at a flow rate of $0.2\,\mathrm{m\,s^{-1}}$, so both cases are filled to the same height with batch one. Both cases are then filled with batch two for the remaining time at the flow rate experienced by the experimental cases: $0.4\,\mathrm{m\,s^{-1}}$ and $0.2\,\mathrm{m\,s^{-1}}$ for Case One and Case Two, respectively.

Starting with Case One, fig. 4.9a-b show the same early, horizontal spreading as in the physical case. As with the experimental case, the simulated second batch extends all the way to the edges but leaves a small portion of batch one in the lower corners. By 8 s the second batch of concrete in the simulated Case One has spread horizontally towards the edge of the box, bisecting batch one into a lower portion in the bottom corners and the larger ‘plug’ atop the flow. At 14 s the final flow pattern shows an unconstrained second batch, able to push all of the original batch vertically aside from the small amount left the lower corners.

For the second case, fig. 4.9e-h, where a horizontal and vertical bars are included in the mesh, the behaviour at 2 s is similar to that of Case One. However, as with the experimental

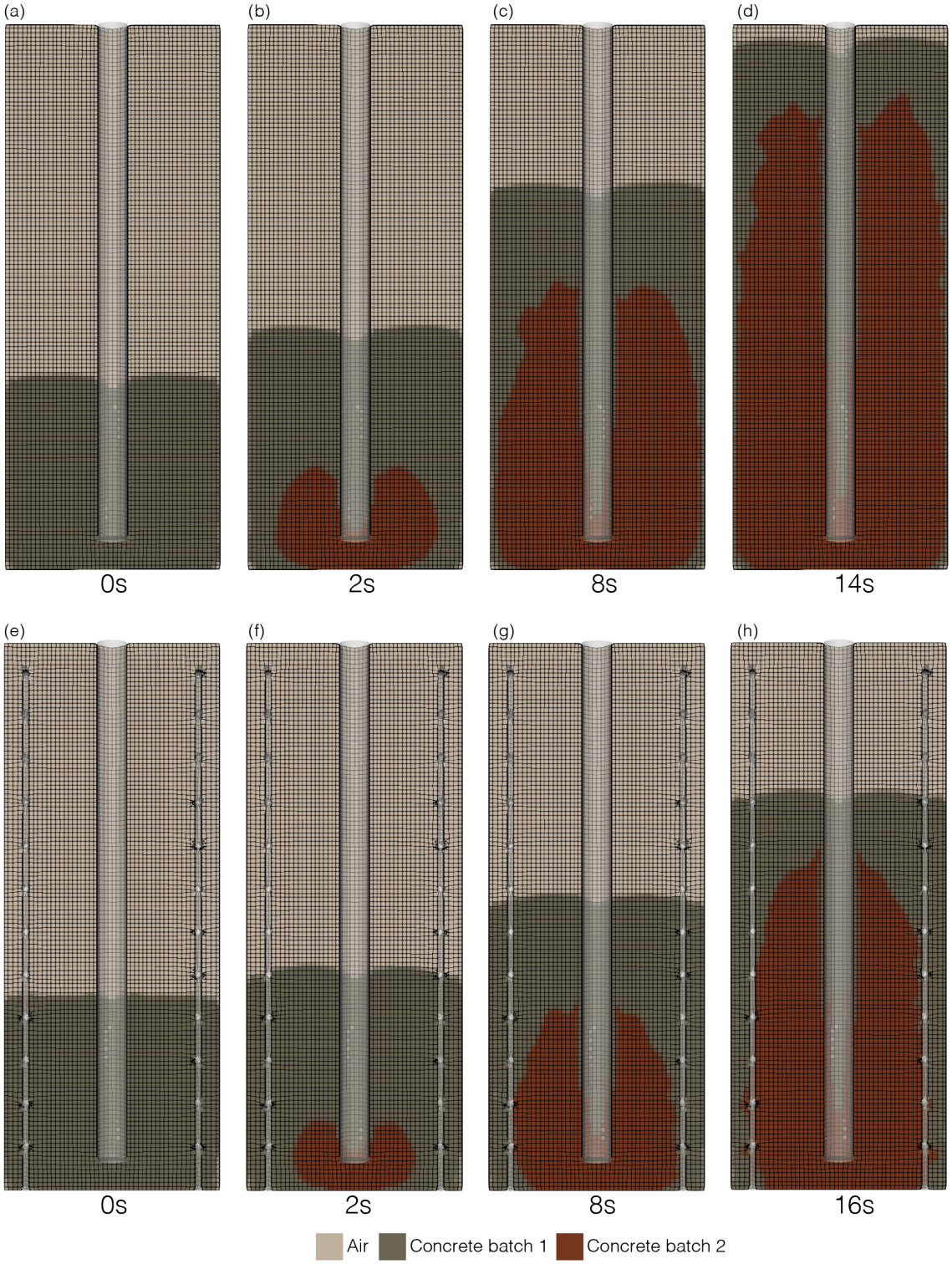

Fig. 4.9 a)-d) GFB evolution of batch two at $0, 2, 8$ and $14\,\mathrm{s}$ for Case One. e)-h) GFB evolution of batch two at $0, 2, 8$ and $14\,\mathrm{s}$ for Case two.

analysis, by 8 s the continued horizontal spreading has been prevented by the restriction to flow caused by the reinforcement inserts. Compared to Case One, the second batch has not managed to bisect batch one, instead the cover zone is entirely formed of the original batch. At 16 s the second batch still has not managed to spread horizontally past the reinforcement in the majority of places. Therefore, the reinforcement bars are restricting the flow to the area surrounding the pipe.

Figure 4.10a presents a side-by-side comparison of simulated vs experimental results at 8 s of flow-time for Case One. It shows a comparison of the physical (left) and modelled (right) results, demonstrating the behaviour of the second batch is being captured well by the simulation. Where the physical and simulated case differ at this point in time is the degree to which the second batch of concrete flows towards the vertical edges. In the experimental case, there is still a presence of batch one on the outermost edges, whereas, in the simulated case, batch two has reached the edge.

Figure 4.10b and c show the simulated flow behaviour of batch 2 at 2 s and 8 s of flow-time, with the outline of the position of batch two in the experimental analysis overlain on the numerical results. There is a strong agreement between the modelled and physical concretes for both time-intervals.

Figure 4.10d shows the side-by-side comparison of simulated vs experimental results at 8 s of flow-time for Case Two. Once again, this demonstrates the ability of the numerical techniques and material model to represent the behaviour of concrete during the experiments. Figure 4.10e and f feature the experimental position of batch two overlain over the simulated concrete at the same point in time. During the experiment, the tremie pipe became slightly off centre, this has been corrected for in fig. 4.10. Nonetheless, the simulated and experimental concretes are in agreement.

The agreement between the CFD modelled concrete and the experiments in the GFB confirms the findings of Fierenkothen [52], that CFD is able to predict the bulk flow behaviour of concrete with a good degree of accuracy. This is now supported for both simple flow studies and more complex flow problems.

EFFC and DFI [47] proposed that resistance to flow in the form of a dense reinforcement cage or high frictional boundary conditions may cause the behaviour of one flow pattern over another. Both the experimental and simulated GFB demonstrated that this hypothesis does hold true. The presence of a cage restricts the flow, forcing an earlier and more rapid vertical rise. Whereas when the confining forces on the secondary batches of concrete are low, be it the lack of a cage or any other conditions that would prevent the free flow of the in situ

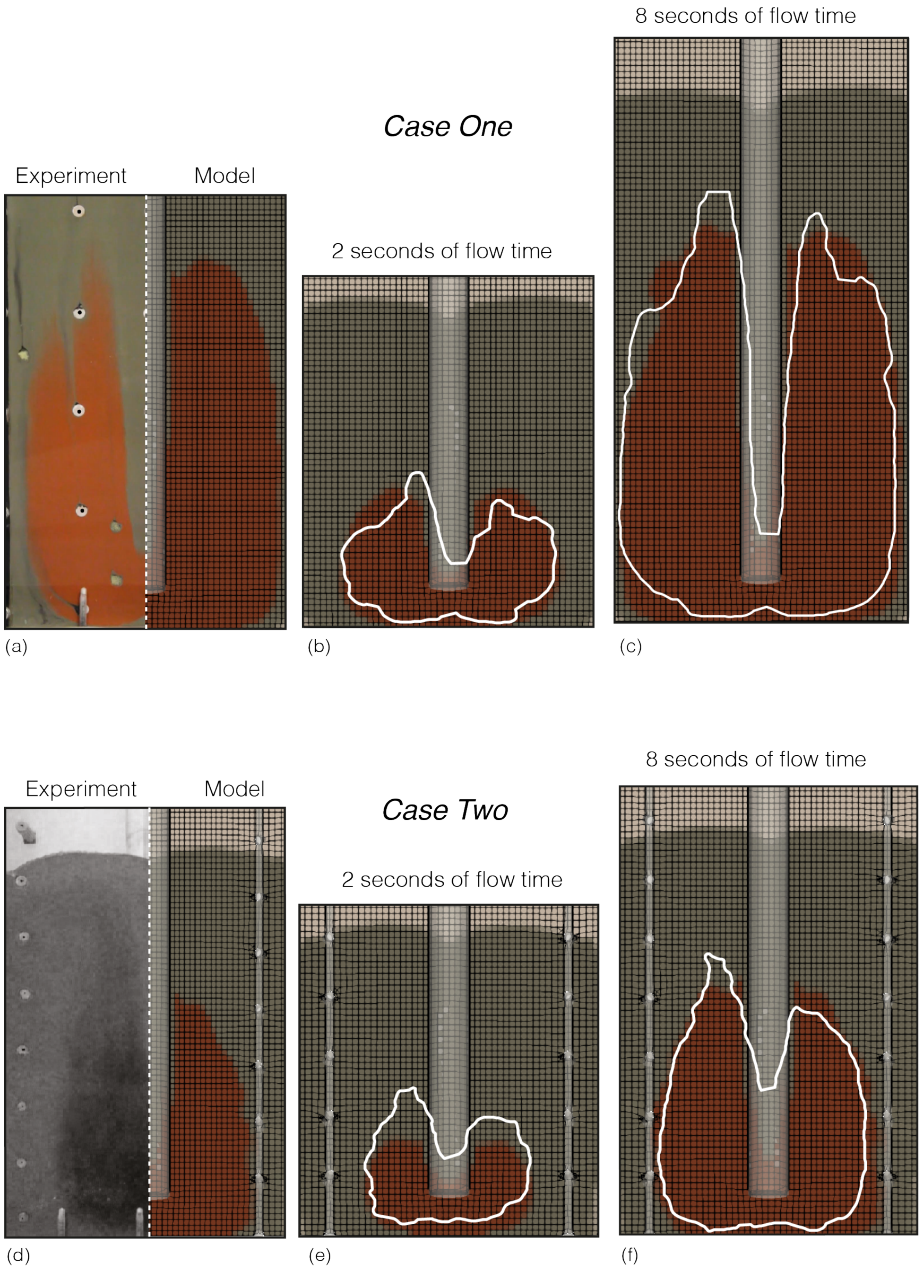

Fig. 4.10 a) and d) Side by side comparison of experimental result (left) and simulated result (right) for Case One and Two respectively. b-c) Simulated concrete at different flow-times with the extent of batch to in the experimental case, overlain and scaled to the size of the simulated box, for Case One. e-f) Simulated results with overlain experimental extents of batch two for Case Two.

batch, the secondary batch is able to spread horizontally unrestricted. In terms of the flow patterns presented in the earlier sections of this paper, the most likely flow pattern for an unrestrained concrete would correspond to a plug flow, and for a restricted concrete it would be bulging flow. However, for the purposes of this study, the new terminology of restricted and unrestricted flows are preferred, as they offer the ability to be applied to a scale, rather than a set pattern.

Figure 4.11 is a schematic diagram of how the level of restriction on the concrete flow may influence the flow behaviour of the concrete. On the left is a schematic of a pile where the flow restriction is low and on the right is a schematic of a pile where the flow is highly restricted. At a high level of restriction, there is an increased vertical flow of concrete in the area surrounding the pipe. As fluid flow will take the path of lowest resistance, when the flow is restricted, it requires more force to displace the concrete outside of the cage, leading to higher vertical flow. When restricting forces are low, the in-place concrete batch can be displaced more easily by the incoming concrete, leading to a rising head of older concrete.

The impact on operational processes for an unrestricted flow is the necessitation of additive use to maintain a workable flow front. Additives increase the dormant period of the hydration reaction, lengthening the period of optimum workability. If a large body of low-shear, aged concrete at the flow front is likely to occur, it is advisable to lengthen the setting time of the concrete. A large body of concrete at rest at the flow front is likely to require more fluid pressure underneath to displace, potentially halting the filling process. For a restricted flow, the operator may want to consider increasing the minimum embedment depth of the tremie pipe to reduce the likelihood of frequent flow-front breaches of secondary concrete batches, a process which may encourage the occurrence of foundation defects like inclusions.

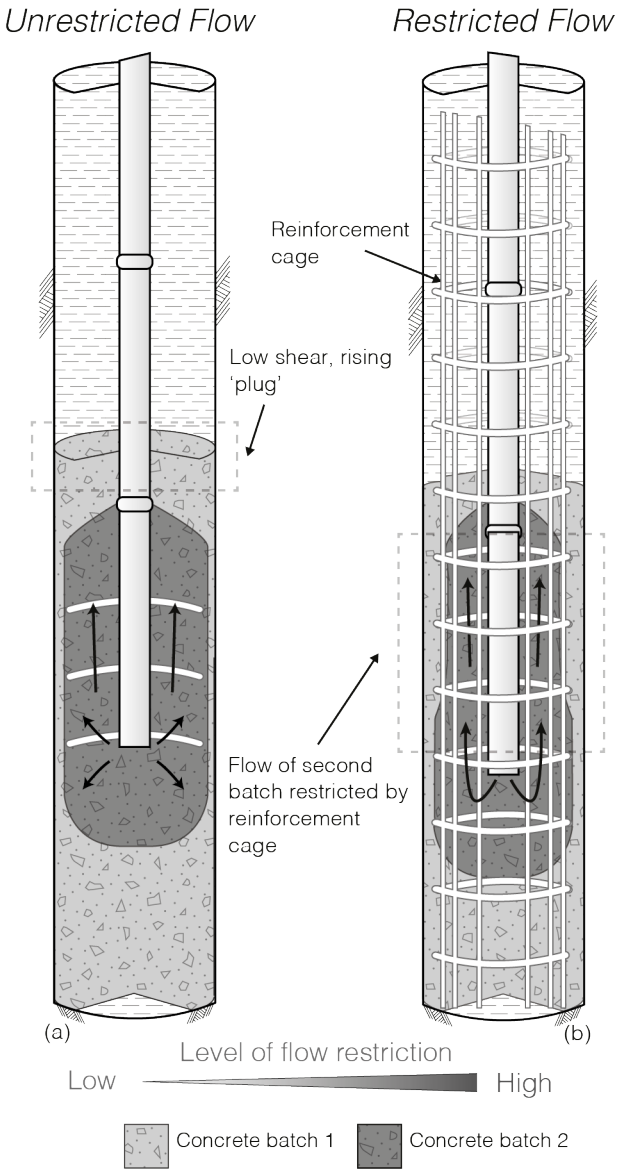

Fig. 4.11 Schematic demonstrating the scale of restricting effects and the behaviour at opposing ends of the scale.

4.4 Conclusion

In this chapter it was demonstrated that an increased restriction to concrete flow is caused by the use of a reinforcement cage. This was demonstrated physically by using a novel experimental apparatus designed to represent the conditions present in a cast-in-place pile. Computational Fluid Dynamics models of the same novel apparatus appeared to be in good agreement with the physical test, suggesting CFD simulations of concrete can be used for more complex modelling of concrete. This validates previously conducted back-calculations of the origin of flow patterns. Finally, a new scale of flow behaviour is presented based on the level of flow restriction occurring within the foundation. The scale includes the previously existing concepts of plug and bulging flow alongside the new reasoning behind why one flow pattern is occurring rather than another, in the form of a restriction scale.

Chapter 5

Thixotropic Tremie Concrete in MPM

5.1 Introduction

The use of Tremie Concrete in deep foundations requires it to flow around obstacles like a congested reinforcement cage easily, or through a small pipe opening, needing a high degree of workability. Left undisturbed, tremie concrete stiffness will progressively increase during the dormant period of the hydration reaction [96, 103], leading to a reduction in the ease with which it can flow. Fortunately, the loss of mobility due to stiffening can be recovered with an application of stress, so long as the applied stress is significant enough to break down the hydration byproducts causing the elevated strength [103]. The temporary reduction in concrete mobility that can be alleviated by stress application is referred to as thixotropy.

Thixotropy poses a severe issue in the construction industry as changes to flow behaviour can hinder the ability of new concrete to mix with the existing concrete, thereby creating weak points at the interface [96]. Furthermore, thixotropic changes in concrete could prevent concrete from flowing freely around reinforcement bars during long pile casting operations [118].

Despite numerical models of concrete progressing rapidly, comprehensive reviews of numerical models [125, 104] highlight, with the notable exception of [96], the difficulty of models in simulating time-dependent concrete behaviour due to a combination of method limitations or complexity of implementation. The Material Point Method (MPM) [111, 112] is an emerging numerical method capable of simulating high deformation, time-dependent material allowing for the simulation of thixotropic concrete.

The objective of this chapter is to develop a comprehensive thixotropic model in the Material Point Method (MPM) framework, to accurately capture the history-dependent nature of the flow behaviour of Tremie Concrete. This chapter provides unique insights into the history-dependent nature of Tremie Concrete and the associated flow response by exploring the challenges associated with testing and simulating thixotropic concrete.

5.2 Flow Behaviour

5.2.1 Slump-flow test

The Slump-flow test [26] (fig. 5.1), is an empirical test that quantifies a concrete's flow behaviour by measuring the distance it spreads before stopping when emptied from a rising cone [66]. Even in its simplicity, it is able to capture remarkably well a snapshot of concrete behaviour at a single point in time, however, the test has drawn criticism for its inability to observe or provide insight on the behaviour of concrete following a period of rest [74, 50]. Recent analysis of concrete SFs [128, 99, 105] found a good degree of correlation between fresh concrete and the Bingham model.

Correlations between SFs and rheological model parameters such as the Bingham model yield stress, are fundamental to validating numerical methods as rheological measurements obtained from a rheometer can be input directly into a numerical model and the associated flow behaviour, as represented by an SF, observed and compared with expectations. Thus, SF results paired with rheological measurements not only provide a way to validate a numerical model, but also a pathway to overcome the limitations of foundation design and practices by creating a method to directly translate readily available data into operational benefits.

A_{thix}, as discussed in Chapter 2, represents the increase in yield stress [Pa] per second of rest. A_{thix}values of over 3.0 for some Tremie Concretes were reported by [74, 50] for concrete with a rest time of 240 s. This represents a large increase in yield stress over a relatively short period. It is reasonable to expect a significant decline in SF after a period of rest for highly thixotropic concrete, given such a large increase in yield stress. The difference in Slump-flow before and after a period of rest is written as ΔSF, where:

$$\Delta SF = SF_0 - SF_{240}\,. \tag{5.1}$$

with SF_0 and SF_{240} representing the SF measured following 0 s of rest and 240 s of rest respectively.

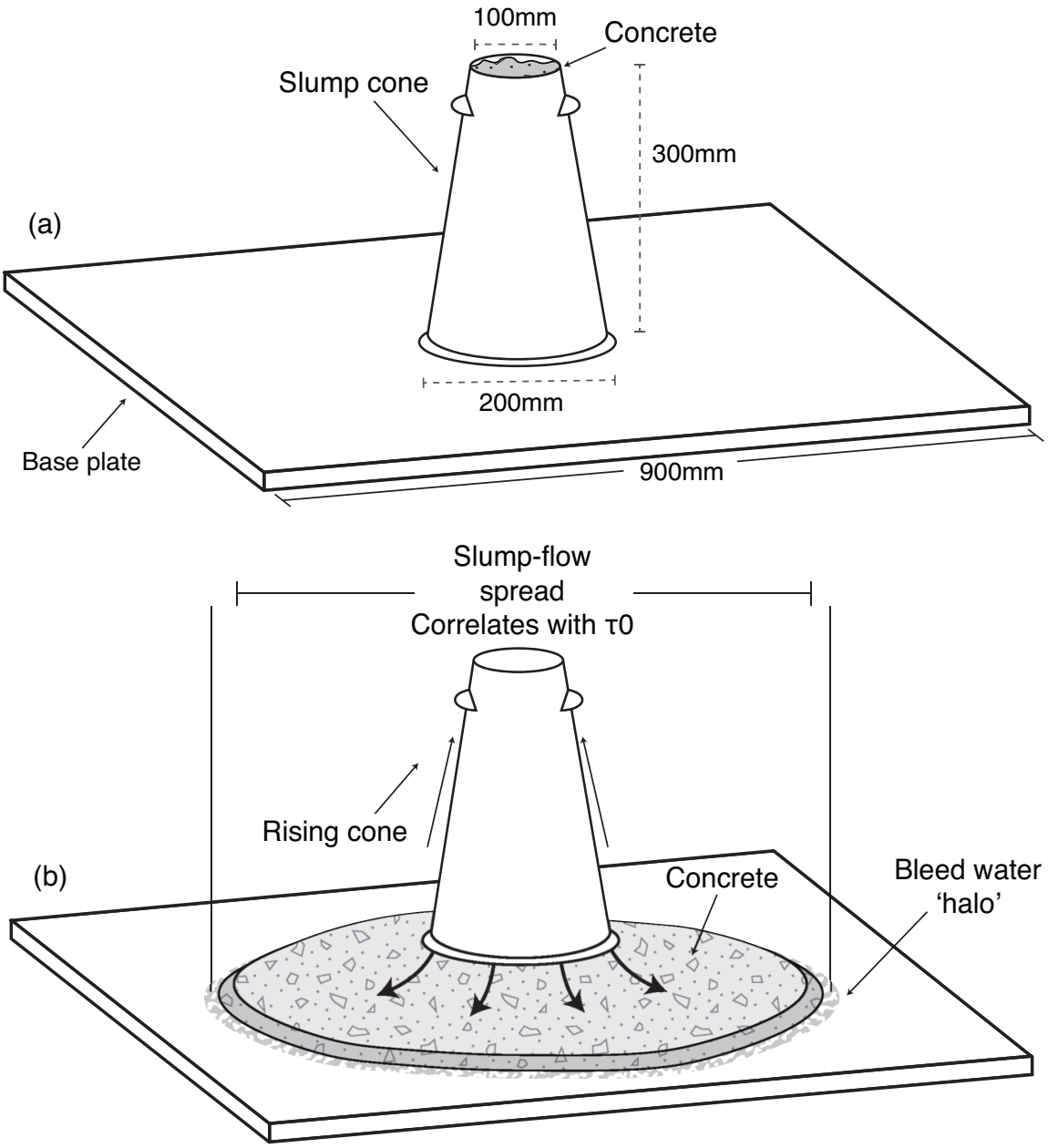

Fig. 5.1 a) Slump-flow test apparatus in accordance with BS EN 12350-8:2019. b) Representation of a typical Slump-Flow spread (SF).

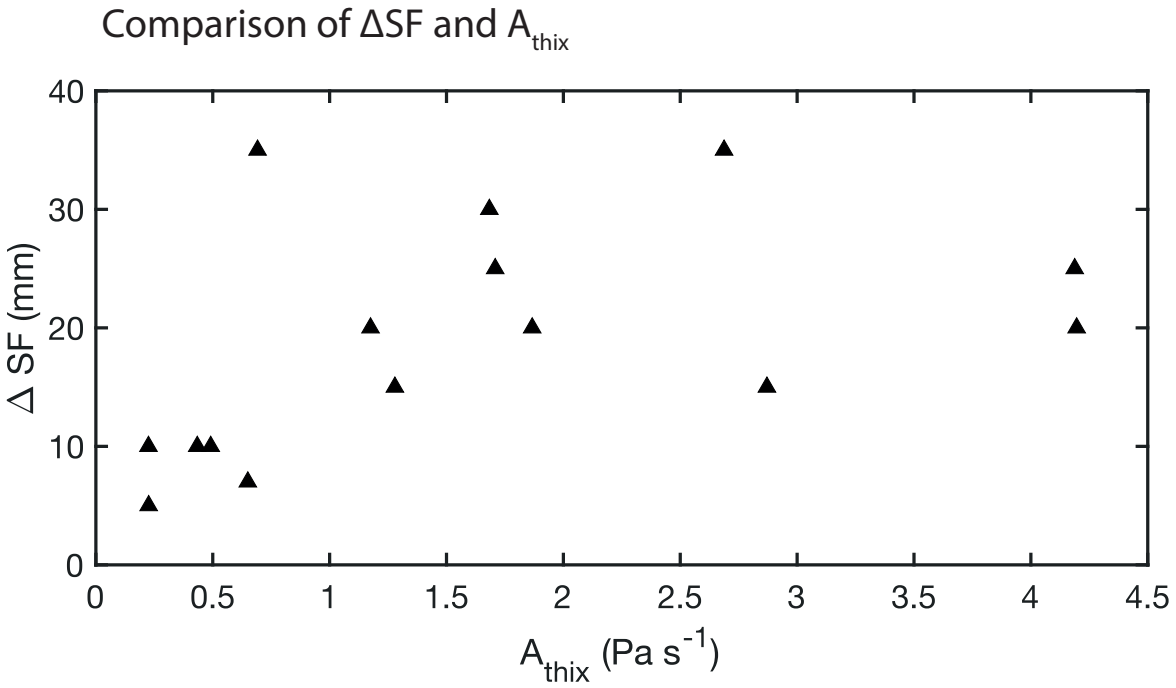

Fig. 5.2 Comparison of change in SF at 240 s and 0 s (ΔSF) with A_{thix}. Created using data from [74, 50].

The comparison of slumps before and after 240 s for different concrete mixes, shown in fig. 5.2, indicates only small changes in SF despite large A_{thix} values [74], although a general pattern of increasing ΔSF with A_{thix} is observed, no confident trend can be identified.

According to Kraenkel and Gehlen [74], the reduction of SF from 700-500 mm requires an increase in yield stress of 50 Pa, the reduction from 500-400 mm requires an increase in yield stress of 100 Pa, and a reduction 400-300 mm requires an increase in yield stress of over 300 Pa. This suggests that when a concrete has an initial SF of around 400 mm, even large increases in yield stress will have a reduced impact on SF. This is one possibility of why ΔSF and A_{thix} show little correlation. However, for concretes with a high SF, dramatic changes in yield stress caused by thixotropy, represented by a large A_{thix}, should give rise to a large SF. Interestingly, this is not observed experimentally.

One mix with an A_{thix} of 2.87 resting for 240 seconds experienced a reduction in SF of only 15 mm despite an increase in yield stress of 688 Pa from a starting point of 130 Pa. Even taking into consideration that stiffer concretes will have smaller ΔSF values due to the non-linear relationship between SF and Yield stress, a yield stress this high should give an SF that is no longer within the acceptability limits for a Slump-flow test, which that did not occur in this case. This can be explained partially by the underlying relationship between

yield stress and plastic viscosity created by mix designers to maintain stability at low yield stresses or low viscosities. To maintain stability, the yield stress of a low viscosity concrete would be increased, and vice versa. Thus, an elevated yield stress, relatively low viscosity concrete will not have the same SF/Yield stress relationship as in fig. 2.9. Nevertheless, given the significant effect yield stress has on SF, a decrease in SF of at least 100 mm would not be unexpected for an increase in yield stress as dramatic as 688 Pa.

The unexpectedly small ΔSF values shown in fig. 5.2 could be further explained by examining the experimental procedure used to gather the data. During the 240 s rest period, the concrete remains undisturbed in the cone on a base-plate. As the cone is not sealed on the base plate, bleed water from the concrete can accumulate at the base and seep out. The test standard BS EN 12350-8:2019 [26] specifies a maximum wait time of 30 s to avoid potential issues like dewatering, as any water at the base can reduce friction between the concrete and the base plate, leading to a larger SF. Kraenkel and Gehlen [74] also reported a 30 mm variation in SF, indicating potentially large inaccuracies. Some concretes in the data-set saw a 100% increase in yield stress in just 30 s of rest. Considering that BS-EN 12350-8:2019 [26] allows up-to 30 s rest before the cone is raised, it is conceivable that the concrete has already accrued some degree of thixotropy in the regular test that the SF_0 figures represent.

Hence, obtaining any meaningful thixotropy effects in a physical Slump-flow test can become highly challenging [74, 50, 97]. If the thixotropic behaviour of concrete is not correctly understood, issues during the construction process could occur. Hence, the measurements of thixotropy can be of great importance in practice. Numerical models can minimise the variability of physical tests by allowing for greater control over all variables, creating an ideal testing situation, thereby offering unique insights into concrete flow behaviour by accurately considering the influences of thixotropy which are otherwise obscured by physical testing.

Boundary Conditions

A frictional boundary algorithm is used to describe the interaction between the concrete material points and the surface on which it flows. A description of this friction algorithm is available in Bandara [10], which involves reducing the acceleration of a point based on a Friction Coefficient (FC). The FC in the Slump-Flow test represents the kinetic and static friction between the concrete and the steel plate. It is well documented in the literature that FC is influenced by rheology, mix design (such as cement/water ratio) and surface roughness of the plate. Roussel and Gram [101] describes friction as a key variable for simulating concrete flow. However, a wide variation in the suitable values of FC can be observed in the literature. For simulating concrete with an SF of 800 mm, Deeb et al. [41] recommended a

dynamic FC of 0.55. While Djelal et al. [43] reported a FC of 0.06-0.1 for concrete with an SF of 700 mm. For an L-box test, which is similar to the SF test, Hosseinpoor et al. [65] observed good correlation with experimental results for an FC of 0.4. It is clear then, that FC is often used as a calibration parameter in simulations of concrete flow.

Bouharoun [22] observed that the volume of paste and the amount of superplasticiser affects the friction at the concrete plate interface. The friction stresses at the interface were observed to increase with increasing paste volume due to the enrichment of the boundary layer caused by the availability of more fines. The greater thickness of the boundary allows more cement grains to be trapped in the roughness of the metal plate. Bouharoun [22] also demonstrated that friction stress, which is proportional to the friction coefficient, decreases with increasing plastic viscosity. In the present study, calibrated FC values between 0.35 and 0.45 are used to represent the friction between Tremie Concrete and the base-plate, as shown in table 5.1. FC also increases with decreasing plastic viscosity to align with the observations made in [22].

There is the additional possibility that the changing friction coefficient observed for concretes of differing properties is not wholly related to cement/plate interaction, but the geometric wall effect. Commonly observed in concrete pumping, the geometric wall effect is a form of dynamic segregation where aggregates are observed to move to the centre of the pipe [121]. For the Slump-Flow test, this could result in a reduced interaction between aggregate and the plate, or an increase in cement/plate contact as aggregates move away from the plate. This would, in turn, lead to a change in the observed frictional relationship between the concrete and the plate. It is also reasonable to expect different concretes to have different geometric wall effects, less viscous concretes might allow aggregates to move away from the plate more freely, allowing a greater cement/plate interaction and a higher friction coefficient.

5.2.2 Constitutive Model

According to Reddy [94], in 3 dimensions, the gradient of the velocity u is a second-order tensor which can be expressed as the matrix $\mathbf{L}_{ij}$:

$$\mathbf{L}_{ij} = \frac{\partial u_i}{\partial x_j}. \tag{5.2}$$

$\mathbf{L}_{ij}$ can be decomposed into the sum of a symmetric matrix $\mathbf{D}_{ij}$ and a skew-symmetric matrix $\mathbf{W}_{ij}$ as follows

$$\mathbf{D}_{ij} = \frac{1}{2}(\mathbf{L}_{ij} + \mathbf{L}_{ij}^T) \tag{5.3}$$

$$\mathbf{W}_{ij} = \frac{1}{2}(\mathbf{L}_{ij} - \mathbf{L}_{ij}^{T}) \tag{5.4}$$

where $\mathbf{D}_{ij}$ and $\mathbf{W}_{ij}$ are the rate of deformation tensor:

$$\mathbf{D}_{ij} = \begin{bmatrix} \frac{du_x}{dx} & \frac{1}{2}(\frac{du_x}{dy} + \frac{du_y}{dx}) & \frac{1}{2}(\frac{du_x}{dz} + \frac{du_z}{dx}) \\ \frac{1}{2}(\frac{du_x}{dy} + \frac{du_y}{dx}) & \frac{du_y}{dy} & \frac{1}{2}(\frac{du_y}{dz} + \frac{du_z}{dy}) \\ \frac{1}{2}(\frac{du_x}{dz} + \frac{du_z}{dx}) & \frac{1}{2}(\frac{du_y}{dz} + \frac{du_z}{dy}) & \frac{du_z}{dz} \end{bmatrix} \tag{5.5}$$

and the vorticity tensor or spin tensor respectively, with $x = 1$, $y = 2$ and $z = 3$. In CB-GEO MPM, the strain rate tensor $\dot{\varepsilon}$ is calculated as $\mathbf{B}u$, where $\mathbf{B}$ is the strain-displacement B-matrix [135] to give

$$\dot{\varepsilon} = \mathbf{B}u = \begin{bmatrix} \frac{du_x}{dx} & (\frac{du_x}{dy} + \frac{du_y}{dx}) & (\frac{du_x}{dz} + \frac{du_z}{dx}) \\ (\frac{du_x}{dy} + \frac{du_y}{dx}) & \frac{du_y}{dy} & (\frac{du_y}{dz} + \frac{du_z}{dy}) \\ (\frac{du_x}{dz} + \frac{du_z}{dx}) & (\frac{du_y}{dz} + \frac{du_z}{dy}) & \frac{du_z}{dz} \end{bmatrix} \tag{5.6}$$

such that the rate of deformation tensor can also be represented as a 6x1 function of the rate of strain

$$\mathbf{D}_{ij} = \left[\dot{\varepsilon}_{xx}, \dot{\varepsilon}_{yy}, \dot{\varepsilon}_{yy}, \frac{1}{2}\dot{\varepsilon}_{xy}, \frac{1}{2}\dot{\varepsilon}_{yz}, \frac{1}{2}\dot{\varepsilon}_{zx}\right]^{T}. \tag{5.7}$$

Using the rate of deformation, eq. (2.1) can be expressed as

$$\tau_{ij} = 2\left(\frac{\tau_0}{\dot{\gamma}} + \mu\right)\mathbf{D}_{ij} \quad \text{if} \quad |\tau_{ij}| \geq \tau_0 \tag{5.8}$$

where τ_{ij} is the deviatoric stress tensor and $\mathbf{D}_{ij} = 0$ if $|\tau_{ij}| < \tau_0$. The shear rate $\dot{\gamma}$ can now be described as

$$\dot{\gamma} = (2\mathbf{D}_{ij}\mathbf{D}_{ij})^{1/2}. \tag{5.9}$$

The total stress σ_{ij} can be calculated from the deviatoric stress tensor, the thermodynamic pressure P and the Dirac Delta function δ_{ij} by:

$$\sigma_{ij} = -P\delta_{ij} + \tau_{ij} \tag{5.10}$$

where pressure P is

$$P = p_0 - Kd\varepsilon_v \,. \tag{5.11}$$

Here, p_0 is the initial thermodynamic pressure (calculated as the mean initial stress) $d\varepsilon_v$ is the volumetric strain and K is the bulk modulus .

In this study, a Young's Modulus E of 0.1 MPa [103, 19] and a Poisson's ratio v of 0.45 is used to represent a weakly incompressible material. The thermodynamic pressure is calculated at the centre of the MPM cell to minimise pressure oscillations.

Fresh concrete modelled using a viscoplastic Bingham material behaves like a rigid body before yielding, and as a viscous material upon yielding. In order for the material to transition from rigid to viscous, the magnitude of the deviatoric stress tensor must exceed the yield stress. Based on eq. (5.8), total stresses will remain zero when the material is in the rigid region because the rate of deformation will also be zero. In reality, this is not physically possible as a material in the rigid zone will still exhibit non-zero stresses, despite not flowing. Hence, a modification to this model is needed to allow non-zero stresses to develop before the material yields.

One such modification, or regularisation, is to define the behaviour before and after yield as two separate materials. The most commonly adopted modification is the Bi-viscous model [15], which uses a critical shear rate $\dot{\gamma}_c$ to define the shear rate at which the transition between rigid and viscous behaviour occurs. The Bi-viscous model is written as:

$$\tau_{ij} = \begin{cases} 2\mu_0 \mathbf{D}_{ij} & \text{if } |\dot{\gamma}| \leq \dot{\gamma}_c \\ 2\left(\frac{\tau_0}{\dot{\gamma}} + \mu\right)\mathbf{D}_{ij} & \text{otherwise} \end{cases} \tag{5.12}$$

where μ_0 represents the viscosity of the material in the pre-yield region, and typically has a value three orders of magnitude higher than the dynamic viscosity μ.

The Bi-viscous model offers a clear differentiation between the yielding and pre-yield regions by using a critical yield stress. However, the abrupt discontinuity at the transition between the regions still presents a computational hurdle. An alternative regularising method involves adopting a continuous model which does not have a distinct discontinuity between rigid and plastic regions. The Papanastasiou [90] model represents the most popular of these kinds of continuous models. The exponential regularisation of the Bingham model often referred to as

the Bingham-Papanastasiou model, introduces a parameter m which controls the exponential growth of stress. The 3D representation of this regularisation is:

$$\tau_{ij} = 2\left[\mu + \frac{\tau_0}{\dot{\gamma}}(1 - e^{-m\dot{\gamma}})\right]\mathbf{D}_{ij}\,. \tag{5.13}$$

The larger the regularisation parameter m, the closer the numerical representation will be to the Bingham model in eq. (5.8). Combining Roussel's thixotropic equations which describe time-dependent concrete behaviour with a continuous Bingham model by substituting eq. (2.5) into eq. (5.13) gives:

$$\tau_{ij} = 2\left[\mu + \frac{(1 + \lambda_0 e^{-\alpha\dot{\gamma}t})\tau_0}{\dot{\gamma}}(1 - e^{-m\dot{\gamma}})\right]\mathbf{D}_{ij}\,. \tag{5.14}$$

This new model will be referred to as the the Papanastasiou-Roussel Bingham (PR-Bingham) model for the remainder of this thesis. Equation (5.14) is valid for all strain-rates and degrees of concrete thixotropy. However, for computational purposes, there is still a need to define a point at which thixotropy is increasing (the material is at rest) and thixotropy is decreasing (the material is flowing). In this work, a critical shear rate, $\dot{\gamma}_c$, is used to define a yield point, similar to the approach taken by Beverly and Tanner [15]. In the model adopted here, any material with a shear rate below the critical shear rate is considered to be at rest, allowing thixotropy to build. However, material at these low shear rates may still exhibit a degree of movement as a result of using the Papanastasiou model. From an engineering perspective the material can still be considered at rest even with a small, often negligible, degree of deformation as noted by Franci and Zhang [54].

Roussel et al. [102] suggested the use of a stopping criterion which allows for the definition of the final shape of the free surface of the material regardless of any continued, negligible deformation. This criterion has taken the form of a flow-cut off time in previous studies [52], where it is assumed that any flow occurring after this point is a result of the limitations of the constitutive model. The stopping criterion used in this study is 20 s of flow time, in line with that used by Fierenkothen [52]. This represents more than the maximum SF time for concretes in the data-set [74, 50].

Figure 5.3 shows the Algorithm used to build up thixotropic stresses in CB-GEO MPM in accordance with eq. (5.14), where t represents the length of a time-step (1.0×10^{-4} s), $\lambda_{n^{-1}}$ the flocculation state of the previous time-step, and the addition of a yield criterion in the

if $(\dot{\gamma} \cdot \dot{\gamma}) > (\dot{\gamma}_{critical} \cdot \dot{\gamma}_{critical})$;
then
  if $(\lambda_{n^{-1}} > 0)$;
  then
    $\lambda_n = \lambda_{n^{-1}} e^{-\alpha\dot{\gamma}t}$;
    if $(\lambda_n > 0)$;
    then
      $\tau_{0\,temp} = (1 + \lambda_n) \cdot \tau_0$
      $\boldsymbol{\tau}_{ij} = 2\left[\mu + \frac{\tau_{0\,temp}}{\dot{\gamma}}(1 - e^{-m\dot{\gamma}})\right]\mathbf{D}_{ij}$
      $rt = 0$
    else
      $\lambda_n = 0$;
      $\boldsymbol{\tau}_{ij} = 2\left[\mu + \frac{\tau_0}{\dot{\gamma}}(1 - e^{-m\dot{\gamma}})\right]\mathbf{D}_{ij}$
      $rt = 0$
    end
  else
    $\boldsymbol{\tau}_{ij} = 2\left[\mu + \frac{\tau_0}{\dot{\gamma}}(1 - e^{-m\dot{\gamma}})\right]\mathbf{D}_{ij}$
    $rt = 0$;
  end
else
  if $\lambda > 0$ **then**
    $apparent\,rt = \frac{\lambda * \tau_0}{A_{thix}}$
  else
    $apparent\,rt = rt$
  end
  $apparent\,rt \mathrel{+}= \partial t$;
  $\tau_{0\,temp} = \tau_0 + (A_{thix} * apparent\,rt)$;
  $\lambda_n = \left(\frac{\tau_{0\,temp}}{\tau_0}\right) - 1$;
  $\boldsymbol{\tau}_{ij} = 2\left[\mu + \frac{\tau_{0\,temp}}{\dot{\gamma}}(1 - e^{-m\dot{\gamma}})\right]\mathbf{D}_{ij}$
end

Fig. 5.3 The Papanastasiou-Roussel Bingham (PR-Bingham) algorithm implemented in CB-GEO MPM.

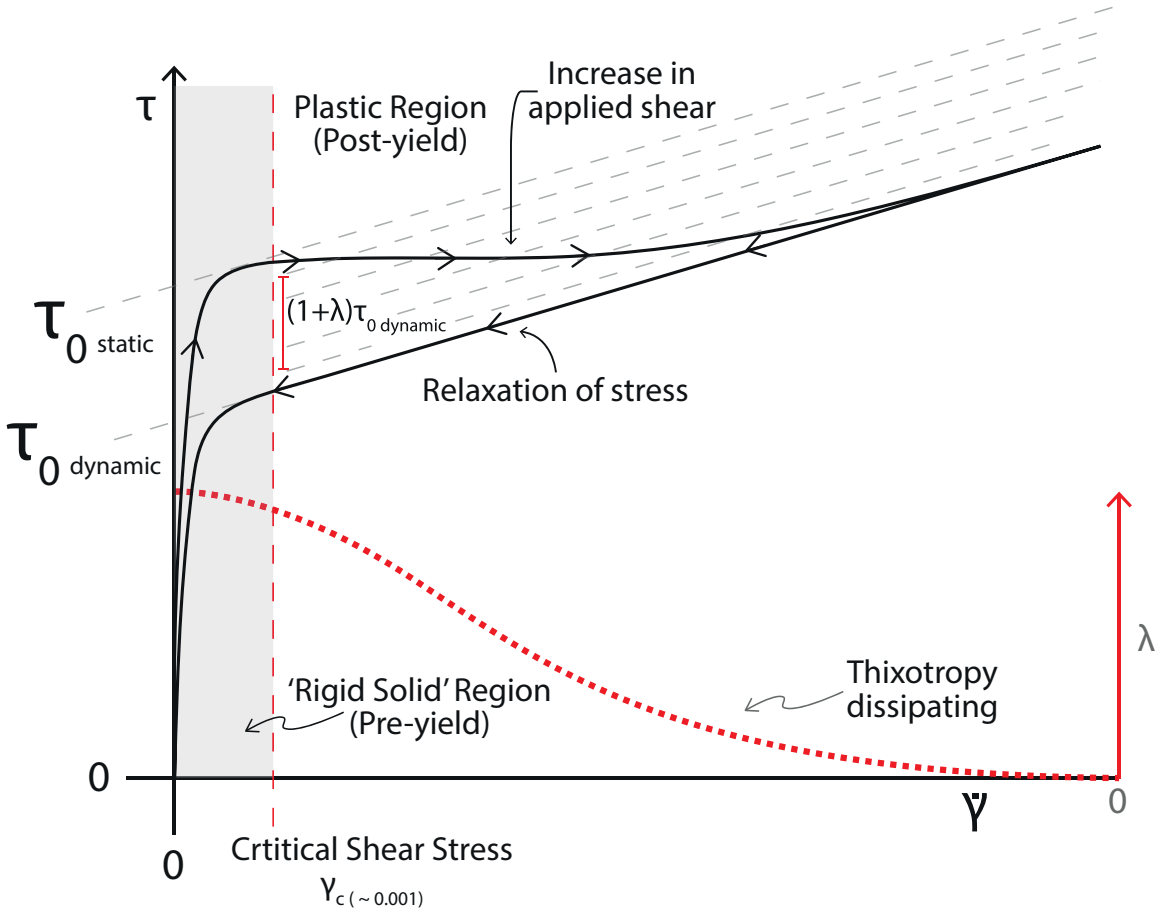

Fig. 5.4 1D Bi-viscous Thixotropic Bingham hysteresis loop

form of a critical shear rate. All results in the following section use this algorithm to calculate the stress state of the material over time.

An appropriate way to characterise a thixotropic system is to use the hysteresis loop of the flow curve, representing an applied shear stress (upward) followed by a relaxing of the stress (downward) [8]. Figure 5.4 represents a 1D single hysteresis loop analogous to fig. 5.3, demonstrating how the thixotropy multiplier λ increases the yield stress after a period of rest and dissipates to 0 during shearing, resulting in a hysteresis loop.

A parametric study is performed to understand the effect of the model parameters (τ_0, μ, α, A_{thix}, m and rest time) on the shear stress and the thixotropic multiplier λ following a 100 s rest period. To conduct the parametric study, a standalone code was developed that enables the manipulation of a 1D model and the corresponding behaviour [39].

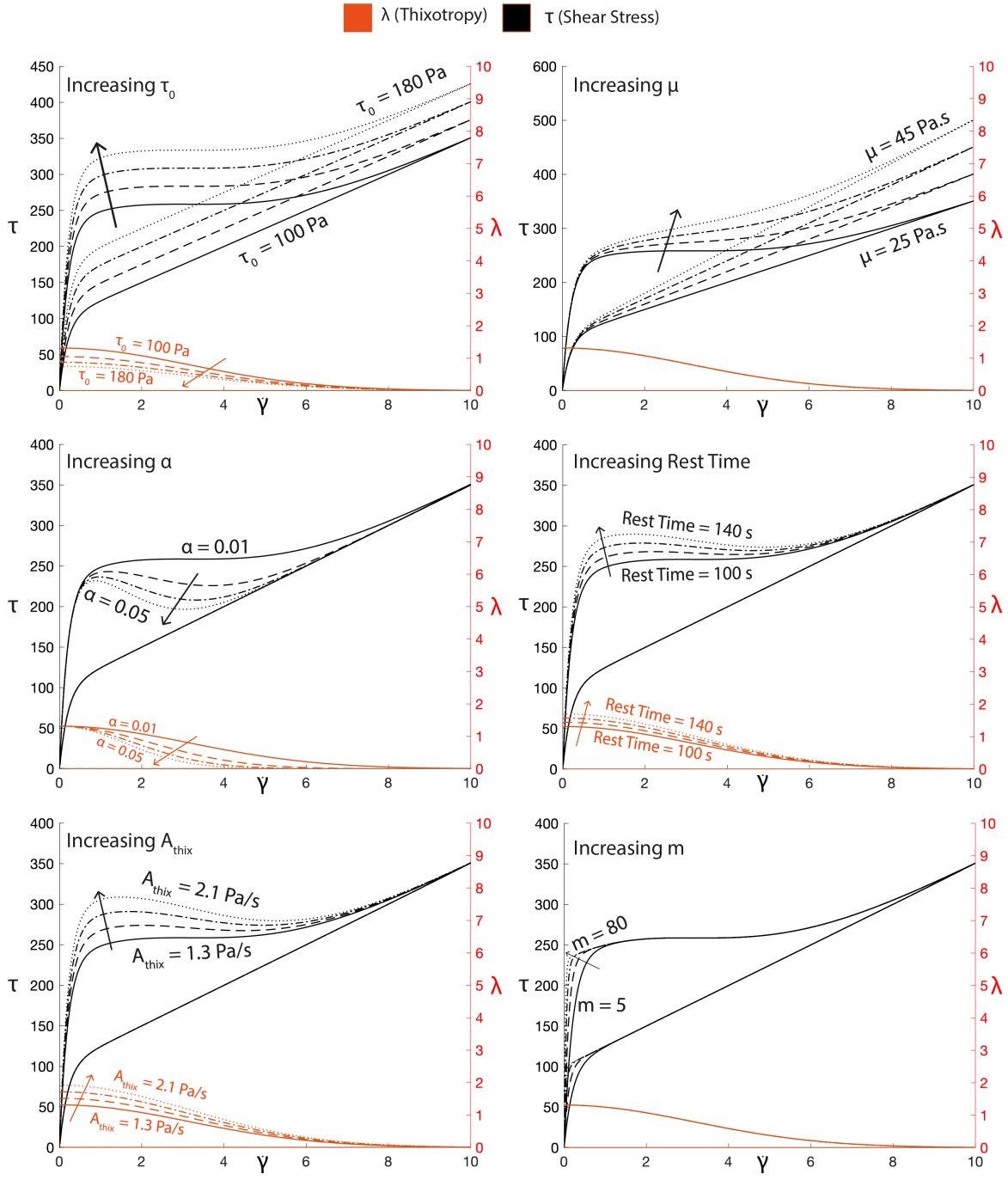

Fig. 5.5 Parametric study of thixotropic algorithm. Blue represents the shear stress and orange the thixotropic multiplier λ.

	$\tau_{0_{dynamic}}$ $[Pa]$	μ $[Pa \cdot s]$	A_{thix} $[Pas^{-1}]$	$SF_0 \pm 30$ [mm]	$SF_{240} \pm 30$ [mm]	FC
Mix A	54	35.8	1.3	590	575	0.35
Mix B	61	29	1.8	550	530	0.45
Mix C	130	30.2	2.9	500	485	0.43

Table 5.1 MPM input parameters of Mixes A-C, based on [74]

The results of the parametric study are presented in fig. 5.5. An increase in τ_0 causes an upward translation of the shear stress intercept, and a downward translation of λ as the constant increase in yield stress over time is now proportionately smaller than the initial yield stress. Increasing μ sees the gradient of the $\tau/\dot{\gamma}$ curve steepen, creating higher stresses at lower shear rates. Changes in rest time and A_{thix} both increase the $\tau_{0_{static}}$ reached after a period of rest. A larger α value causes a reduction in the time required for the elevated $\tau_{0_{static}}$ to reduce to the $\tau_{0_{dynamic}}$ during shearing. Finally, as discussed previously, a larger m results in a model closer to the true Bingham model, but at a cost of increasing the stresses at lower shear rates.

5.2.3 Calibration of input parameters

To demonstrate the capability of the developed PR-Bingham MPM model in simulating Tremie Concrete, the results of numerical simulations are compared against experimental slump-flow tests [74, 50]. Dynamic yield stress, plastic viscosity, A_{thix}, SF_0 and SF_{240} values were obtained from an EFFC and DFI data-set [74] of concrete tests performed on Tremie Concrete from numerous European sites. Three concretes from this data set, referred to as Mix A-C, are chosen based on the range of concrete properties they represent. The model parameters for Mixes A-C used in this study are shown in table 5.1, where SF_0 and SF_{240} represent the measured SF in mm for 0 seconds of rest and 240 seconds of rest, respectively, for the physical test. For simplicity, a density of 2400 Kg/m^3 is maintained for all three mixes.

Mix A is a low yield stress, high viscosity concrete with a low level of thixotropy. This produces a SF of almost 600 mm which is in the upper range of acceptability. Mix B has a similar yield stress to Mix A, but has a significantly lower viscosity, resulting in lower FC requirement and a mid-range SF of 550 mm. Mix B also has a slightly higher level of thixotropy, as represented by the increase in A_{thix} of 0.5 from Mix A. Finally, Mix C has a significantly higher yield stress, resulting in a SF of only 500 mm, near the lower limit of acceptability. Mix C also has a significantly higher degree of thixotropy, with an A_{thix}

of 2.9. The SF behaviour of three different mixes and their comparison with the physical experiments are presented in the following section.

Also evaluated in the following section is the influence of thixotropy on simulated concrete. A rest time of 240 s is introduced in the PR-Bingham algorithm to induce time-dependent changes in the concrete as described in fig. 5.3. Depending on the duration of the rest time, an appropriate increase in the λ value causes an increase in the shear stress to $\tau_{0_{static}}$.

In the present study, an α of 0.01 is used for all concretes as the raw rheometer data for the examined concretes is unavailable. However, this value represents an α supported by Roussel [96] and an analysis of the tremie concrete displayed in fig. 2.6.

Geometry

In section section 3.2.6, it was determined that 4 PPC provide the optimum balance between reduced point splitting and reduced GIMP functionality due to too many PPC. To determine the geometry for the Slump-flow simulations, a comparison of different mesh densities is presented.

However, one issue not discussed in that section is the effect of volumetric locking within MPM. Volumetric locking is caused by an over-stiffness arising from excessive constraints placed on an element's deformation by the points used to integrate the stiffness of the element [33]. Locking effects in MPM can be mitigated by reducing the number of material points in cells and calculating the volumetric deformation at the centre of the cell [33]. However, the formulation of the MPM in the CB-GEO code does not allow for use of the deformation gradient, as the velocity gradient is used instead. The calculation of pressure at the centre of the cell by reduced integration also helps to reduce volumetric locking. Nevertheless, during the selection of an appropriate geometry for slump flow simulations, volumetric locking was observed.

Within the MPM the effects of volumetric locking can present as a chequerboard effect, demonstrated in fig. 5.6. The chequerboard effect is a result of stresses alternating from high in one cell, to low in the adjacent cells. In the case of fig. 5.6, the stress magnitude is used to display an alternating effect of high stresses and low stresses producing the effect, taken from a Slump-flow simulation where locking was present. The overlain mesh shows how the effect alternates with each cell in the mesh. The resulting deformation from a locked simulation will often depend on the severity of the locking. Partial locking may not have a significant impact, but total locking, shown in fig. 5.6 will misrepresent the behaviour of the simulated material.

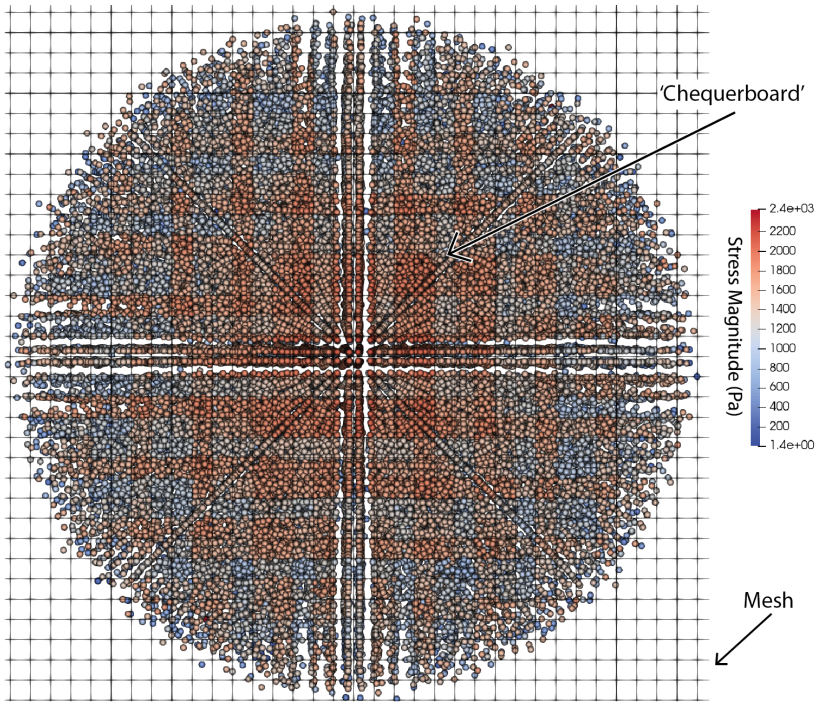

Fig. 5.6 Chequerboard effect produced by volumetric locking in a Slump-flow simulation of stiff concrete.

To determine the the optimum geometry that reduces volumetric locking to an acceptable level, a mesh sensitivity analysis can be conducted. What follows is a discussion of different mesh and PPC conditions and the resulting effects on volumetric locking.

5.2.4 Mesh Sensitivity

An alternative method for detecting the presence of volumetric locking in more detail is to plot the stresses of a single direction ((0,1,2) or (x,y,z)) to look for any oscillations in stresses from once cell to the next. A plot at 1 s of flow-time is given in fig. 5.7. As stiffer material is more likely to have locking issues, all simulations presented herein use the properties of concrete Mix C, rested for 240 s, as that will be the stiffest concrete used in any simulation within this chapter.

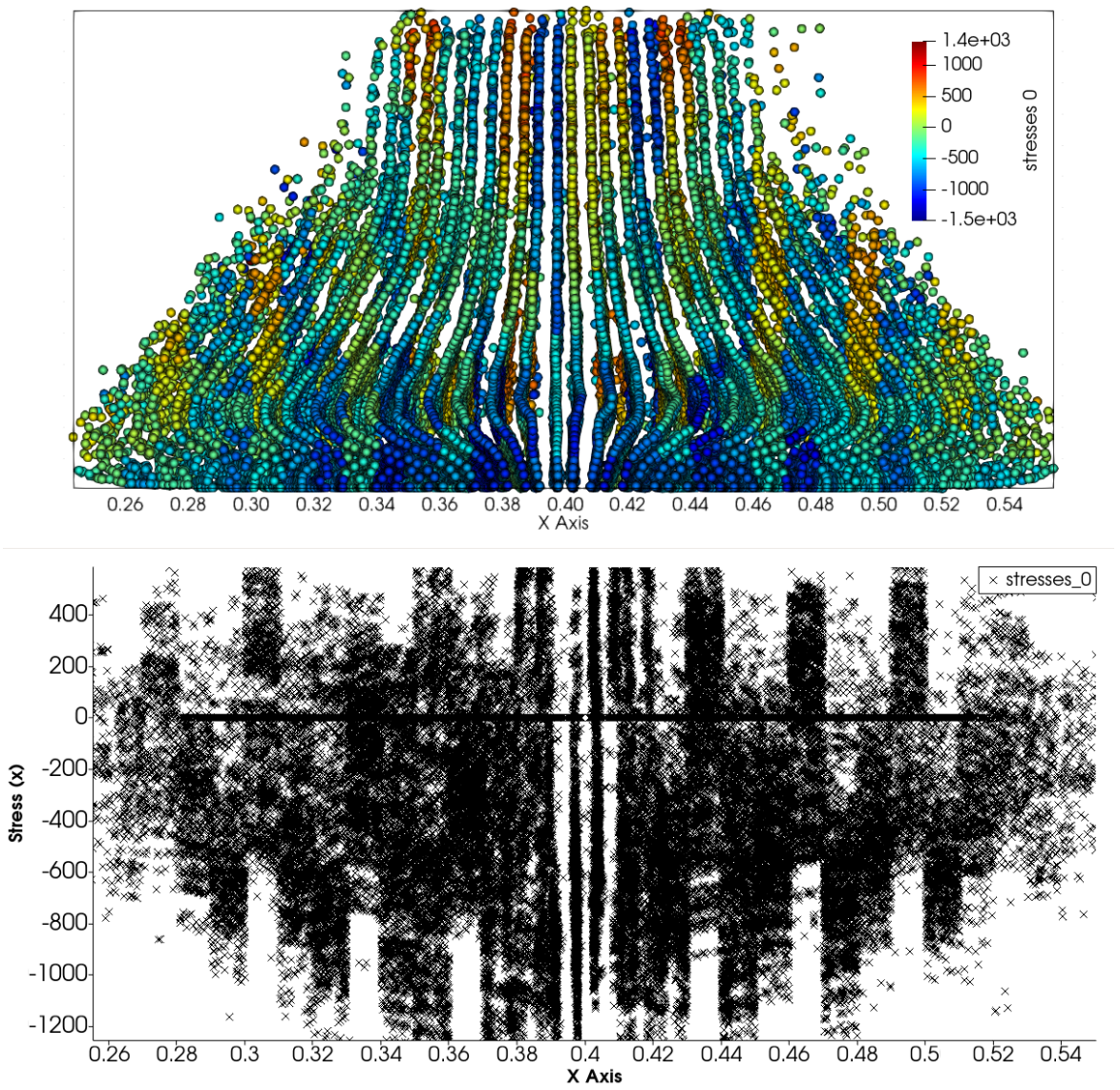

Fig. 5.7 8 PPC, fine mesh with stepped cone walls. Top image: Slice through a Slum-Flow simulation showing stress [Pa] for the 0/x direction. Bottom image: Plot of 0/x stress [Pa] against x-coordinate.

The x-axis of the bottom image fig. 5.7 is the x-coordinate the material point. For each material point in this case, the stress in the x-direction (direction 0) is plotted. For this case, 8 PPC is used for a mesh with spacing of 10 mm. The result is a fine-mesh with approximately $50,000$ points representing the cone domain. The background mesh is comprised of hexahedra cells which makes defining a cone geometry with a constant PPC and a sloping side, difficult. The result is a cone where the inclined plane is created by a series of steps, fig. 5.8.

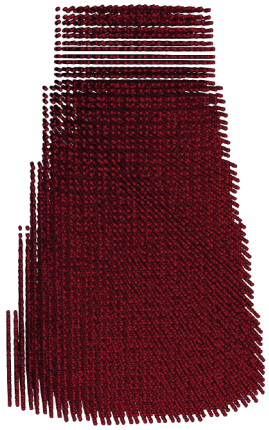

Fig. 5.8 Demonstration of stepping used to create inclined plane in a cone geometry.

If the same approach is taken for the outside cone, then a similar stepping effect is required. What results from a 10 mm cell spacing with eight PPC, is a mesh and PPC combination very susceptible to volumetric locking, seen in the lower graph of fig. 5.7. Along the x-axis of the lower graph, the stresses alternate between positive at intervals equivalent to the cell spacing, thus, volumetric locking has occurred. The line at 0 stresses represents the stresses of the points that make up the cone geometry that have been reduced to zero, to represent a rigid body.

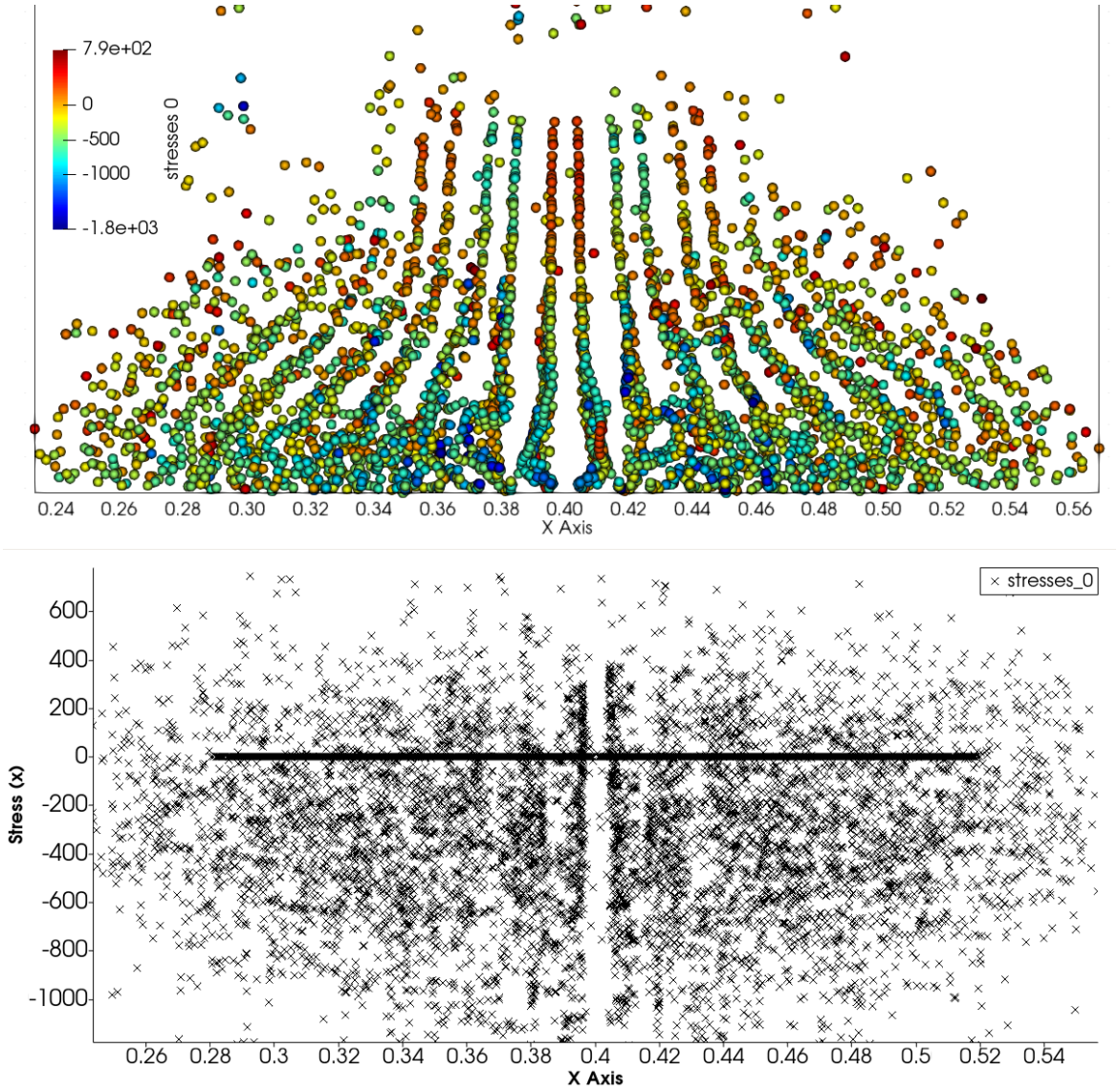

Fig. 5.9 1 PPC, fine mesh with stepped cone walls. Top image: Slice through a Slum-Flow simulation showing stress [Pa] for the 0/x direction. Bottom image: Plot of 0/x stress [Pa] against x-coordinate

Reducing the PPC in the fine, 10 mm spacing mesh or increasing the mesh size should decrease the amount of locking, as per [33]. First, reducing the PPC is presented in fig. 5.9. By reducing the PPC to one, the oscilations seen in fig. 5.7 have reduced considerably. However, a new issue has presented itself. In section 3.2.6, it is discussed that while reducing points is sometimes beneficial, points may split from the continuum body due to acceleration spikes. This is evident within the top image of fig. 5.9, where many points have left the larger continuum body, compared to the fine-mesh, eight PPC case. This is also likely due

to the interaction of the points and the cone. When two materials meet in MPM, without a specified contact boundary, a no-slip condition is preserved. This means the points on the boundary with another continuum will take on the velocity (as defined by shapefunctions) of the points they contact. Whilst this is natively resolved effectively, preserving good contact relationships, it means that single-points in contact with another material may be more unstable and pulled from one continuum to another. This suggests that more points, particularly on the areas of contact between the cone and the concrete may be appropriate.

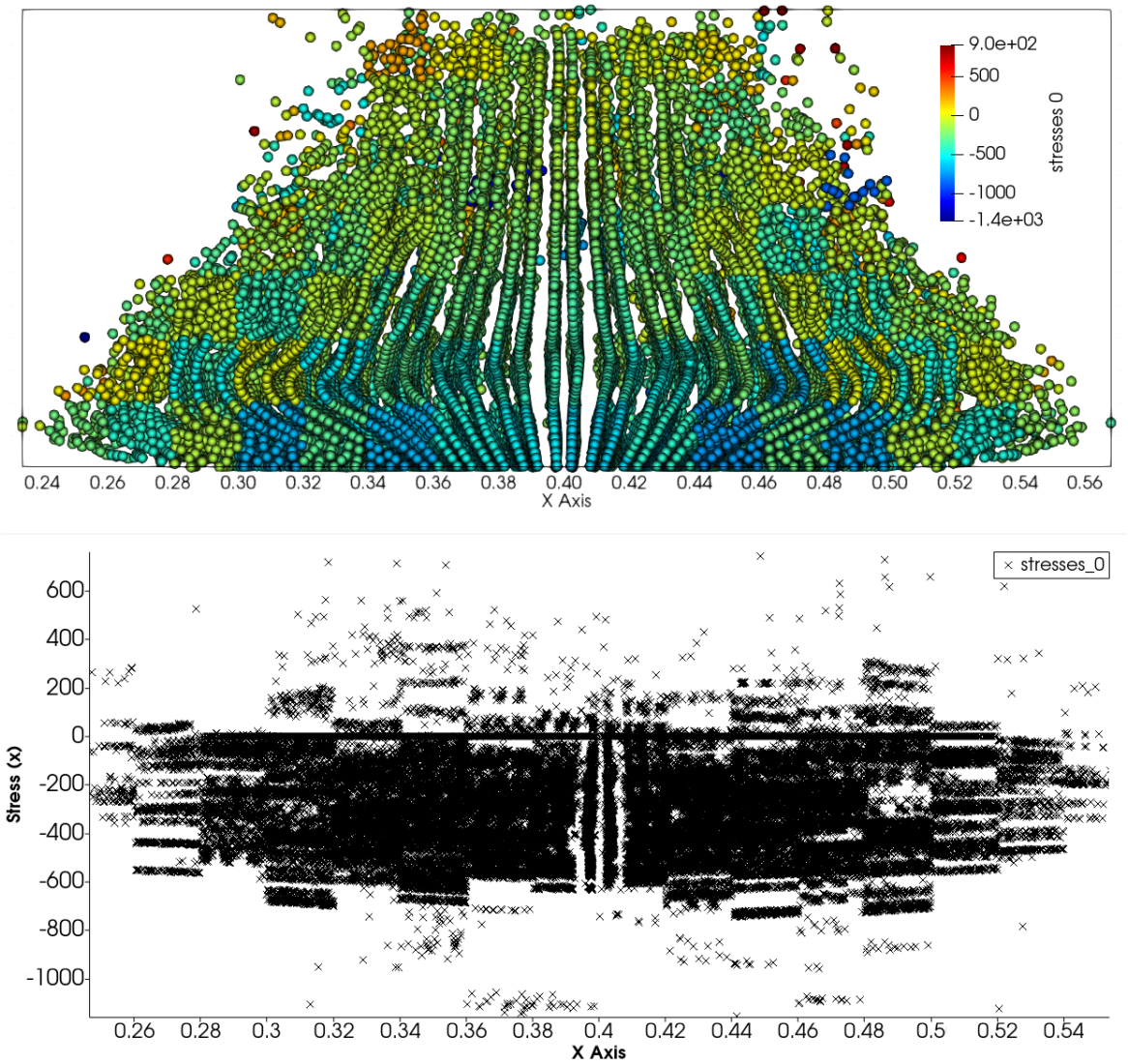

Fig. 5.10 64 PPC, coarse mesh with stepped cone walls. Top image: Slice through a Slum-Flow simulation showing stress [Pa] for the 0/x direction. Bottom image: Plot of 0/x stress [Pa] against x-coordinate

Reducing the cell spacing is demonstrated by fig. 5.10. Here, the cell spacing has been increased from 10 mm to 20 mm, decreasing the number of cells. Maintaining the same number of points as fig. 5.7 results in a PPC of 64. An interesting change from a fine mesh to a coarse mesh, with an increased PPC, is that whilst the oscillations in stress from one cell to another still exist, the degree with which the oscillations occur is reduced. This is evident by the reduced number of points where the stress in one cell is negative, and the adjacent positive, as in fig. 5.7. Despite the reduction, the top image, (a slice through the Slump of concrete) of fig. 5.10 displays some point separation. Thus far, only the fine mesh and higher PPC have managed to reduce the number of single-point tearing.

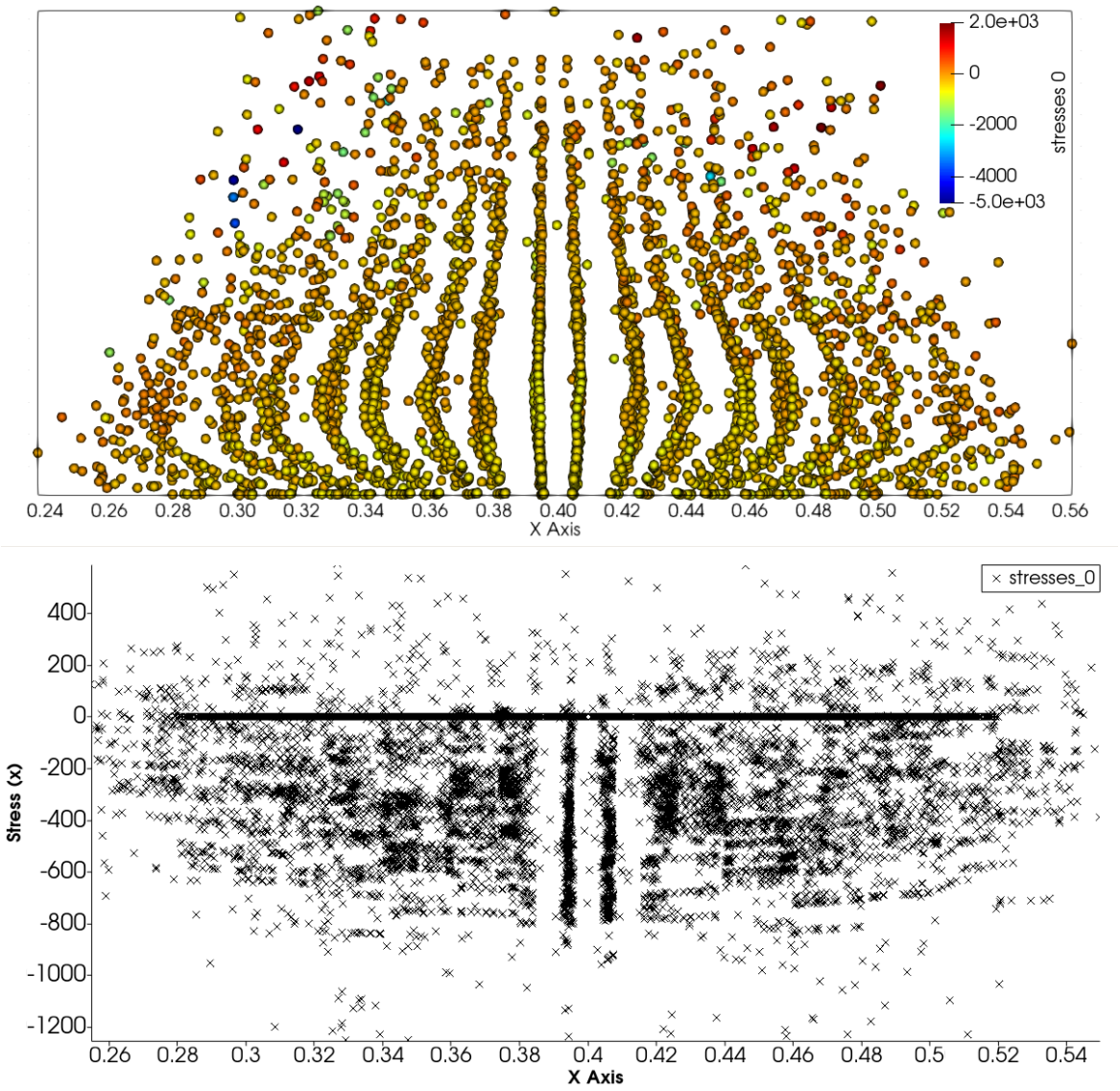

Fig. 5.11 8 PPC, coarse mesh with stepped cone walls. Top image: Slice through a Slum-Flow simulation showing stress [Pa] for the 0/x direction. Bottom image: Plot of 0/x stress [Pa] against x-coordinate

So that a direct comparison can be made, the 20 mm cell spacing case is also tested at 8 PPC, shown in fig. 5.11. Similar to the 64 PPC case, the oscillations rarely go above zero, suggesting a reduced degree of locking, but again point splitting has become an issue.

From analysing the potential meshes, the ideal mesh would use a fine mesh to reduce point splitting, but less than eight PPC to reduce the degree of locking. This is based on the summary of the mesh sensitivity presented in table 5.2.

Fig	PPC	Mesh	Spacing	Locking	Tearing
5.7	8	Fine	10 mm	High	Low
5.9	1	Fine	10 mm	Low	High
5.10	64	Coarse	20 mm	Mid	Mid
5.11	8	Coarse	20 mm	Low	High

Table 5.2 Results from mesh sensitivity analysis for a simulated Slump-Flow test.

For the simulations in this chapter, the concrete is discretised using a range of PPC, with higher concentrations of points at the boundaries to reduce splitting. The distribution of points is shown in the pie chart, fig. 5.12.

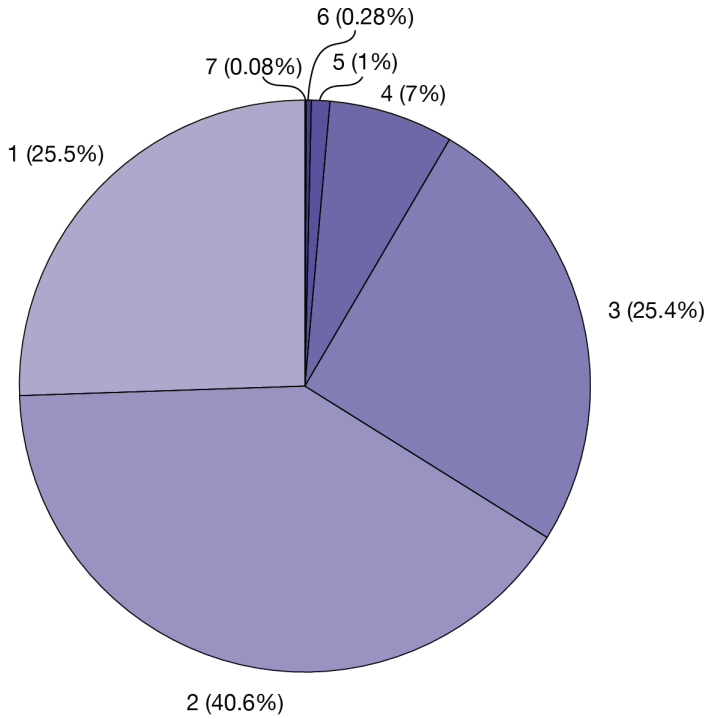

Fig. 5.12 Distribution of points per cell used within MPM simulations of SF test.

A variety of PPC are used to define the geometry, taking into consideration the observations presented in this section. The geometry itself was generated using the open source software, GMSH [56], a free tetrahedral mesh generator. This mesh was converted to points for use in CB-GEO MPM by using the *gmshToFoam* tool, part of the OpenFOAM® software package, to generate points at the centre of a each element of the mesh. Which can easily be converted to the required ascii format required by CB-GEO MPM.

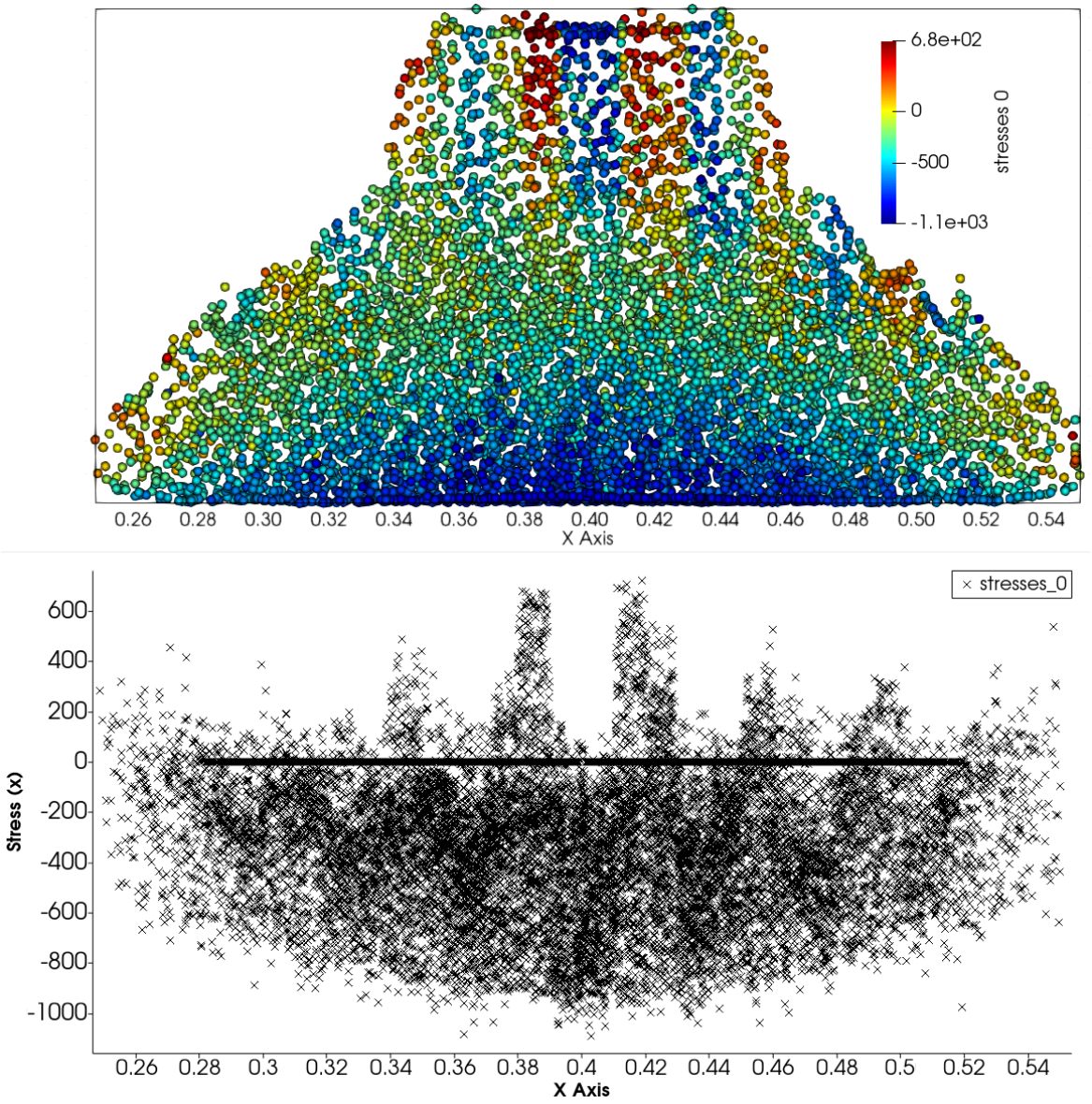

Fig. 5.13 Mixed PPC, fine mesh with smooth cone walls. Top image: Slice through a Slum-Flow simulation showing stress [Pa] for the 0/x direction. Bottom image: Plot of 0/x stress [Pa] against x-coordinate. Minimal volumetric locking present.

The resulting plot of stresses from using the mixed-PPC mesh is presented in fig. 5.13, where the bottom plot shows a reduced locking and good stress profile at 1 s of simulation time. Although some locking is present, it is confined to upper areas unlike the wide-spread locking exhibited in other cases. Additionally, the geometry has a low occurrence of single-point tearing. For comparison, a simulation of Mix A, a concrete with a lower stiffness after the

same rest period, is presented in fig. 5.14. Here, a stress profile devoid of any noticeable locking effects is presented.

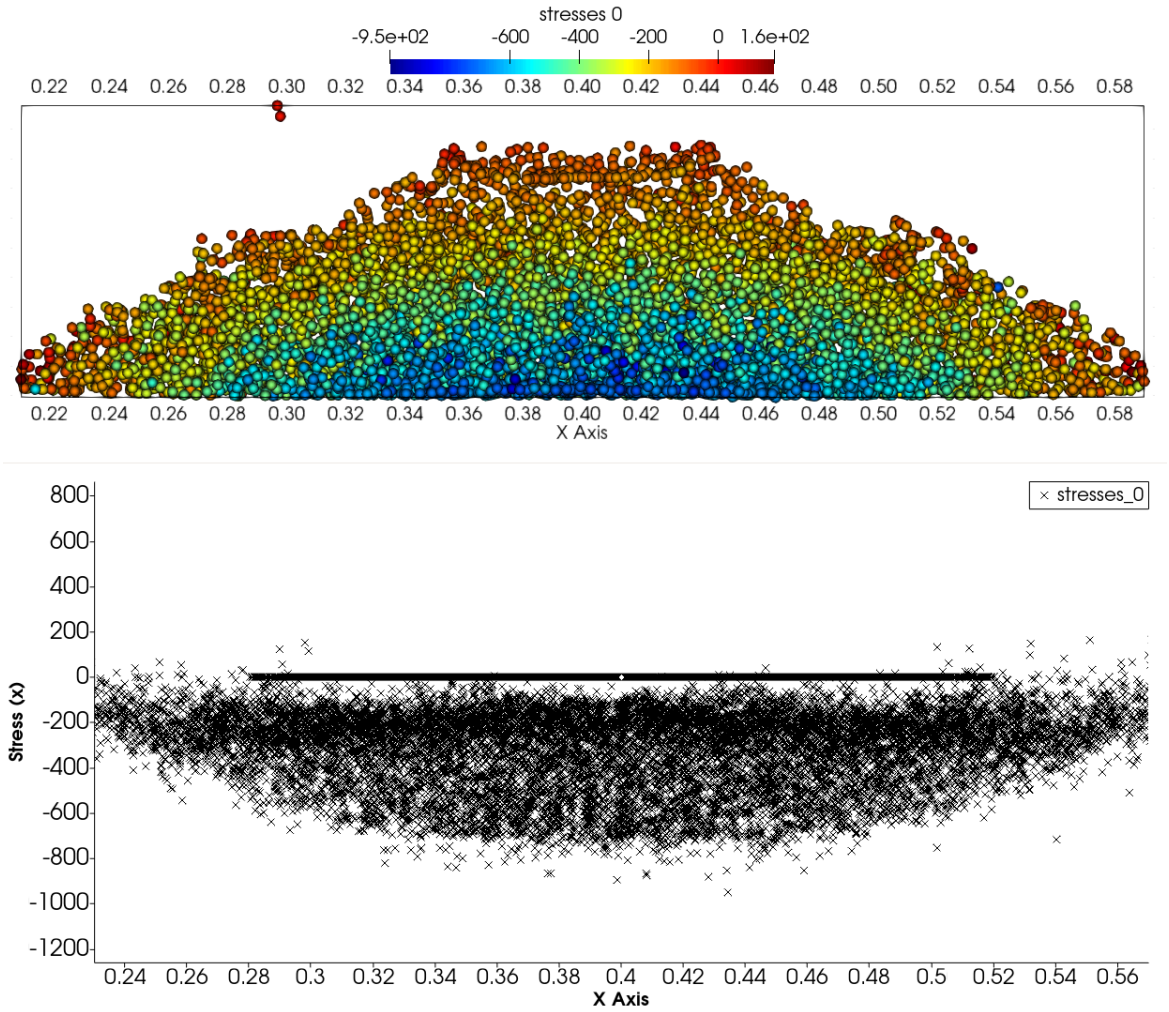

Fig. 5.14 Mixed PPC, fine mesh with smooth cone walls. Top image: Slice through a Slum-Flow simulation showing stress [Pa] for the 0/x direction. Bottom image: Plot of 0/x stress [Pa] against x-coordinate. Very low volumetric locking present.

The mixed-PPC geometry used in fig. 5.14 and fig. 5.13 is presented in fig. 5.15 with the chosen mesh, a spacing of 10 mm. The geometry of the Sump-Flow test in 3D is discretised using approximately 17,000 material points. 4000 points represent the Slump-cone with the remainder representing Tremie Concrete. High density, rigid material points are used to model the Slump-cone to prevent any unwanted outward flow of concrete from the cone. It is important to simulate the cone as it confines the initial flow of concrete, reducing the overall

spread. Without the cone, the simulations are not subject to the correct confining forces, producing an unrealistic early geometry of the flow. At the start of the simulation, the cone is raised at a speed of $15\,\mathrm{cm\,s^{-1}}$ so as to raise the cone in 1-3 s as per the BSI [26] guidelines. The background mesh is discretised with $256,000$ nodes creating $219,373$ hexahedra GIMP elements.

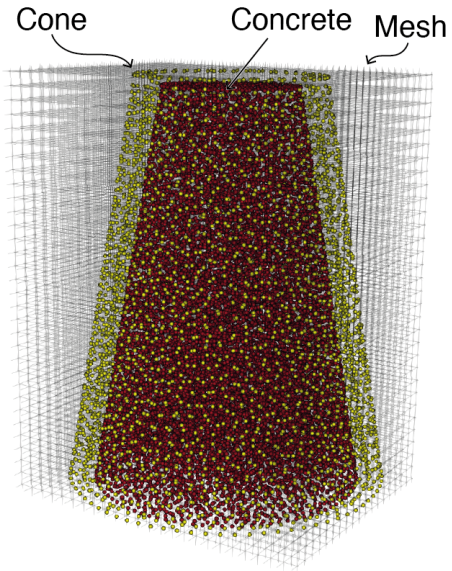

Fig. 5.15 Geometry of mesh and points used in MPM simulations of the Slump-flow test.

Figure 5.14 represents the target stress profile, which required calibrating some of the PR-Bingham model parameters to achieve. The amount of locking is proportional to the stiffness of the material, the stiffer the material: the higher the amount of locking. Thus, any model parameter that increases the material stiffness will increase the likelihood of locking, as seen by the disparity between locking of Mix C and Mix A in the sensitivity analysis. Another such property would be the m parameter used by the Papanastasiou part of the PR-Bingham model. As per fig. 5.5, an increase in m will create a model closer to the Bingham model by increasing the slope of the curve at low shear rates. This will result in a significant increase in the apparent viscosity at low strain rates leading to an increased stiffness and, therefore, an increase in volumetric locking. This can easily be demonstrated by increasing the m parameter used in fig. 5.14, from 5, to 100. This produces locking in the model, as per fig. 5.16. Franci and Zhang [54] demonstrated how different m values have a marginal impact on the behaviour of a Bingham representation of cement paste but can influence the stability of a model. Therefore, using a reduced m value should not effect the model, other than to prevent locking. An m of 5 is subsequently used in all simulations in this study.

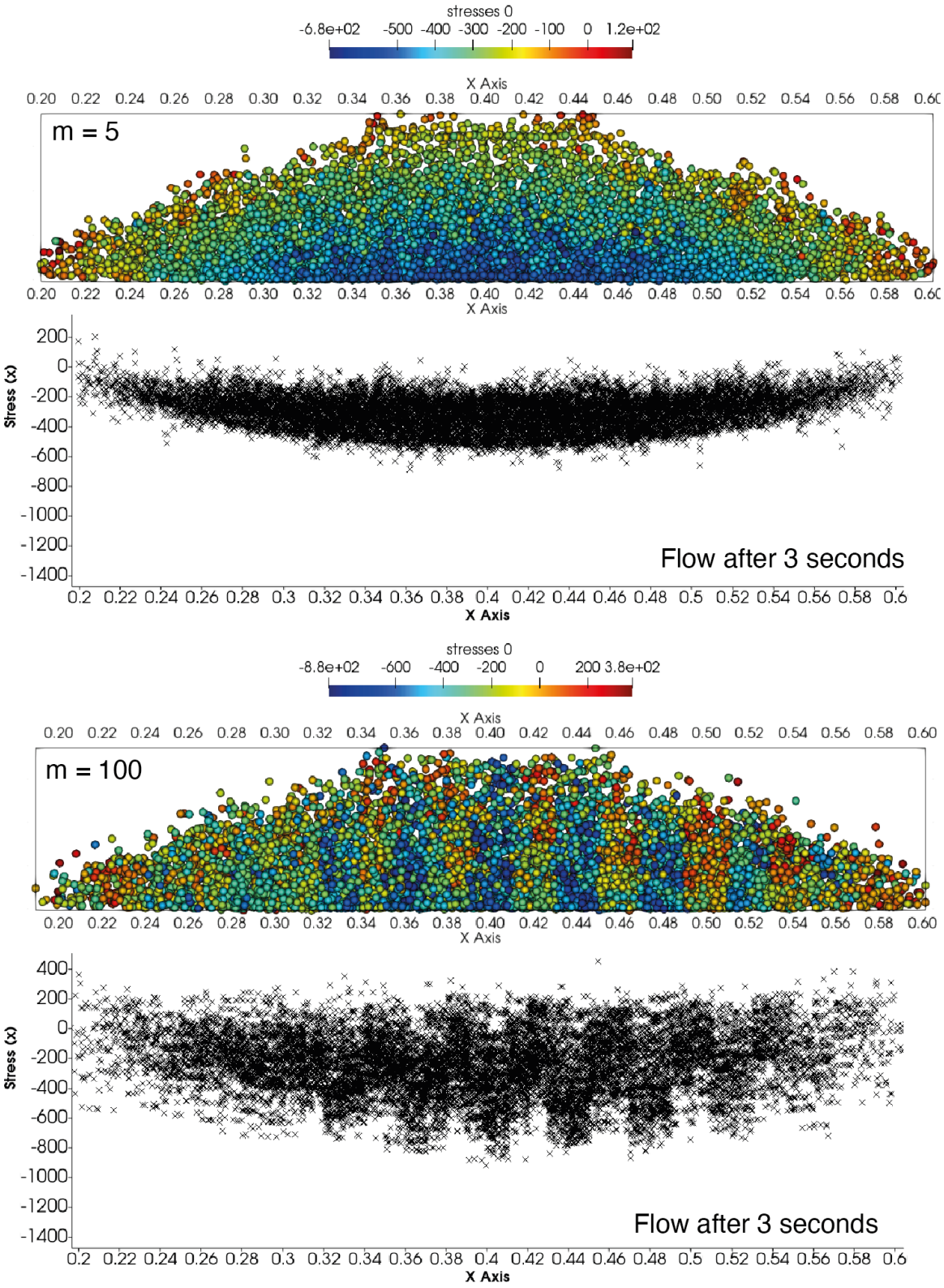

Fig. 5.16 Comparison of different m values and the effect of volumetric locking after 3 seconds of flow time. Top image of each m value: Slice through a Slum-Flow simulation showing stress [Pa] for the 0/x direction. Bottom image of each m value: Plot of 0/x stress [Pa] against x-coordinate

5.3 Results and Discussion

5.3.1 Dynamic Property Simulations

Figure 5.17 shows the time-evolution of the Slump-flow spread in mm for Mixes A-C (see table 5.1) where no rest time is present. For Mix A, a highly viscous low yield stress concrete, the MPM SF_0 reaches the corresponding Physical SF_0 around 18 s. This is expected for a high viscosity concrete like Mix A. The MPM simulations of Mixes B and C reach the physical SF at approximately 10 s and 12 s respectively, as both mixes have a lower viscosity in comparison to Mix A. The MPM SF_0 for Mixes A and B continues to grow at a negligible level after reaching the physical SF_0 due to low shear deformation caused by PR-Bingham mode. Despite this continued growth, the MPM SF_0 for mixes A and C remain within the margin of error [79]. The MPM SF_0 for Mix C does continue to grow at a higher rate after reaching the physical SF_0, but still reached a stable level within the physical SF_0 margin of error. The continued growth of Mix C is due to the constant deformation at a low shear rate characteristic of the PR-Bingham model with larger yield stress.

Figure 5.18 shows the three-dimensional isometric view of the evolution of all three mixes as they leave the cone at 0.3 s and the final shape at 20 s. Figure 5.18 shows a clear difference in spread diameter for the mixes at 0.3 s. The final spread are significantly different, but the three mixes maintain a uniform shape and thickness.

The good level of correlation between the physical and numerical SF_0 indicates that the PR-Bingham model developed in the MPM framework is capable of modelling the rheological behaviour of Tremie Concrete.

5.3.2 Thixotropic Simulations

The time dependent thixotropic behaviour of Tremie concrete is simulated by introducing a rest time to build the yield stress of Tremie Concrete. Figure 5.19 compares the evolution of the MPM SF_{240} and the Physical SF_{240} for Mixes A-C. After an initial rest period of 240 s all three concretes fall short of reaching the final experimental SF by approximately 60-80 mm.

The difference in the SF run-out with and without the initial rest time of 240 s is defined as ΔSF. The ΔSF values for the MPM simulations are summarised in table 5.3 for Mixes A-C, showing an approximately 100 mm change in the SF following a 240 s rest. Conversely, as discussed earlier in this work, the experimental ΔSF values for Mixes A-C measured in the physical tests are significantly lower, ranging from 15 mm-20 mm. In the PR-Bingham model, the values of A_{thix} over 1 cause an increase in the yield stress of over 240 Pa during a

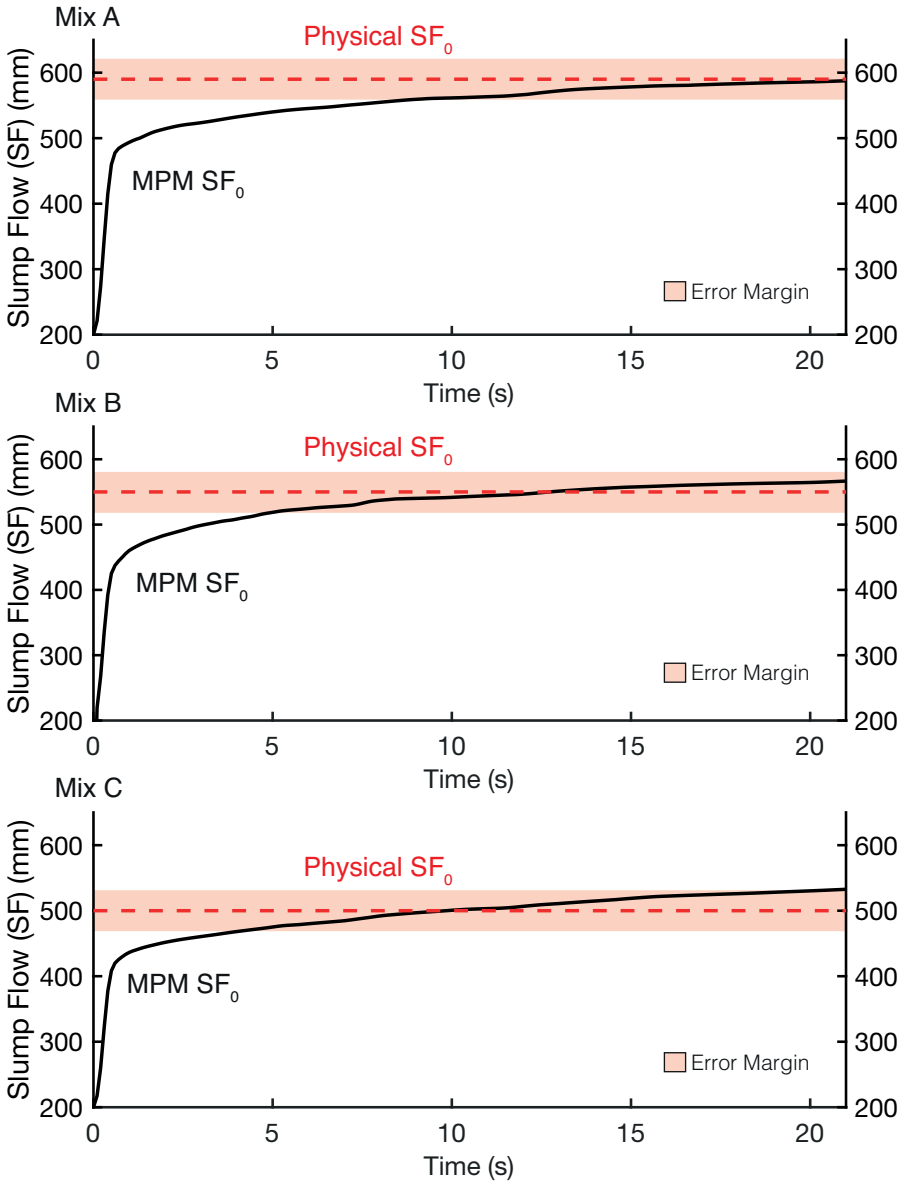

Fig. 5.17 Evolution of MPM simulated SF_0 over time for each concrete mix, dashed line indicates the physical SF_0 and MPM simulated SF_0 from table 5.1.

	ΔSF (mm)		ΔSF (% of SF_0)	
	Physical	MPM	Physical	MPM
Mix A	15	105	2.6	18.0
Mix B	20	94	4.0	18.8
Mix C	15	98	3.1	20.2

Table 5.3 Difference in Slump-flow following a period of rest for physical tests and MPM simulations.

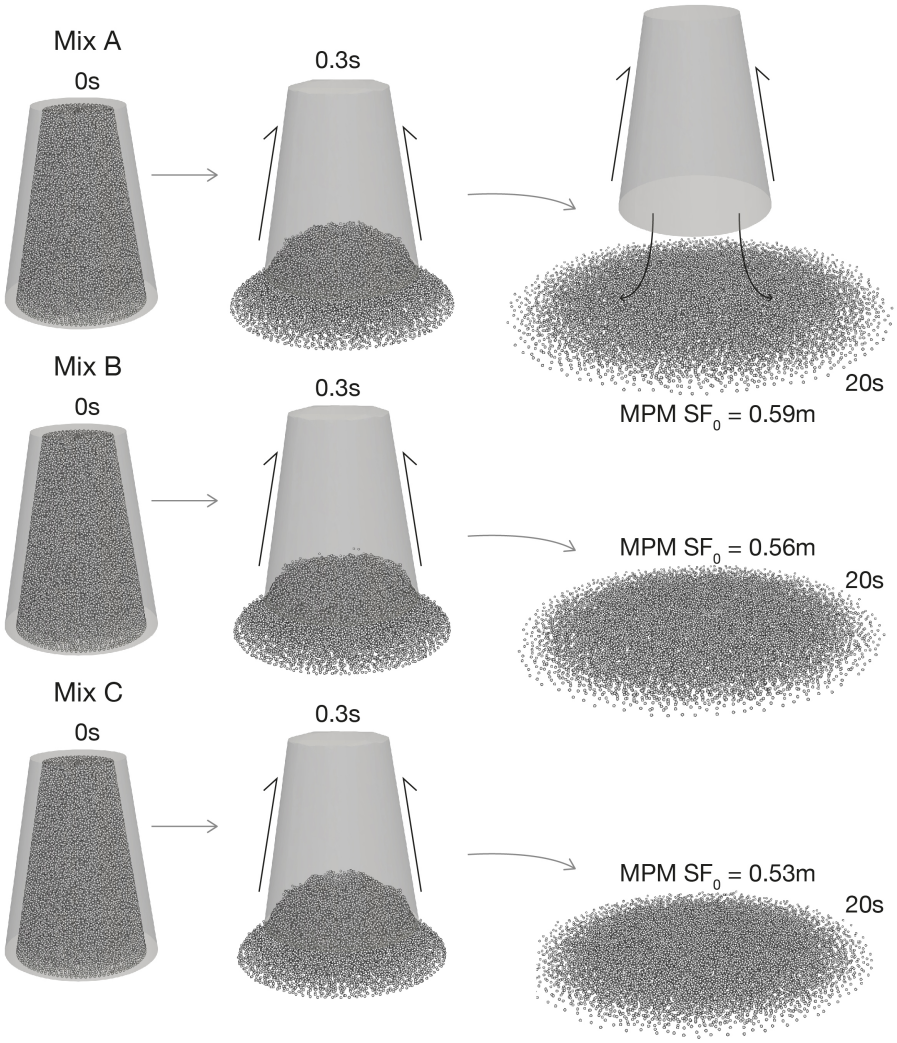

Fig. 5.18 Time evolution of Slump-flow test for all mixes. From top to bottom: Mix A, Mix B and Mix C

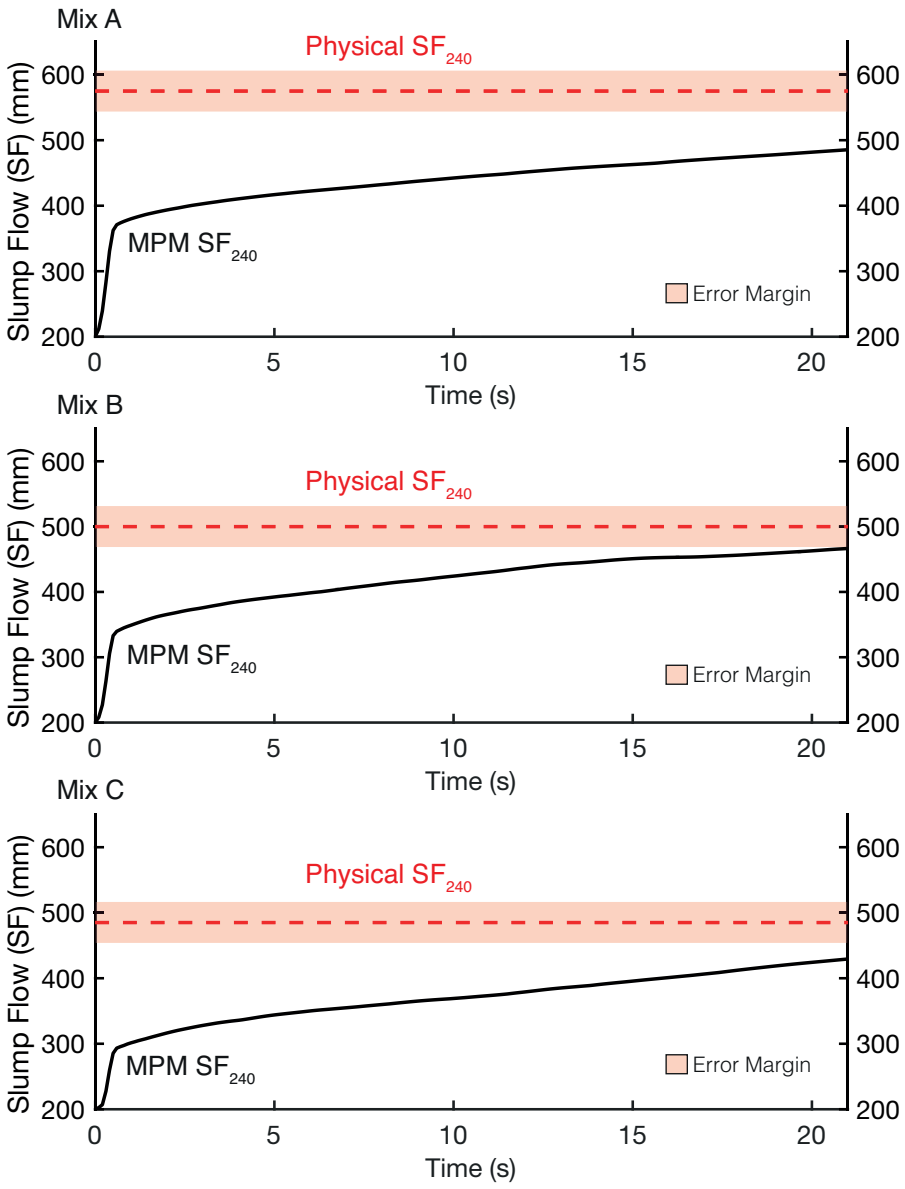

Fig. 5.19 Evolution of MPM simulated SF_{240} over time for each concrete mix, dashed line indicates the physical SF_{240} from table 5.1.

rest period of 240 s. Figure 2.9 shows that an increase in yield stress of over 240 Pa should yield a significant ΔSF, more than the observed 15-20 mm difference. The ΔSF observed in MPM simulations are still lower than what is the expected given the generalised empirical relationship between SF and τ_0 for a concrete with a yield stress of >250 Pa, but is closer to the expected behaviour than the ΔSF Physical values.

As discussed in section 2.3.2, [74, 50] could not find a consensus on why the physical Slump-flow test could not accurately represent thixotropic concrete, just that it was inadequate at doing so. This is supported by the small ΔSF physical values in table 5.3. Interestingly, the MPM simulations appear to capture a behaviour closer to the expected flow behaviour, with large ΔSF values reported in the MPM simulations. It is possible that the simulations overcome some physical artefacts that prevents the physical Slump-Flow test from representing the true flow behaviour of thixotropic concrete. The MPM simulations also align better with the rheometer measurements of Mixes A-C reported by [74, 50], which describes large increases in yield stress (material stiffness) over short rest periods, as noted by the high A_{thix} values in table 5.1.

It is possible that high shear rates during the slump-flow test remove a significant portion of thixotropy, preventing the test from accurately representing thixotropic concrete. This proposition can be disproved by examining the mean average shear rate occurring during a Slump-flow test, fig. 5.20a. In Mix A, the peak shear rate is approximately $12\,s^{-1}$ and $9\,s^{-1}$ for 0 s rest and 240 s rest, respectively. However, the slump-flow test experiences this peak shear rate only for a very short duration and is not sufficient to dissipate the large amount thixotropy developed at rest. The shear-stress that occurs as the SF spreading rate declines will also not be sufficient to remove a significant portion of thixotropy. This can be further supported by the time required to reduce static shear stresses to dynamic in a rheometer, which is around 10 s and requires a constant shear-rate of up to $12\,s^{-1}$ [72]. The Slump-flow test does not experience shear rates high enough to dissipate much thixotropy. The implication of this observation is that if the slump flow test does not experience enough shear forces to break down thixotropy, then the ΔSF for the physical test should be much larger, as it is with the MPM ΔSF. This supports the observation that MPM is not only capable of simulating dynamic concrete properties, but also static properties of thixotropic concrete.

Figure 5.21 shows the dissipation of λ with time for all mixes. At 20 s of flow-time, the result of the relatively low shear rates experienced by the concrete has prevented any notable dissipation of thixotropy. As the lowest shear rates are experienced close to the centre of the spread, the thixotropic dissipation has occurred the least in these areas. For all three mixes shown in fig. 5.21, the centre potions report higher λ values than the edges. This again

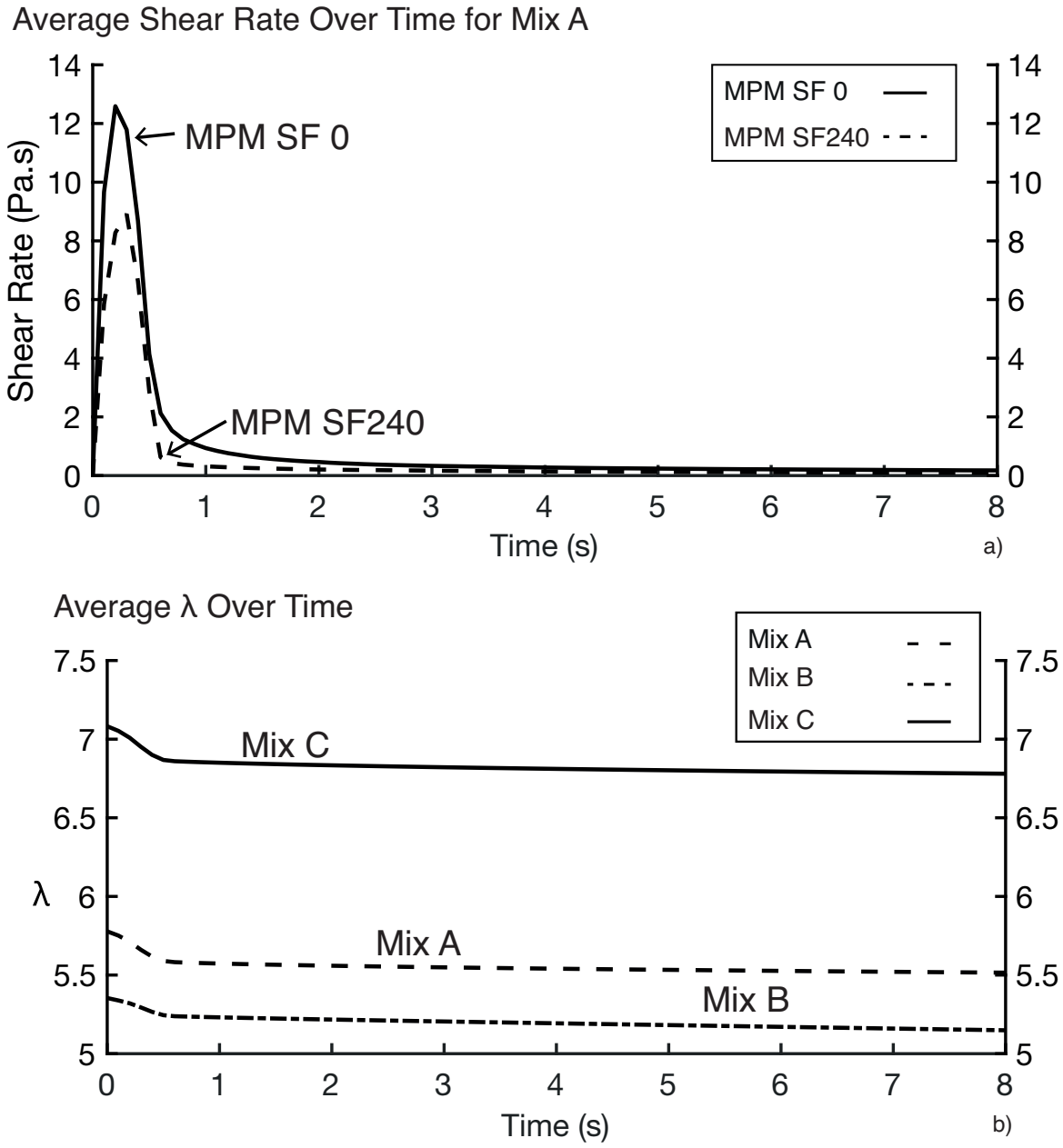

Fig. 5.20 A) Mean average shear rate for Mix A during the Slump-Flow test for 0 s rest and 240 s rest. B) Time evolution of λ for all mixes following a rest period of 240 s. From top to bottom: Mix B, Mix A and Mix C

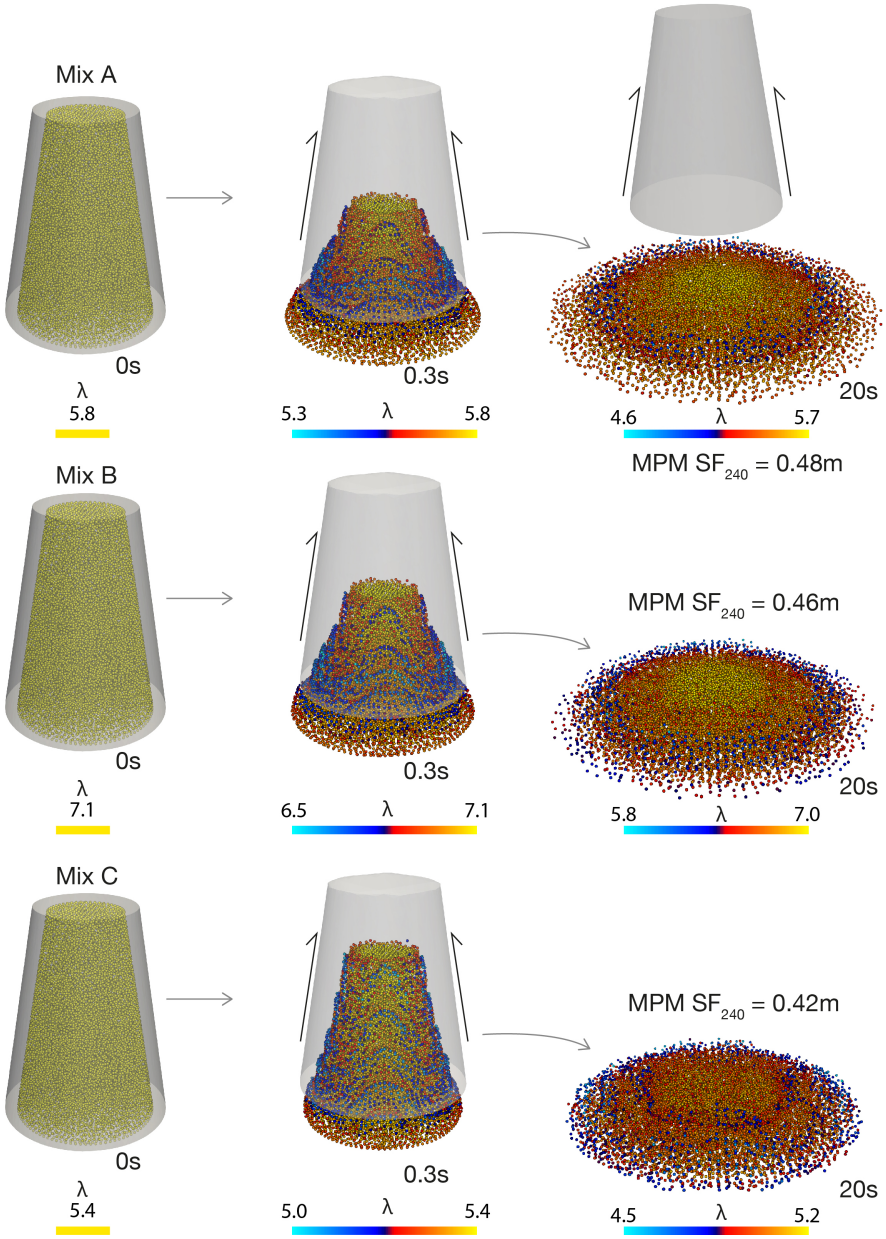

Fig. 5.21 Time evolution of Slump-flow test for all mixes following a rest period of 240 s. From top to bottom: Mix A, Mix B and Mix C

supports the argument that the Slump-flow test is not capable of dissipating a significant amount of thixotropy.

Figure 5.20b reveals the rate of dissipation of the mean λ over time during the test for all three mixes. It can be noted here that from approximately 3 s of flow time, the gradient of the slope remains relatively constant. Therefore, the bulk of thixotropy dissipation is likely to happen within the initial period of the test.

One final piece of evidence suggesting the inability of the Slump-flow test to dissipate thixotropy is presented by fig. 5.22a. Here, a simulation is conducted where all starting properties are equal to Mix A MPM SF_0, apart from the starting yield stress, which has been increased to 367 Pa. This value is equal to the static yield stress of Mix A following a 240 s rest. The final SF measurements and the evolution of SF are almost identical, as shown by the overlain curve (dashed line) of Mix A MPM SF_{240}. This suggests that the thixotropy dissipation within concrete has had a minimal impact on the final result, but the elevated yield stress does impact the result.

In the previous section of this chapter, a parametric study (fig. 5.5) of the PR-Bingham parameters was shown. One parameter, α, influenced the rate at which thixotropy would dissipate following the application of stress. For the MPM simulations presented, an α of 0.01 was used, to be inline with experimental observations from a rheometer and observations in the literature. To provide continued evidence that the Slump-flow test does not dissipate thixotropy significantly, fig. 5.22b demonstrates the effect on thixotropy dissipation for an alpha three times larger, of 0.03. What can be observed, for Mix A, is that an increase in alpha from 0.01 to 0.03 causes a reduction of thixotropic multiplier λ from 5.7 to approximately 4.8, as opposed to approximately 5.4 for an α of 0.01. While this does represent an increase in thixotropy dissipation, the final SF was within 5 mm of Mix A MPM SF_{240}. Thus, even concrete significantly more susceptible to thixotropic dissipation still retains an increased stiffness during the Slump-flow test.

The MPM framework with PR-Bingham model has been successful in offering insights into the flow behaviour of thixotropic concrete. The model suggests that the flow of concrete should be impacted by its thixotropic properties on a greater scale than empirical testing seems to suggest, and in line with observations from a rheometer.

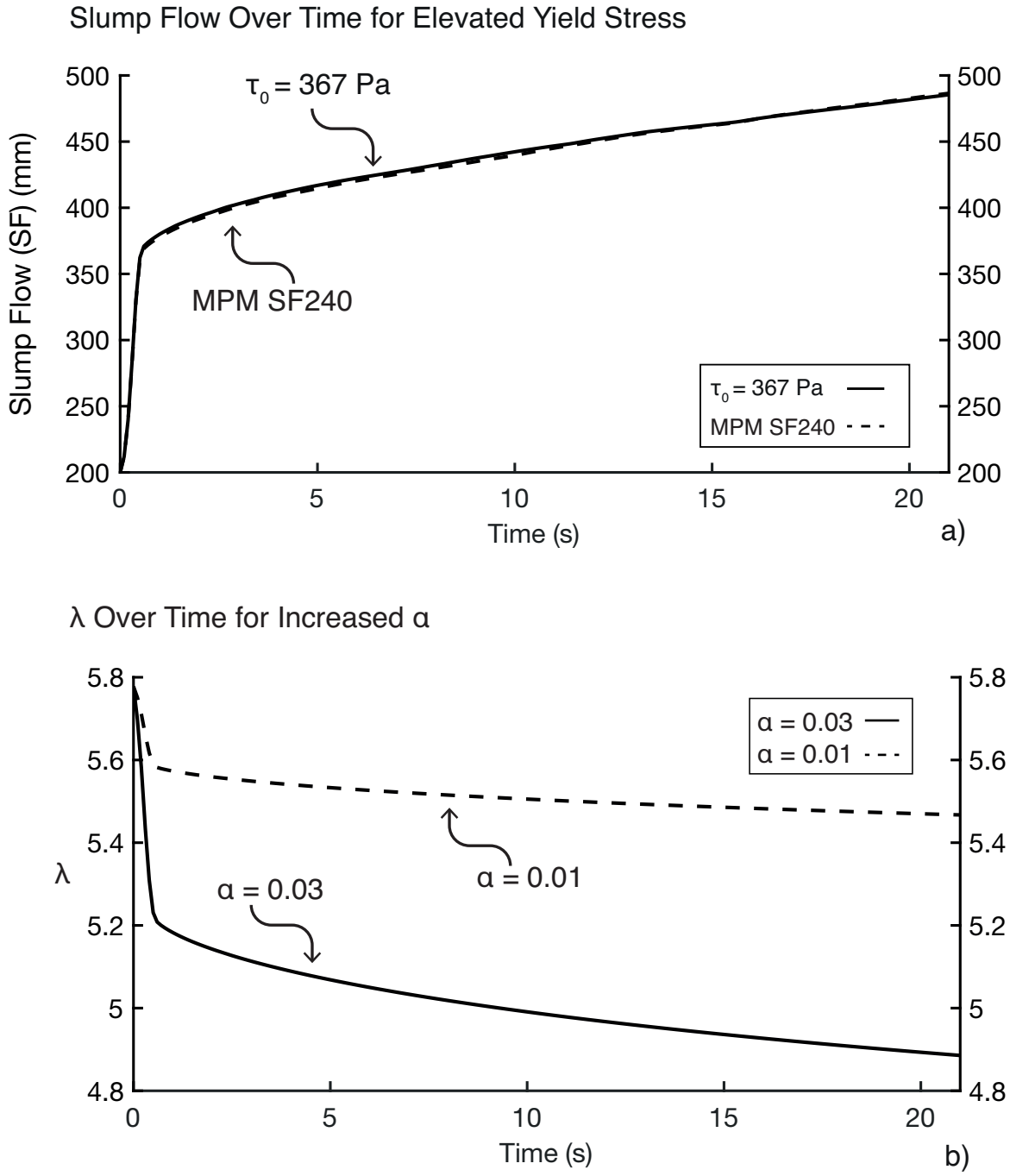

Fig. 5.22 A) Time evolution of Slump-flow test for Mix A following a rest period of 240 s and from 0 s rest but with a starting yield stress equal to Mix A at 240 s rest. B) Effect of alpha increase on dissipation of λ.

5.3.3 Computational Fluid Dynamics Comparison

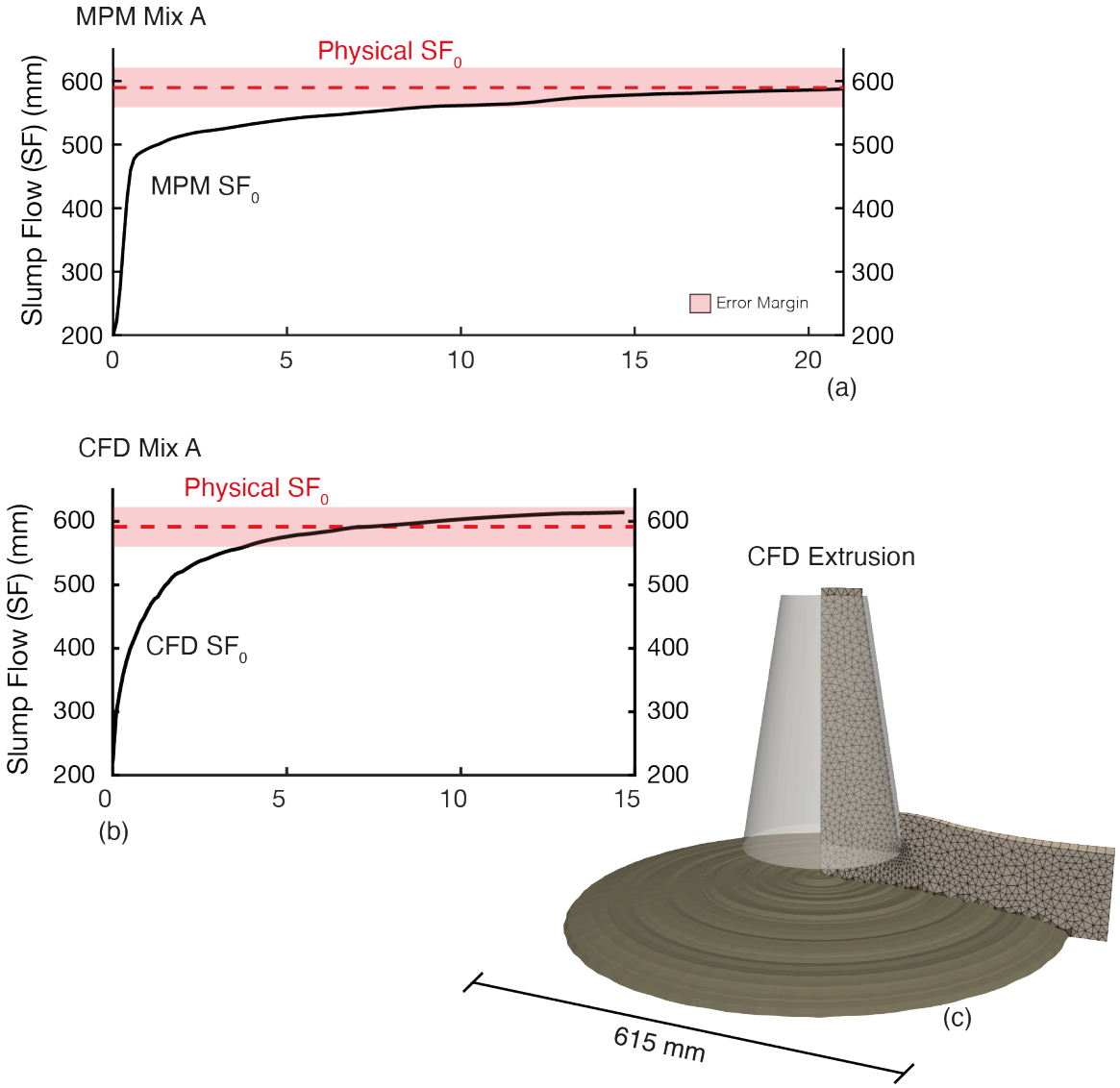

Fig. 5.23 Time evolution of Slump-flow test for Mix A in MPM (a) and CFD, OpenFOAM® (b). Also shown is a 360°rotational extrusion of the Slump-flow spread obtained from the axisymmetric CFD simulation (c).

.

Figure 5.23a and b are the time evolution of the SF of Mix A for MPM and CFD respectively. The CFD simulation uses the same Bingham inputs as the MPM simulations of Mix A, however, there is no FC input into the model. The CFD simulation also uses the same OpenFOAM® parameters as the Slump-flow simulations presented in Chapter 4. The spreading rate of the CFD simulation appears to be steadier than the MPM simulation where

a clear change in spreading rate can be seen. The SF of the CFD simulation seems to spread around 25 mm further than the physical result, though this is still within the margin of error of the physical test. The spreading rate of a physical Slump-flow test presented by Fierenkothen [52], seems to suggest a discontinuous spreading rate where a phase of rapid growth is followed by a period of low rate spreading. This would suggest the MPM simulations represent the behaviour more accurately, though more work is needed to confirm this as the spreading rate is heavily influenced by the rising speed of the cone [101]. It is worth noting that the CFD cone was raised 1/3 of the speed the MPM cone was raised due to complications with distortion of the mesh when faster rates were attempted. This could account for the disparity in spreading rate behaviour.

In general, it seems CFD SF measurements appear to spread slightly further than expected, which is likely due to a lack of calibration ability regarding the frictional boundary with the base plate. The CFD simulation used a moving wall boundary rather than a different material to represent the rising cone, which has a more complex method of implementation than the cone points within MPM. Overall, it seems that the MPM simulations of concrete flow are at least on par with the ability of CFD to simulate dynamic properties of concrete, with the added ability to modify boundary conditions and the all important thixotropic behaviour.

5.4 Conclusion

The objective of this chapter was to model thixotropic Tremie Concrete for the first time, using the Material Point Method to explore the challenges of testing concrete and how numerical modelling can provide unique insights into concrete flow behaviour. The following observations are made:

- The New MPM PR-Bingham model that combines the Papanastasiou-Bingham model with Roussel's simplified thixotropy equations is successful in accurately representing concrete flow behaviour in both dynamic and thixotropic conditions.
- MPM simulations of weakly compressible materials such as tremie concrete results in numerical errors such as volume locking. Volume locking in weakly compressible flows are reduced using higher order shape functions, setting the m parameter in the PR-Bingham model to a low number and using reduced integration for pressures.
- A comprehensive calibration and material property assessment procedure, outlined in this chapter, can be used to verify simulated Tremie Concrete.

- Finally, a comparison of physical and numerical results of the Slump-Flow test for thixotropic concrete reveal for the first time, a decline in concrete workability during the Slump-Flow test for simulated concrete, in line with theoretical predictions, that was not captured by the physical version of the test.

Chapter 6

Thixotropic Tremie Concrete in Deep Foundations

6.1 Introduction

It was established in Chapter 4 that boundary conditions can influence the flow patterns of secondary concrete batches in cast-in place foundations. This was concluded after computational fluid dynamics models of concrete flow highlighted how introducing a reinforcement cage was sufficient to restrict the flow to the area surrounding the tremie pipe. One of the drawbacks to that work was the inability of the CFD package to readily simulate time-dependent behaviour of concrete. Additionally, the chosen CFD package had limitations on the way boundary conditions, like friction, could be implemented.

In Chapter 5, a new method of simulating time-dependent behaviour in the Material Point Method framework was presented and validated using the simple Slump-flow test and a comparison of simulated results with experimental data. This demonstrated the ability of MPM to model the behaviour of thixotropic concrete accurately.

Combining the numerical groundwork provided by Chapter 5 with the new experimental apparatus and improved understanding of flow behaviour in Chapter 4 should complete the picture of how concrete flow patterns form, by adding in time-dependence.

It was surmised the Chapter 4 that a restricted Flow pattern of concrete is likely to occur due to high confining forces. It is reasonable to assume that high levels of concrete thixotropy could contribute to the restricting forces acting on concrete flow in a foundation due to the increased flow resistance caused by an elevated static yield stress. Thus, concrete

experiencing high levels of thixotropy will likely exhibit Restricted Flow behaviour if the flow around reinforcement bars is inhibited.

The present chapter has two main objectives: The first is to use one of the most common concrete testing methods, the L-box test, to demonstrate how thixotropy affects concrete flow around obstacles. The second objective is to perform simulations of concrete flow in the GFB apparatus, to clarify how the behaviours identified by the first objective influence the flow behaviour of concrete in more field-like conditions.

6.2 Methods and Materials

MPM simulations presented in this chapter use some of the same conditions outlined in Chapter 5. All simulations feature the use of a regular hexahedra GIMP mesh built with [35], used to perform the background calculations. The specific details of the model geometries are given in the following sections. All materials simulated within this chapter will use the PR-Bingham model as the constitutive model. Boundary conditions within all models are applied via a friction coefficient that is determined by the rheology of the simulated concrete, discussed in chapter 5.

6.2.1 L-box Geometry

Figure 6.1a displays the geometry used in the MPM simulations of the L-box test. It uses the recommended [46] 2-bar spacing configuration of the L-box, where two bars are spaced at 60 mm distance. The L-box specifications [25] recommend a cylindrical bar with a diameter of 12 mm, however, due to constrictions on the mesh, a 10 mm wide cuboid is used instead. A zero velocity condition is applied to the reinforcement bars, much like the conditions imposed on the outer walls of MPM simulations to represent a solid wall.

As discussed in the Chapter 2, there are several measurements that can be taken from the L-box test to assess the consistence of a Tremie concrete. In summary, they are the time taken for the concrete to reach the end of the horizontal section, the Flow-time (FT), the difference in heights at each end of the horizontal section, and the passing ratio, *PL*:

$$PL = \frac{H2}{H1} \tag{6.1}$$

Where H2 is the measured depth at the end of the horizontal section, and H1 is the measured depth in the vertical section, as demonstrated in Figure 6.1b. For this work, H1 and H2 are

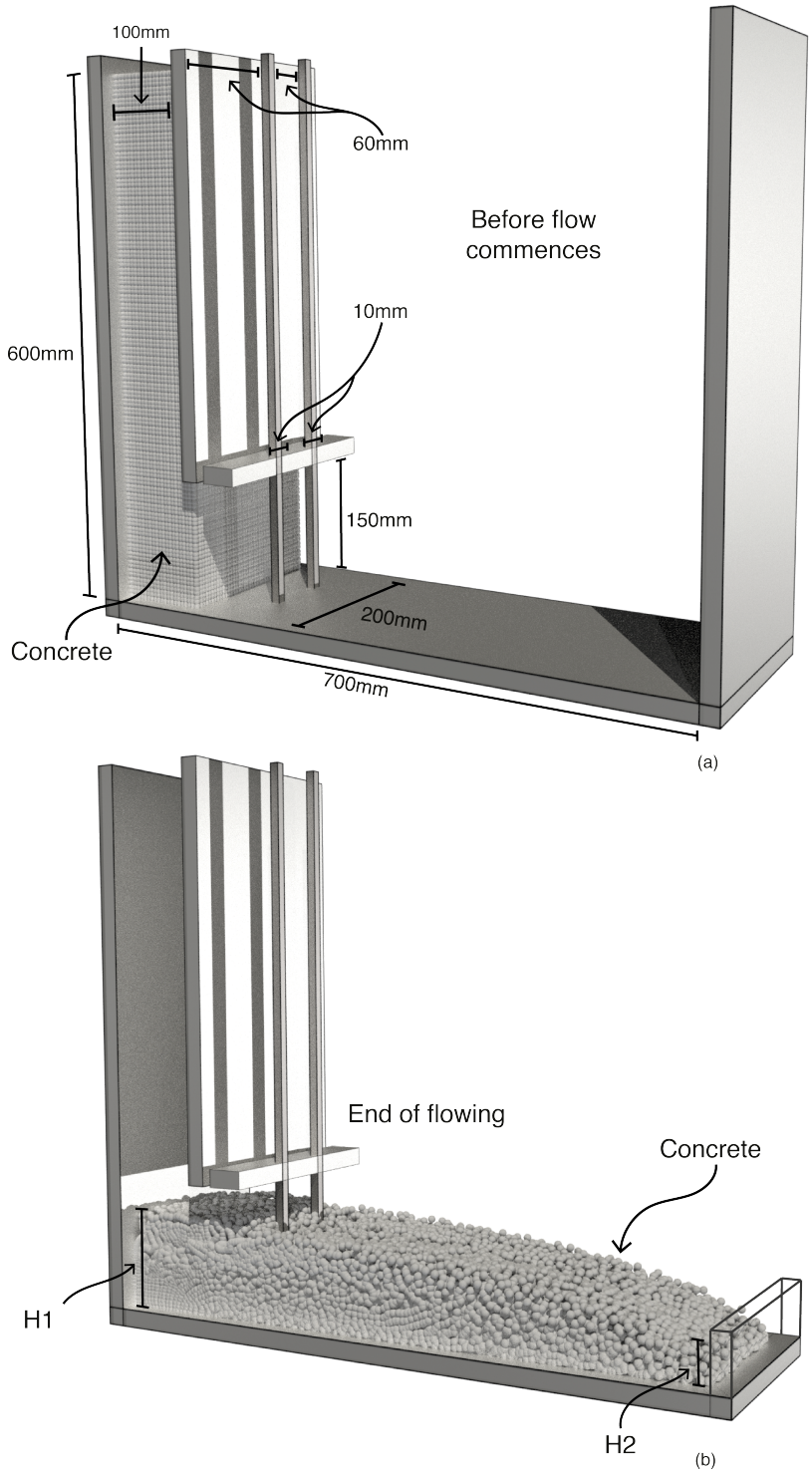

Fig. 6.1 a) Geometry of L-box test in MPM simulations and starting position of concrete. b) End position of concrete and typical location of H1 and H2 measurements.

taken as the highest depth recorded within 100 mm of the respective edge of the L-box. This could incur issues where slight separation of points over-estimate the value.

An accumulation of aggregate building up behind the bars due to segregation, referred to as blocking, will reduce the ability of concrete to flow leading to a lower passing ratio [119]. Thus, the passing ratio is also a measurement of the ability of a concrete mix to resist dynamic segregation. However, for the purposes of this study, only the link between passing ratio and yield stress is considered, since the constitutive model is not able to account for segregation or the particulate nature of concrete.

The MPM simulation of the L-box test is futher simplified by the removal of the rising gate used to release concrete from the vertical section into the horizontal one. This avoids the extra computational time in both pre-processing mesh building and run-time associated with moving rigid bodies with minimal effects on the results.

According to EFFC and DFI [46], if concrete does not reach the end of the horizontal section, the test is considered a fail. It is also noted that $H1$ and $H2$ measurements should be taken at the point at which flow has stopped. Unfortunately, the point at which flow stops is seldom the point at which the flow has reached the end of the horizontal section, so additional simulation time is needed to account for any flowing after the flow reaches the end of the horizontal section. As was the case in Chapter 5, the PR-Bingham model will continuously exhibit a small degree of deformation even at very low shear rates. Thus, the point at which flow has stopped is difficult to discern. Therefore, as with Chapter 5, a flow-cutoff time is required. A cut-off time of 20 s is chosen for this work, as very little deformation is was observed past this point for all simulations.

The cell size of the background mesh is governed by the smallest feature to be examined. In the case of the L-box, this is the reinforcement bars. Analysis of MPM mesh conditions and PPC (points per cell) in the previous chapters found that larger meshes are less subject to volumetric locking. For the L-box, the largest mesh possible would be the diameter of the reinforcement bars due to the application of boundary conditions on nodes to create solid, frictional walls. Thus, a 10 mm hexahedron mesh is used for the background grid. A PPC of 8 was chosen, rather than the varying point density approach of Chapter 5, as no sloping walls are present during the initiation of the problem, reducing the need for a complex PPC. It is worth noting that a PPC of 64 resulted in excessive locking for thixotropic concrete and should be avoided. At 8 PPC, the concrete is discretised into $96,000$ points.

Table 6.1 MPM input parameters of Mixes A-C for L-box Simulations, based on [74, 50].

	$\tau_{0_{dynamic}}$ $[Pa]$	μ $[Pa \cdot s]$	A_{thix} $[Pas^{-1}]$	FC
Mix A	54	35.8	1.3	0.35
Mix B	61	29	1.8	0.45
Mix C	130	30.2	2.9	0.43

6.2.2 L-box Input

The three concrete mixes examined in chapter 5 which were obtained from the data collected by Kraenkel and Gehlen [74] on the behaviour of concrete mixes will be used within this chapter also. Each mix design will be simulated within the L-box test using the dynamic values and different rest-times to generate thixotropic changes to the yield stress. However, unlike in previous work, three, rather than two rest-times will be used as a result of the testing procedure of the L-box test.

The first rest-time, 0 s, is used to represent the dynamic properties of the mix designs. The L-box testing procedure described in BS12350-10 [25] requires concrete to rest for 60 s in the vertical chamber of the apparatus. Thus, the second rest time to be examined is 60 s of rest. Resting for this amount of time should induce a notable increase in yield stress due to thixotropy. It is expected that the greatest correlation between physical L-box results and simulation results will be observed with the 60 s rest period rather than 0 s rest, but the reality is likely to be somewhere in-between the two due to human error in the test procedure of both the L-box and the obtaining of rheological measurements.

Finally, the third rest period of 240 s will be used to monitor the effect a large amount of thixotropy has on both the passing ratio and the flow time.

Table 6.2 presents the experimental results for the Flow-time (FT) for each mix, where the subscript value indicates the amount of time spent at rest. Also given in table 6.2 is the H2 measurement, which is the depth of concrete at the end of the horizontal section. Unfortunately, no data on H1 was available, so an estimation of passing ratio was not possible. However, due to the work conducted by Chamani et al. [28], a comparison with expected passing ratio and yield stress can be made in section 6.3.1 of this chapter. The results for dynamic properties (0 s of rest) are intentionally blank, as it is assumed that standard testing procedure was followed, thus, the experimental results have a minimum of 60 s of rest.

From table 6.2, it can be observed that a rest time has a minimal impact on the FT, and a slightly larger impact on the H2 reading. As with the Slump-flow test discussed in Chapter 5,

Table 6.2 L-box results for Mixes A-C, based on [74, 50]. Asterisk indicates flow did not reach end of horizontal section, and ceased to flow after the recorded time.

	0 Seconds		60 Seconds		240 Seconds	
	FT_0	$H2_0$	FT_{60}	$H2_{60}$	FT_{240}	$H2_{240}$
Mix A	-	-	3.1	90	3.3	80
Mix B	-	-	3	70	3.4	55
Mix C	-	-	6*	N/A	6.5*	N/A

the results from an L-box test can be correlated with rheology. Specifically, the passing ratio shows a weakly negative correlation with yield stress in [28]. Therefore, any change in yield stress should induce an notable reduction in passing ability of concrete. However, the difference in FT between 60 s and 240 s is negligible. Alongside investigating the physical effects of thixotropic flow around rebar, this work will also look to examine whether a negligible reduction in PL is also present in simulations.

6.2.3 Gravity Flow Box

Figure 6.2a displays the geometry used in the MPM simulations of the GFB. The MPM GFB geometry is a 600 mm tall, 37 mm deep and 190 mm wide box. It features a 50 mm, cuboid tremie pipe with a 30 mm wide opening at the base and a 30×30 mm square injection plane at the top. Some simulations will also feature horizontal reinforcement inserts spaced at 50 mm measuring $37 \times 5 \times 5$ mm and a $600 \times 10 \times 5$ mm vertical insert located at the centre of the horizontal rebars. There are minor differences between the experimental setup of the GFB and the geometry used in the MPM, namely, a slight reduction in width of 10 mm and a reduction in depth of 13 mm, however, these are not considered sufficient enough to alter the behaviour of the concrete.

The mesh itself is an eight point per cell, 5 mm hexahedron mesh. As with the L-box mesh, the optimum cell size is the largest size possible. In the GFB, the largest cell size corresponds to the width of the horizontal rebar, 5 mm. 64 points per cell resulted in large amounts of volumetric locking, whereas eight points per cell produced a low degree of locking for the chosen mix, irrespective of the degree of thixotropy.

The simulation starts with a concrete batch already present in the simulation, batch 1, filling the first 200 mm of the GFB, Figure 6.2a. The pipe is also full of concrete at the beginning of the simulation, as it must always remain charged when concrete is flowing [66]. The concrete present in the pipe at the start of the simulation is referred to as the Pipe batch. Once the simulation begins, batch 2 is injected at the top of the tremie pipe as empty cells arise due to

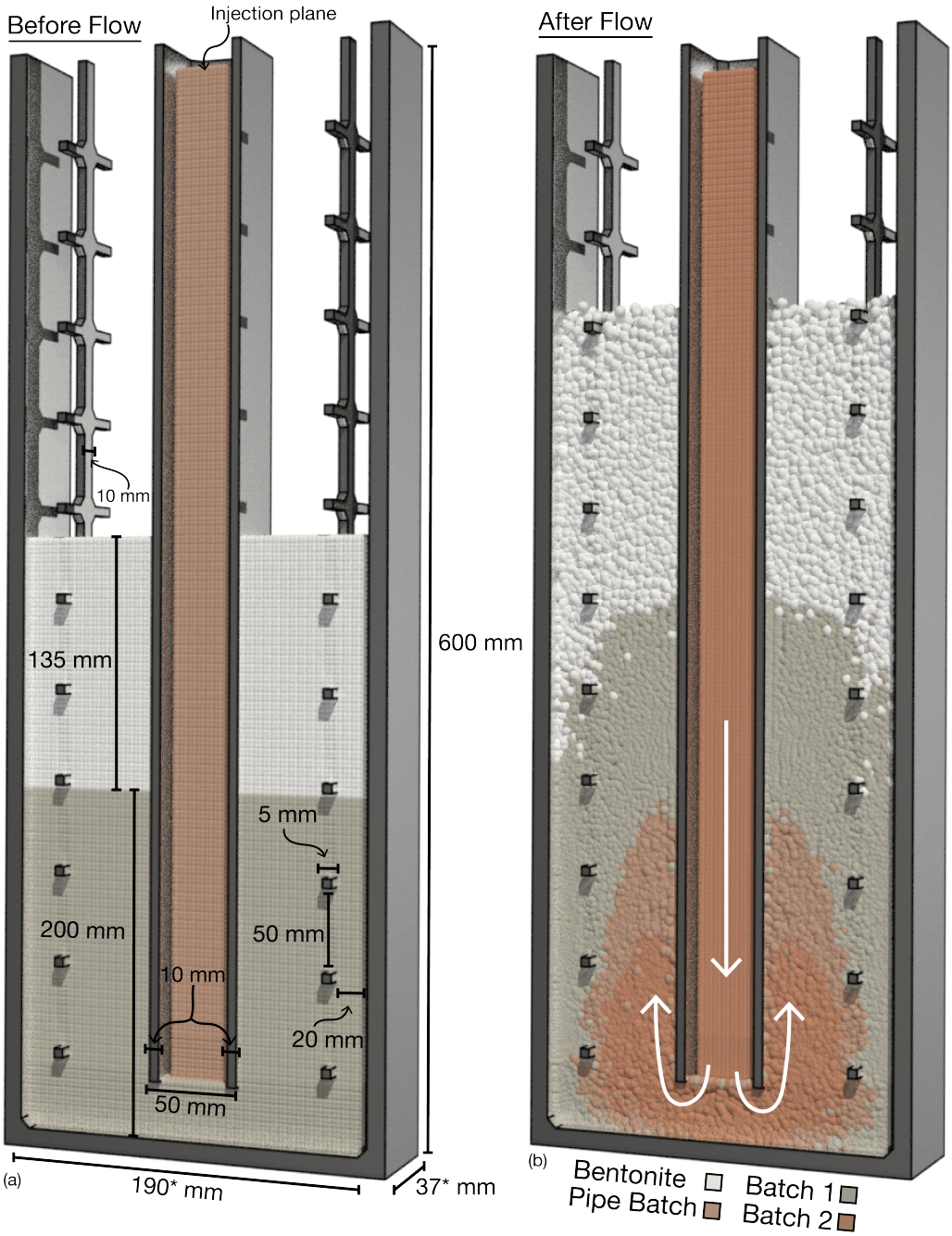

Fig. 6.2 a) Geometry of GFB in MPM simulations and starting position of concrete and support fluid. b) Final position of concrete and support fluid for a simulation with reinforcement inserts.

Table 6.3 Rheological properties of bentonite support fluid.

	$\tau_{0_{dynamic}}$ $[Pa]$	μ $[Pa \cdot s]$	$Density$ $[Kg/m^3]$	Poisson's Ratio	Young's modulus (E) $[Pa]$
Mix A	7	0.03	1075	0.49	1000

the downward flowing of concrete in the pipe. The replenishing of points into empty cells at the top of the pipe continues for 10 s.

Point injection within CB-Geo MPM operates on the condition that if a chosen cell is empty a specific number of points are injected at the Gauss locations in the cell. For the MPM GFB simulations, this takes the form of 8 points per cell to be injected when the cell is empty. It is also possible to prescribe a velocity to the points when they are injected. However, rather than adding an artificial velocity, as was the case with the CFD GFB simulations in Chapter 4, the injected points velocity is caused by the free-falling of the concrete through the pipe. This gives more freedom for velocity to fluctuate depending on the ability of one batch of concrete to displace another.

It was proposed in Chapter 2 that a flow-front differential (height difference between the concrete inside the cover zone and that closest to the pipe) could encourage concrete/support fluid interaction, as supported by [86]. Interaction, or mixing, of the concrete and support fluid creates a low strength cementitious layer called the interface layer. A small build up of an interface layer is typical and usually not cause for concern. However, if the flow-front differential is too large it is possible that a higher degree of concrete/support fluid mixing is possible. This gives rise to more opportunities for the material to become included into the foundation. A build up or inclusion of low-strength interface material could reduce the durability and strength capacity of the finished foundation [46]. Therefore, in some simulations a bentonite support fluid will be added to assess level of mixing. Table 6.3 details the Bingham properties used to represent the bentonite support fluid, obtained from rheometer testing of bentonite support fluid in [108]. The PR-Bingham model is used for the bentonite with all properties relating to thixotropy are set to zero. Although bentonite is known to be thixotropic, measurements of the A_{thix} over the short term were unavailable for this work. The zero values revert the PR-Bingham model to the Papanastasiou model, an appropriate representation of the bentonite support fluid. The same low m value of 5 is also used for the support fluid to reduce volumetric locking.

The second objective of this chapter is to understand how thixotropic behaviour influences the flow of concrete in a deep foundation. Thus, an analysis of thixotropic concrete must

be undertaken in pile-like conditions. To do this, a series of comparisons will be made on a system of eight simulations arising from 6 options. The 6 possible options are:

1. With Reinforcement (R)
2. No Reinforcement (NR)
3. With Support fluid (S)
4. No support fluid (NS)
5. With thixotropy (T)
6. No thixotropy (NT)

In accordance with the options presented, the eight simulations to be conducted are presented in table 6.4.

Table 6.4 Table of showing the conditions of each MPM GFB simulation.

Simulation	Option					
	R	NR	S	NS	T	NT
1		✓		✓		✓
2		✓		✓	✓	
3		✓	✓			✓
4		✓	✓		✓	
5	✓			✓		✓
6	✓			✓	✓	
7	✓		✓			✓
8	✓		✓		✓	

One mix will be investigated in the MPM simulations of the GFB. This mix corresponds to Mix A in table 6.1. If the simulation requires the addition of thixotropy, a rest time of 240 s is added to both the concrete already in place at the start of the simulation (batch 1) and the concrete already in the pipe (Pipe batch). If the simulation requires support fluid, 135 mm is added atop batch one at the start of the simulation. Depending on the choice of starting conditions, simulations typically start with approximately $100,000$ points, and end with approximately $350,000$ points after 10 s of point injection.

6.3 Results

6.3.1 L-box

The results for each Mix are presented as Mix A, B and C for 0 s rest, Mix A60, B60 and C60 for 60 s rest, and Mix A240, B240 and C240 for 240 s rest.

Figure 6.3 shows the three-dimensional, isometric view of the concrete flow in the simulated L-box test, where no rest time has been added to the concrete. Three time intervals are presented, 1 s of flow time, the time the flow reached the end of the horizontal section, and 20 s, the end of the simulation.

In fig. 6.3, Mix A, a highly viscous but low yield stress concrete, has an FT of approximately 3.2 s. At 1 s of flow time, there exists some grooves caused by the flow of concrete passing around the reinforcement bars, however, they are no longer present once the flow has reached the end of the section. By 20 s of flow time, the flow has all but levelled out, with only 12 mm difference between the measured H1 and H2. Mix B, a low viscosity and low yield stress concrete, has slightly faster FT than Mix A, of 3 s. This is to be expected given the hypothesis described in Chapter 2 that viscosity can influence the rate at which concrete spreads. Mix B also shows some flow grooves caused by spreading around reinforcement bars that are no longer seen once the flow reaches the end of the horizontal section. The observed H1 and H2 measurements for Mix B are now notably different, with a 20 mm difference. Although Mix A and B have similar H2 values, there is likely an overestimation of H2 for Mix B due to some slight point separation. Finally, Mix C, a medium viscosity but very high yield stress concrete, has a FT of 8 s. This is considerably slower than the other mixes. At 1 s the flow front (the leading front of the flow) is somewhat further back than the other mixes, as is expected. Additionally, indentations caused by blocking present at 1 s are no longer present once the flow has reached the end. Finally, the difference between H1 and H2 at 20 s is over three times larger than Mix B.

Figure 6.4 presents the time evolution of the flow of concrete in the horizontal section in terms of the Distance From End (DFE) for each Mix. The DFE represents how far from the end of the horizontal section the flow is, at a given time. This value ranges from 600 mm, at the start of the simulation, to 0 mm once the flow has reached the end of the section. Also plotted in fig. 6.4 is the time at which the physical DFE reached 0 mm. For a rest time of 0 s the 60 s values from table 6.2 are overlain, as true 0 s physical values are unavailable. For Mix A, the DFE reaches 0 mm at approximately 3.2 s, just 0.1 s faster than the physical result for 60 s. Similarly, the DFE for Mix B reaches 0 mm at the same time as the physical result, 3 s. Conversely, the physical DFE for Mix C never reached 0 mm, instead reaching 100 mm

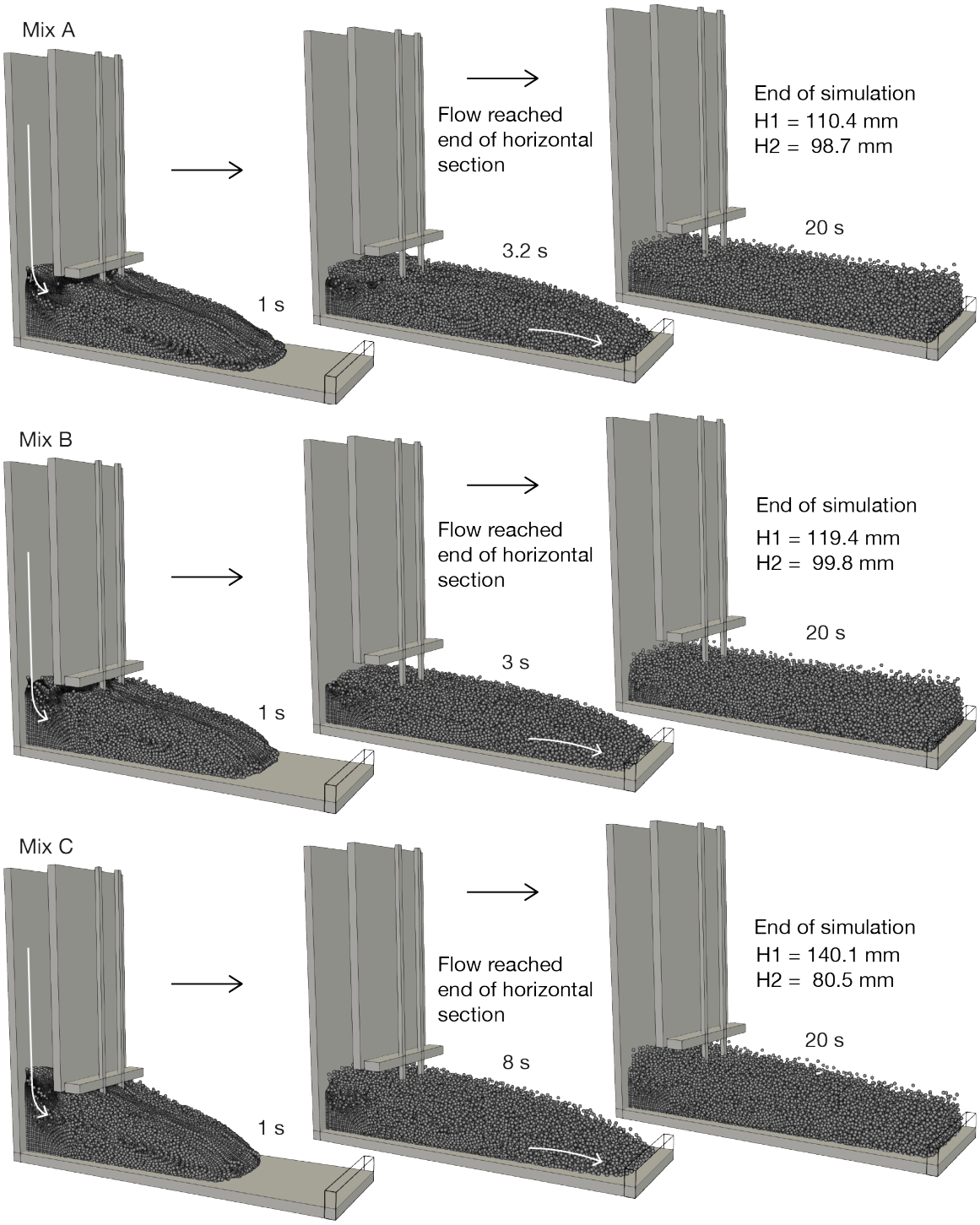

Fig. 6.3 Three-dimensional, isometric view of the concrete flow in the L-box test for Mix A, B and C with a rest time of 0 s.

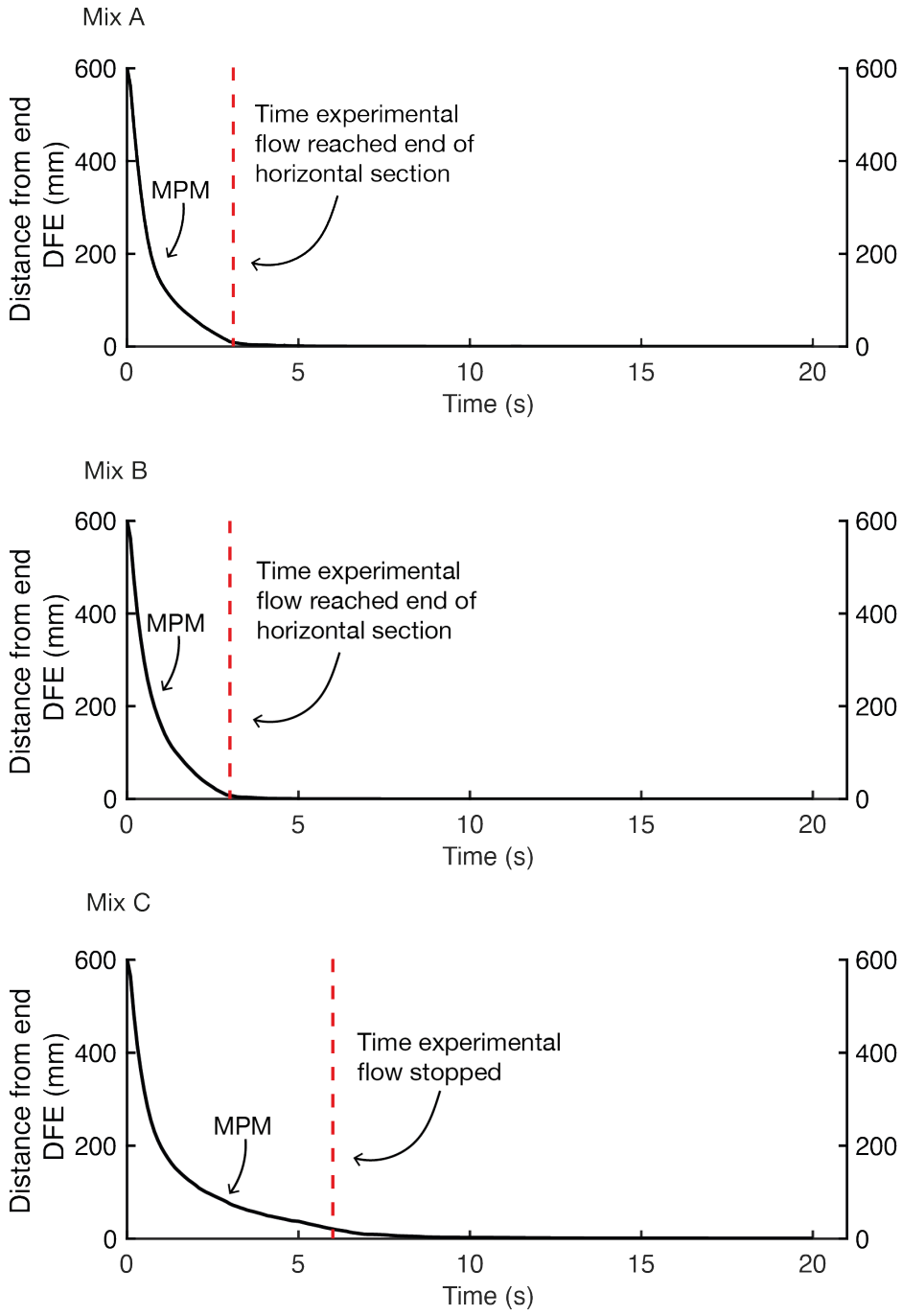

Fig. 6.4 Plots of Distance from end (DFE) over time for Mix A, B and C for a rest time of 0 s.

before the flow stopped. The simulated Mix C, however, did reach the end of the section, at approximately 8 s.

Moving onto the passing ratio, fig. 6.5 presents the H1 and H2 measurements over time for each Mix, after no rest period, with the physical H2 for 60 s rest plotted also. Additionally, the passing ratio is also presented alongside the static yield stress (the starting elevated yield stress after a period of rest). The passing ratio is calculated at the end of the simulation. For Mix A, the physical and experimental results are very similar at the end of the simulation, whereas the measured H2 is lower than the simulated for Mix B. For Mix C, the physical result did not reach the end of the section, thus, no physical H2 is measured.

As is expected, the simulated 0 s rest and physical 60 s rest measurements are close, however, there are some significant differences, especially concerning Mix C. It is reasonable to assume that some degree of thixotropy must be present in the concrete of the physical tests to account for why Mix C did not reach the end of the flow box. Additionally, a lack of any thixotropy could account for why the simulated H2 for Mix B is notably higher than the physical test, indicating a low degree of obstruction by the rebar.

Figure 6.6 shows the three-dimensional, isometric view of the concrete flow in the simulated L-box test, where 60 s of rest time has been added to the concrete. Three time intervals are presented, 1 s of flow time, the time the flow reached the end of the horizontal section, and 20 s, the end of the simulation.

In fig. 6.6, Mix A60, has a FT of 9 s. This is almost 3 times slower than Mix A. Likewise, Mix B60 reaches the end of the horizontal section at 10 s, over three times slower than Mix B. As with the extended flow-time, the difference between H1 and H2 also increases for Mix A60 and Mix B60. For Mix C60, the flow no-longer reaches the end of the horizontal section. The asterisk on Mix C60 H2 indicates the depth of the concrete up to 100 mm from the end of the horizontal section. Indentations caused by the flow around reinforcement bars seen at 1 s of flow-time are no longer present at the end of the simulation. Although it is worth noting that the grooves caused by flow around the reinforcement bars are slightly more pronounced in Mix C60 than Mix C.

Figure 6.7 presents the time evolution of the DFE over time for each 60 s Mix. The most obvious difference between the simulated and physical result for both Mix A60 and Mix B60 is the longer time taken to reach the end, than in the physical test. The physical test for Mix C was reported to reach no further than a DFE of 100 mm, reaching that point at 6 s. The simulated Mix C60 did surpass this point, however, it did not reach a DFE of 0 mm, even after 20 s of flow-time.

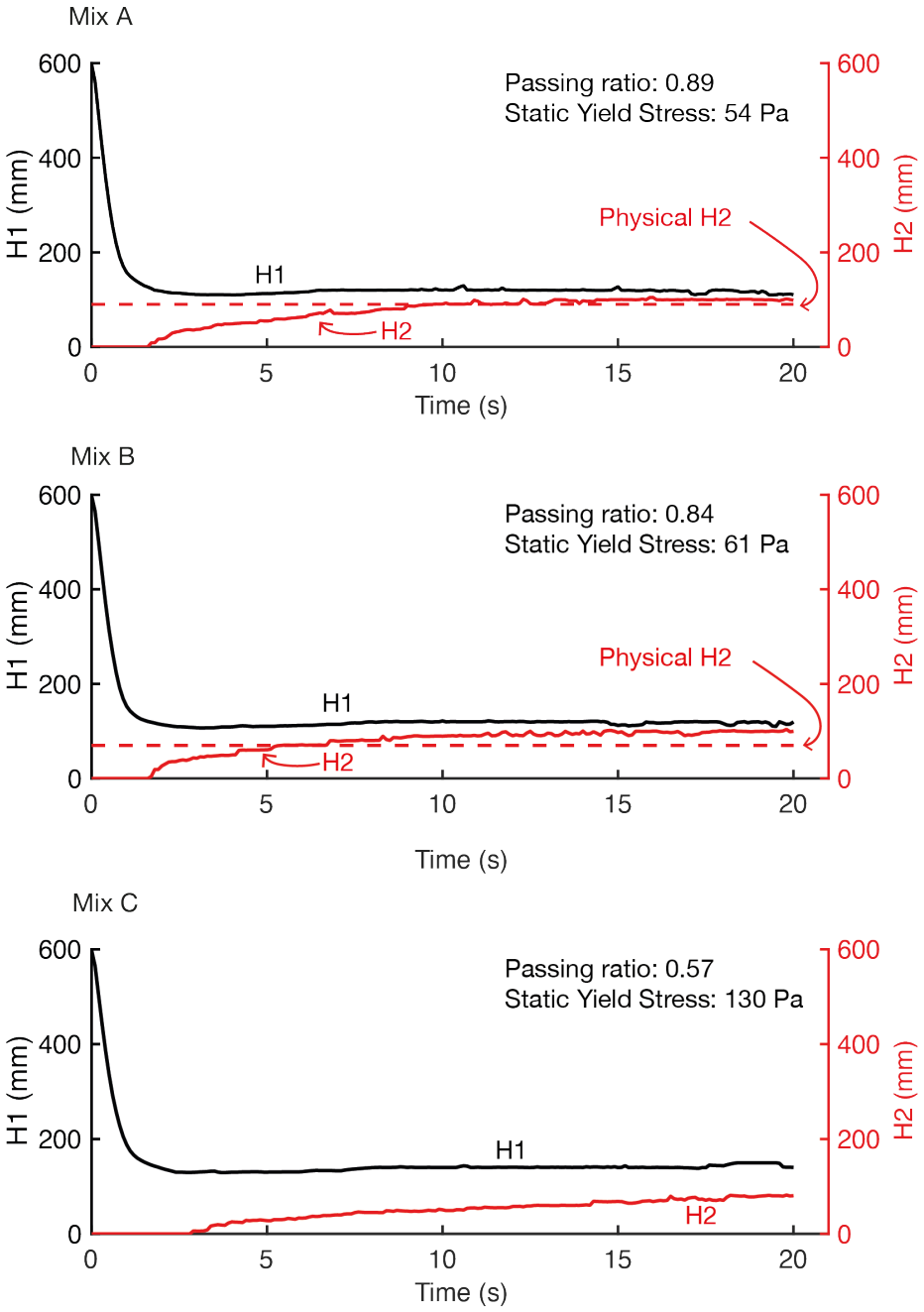

Fig. 6.5 Plots of H1 and H2 for Mix A, B and C for a rest time of 0 s.

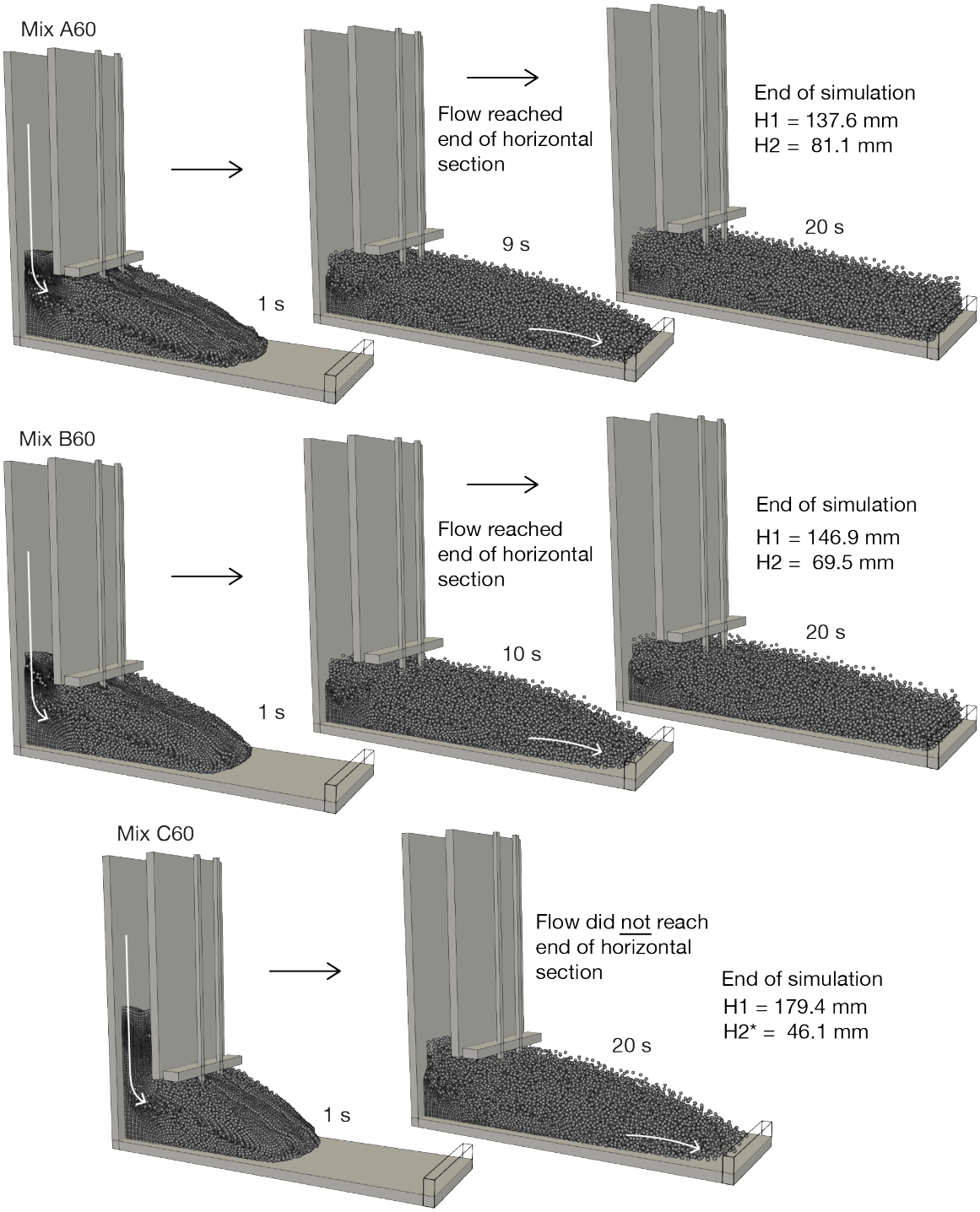

Fig. 6.6 Three-dimensional, isometric view of the concrete flow in the L-box test for Mix A60, B60 and C60. * Indicates flow did not reach end of horizontal section.

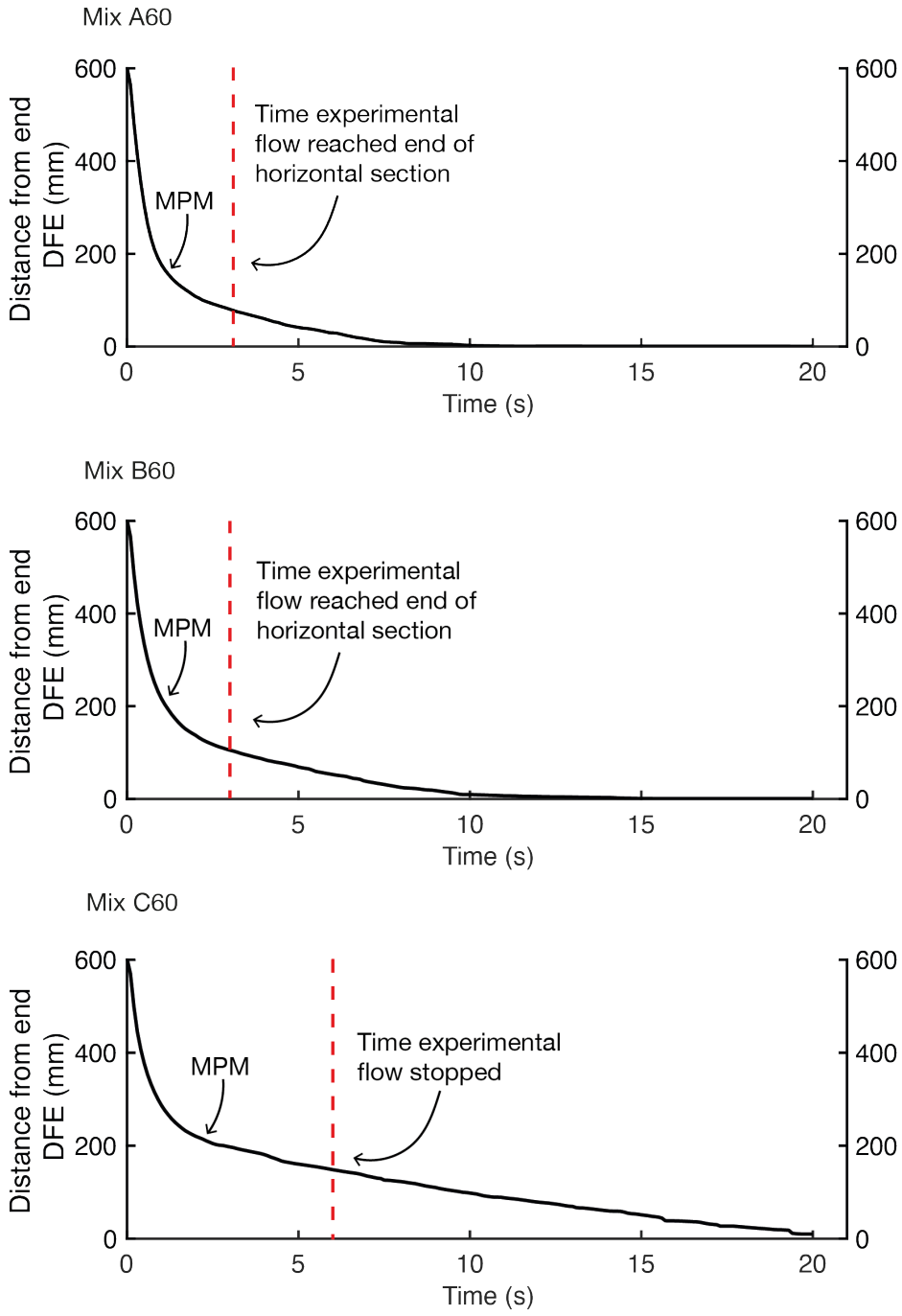

Fig. 6.7 Plots of Distance from end (DFE) over time for Mix A60, B60 and C60.

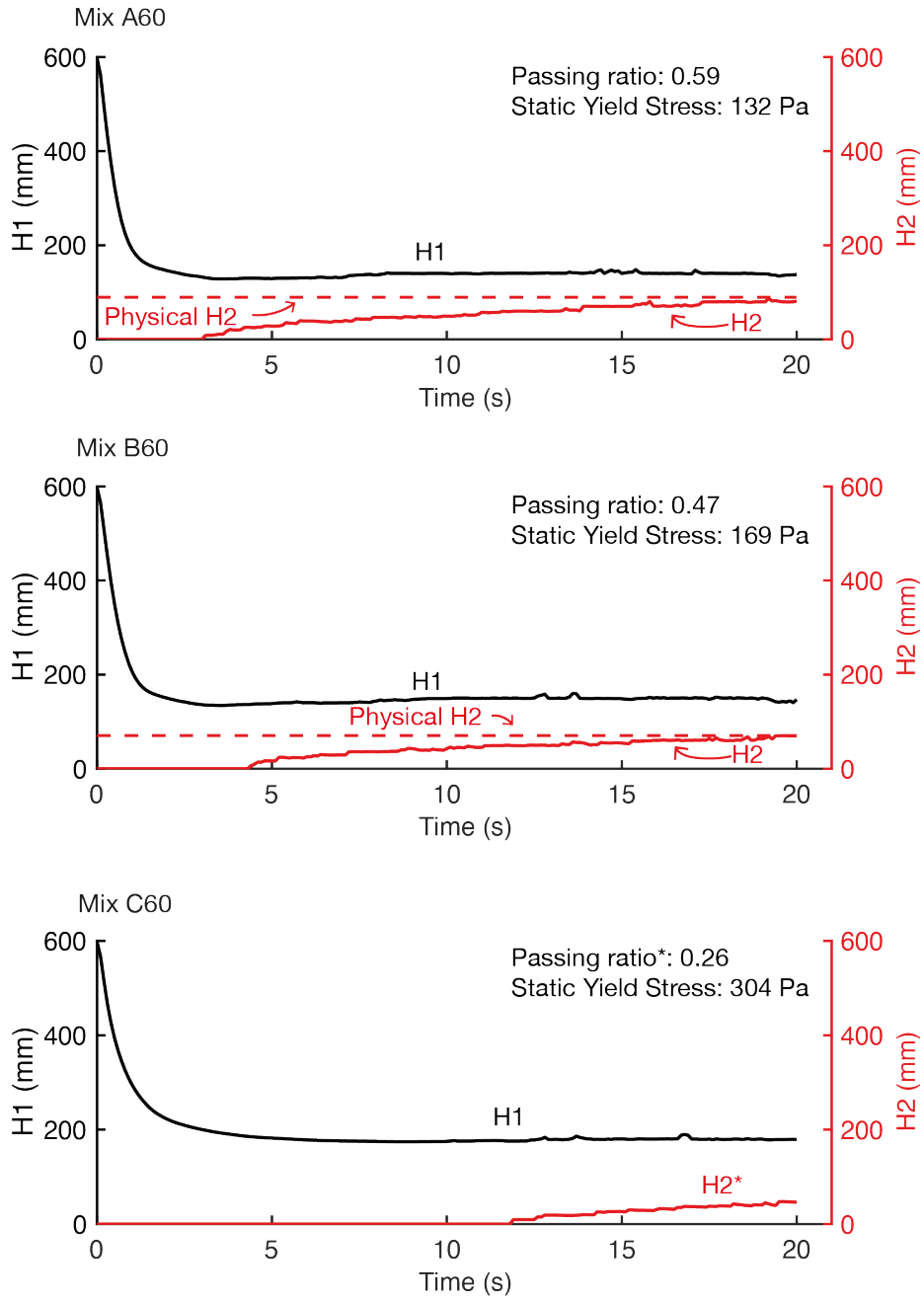

Fig. 6.8 Plots of H1 and H2 for Mix A60, B60 and C60. * Indicates flow did not reach end of horizontal section.

The differences between simulations and physical results for 60 s of rest are less prominent when looking at the passing ratios for Mix A60, B60, and C60. For Both Mix A60 and Mix C60, the H2 measurements at the end of the simulations are very close to the physical result, suggesting a good degree of agreement in the final geometry of the physical and simulated cases. Mix C60 does present a H2* indicating there was a maximum depth of 46 mm, 100 mm away from the end the horizontal section.

The results from Mix A60, B60 and C60 are in agreement in some areas, like the H2 depth (and presumably the passing ratio), however the FT results do appear to be quite different. It is difficult to determine the exact level of thixotropy present in the physical test, given the procedure of filling the L-box will differ each time. However, there is likely a point somewhere between 0 s of rest and 60 s where the difference between results from simulations and physical is less pronounced.

Figure 6.9 shows the three-dimensional, isometric view of the concrete flow in the simulated L-box test, where 240 s of rest time has been added to the concrete. Two time intervals are presented, 1 s of flow time and the end of the simulation, 20 s.

In fig. 6.9, none of the three mixes reaches the end of the horizontal sections, indicating that the increased rest time has heavily influenced the workability of the simulated concrete. Although there are products of blocking present for Mix A240 and B240 at 1 s, like grooves or indentations, they are no longer present at the end of the simulation. Mix C240 has not yet passed the bars at 1 s, and products of poor flow around reinforcement bars are not present at the end of the simulation.

Comparing the time evolution of the DFE for each 240 s Mix in fig. 6.10 reveals the extent at which thixotropy influences the simulated concrete. Mix A240 does not reach the end of the section, however the physical result reached the end at 3.3 s. A similar observation can be made regarding Mix B240, which also failed to reach the end of the section while the physical concrete reached the end at 3.4 s. Mix C240 also did not reach the end of the section, much like it's physical counterpart. However, it was reported that the physical mix did not flow past 6.5 s, which is in contrast to the simulated concrete.

The same difference observed between the simulated FT and physical FT for Mixes A240, B240 and C240 is also represented in the passing ratio. As both 240 s physical mixes reached the end of the section in the physical test, there is a measured H2 value to be compared against. Conversely, although the simulated mixes flowed to within 100 mm of the end of the horizontal section, the measured H2 was very low. This is also reflected by the passing ability ratio, where Mix A240 has reduced from 0.59 to 0.19 with only 180 s of additional rest time.

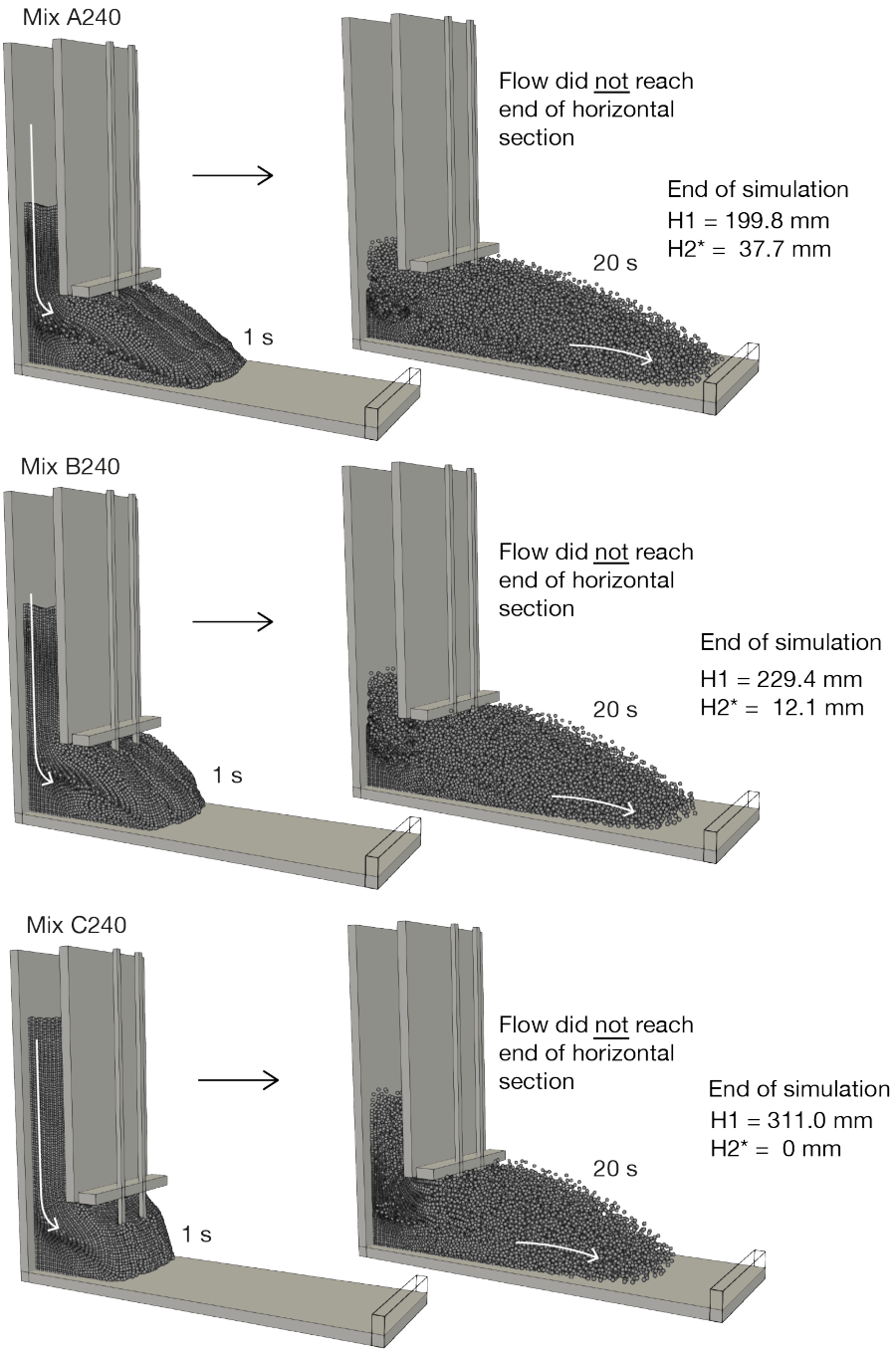

Fig. 6.9 Three-dimensional, isometric view of the concrete flow in the L-box test for Mix A240, B240 and C240. * Indicates flow did not reach end of horizontal section.

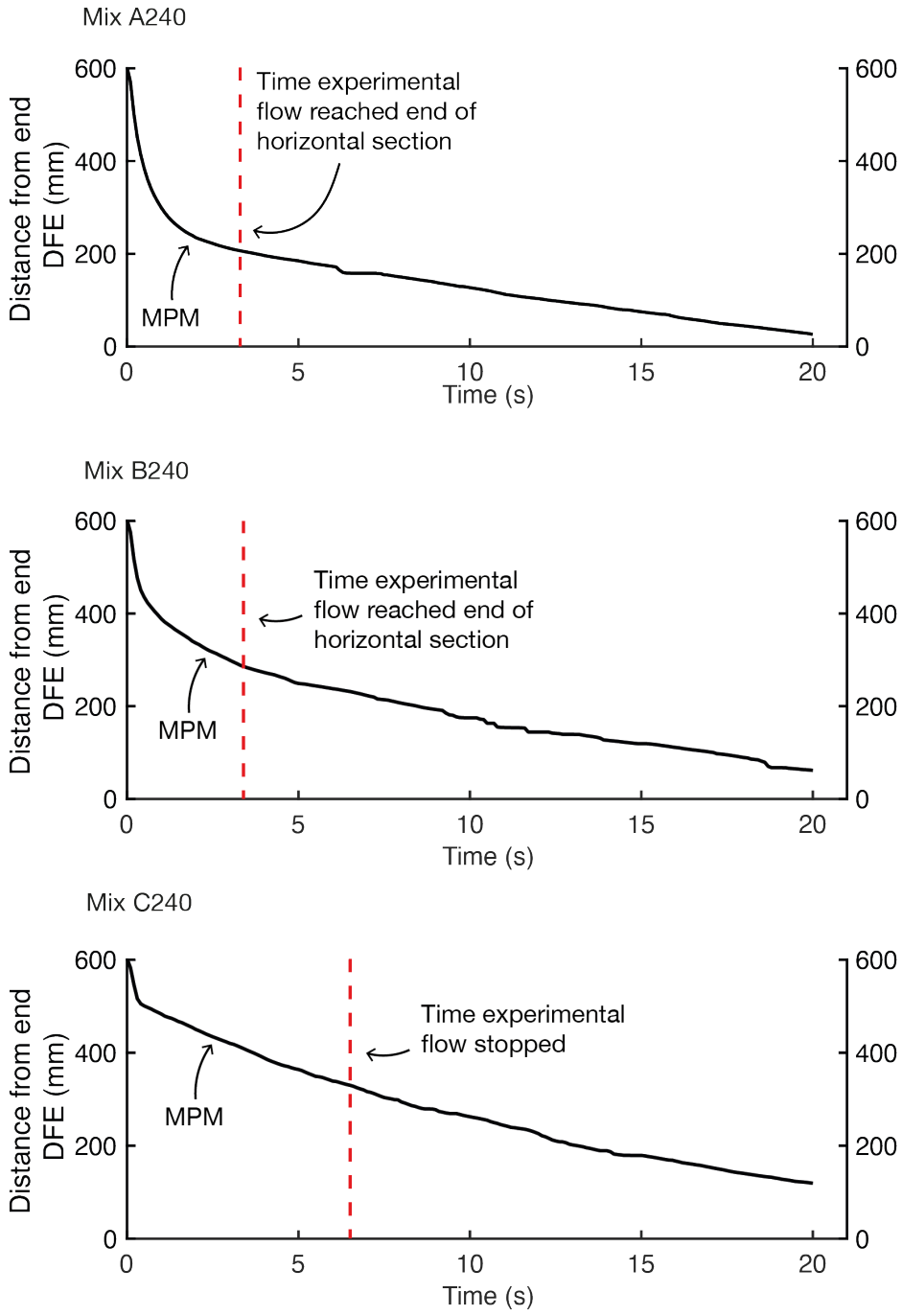

Fig. 6.10 Plots of Distance from end (DFE) over time for Mix A240, B240 and C240.

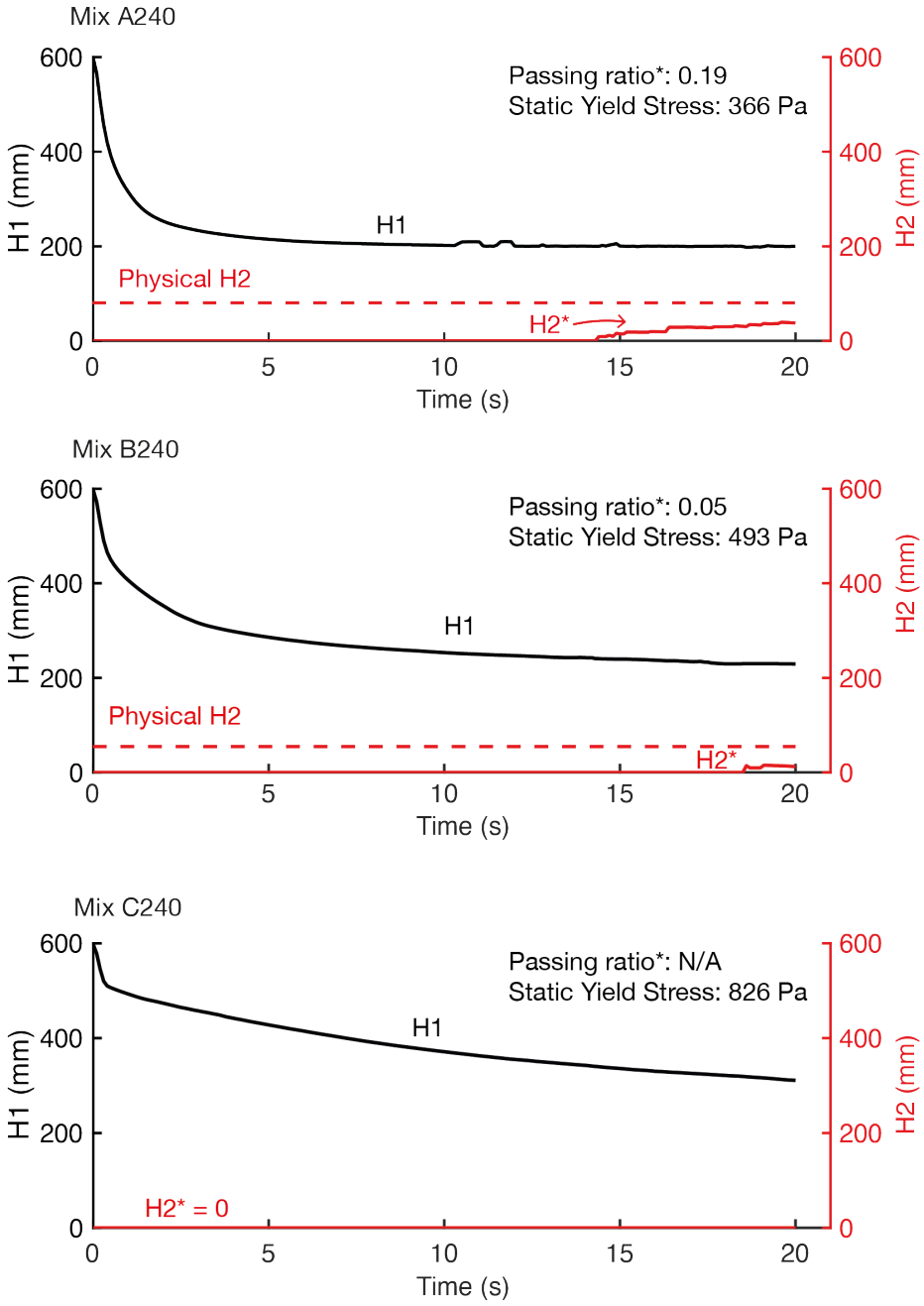

Fig. 6.11 Plots of H1 and H2 for Mix A240, B240 and C240. * Indicates flow did not reach end of horizontal section.

As was the case with Mix A240, Mix B240 also notes a significant drop in passing ability ratio between 60 s and 240 s of rest, reducing from 0.47 to 0.05. As neither the simulated or physical Mix C240 reached the end of the section, no passing ability ratio can be compared.

In the outset of this work, the method for calculating α was defined. It was also expressed in Chapter 5 how important α is when calculating the correct rate at which thixotropy will dissipate in a concrete. For all simulations thus far, an alpha of 0.01 was used. Increasing this value will reduce the amount of time required to dissipate thixotropy, effectively speeding up the rate at which thixotropy dissipates. In terms of concrete behaviour, this would reduce the yield stress of the concrete in a shorter time-frame, leading to a faster FT and higher PL. To examine this effect, a simulation of Mix A240 was performed using an α of 0.03. A comparable simulation was performed on Mix A in Chapter 5 where the SF_{240} simulation was re-run with a higher α. The result was a decrease in the average level of thixotropy present in the simulated concrete at the end of the simulation, but overall it did not influence the final spread. In the case of the L-box test, there was also a difference in average level of thixotropy present at the end of the simulation between two simulated concretes of differing α's.

Figure 6.12a shows the change in mean λ, the thixotropy parameter that effects yield stress, for Mix A240 for an α of 0.01 and 0.03. The difference in mean λ remaining is approximately 1. This is difference is approximately 0.2 higher than the Slump-flow test, suggesting higher, or more sustained, shear rate is present in the L-box test than the Slump-flow test. Nevertheless, the difference in the behaviour of the DFE over time is very small, fig. 6.13c.

As previously discussed, the differences in shear rate in L-box test are likely to be higher than the Slump-flow test. This is partially due to the interaction with the rebar in addition to the faster and thicker flow, leading to a higher shear rate. Figure 6.13b presents the difference in mean shear rates for Mix A240 (L-box) and the results from Slump-flow simulation SF240 that use the same input parameters. The most important feature of this graph is that although the peak shear stresses are higher in the Slump-flow test, they dissipate more rapidly than the L-box test. This results in more shear-stresses being exerted on the concrete in the L-box test than in the Slump-flow test. In turn, this leads to a greater reduction in thixotropy present in the material.

The disparity between physical and simulated L-box results was expected, given the same differences are observed in thixotropic simulations of the Slump-flow test. It was proposed in Chapter 5 that some physical process not accounted for in the simulation could be changing. One hypothesis suggested that during the extended rest, the frictional boundary condition

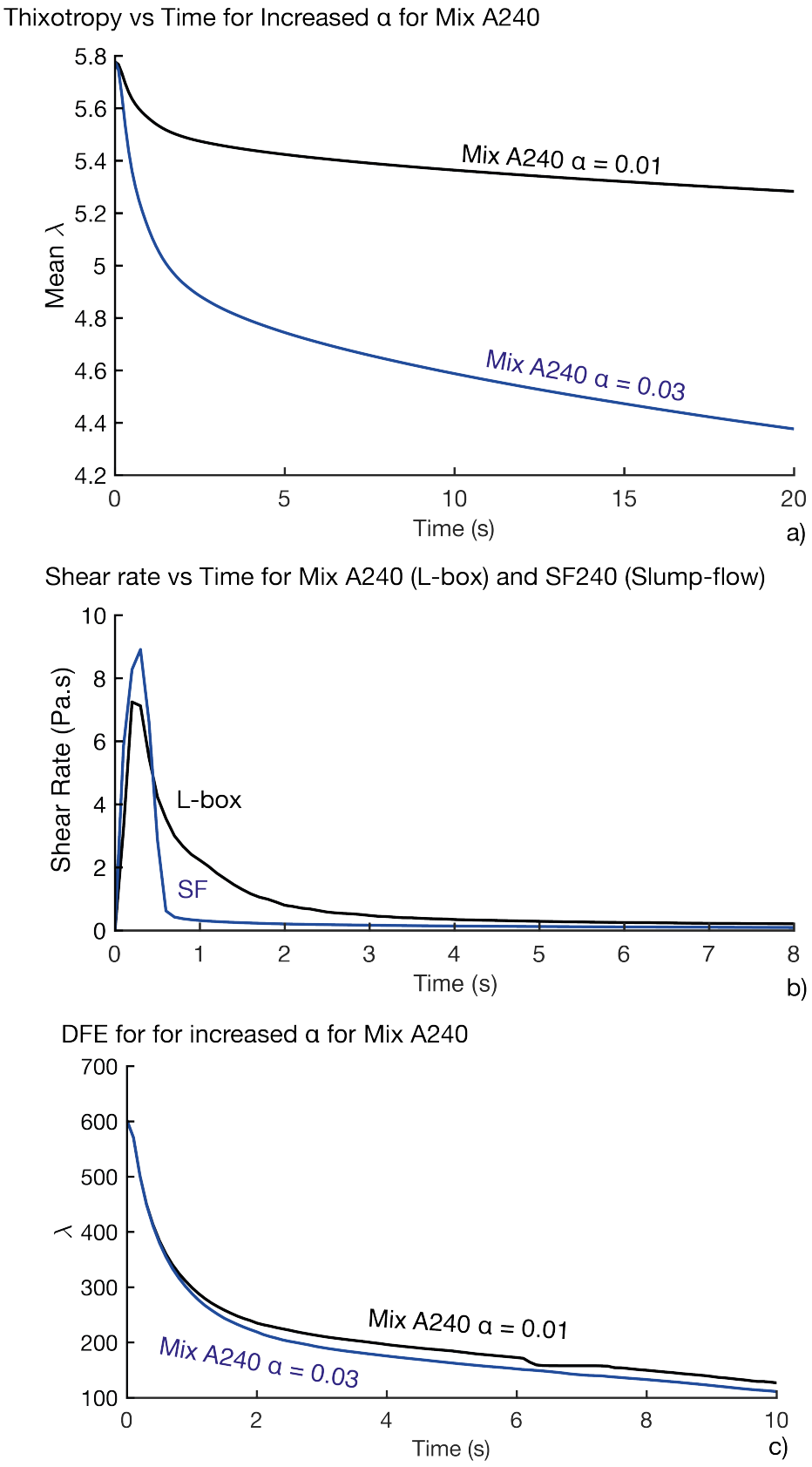

Fig. 6.12 a) Comparison of mean λ for $\alpha = 0.01$ and $\alpha = 0.03$. b) Comparison of shear rate for L-box test and Slump-flow test (SF). c) Comparison of DFE over time for $\alpha = 0.01$ and $\alpha = 0.03$.

changed, resulting in a lower coefficient of friction (FC). This could be due to de-watering (early onset of concrete bleed) or another process. Bouharoun [22] demonstrated friction stresses decrease with an increase in plastic viscosity, thus, FC decreases with increasing plastic viscosity. If the plastic viscosity of the concrete were to increase, along with the yield stress, then it is possible the friction coefficient would also decrease. A similar effect may also be possible if the volume of paste changes by way of more CSH bridges forming between cement particles during the chemical processes that lead to thixotropy.

Figure 6.13a is the time evolution of the DFE for Mix A240 with two different FC values, the calibrated value based on the dynamic properties of Mix A, 0.35, and an estimated value that gives a close approximation to the physical result of Mix A resting for 240 s, 0.15. This represents a significant decrease in FC, and would require experimental evidence to validate. What can be seen in Figure 6.13a is a reduction in FT which brings the lower-friction simulated concrete in-line with the physical results. The passing ratio and H2 measurements for the low-friction concrete are presented in Figure 6.13b are also closer to the physical result. Based on the significant effect friction has on the final result, it is recommended that future work on simulated, time-dependent concrete behaviour should focus on the time-dependency of boundary friction.

The objective of analysing concrete flow in the L-box test was to determine the effect concrete thixotropy has on the ability of concrete to flow around reinforcement bars. From a simulation standpoint, thixotropy has a significant influence on the ability of concrete to flow in the L-box test. Figure 6.14a compares the relationship between yield stress and passing ratio in the simulated concrete (MPM) and the results from experimental analysis conducted by Chamani et al. [28]. Although the range in yield stresses in Chamani et al. [28] is smaller than the simulated concrete, similar trends are identified. However, it is worth noting that only a slight trend is visible in the Chamani et al. [28] data set. Nevertheless, this provides supporting evidence that increasing yield stress should decrease the passing ability of concrete, as is seen in the simulations but not the thixotropic concrete data provided in [74, 50]. In terms of the objective to identify how thixotropy could influence the passing ability of concrete, fig. 6.14b shows how each concrete mixed changed over time, and the passing ratio associated with the change in yield stress caused by thixotropy. Thus, it is reasonable to state that if all other conditions (friction) remain constant, then thixotropy will reduce the ability of concrete to flow around reinforcement bars.

The results from the GFB presented in the following section aims to test this hypothesis in conditions closer to a deep foundation.

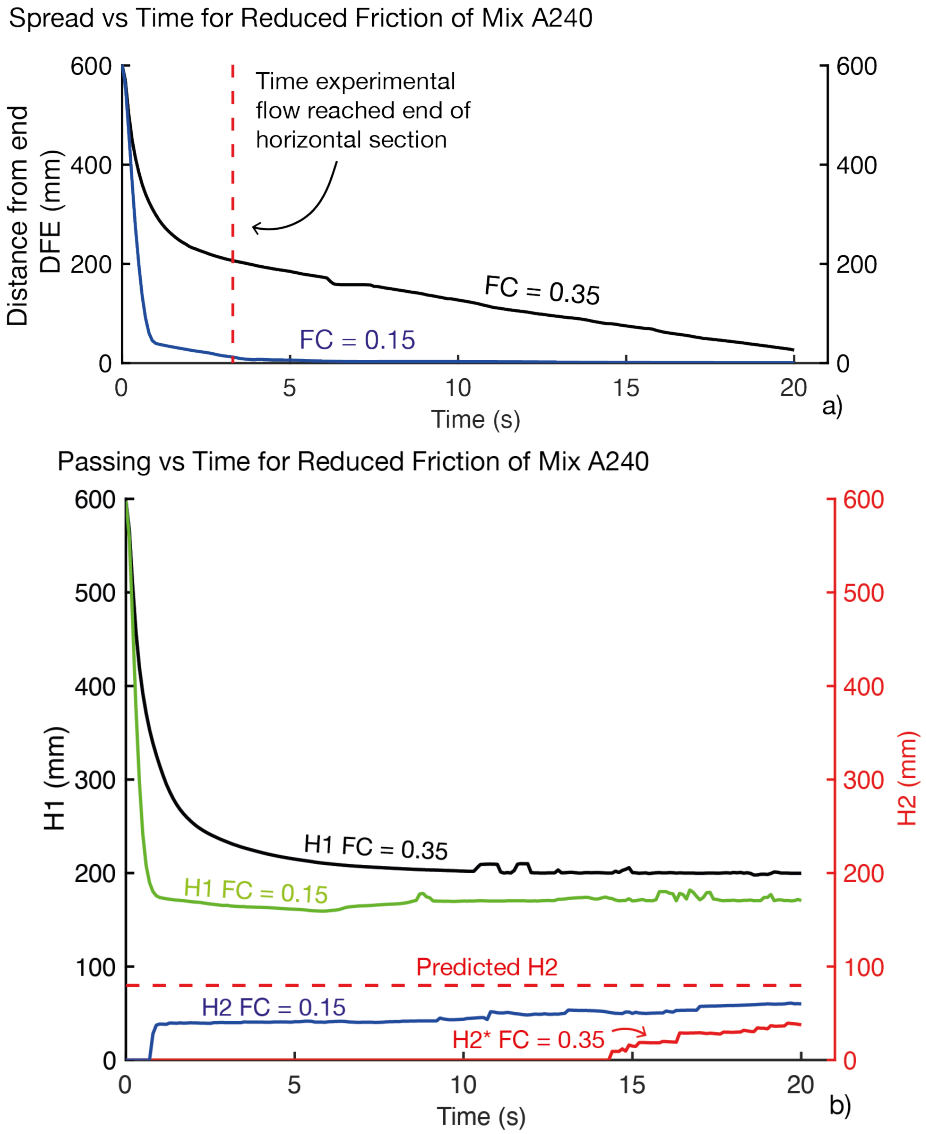

Fig. 6.13 a) Comparison of DFE over time for normal friction and lowered friction simulations. b) Comparison of passing ability for normal friction and lowered friction simulations. * Indicates flow did not reach end of horizontal section.

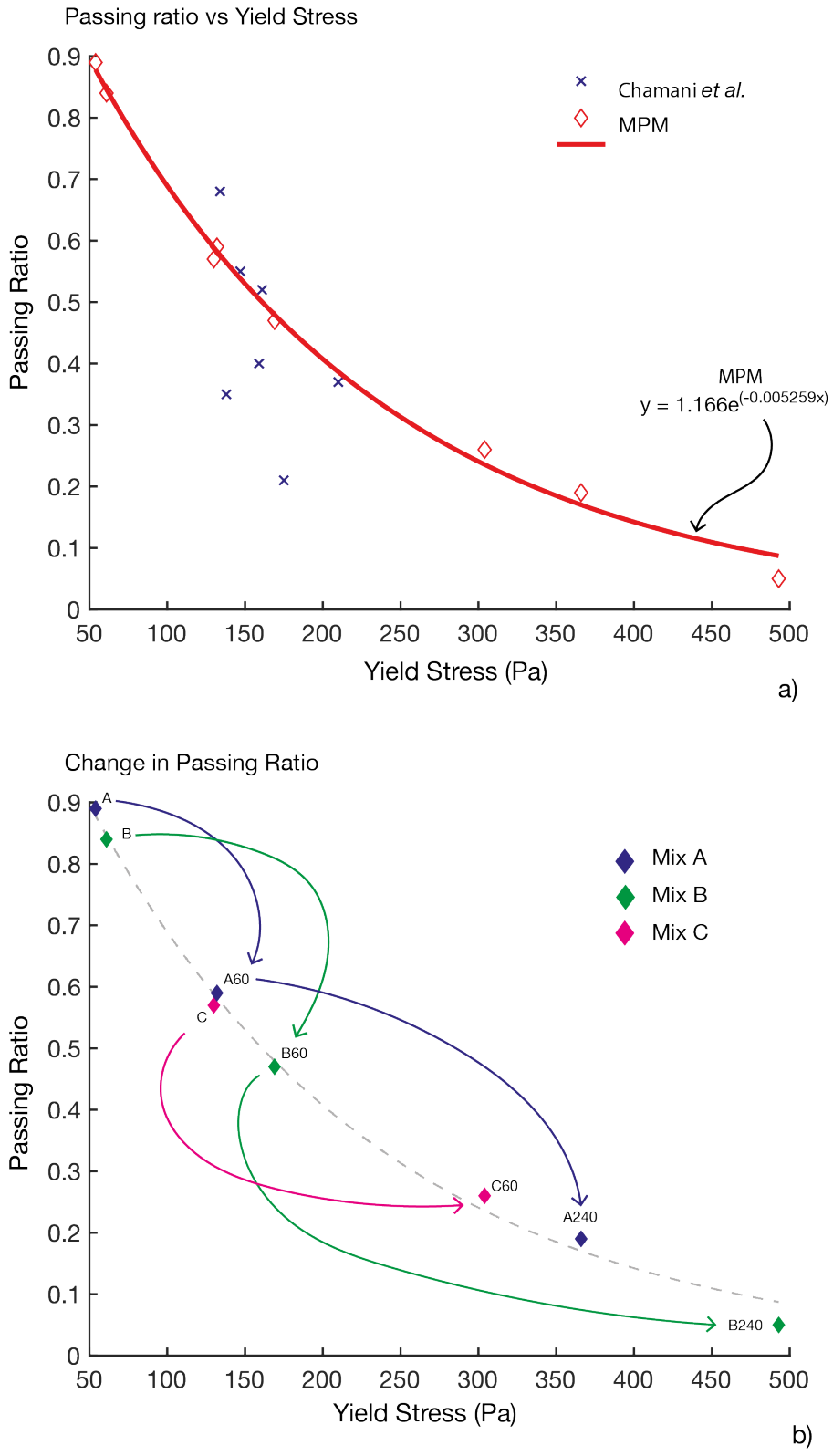

Fig. 6.14 a) Correlation of passing ratio and yield stress for MPM simulations and experimental results of Chamani et al. [28]. b) Evolution of passing ratios in MPM simulations for Mix A-C.

6.3.2 GFB

Figure 6.15a-d shows the results from Simulation 1, each image depicts a slice through the centre of GFB at time intervals of $0, 2, 6$ and 10 s. Simulation 1 is a no rebar, no support fluid, no thixotropy simulation of the GFB in MPM. The simulation starts with 200 mm of batch 1 in-place and a pipe full of the pipe batch. As the simulation starts, the pipe batch begins to flow downwards, initiating an injection of points of batch 2 in the now empty cells at the top of the pipe. The flow initially flows horizontally before beginning to flow vertically. After 2 s, fig. 6.15b, the entirety of the pipe batch has been displaced, and batch 2 is now flowing into the box. The general trend of the flow is moving vertically, with some horizontal spreading. By 6 s, fig. 6.15c, batch 1 is now bisected into a larger portion at the front of the flow, and a small portion in each of the lower corners. At 10 s, fig. 6.15d, batch two has now moved almost to the side edges of the GFB, and has displaced both the pipe batch, and batch 1 vertically. The flow front of the pipe batch appears to be slightly rounded, however, the flow front of batch 1 appears to be relatively flat.

For comparison, fig. 6.15e-h represents time interval slices for Simulation 2. Simulation 2 is also a no rebar, no support fluid simulation, however, thixotropy is now present in the simulation by way of a 240 s rest period added to both batch 1 and the pipe batch. As with simulation 1, the flow of the secondary batches in Simulation 2 begins by spreading horizontally before starting an upward trend, finally, by 10 s, fig. 6.15h, it has displaced batch one into a large upper portion and two smaller portions in the lower corners. Despite the behavioural similarities, the key difference between the two simulations is the shape of the secondary batches. In Simulation 1, the secondary batches form a rounded flow front, whereas the flow front of the secondary batches in Simulation 2 forms an arrowhead shape with steep sides converging to a point at the front of the flow. Interestingly, the flow front of batch 1 appears to be much the same in both Simulation 1 and 2, suggesting little operational differences would occur due to thixotropy in this scenario. It is worth noting, however, a slight difference in natural flow rate (the rate of flow in the pipe is governed by the injection of points into empty cells, rather than a prescribed velocity) with Simulation 2 having a slightly slower flow rate than Simulation 1. This is evident by the slightly lower volume of batch 2 present at 2 s. The implication being that thixotropy is reducing the rate at which concrete can flow into the box, due to the added stress required to overcome the elevated yield stress in the thixotropic concrete.

The addition of 135 mm of support fluid to Simulation 1 and 2 results in Simulation 3 and 4 respectively. Figure 6.16a-d shows the results from Simulation 3, and fig. 6.16e-h shows the results from Simulation 4. Starting with Simulation 3, the flow behaviour of the secondary

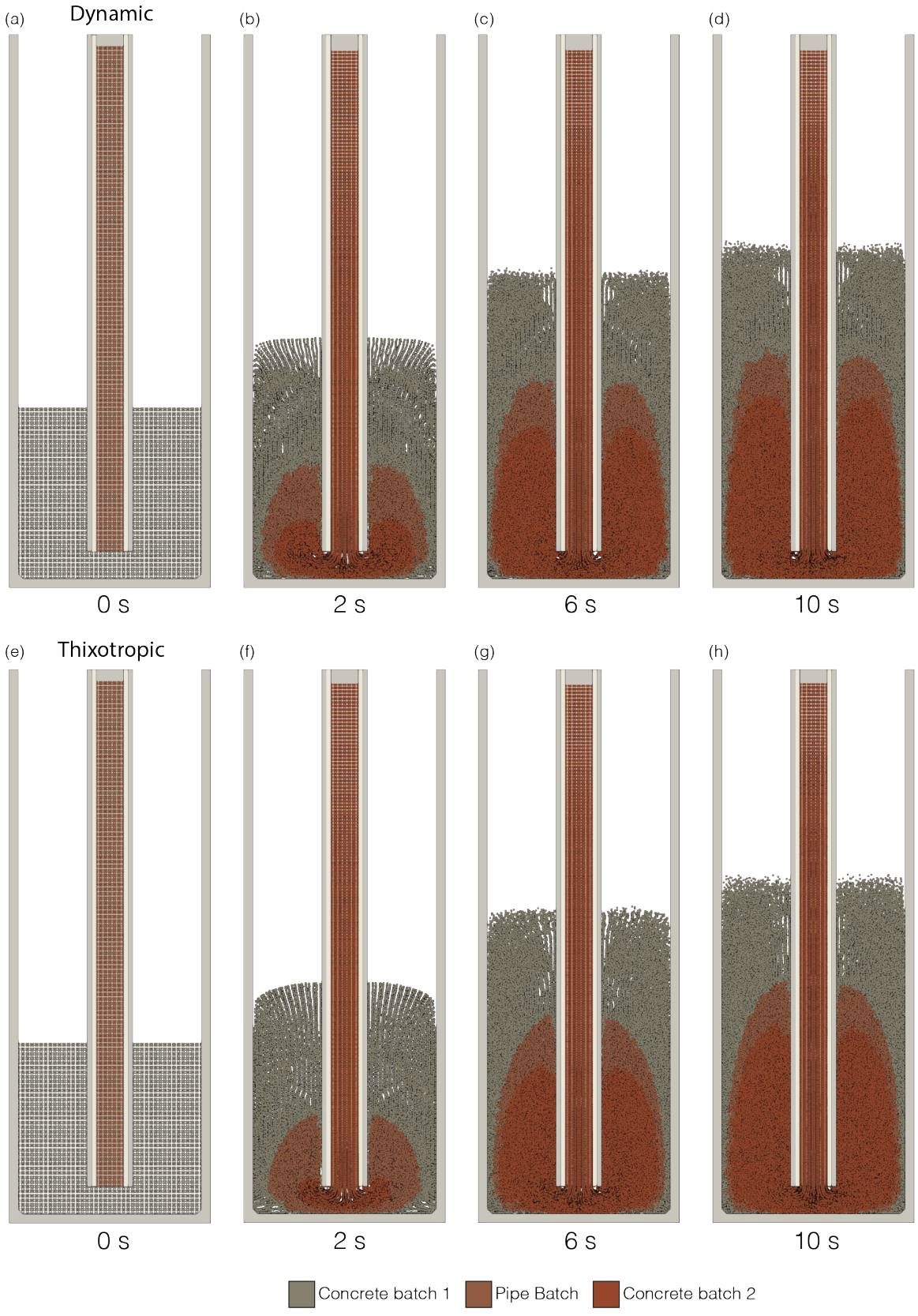

Fig. 6.15 a)-d) Shows the evolution over time of the flow pattern of Simulation 1. e)-h) Shows the evolution over time of the flow pattern of Simulation 2.

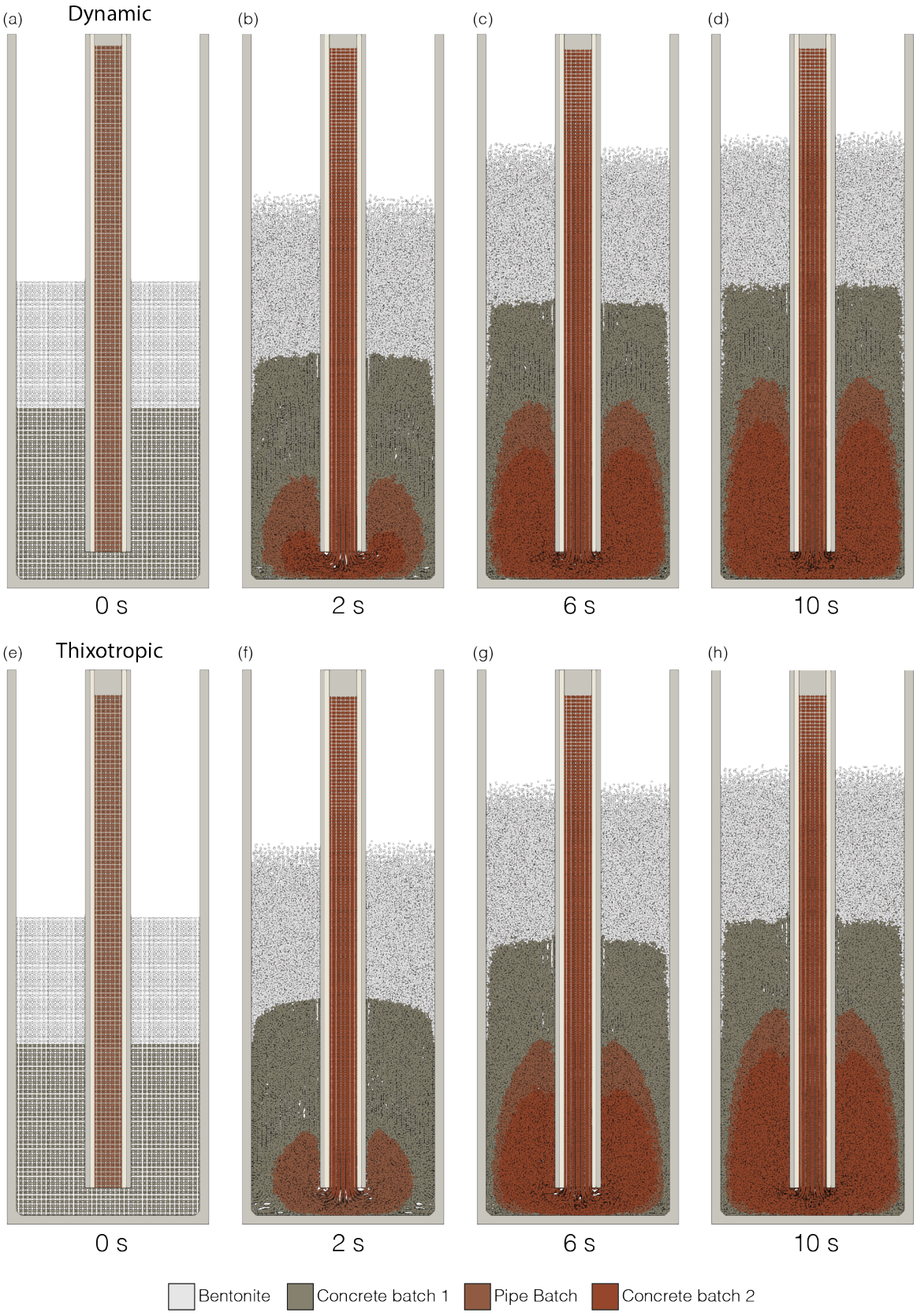

Fig. 6.16 a)-d) Shows the evolution over time of the flow pattern of Simulation 3. e)-h) Shows the evolution over time of the flow pattern of Simulation 4.

batches mostly conforms with the behaviour of the same batches in Simulation 1. One key difference is the reduction in flow rate between Simulation 1 and 3, likely due to the need to displace more material in Simulation 3 than in simulation 1. Moving to Simulation 4, the same modification in appearance of the secondary batches from a flat, round shape in Simulation 3 to an arrowhead shape is observed, with an additional reduction in flow rate. Thus, for the no rebar series of simulations, the flow rate is lowest when both support fluid and thixotropy are present. With the addition of support fluid to the system there is some evidence of support fluid interaction with batch 1, evident by the presence of support fluid at the vertical edges of the GFB. Though this small level of interaction unlikely to cause inclusions or defects.

In terms of plug vs bulging, or rather the new terms discussed in Chapter 4 of restricted and unrestricted: the flow behaviour of Simulations 1 and 3 present features associated with a very low degree of restriction. This is attributed to the low yield stress of the concrete requiring a low amount of applied stress to displace. Simulations 2 and 4 display flow behaviours of a secondary batch that is experiencing some restriction. This is evident by the lower flow rate, and the 'arrow-head' like shape, suggesting the secondary batches are not as effective at displacing batch 1. Thus, it is possible to include the degree of thixotropy as an additional method of flow restriction.

Figure 6.17 shows the results from Simulations 5 and 6. Each image is represents a time intervals of $0, 10$ and 10 s. Figure 6.17a-c and e-g represent slices through the centre of the GFB, whereas, fig. 6.17d and h represent the front face of the flow-box. A slice and front denote which images are captured as slices through the GFB and those that represent what would be seen from the front viewing panel of the GFB. Simulations 5 and 6 are equivalent to Simulations 1 and 2 with the addition of reinforcement inserts.

By 2 s of flow time, fig. 6.17, the appearance of the secondary batches of concrete in Simulation 5 is already visibly different from the simulations where reinforcement is not present. The restriction of the flow caused by the rebar inserts has caused and arrowhead shaped flow front, much like that observed in simulations 2 and 4 which was attributed to the flow restriction imposed on the concrete by way of thixotropy. At 10 s of flow time, the slice, fig. 6.17c and front, Figure 6.17d, show different characteristics of the secondary batches. Starting with the slice, the flow has been entirely restricted to the area immediately surrounding the pipe. This is likely a result of the vertical rebar restricting outwards flow along the plane the of the slice. From the front, the flow appears to be less restricted, flowing adequately around the horizontal reinforcement inserts. This could suggest either the vertical

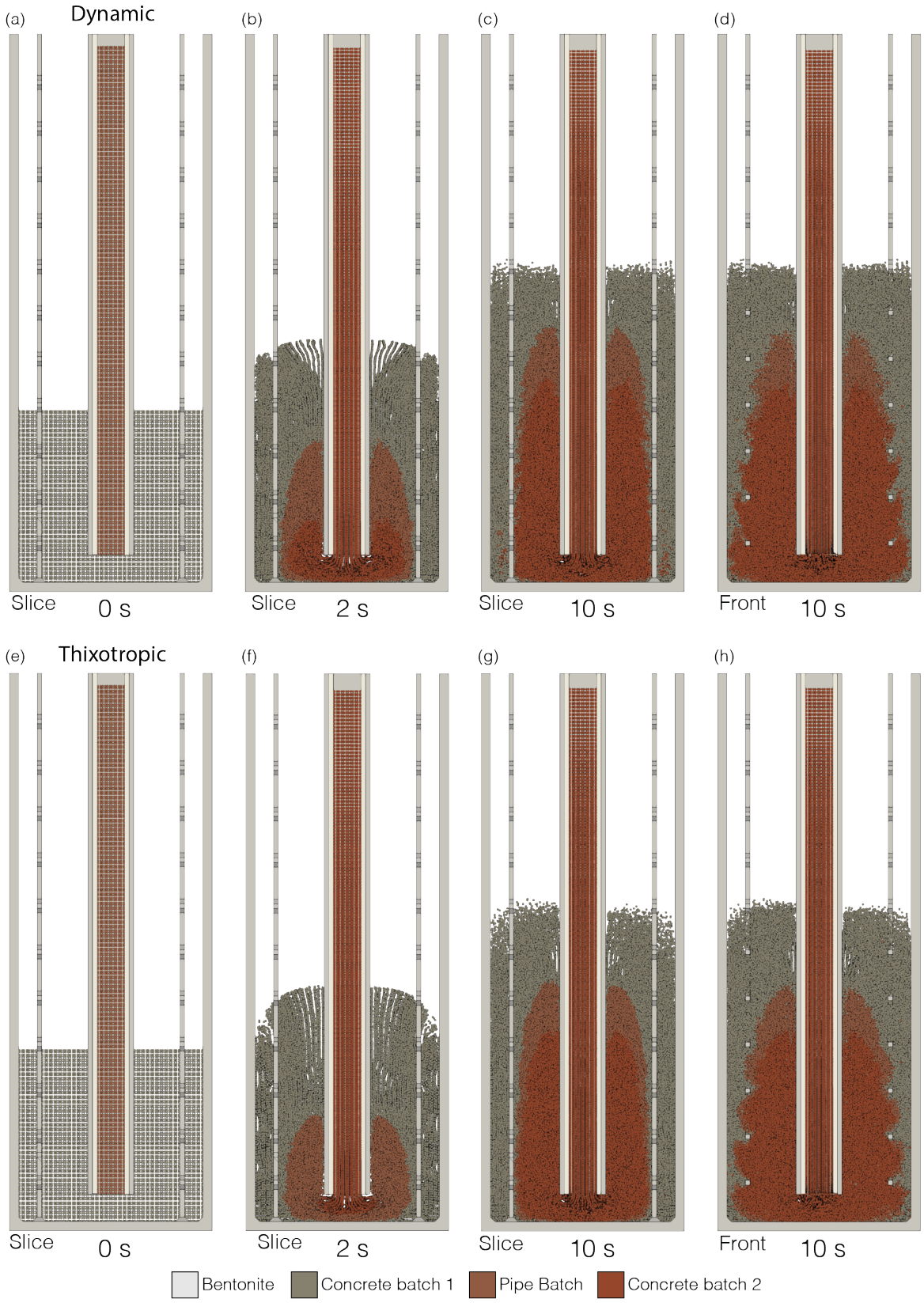

Fig. 6.17 a)-d) Shows the evolution over time of the flow pattern of Simulation 5. e)-h) Shows the evolution over time of the flow pattern of Simulation 6.

bars in reinforcement cages or the junction where vertical and horizontal meet present the greatest obstacles to flow.

Introducing thixotropy to Simulation 5 gives rise to Simulation 6, fig. 6.17e-h, where some significant changes in flow patterns arise. The first notable difference can be seen in the 2 s slice, fig. 6.17e, where a visible flow-front differential in batch 1 between concrete inside the cover zone and that closest to the pipe can be observed. Although this flow-front difference is also present in Simulations 5, fig. 6.17b, it is more pronounced with the addition of thixotropy. Flow front height differences between concrete inside and outside the cover zone could lead to increased support fluid interaction, thus, the increasing of the front-difference due to thixotropy is an important observation. In the front view of Simulation 6, fig. 6.17h, the flow of the secondary batch appears once more to be additionally restricted by the addition of thixotropy to the simulation. Finally, one additional element of Simulation 6 that is interesting, is the reduction in flow-front height difference from 2-10 s. Although flow-front height difference is present at the end of the simulation, it is much larger during the initiation of flow. This could suggest that the greatest risk of mixing with support fluid arises at the restarting of flow following a period of rest.

The addition of a bentonite support fluid to Simulations 5 and 6 results in Simulations 7 and 8, shown in fig. 6.18. Starting with the simulation without thixotropy, Simulation 7, fig. 6.18a-d, the first key difference between Simulation 5 and 7 is the larger, and more prominent front-difference of batch 1 inside and outside the cover zone. The presence of a larger flow-front differential is cause for concern on its own, however, possible entrapment of support fluid in the trough caused by the flow-front differential is the more serious concern. At the end of the simulation the differential has reduced considerably, and there is only a small degree of support fluid trapped at the sides of the box. This could suggest that in this particular case, batch 1 was able to displace most of the support fluid. It is difficult though, to gauge the level of mixing that would occur in physical experiment of this kind. The behaviour of the secondary batches of concrete are in close agreement with Simulation 5, with a slight decrease in flow rate. It is worth noting that the simulation cannot fully capture small pockets around the rebar which can become moisture conduits or voids.

The final simulation to be assessed is Simulation 8, fig. 6.18e-h. A simulation where reinforcement inserts are present, support fluid is used, and batch 1 and the Pipe batch have undergone a rest period of 240 s. This simulation represents the most complex of the chapter.

The flow-front differential at 2 s is now more distinguished than in any of the previous simulations. This suggests the increase in flow restrictions due to thixotropy are having a significant effect of the ability of newer concrete batches to displace that which is already

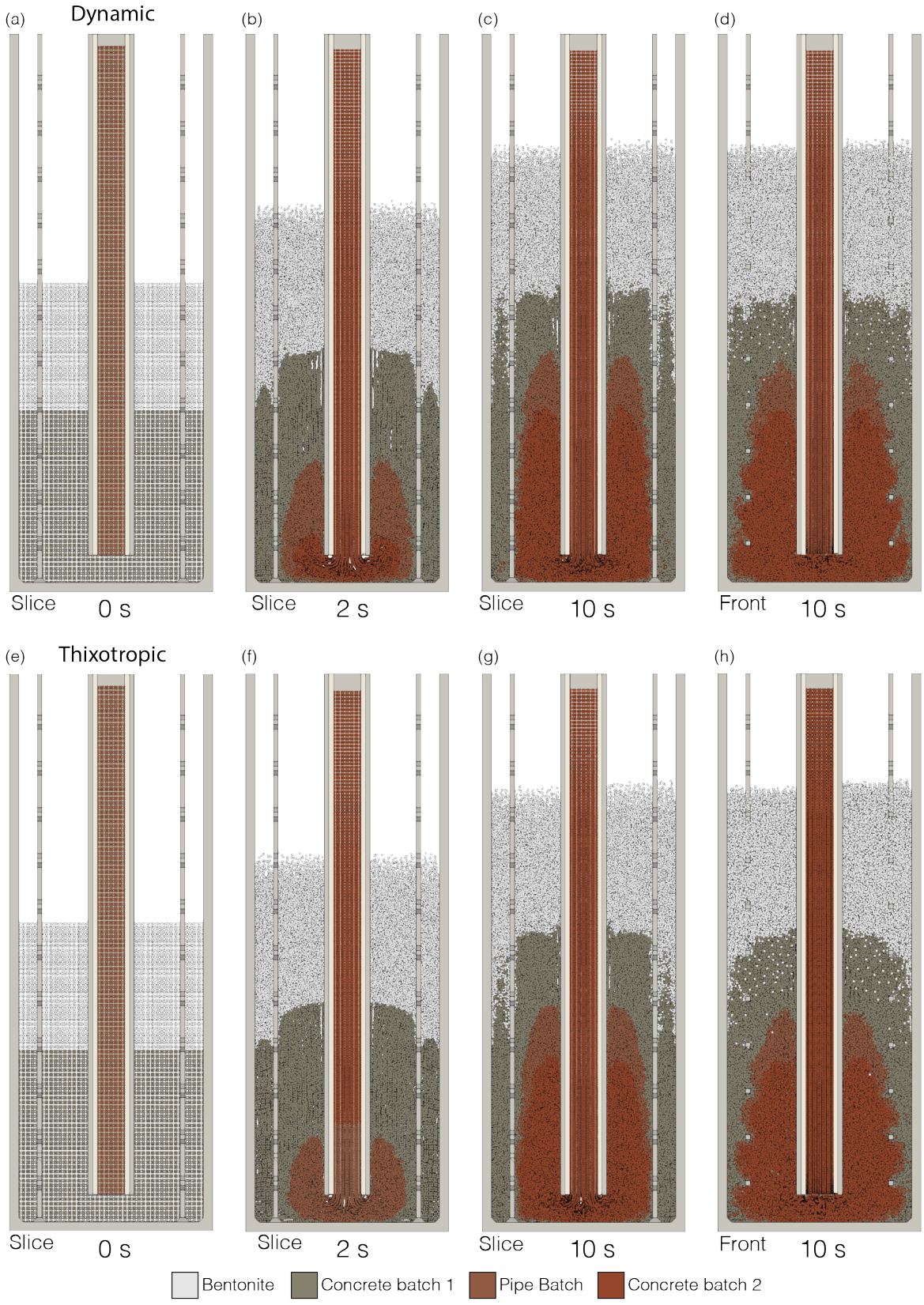

Fig. 6.18 a)-d) Shows the evolution over time of the flow pattern of Simulation 7. e)-h) Shows the evolution over time of the flow pattern of Simulation 8.

present in the cover zone. The slice at 10 s, fig. 6.18g, once again has a flow-front differential between concrete inside and outside the cover zone larger than any of the previous simulations at this stage in time. There also appears to be a great deal of interaction between the support fluid and the concrete of batch 1, which might lead to the development of interface material should this behaviour occur in a physical foundation. Figure 6.18h, the front view of Simulation 8, is also unique in that it shows a clear flow-front differential at the end of the simulation, whereas the front panel of previous simulation showed a limited flow-front differential. This again supports the theory that thixotropy reduces the ability of concrete to flow freely in the cover zone due to thixotropy.

The reduction in flowability of concrete in the cover-zone due to thixotropic changes in concrete rheology is also supported by the changes in passing ratio seen in L-box simulations discussed in section 6.3.1, where compelling evidence of a reduction in the ability of concrete to flow easily around rebar inserts after a period of rest was demonstrated.

The degree of restriction on the flow of secondary concrete batches in Simulations 5-8 can be further analysed by looking at the magnitude of the displacement vector. That is, the vector that describes the amount of displacement a material point has experienced from it's starting position. It is a useful tool to assess how the original concrete, batch 1, has displaced over time. Particularly, it is a useful metric to determine if there is significant movement of the concrete in the cover zone, or in the flow front. A high degree of horizontal displacement in the front of the flow would suggest 'plug' flow is not occurring.

Figure 6.19 shows the magnitude of the displacements for material points in Simulations 1, 2, 5 and 6, at 10 s of flow time. Starting with Simulation 1, the highlighted zone in fig. 6.19a signifies the flow front, where a low degree of displacement has occurred. There appears to be more displacement closer to the pipe, with less displacement towards the upper edges. Along the vertical edges of the flow box, there appears to be a very low area of displacement. At the bottom of the highlighted section, above the flow front of the secondary batch there appears to be a section of very low displacement. This is a result of the concrete in that area returning to the same height as it started within the pipe. The addition of thixotropy in Simulation 2 has caused the outer edges to have a lower degree of displacement whilst the area closer to the pipe has incurred a higher degree of displacement, fig. 6.19b.

The simulations with rebar inserts, Simulations 5 and 6, fig. 6.19c and d, show a higher degree of displacement closer to the pipe, and a significantly lower degree of displacement in the cover zone. The increase in flow restriction appears to encourage flow closer to the tremie pipe, an expected result.

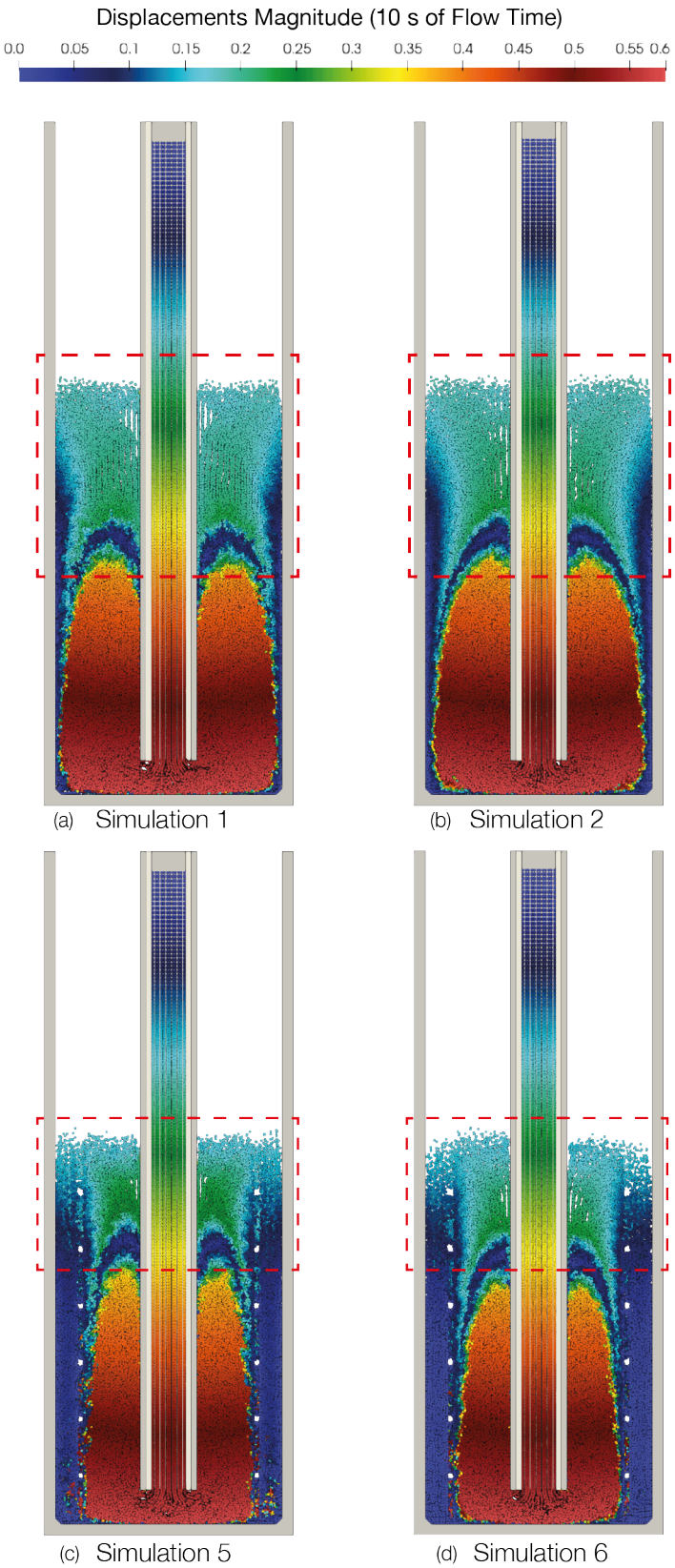

Fig. 6.19 Comparison of the magnitude of displacement for Simulations 1(a), 2(b), 5(c) and 6(d). Highlighted area shows the behaviour of batch 1 as it rises.

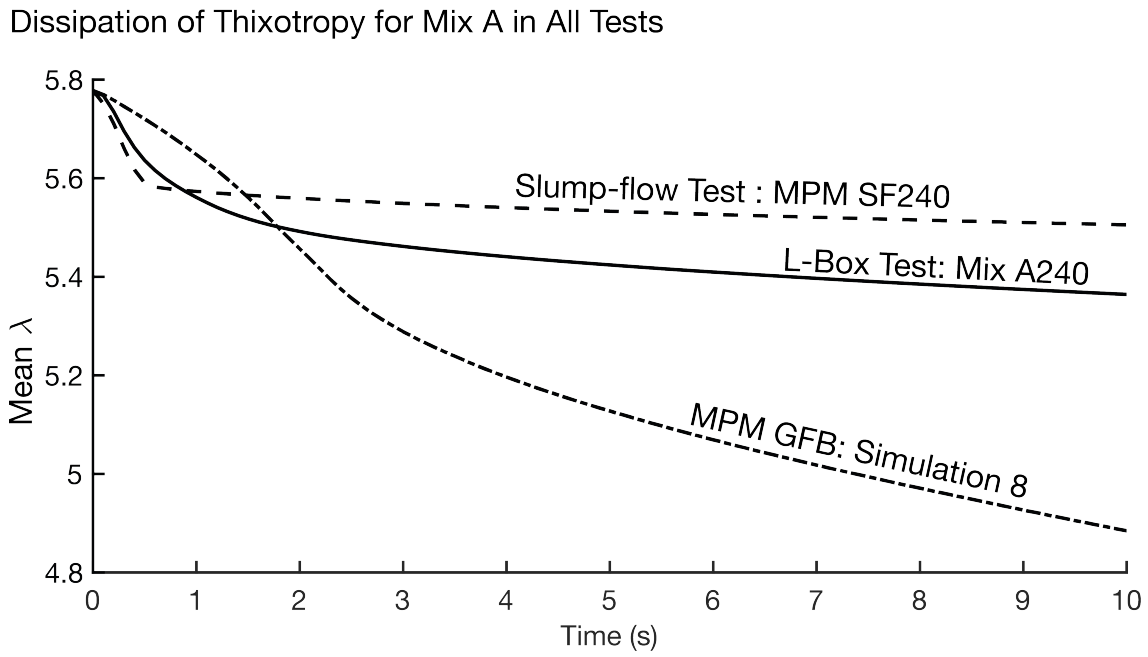

Fig. 6.20 Comparison of mean λ for Mix A in three different MPM simulations.

The dissipation of thixotropy was discussed with reference to the L-box in section 6.3.1, and the Slump-flow test in Chapter 5. A comparison between the rate of dissipation of thixotropy for all three testing set-ups is presented in fig. 6.20. What stands out the most is that the rate of dissipation of thixotropy appears to be greater in the simulations of the GFB than in any of the simulated concrete testing devices. It is possible, therefore, that the L-box and Slump flow test are not as suited to testing the effect thixotropy as the GFB, due to the lower level of thixotropic dissipation experienced. Furthermore, fig. 6.21 demonstrates the areas where thixotropy has dissipated at 0, 2 and 10 s, evident by a reduction in λ from the initial starting point of approximately 5.8. As expected, there is a large degree of dissipation in the concrete closest to the pipe and inside the reinforcement, mainly comprised of the concrete within the pipe during the rest period. Additionally, although not immediately obvious, there is a slightly higher degree of thixotropic dissipation in the centre of the cover zone of the 10 s slice. Possibly indicating that although movement in this area is heavily restricted, there is still some flowing occurring. Due to the low shear-forces experienced throughout being larger than the critical shear-rate, there are no areas with a notable increase in thixotropy during the 10 s.

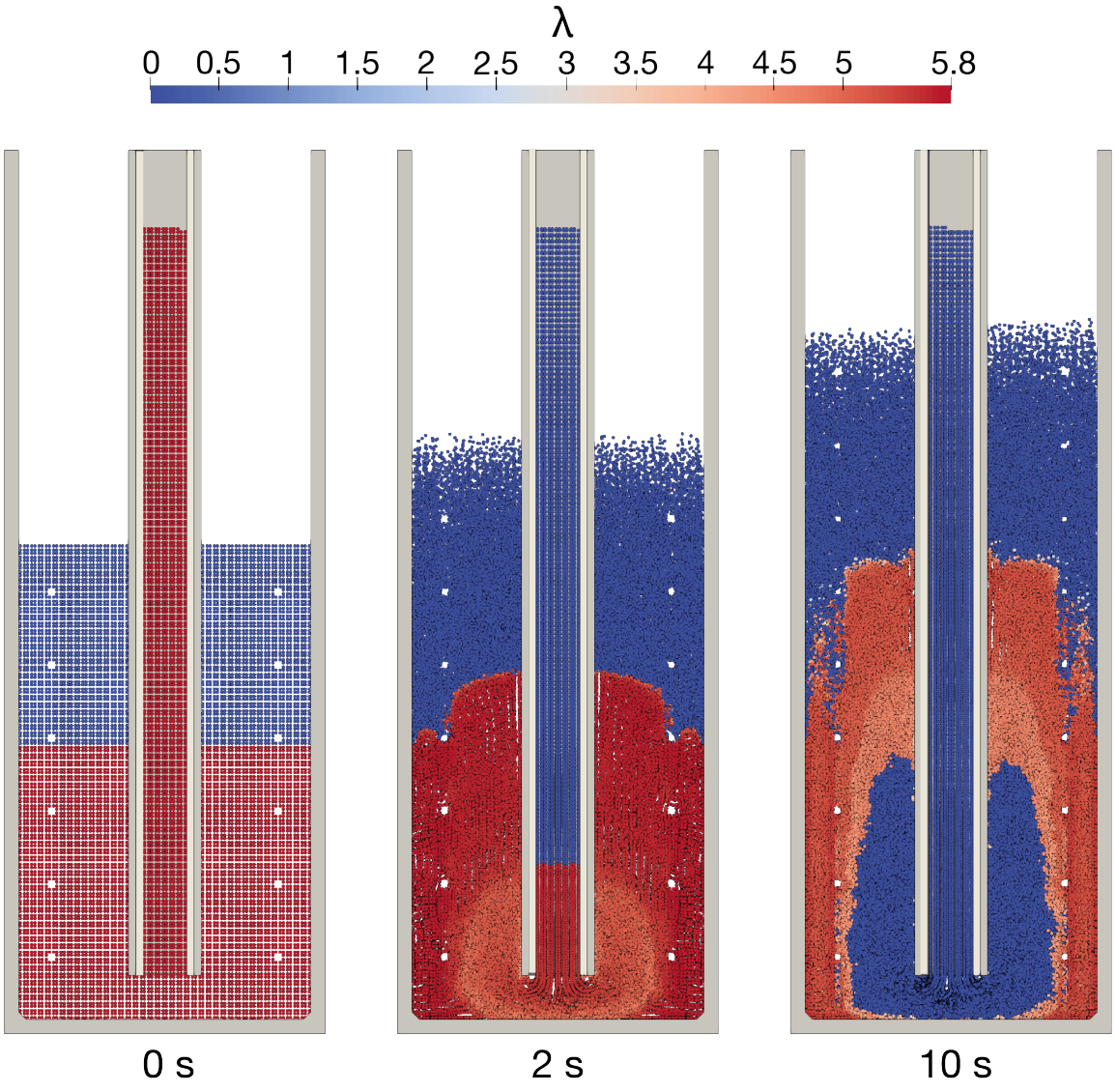

Fig. 6.21 Dissipation of λ over time for Simulation 8.

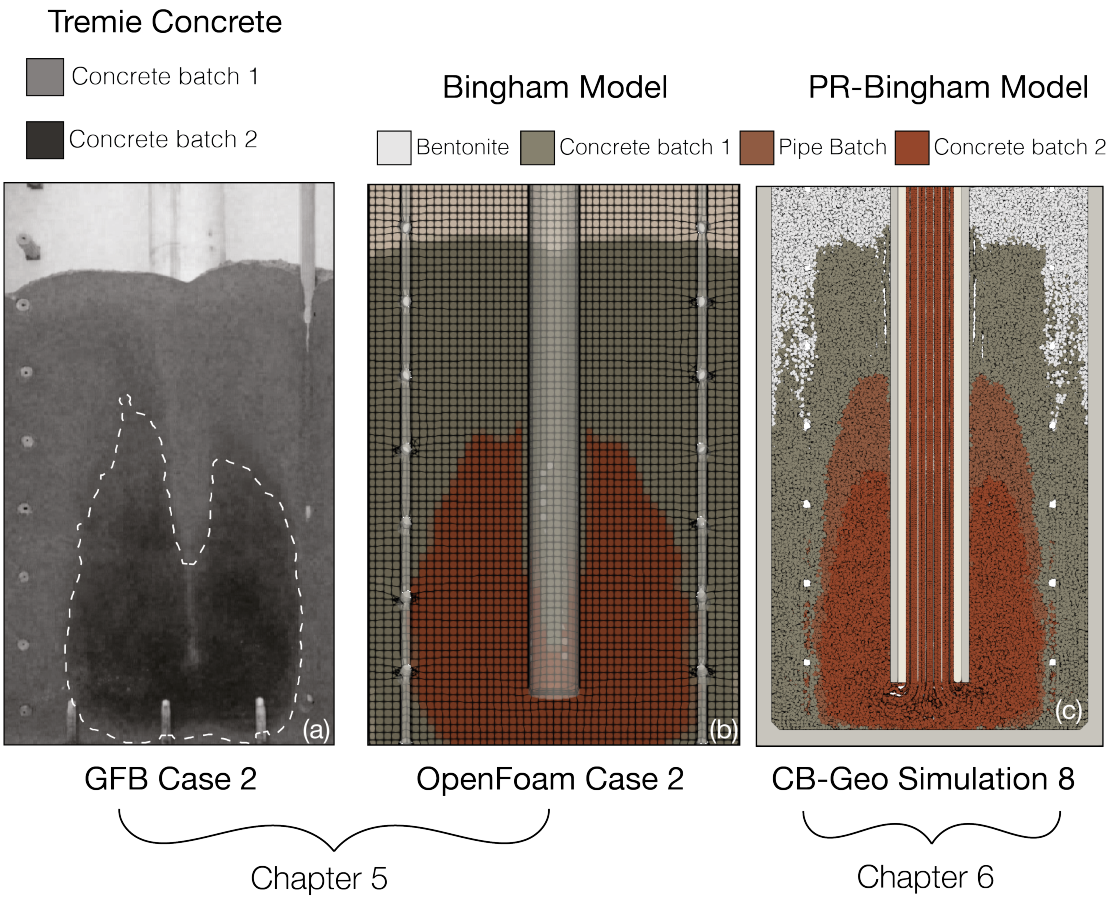

Fig. 6.22 Comparison of experimental analysis (a), and CFD (b) and MPM (c) simulations of the GFB with reinforcement present at 8 s of flow time.

6.3.3 Computational Fluid Dynamics Comparison

Figure 6.22a, b and c are slices of the gravity flow box apparatus at 8 s of flow time for the experimental Case Two, CFD Case Two and MPM Simulation 8. The CFD simulation uses the same Bingham inputs as the experimental case, however Simulation 8 uses Mix A240. The purpose of this figure is to demonstrate the simulation capability of MPM vs CFD, and how that compares with the general behaviour of the experimental results.

The secondary concrete batches of both CFD and MPM are confined by the reinforcement cage, as is the experimental result. So at the very least, MPM is correctly simulating the general behaviour of the experiment well, even with the slightly different Bingham parameters. The CFD simulation of the experimental GFB was able to get a closer geometrical representation of the box, as GIMP dictates that MPM boundaries need to be two cells thick. This could be mediated with targeted mesh refinement within MPM to create smaller boundaries where required. The slightly different geometries make comparison of the flow-

rates difficult, but not impossible. The CFD simulations were set at a $0.2\,\mathrm{m\,s^{-1}}$ flow rate, in accordance with the average flow rate of the experimental case. The MPM simulations naturally achieved flow rate was approximately $0.1\,\mathrm{m\,s^{-1}}$. This is likely due to the smaller geometry and increased restriction on flow due the shorter distance from pipe-edge to reinforcement. However, this does support that MPM is achieving a flow rate that would be expected in a physical test of the same geometry.

Overall, the MPM simulations are as accurate as the industry standard CFD simulations, with the addition of thixotropic behaviour and complex boundary conditions.

6.4 Conclusions

This chapter had two main objectives. The first was to use the L-box test, to demonstrate how thixotropy effects concrete flow around obstacles. In doing so, it was demonstrated that thixotropic behaviour of concrete has a significant effect on simulations of concrete flow within an L-box test. Large reductions in passing ratio and flow-time were seen with 240 s of rest. As a result of this, it is recommended that future work on simulated, time-dependent concrete behaviour should focus on the time-dependency of boundary friction. Conversely, if friction does remain constant then thixotropy will reduce the ability of concrete to flow around reinforcement bars.

The second objective was perform to simulations of thixotropic concrete flow in the GFB apparatus, to clarify how changes in concrete behaviour in the L-box test translated to deep foundation conditions. It was shown that thixotropy was unlikely to pose much of an issue to the construction process of un-reinforced piles, as thixotropy had little impact outside of a slight reduction in flow rate for these simulations. However, a large increase in flow-front differential was observed when thixotropy was added to simulations of reinforced piles where support fluid was present. The flow-front differential was sufficient enough that it could lead to the development of inclusions of interface material, should it occur during construction process. This is highlighted in fig. 6.23 where the increase in restriction from thixotropy, support fluid and reinforcement inserts is demonstrated to impact the initial and secondary batches of concrete.

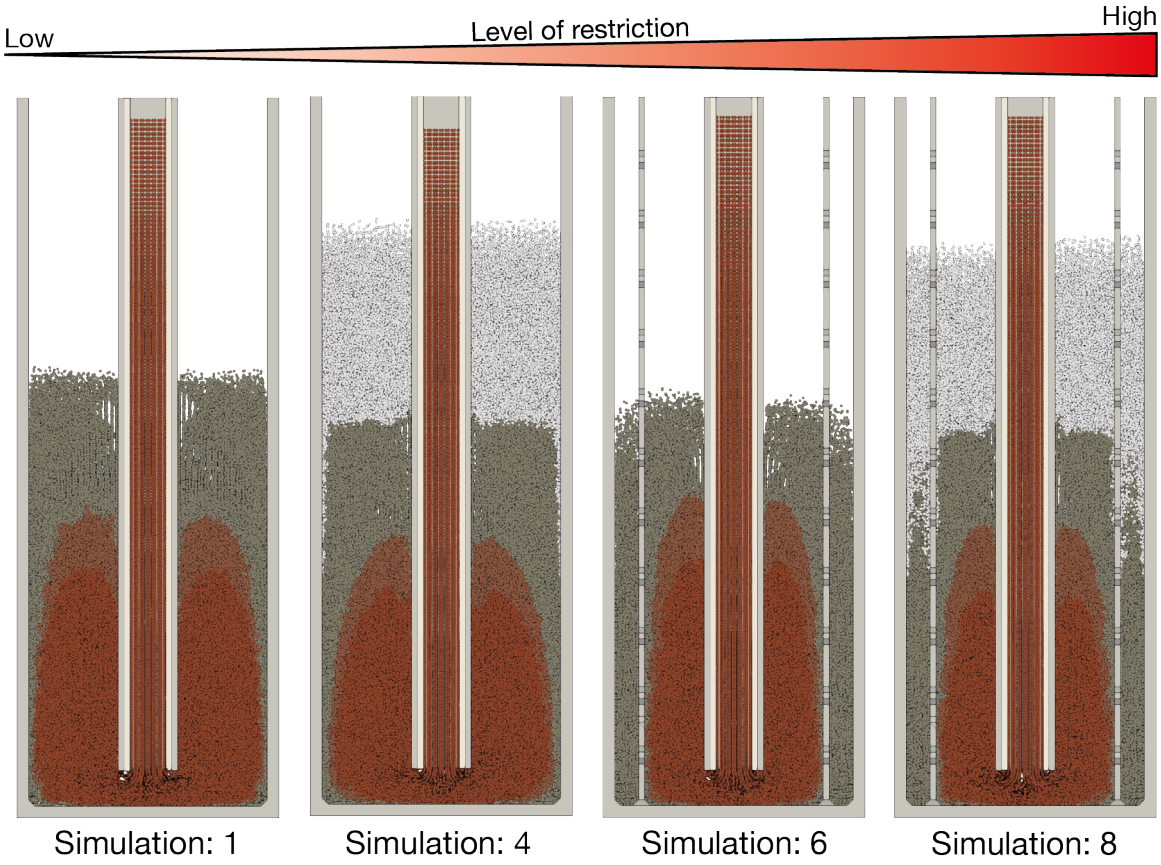

Fig. 6.23 Figure showing the effect increasing restrictions to the flow of concrete have on the flow behaviour of Tremie Concrete at 10 s of flow time.

Chapter 7

Conclusions and Future Work

7.1 Summary

A review of the literature identified key areas of concrete behaviour in the Tremie method that merited further investigation. One area of investigation worthy of continued exploration involved the bulk flow behaviour of concrete as it exits the pipe and begins to fill the excavated shaft. The bulk flow behaviour of concrete was understood to form one of two typical flow patterns, plug flow or bulging flow, each representing a characteristic concrete behaviour in the foundation that has distinct implications for deformations and final performance of the analysis. Although this understanding was based on operational experience and back-calculations performed by numerical models, there was a need to demonstrate this behaviour conclusively using laboratory experiments supported by numerical evidence. A second potential area of investigation identified by the literature review was the effect concrete thixotropy had on the performance of concrete in a deep foundation. The low shear-rate induced stiffening of concrete occurring within the dormant period of the hydration reaction was experimentally demonstrated to cause a 100% increase in yield stress within a 240 s period, yet little was known about the impact such a significant change in rheological properties could have on the behaviour of concrete in a deep foundation. Furthermore, test methods designed to give rapid estimations of a concrete performance appeared unaffected by the rapid change in concrete rheology at rest, an unexpected observation.

The investigation of concrete behaviours necessitated the use of numerical modelling, however, the process of choosing a model is not without complications. A review of existing models revealed many current models have limitations on scalability, material representation, or the ability to model the high levels of deformation needed to simulate Tremie Concrete.

Nevertheless, two numerical methods were chosen. The first, the Material Point Method (MPM), was chosen for its scalability, ability to represent time-dependent concrete behaviour, and ability to handle high levels of deformation. 3D GIMP functionality was added to the CB-Geo MPM code to facilitate the modelling of tremie concrete by way of reducing cell-crossing noise. The second numerical method, Computational Fluid Dynamics, was chosen, in part, because previous work had been successful, but also for its ability to model many of the required concrete behaviours. The open-source OpenFOAM® framework was chosen as the CFD package to be used in this work.

Chapter 4 features a discussion on the flow patterns of concrete, the name given to the bulk-flow behaviour of concrete as it leaves the tremie pipe and enters the excavation. It was concluded that in order to improve on the current understanding of concrete bulk flow behaviour, attention should be focused on observing the early-stage flow behaviour of secondary (not already in-place) batches of concrete. This required the use of a novel apparatus, the gravity flow box (GFB), where footage of concrete flow in conditions closer to those found in the tremie method could be documented. Two cases were investigated in the experimental testing: with or without reinforcement inserts designed to mimic a reinforcement cage. Case one (without reinforcement inserts) showed that the flow of a secondary batch of concrete emplaced in an environment where the flow is unrestricted will fill the available space laterally, and displace the existing concrete vertically. This resulted in a plug-like behaviour of the originally in-place batch. The flow behaviour of the second case had a closer resemblance with the bulging flow pattern, where the secondary batch of concrete was confined to the area between the reinforcement inserts and the tremie pipe, rather than the outside cover-zone.

The OpenFOAM® simulations first required a validation case to demonstrate the viability of the method to simulate the chosen material properties accurately. This was conducted using a benchmark Slump-flow test using rheology input values with a known analytical solution. The benchmark results suggested the chosen implementation of the OpenFOAM® framework was performing within the range of expectations. The flow behaviour of simulated concrete in Case One and Two of the GFB were in good agreement with the experimental results. This suggested that OpenFOAM® was capable of representing the bulk flow behaviour of dynamic concrete. However, the limitations of the chosen package did become apparent during the process of simulating the GFB apparatus. First, there is a limitation on the degree to which boundary friction can be applied. Second, incorporating thixotropic behaviour is a non-trivial task and would require a significant time-investment to implement, without the guarantee of complete functionality.

A large change in concrete flow behaviour was observed in the GFB with only the introduction of flow obstacles in the form of reinforcement inserts. Rather than specific terms that pertain to one flow characteristic, a scale based system was created to explain the different types of concrete behaviour that could occur. The scale depends on the level of restriction to free-flow the concrete will exhibit once it leaves the tremie pipe. In the case of Chapter 4, that level of restriction is increased in Case two from Case one by adding reinforcement.

Chapter 5 begins with a discussion on concrete thixotropy and the documented effect it has on concrete test results. One test in particular, the Slump-flow test, was investigated extensively. The test involves filling a truncated cone resting on a flat base plate with concrete, which once full, is raised to release the concrete. The diameter of the spread is then measured. Evidence was presented that suggested despite test results having a very good correlation with concrete rheology, the dramatic rheological changes induced by thixotropy did not seem to effect the outcome of the test. This was in stark contrast to what would be expected, given such large increases in concrete yield stress measured by a rheometer. In order to investigate this issue numerically, the CB-Geo MPM code's ability to model a materials history dependent behaviour was employed. This first required the development of a constitutive model capable of being used in the MPM in addition to also representing the thixotropic behaviour of concrete. After much investigation, the The Papanastasiou [90] model was found to be the optimal choice for the Bingham representation of the material. The Papanastasiou model regularises the traditional Bingham model, preventing computational discontinuities arising due to shifts in concrete behaviour from viscous to plastic at a given shear-rate. Using a low value regularisation parameter, m was also demonstrated to reduce the occurrence of volumetric locking within the MPM due to potential over-stiffening caused by the viscosity term of the Bingham model. Roussel's [96] thixotropy equations were combined with the Papanastasiou Bingham model to create an MPM-friendly thixotropic Bingham model capable of simulating a wide range of Tremie Concrete behaviours, referred to as the PR-Bingham model.

The PR-Bingham model was used to simulate a Slump-flow test for three different concrete mixes. A low yield stress, high viscosity concrete with a low level of thixotropy, a concrete with a medium level of thixotropy but low viscosity and yield stress, and a high yield stress medium viscosity concrete with a high degree of thixotropy. Each mix had physical Slump-flow tests for both no rest (dynamic) and rested (static) concrete. Thus, simulations of rested and un-rested concrete could be conducted. The result of simulations where a rest time had been added showed a decline in workability not captured by the physical test.

Chapter 6 begins with a discussion on the concrete restriction scale presented in chapter 4. The scale states that restricting forces on concrete flow are the main control on flow patterns. It was theorised that there are many different contributors to flow restriction, one possibility being the rheology of the material itself. To test this theory, the CB-Geo MPM code and the PR-Bingham model presented in chapter 5 were employed to model two testing devices: the L-box test, and the GFB presented in chapter 4. The L-box test was developed as a way to assess the likely behaviour of concrete in a foundation setting. It features a large vertical chamber which is filled with concrete and an empty horizontal chamber where the concrete will flow into, forming an L shape. The horizontal section features two reinforcement bars posing an obstacle to flow, as they would in a foundation setting. Unlike the Slump-flow test, which realistically only measures the stopping effect induced by the yield stress, the L-box combines many aspects of concrete rheology. The two most important measurements are the flow time, the time taken to reach the end of the horizontal section, and the passing ratio, a measurement of height difference in the ends of the horizontal section at the end of the test. The passing ratio gives an indication of how well a concrete can flow around reinforcement bars. The objective is to determine how thixotropy will effect concrete flow in a reinforced foundation, thus, this test offers a way to compare the behaviour of simulated and physical results, in a similar fashion to what was done for the Slump-flow test.

The L-box test requires a 60 s rest period which is likely to cause a notable rise in yield stress due to thixotropy. Thus, simulations of dynamic properties did not have a directly comparable physical result. A rest period of 60 s was added to the virtual concrete, but the physical and simulated flow-time's differed considerably. Interestingly, the dynamic property simulations were closer to the physical test, suggesting that the thixotropic rising of yield stress in the L-box test may not have been active for the entire 60 s rest period. For the next set of simulations, a 240 s rest period was added. Once again, the simulated concrete captured a reduction in workability not observed in the physical test.

The CB-Geo simulations of the GFB used both dynamic and static conditions (where a 240 s rest period had been added to the concrete). The dynamic simulations showed a good degree of conformance with the CFD simulations and the physical results. This reinforced the theory that physical obstacles to flow cause restricted flow behaviour. The inclusion of a rest period, and the associated concrete stiffening, caused two key changes in the flow behaviour. First, the secondary flow of concrete formed an arrow-head shaped flow head, rather than a flat round top, suggesting it was now more difficult to displace the original concrete already in place, an expected outcome. The second change in concrete behaviour related to an increase in the flow-front differential (height difference between concrete

outside and inside the reinforcement cage) of the originally in place batch when both a rest period and bentonite support fluid were included in the simulation. Such a front-differential could increase intermixing with concrete and support fluid, leading to a larger interface layer. An increase in interface layer causes the inclusion of low-strength material within the finished foundation, reducing the structural capacity of the foundation. The final discussion in chapter 4 concludes that the restriction of flow within a foundation should be considered by the designer, and accommodations made to reduce the negative effects caused by the level of restriction.

7.2 Conclusion

7.2.1 Numerical Modelling

In Chapter 5, results of MPM simulations of the Slump-flow test using dynamic rheological properties of real concretes found a good level of agreement between simulated and physical results. The static results, however, were not in agreement. With the introduction of thixotropy after a rest period the simulated concrete became stiffer, resulting in reduced Slump-flow measurements. This was in contrast to the experimental evidence, but in line with the expected behaviour. It was concluded that some process in the physical test was obscuring the true nature of the concrete behaviour, most likely related to a reduction in friction coefficient between the concrete and the steel base-plate of the Slump-flow test.

As with the Slump-flow test, the physical L-box results for concrete resting for 240 s in Chapter 6 showed minimal changes, yet the flowability of the virtual concrete was severely impacted. The difference in behaviour was explored further, with the same conclusion arising from the L-box results as was discussed in regard to the Slump-flow results: A reduction in boundary friction is likely to be occurring. It is hypothesised that this could be a result of one of two main possibilities: Bleeding of concrete during the rest period was creating a lubricating effect between the concrete and steel base, or a change in the availability of fines (or an increase in plastic viscosity) due to thixotropy was reducing the friction coefficient between the steel and concrete.

CFD simulations of the Slump-flow test also performed well when using dynamic properties of experimental and virtual concretes. Both MPM and CFD simulations showed the same change in concrete flow behaviour when reinforcement inserts were added to the simulations. This is consistent with what was observed in the physical case. In general, therefore, it seems that both CFD and MPM are representing the bulk flow behaviour of Tremie Concrete.

CFD will likely struggle to replicate the ability of MPM to represent time-dependent concrete behaviour, however, it is computationally more efficient and there are a multitude of software packages available to suit many different use-case scenarios. Conversely, it is clear that volumetric locking presents an issue to stiffer concretes that must be accounted for in MPM, limiting its ability to simulate a range of concretes. Though it is worth noting that all continuous methods may struggle to simulate high yield stress concretes.

7.2.2 Practical Implications

The objective of this thesis was to use numerical modelling to define what conditions encourage the occurrence of defects in cast-in-place foundations. This has been achieved by numerically modelling concrete testing devices and the Gravity Flow Box.

A new classification system of flow behaviours which relies on a scale of flow restriction was presented, where restriction ranges from high to low. High levels of restriction will lead to: a large flow-front differential that encourages the enveloping of interface material, arrow-head secondary flows which may breach the flow front more regularly, and reduced flow rates that may prevent the adequate flow of concrete. Conversely, low levels of restriction may encourage the formation of a rising plug of old concrete atop the pile, necessitating the use of superplasicisers to maintain good workability. Contributors to flow restriction identified in this thesis are the use of reinforcement cages, high levels of concrete thixotropy and the use of a support fluid. Thus, a greater clarity on the conditions during the flow of concrete within a deep foundation that can lead to defective foundations has been achieved.

Additionally, prior to this study it was difficult to explain why empirical concrete testing was unable to detect thixotropic changes in concrete. However, now there is a clear investigatory path lain out for future researchers to follow, starting with an analysis of the frictional boundary conditions.

The use of MPM for simulations of tremie concrete incur some advantages and disadvantages. The main advantage of using MPM is the ability to simulate the history dependency of concrete. This is a fundamental property that must be considered by any model hoping to represent concrete in an industrial setting. However, MPM simulations are not a trivial task. Mesh generation is a complex and time-consuming process that is often counter-intuitive. In particular, the application of boundary conditions to small areas (like reinforcement bars) is at not an automated process, requiring user input and knowledge of post-processing software. There is also a delicate balance to be struck when determining the mesh/point relationship as detailed in chapter 5 which often necessitates the use of multiple simulations and meshes;

all of which are time-consuming. Modifications to a constitutive model in MPM generally require at least a basic understanding of object oriented programming languages, an ability not easily obtained. Even once the initial set-up of the model is complete, there are other considerations to be made. Issues like volumetric locking and stress anomalies are often prevalent in many MPM simulations and require high-level knowledge of the numerical method itself to mitigate. As with many numerical methods, there is an inherent risk that the simulations are not accurately representing reality due to modifications made to the framework in order to achieve a stable simulation. However, the end result achieved in this work demonstrates that even with all the practical difficulties of MPM simulations, it is possible to achieve a good degree of accuracy, opening the door for both industrial and research applications of the CB-GEO MPM 3D.

7.3 Future Work

7.3.1 CB-Geo modifications

Currently, the CB-Geo MPM code and the PR-Bingham model are capable of simulating concrete where the yield stress does not exceed approximately 500 Pa due to volumetric locking. Implementing the volumetric method improvements suggested by Coombs et al. [33], which requires derivations from the deformation gradient rather than the velocity gradient, may increase the range of Tremie Concrete properties CB-Geo MPM can simulate. Simulations of large-scale, long rest-time scenarios will require this functionality. An ability to create locally refined GIMP meshes may also be beneficial in reducing the size of solid-wall boundaries like the tremie pipe or reinforcement cages, in field-scale simulations.

7.3.2 Tremie Concrete Properties

The nature of the frictional boundaries between concrete and shaft boundaries, or the steel of a testing device has been frequently discussed throughout this work. Further work should focus on identifying how frictional relationships change over time due to thixotropic changes in the concrete. This will enable more reliable assessments of the thixotropic behaviour of concrete.

7.3.3 Additional Simulations

The CB-Geo MPM code has proven its ability to simulate concrete flow behaviour in both dynamic and static conditions. Thus, future work should focus on field-scale simulations

of the Tremie Process. Doing so will also validate the observations seen in the laboratory scale experiments and simulations regarding the behaviour of concrete under different levels of flow restriction. This work has mainly focused on defining the conditions likely to cause defects that are related to issues during the flow of concrete in the tremie process. Simulations of flow initiation, particularly the behaviour of the plug as it leaves the pipe, and debris on the shaft base, would be the next stage in defining what conditions lead to foundation defects. This would allow designers to make adaptations or modifications to processes to reduce defects and the cost associated with remedial work.

Although field-scale simulations are the end goal for numerical modelling of tremie concrete, they are not the only pathway to improving our understanding of the behaviour of concrete. One such alternate path would be the simulation of concrete rheometers. This thesis focused on the simulation of empirical tests, primarily due to their simplicity of design. These empirical tests were then correlated with rheometer data as a validation method. To reduce the possibility of errors occurring when correlating empirical test results with rheometer data, it may be beneficial to simulate the rheometer itself.

Simulating rheometers in MPM would also open up opportunities to improve the PR-Bingham model by providing a validation method for other time-dependent behaviours that cannot be as easily measured by empirical testing, one such example being the changing of plastic viscosity over time. Other constitutive model improvements could be made by undertaking an analysis of boundary effects, like the geometric wall effect discussed in chapter 5.

With an improved PR-Bingham model there are ample opportunities for the MPM framework to be used to simulate other applications of high SF thixotropic concrete. One such application would be the growing field of 3D concrete printing. The printing of 3D concrete structures requires a rapidly stiffening concrete that is capable of flowing through a system of pipes prior to reaching the printing nozzle. There are multiple optimisations and developments to this process that require time-dependent material simulations to analyse. Significantly reducing the cost incurred by multiple iterations of experimental analysis.

Finally, numerically simulated concrete also has potential applications in the realm of extraterrestrial architecture. The construction of permanent extraterrestrial structures will soon be a reality if the current trajectory of space exploration is maintained. Several works have recently been published on the types of concrete that could be generated on the Martian surface. Numerical simulations of the construction processes utilising these concretes could help predict what types of issues are likely to arise, without the need to be there. This would offer unparalleled time and cost savings to an industry where both are a major limiting factor.

References

[1] Abe, K., Soga, K., and Bandara, S. (2013). Material point method for coupled hydromechanical problems. *Journal of Geotechnical and Geoenvironmental Engineering*, 140(3):4013033.

[2] al Kafaji, I. K. J. (2013). *Formulation of a dynamic material point method (MPM) for geomechanical problems*.

[3] Alehossein, H., Beckhaus, K., and Larisch, M. (2012). Analysis of L-box test for tremie pipe concrete. *ACI Materials Journal*, 109(3):303–311.

[4] Alyhya, W. S., Kulasegaram, S., and Karihaloo, B. L. (2017). Simulation of the flow of self-compacting concrete in the V-funnel by SPH. *Cement and Concrete Research*, 100:47–59.

[5] ASTM (2009). Standard Test Method for Bleeding of Concrete. Standard, American Society for Testing and Materials.

[6] ASTM (2014). Standard Test Method for Slump Flow of Self-Consolidating Concrete. Standard, American Society for Testing and Materials.

[7] ASTM (2102). Standard practice for static segregation of hardened self-consolidating concrete (scc) cylinders . Standard, American Association of State Highway and Transportation Official.

[8] Baltazar, L., Henriques, F., and Cidade, M. (2019). Rheology of natural hydraulic lime grouts for conservation of stone masonry—influence of compositional and processing parameters. *Fluids*, 4:13.

[9] Bandara, S. and Soga, K. (2015). Coupling of soil deformation and pore fluid flow using material point method. *Computers and geotechnics*, 63:199–214.

[10] Bandara, S. S. (2013). *Material Point Method to simulate Large Deformation Problems in Fluid-saturated Granular Medium*. PhD thesis, University of Cambridge.

[11] Baniabedalruhman, A. (2015). Dynamic meshing around fluid-fluid interfaces with applications to droplet tracking in contraction geometries.

[12] Bardenhagen, S. G. (2002). Energy conservation error in the material point method for solid mechanics. *Journal of Computational Physics*, 180(1):383–403.

[13] Bardenhagen, S. G. and Kober, E. M. (2004). The generalized interpolation material point method. *Computer Modeling in Engineering and Sciences*, 5(6):477–496.

[14] Bartos, P. J. M., Sonebi, M., and Tamimi, A. K. (2002). *Report 24: Workability and Rheology of Fresh Concrete: Compendium of Tests*, volume 24. RILEM publications.

[15] Beverly, C. and Tanner, R. (1992). Numerical analysis of three-dimensional bingham plastic flow. *Journal of Non-Newtonian Fluid Mechanics*, 42(1):85 – 115.

[16] Biscontin, G. and Pestana, J. M. (2001). Influence of peripheral velocity on vane shear strength of an artificial clay.

[17] Blanchet, G. and Charbit, M. (2006). *Digital signal and image processing using MATLAB*, volume 4. Wiley Online Library.

[18] Bohle, B. and Pulsfort, M. (2014). Fluid and casing supported Execution of bored Piles and their effects on Concrete Flow Behaviour. *DGGT*, 33.

[19] Bolton, M. and McKinley, J. (1997). Geotechnical properties of fresh cement grout—pressure filtration and consolidation tests. *Géotechnique*, 47(2):347–352.

[20] Bonen, D. and Shah, S. P. (2005). Fresh and hardened properties of self-consolidating concrete. *Progress in Structural Engineering and Materials*, 7(1):14–26.

[21] Bonet, J. and Kulasegaram, S. (2000). Correction and stabilization of smooth particle hydrodynamics methods with applications in metal forming simulations. *International journal for numerical methods in engineering*, 47(6):1189–1214.

[22] Bouharoun, S. (2013). Friction behaviour of fresh concrete in the vicinity of formwork. *Journal of the South African Institution of Civil Engineering*, 55:10 – 17.

[23] Brackbill, J. U., Kothe, D. B., and Zemach, C. (1992). A continuum method for modeling surface tension. *Journal of computational physics*, 100(2):335–354.

[24] Brown, D., Wulleman, T., and Bottiau, M. (2016). A comparison of design practice of bored piles/drilled shafts between europe and north america. *DFI Journal - The Journal of the Deep Foundations Institute*, 10(2):54–63.

[25] BSI (2019a). BS EN 12350-10:2010, Testing fresh concrete. Self-compacting concrete. L box test. Standard, British Standards Institute.

[26] BSI (2019b). BS EN 12350-8:2019, Testing fresh concrete. Self Compacting concrete - Slump-flow test. Standard, The British Standards Institute.

[27] Bui, V. K., Montgomery, D., Hinczak, I., and Turner, K. (2002). Rapid testing method for segregation resistance of self-compacting concrete. *Cement and Concrete Research*, 32(9):1489–1496.

[28] Chamani, M. R., Hosseinpour, M., Mostofinejad, D., and Esmaeilkhanian, B. (2014). Evaluation of SCC yield stress from L-box test using the dam break model. *Magazine of Concrete Research*, 66(4):175–185.

[29] Chen, B. (2016). Les stochastic modelling of cavitation with its applications in openfoam.

[30] Chen, Z. and Brannon, R. (2002). An evaluation of the material point method. *Sandia National Laboratories (SAND2002-0482)*.

[31] CIA (2005). Super Workable Concrete. Standard, Concrete Institute of Australia.

[32] Cooke, J. (2016). *Modelling of reactive absorption in gas-liquid flows on structured packing*. PhD thesis, University of Southampton.

[33] Coombs, W. M., Charlton, T. J., Cortis, M., and Augarde, C. E. (2018). Overcoming volumetric locking in material point methods. *Computer Methods in Applied Mechanics and Engineering*, 333:1–21.

[34] Courant, R., Friedrichs, K., and Lewy, H. (1967). On the partial difference equations of mathematical physics. *IBM journal of Research and Development*, 11(2):215–234.

[35] cw646 (2020a). cw646/gimp_mesh: Thesis release, doi: 10.5281/zenodo.4292282.

[36] cw646 (2020b). cw646/gimp_shape_function: Thesis release, doi 10.5281/zenodo.4399302.

[37] cw646 (2020c). cw646/hdf5_parser: Thesis release, doi: 10.5281/zenodo.4399282.

[38] cw646 (2020d). cw646/matlab_bw_trace: Thesis release, doi: 10.5281/zenodo.4321846.

[39] cw646 (2020e). cw646/pr_bingham_parametric: Thesis version, doi: 10.5281/zenodo.4400880.

[40] De Schryver, R., El Cheikh, K., Lesage, K., and De Schutter, G. (2018). Cfd implementation of time-dependent behaviour: application for concrete pumping. In *Symposium on Concrete Modelling (CONMOD2018)*, pages 122–130. RILEM Publications.

[41] Deeb, R., Kulasegaram, S., and Karihaloo, B. L. (2014). 3d modelling of the flow of self-compacting concrete with or without steel fibres. part i: slump flow test. *Computational Particle Mechanics*, 1(4):373–389.

[42] Dhaheer, M. S. A., Kulasegaram, S., and Karihaloo, B. L. (2016). Simulation of self-compacting concrete flow in the J-ring test using smoothed particle hydrodynamics (SPH). *Cement and Concrete Research*, 89:27–34.

[43] Djelal, C., Vanhove, Y., and Magnin, A. (2004). Tribological behaviour of self compacting concrete. *Cement and concrete research*, 34(5):821–828.

[44] Dufour, F. and Pijaudier-Cabot, G. (2005). Numerical modelling of concrete flow: homogeneous approach. *International Journal for Numerical and Analytical Methods in Geomechanics*, 29(4):395–416.

[45] Edesess, A. J. (2018). *Simulated wave hydrodynamics and loading on an offshore monopile*. PhD thesis, University College Cork.

[46] EFFC and DFI (2016). *Best Practice Guide to Tremie Concrete for Deep Foundations*.

[47] EFFC and DFI (2018). *Guide to Tremie Concrete for Deep Foundations*.

[48] Fern, E., Rohe, A., Soga, K., and Alonso, E. (2019). *The Material Point Method for Geotechnical Engineering: A Practical Guide*.

[49] Feys, D., Cepuritis, R., Jacobsen, S., Lesage, K., Secrieru, E., and Yahia, A. (2018). Measuring rheological properties of cement pastes: most common techniques, procedures and challenges. *RILEM technical letters*, 2:129–135.

[50] Feys, D. and Khayat, K. H. (2018). *Testing Concrete For Deep Foundations*.

[51] Feys, D., Khayat, K. H., and Khatib, R. (2016). How do concrete rheology, tribology, flow rate and pipe radius influence pumping pressure? *Cement and Concrete Composites*, 66:38–46.

[52] Fierenkothen, C. (2019). *Numerische Simulationen und Laborversuche zur Ausbreitung von Frischbeton in Bohrpfählen (Berichte des Lehr- und Forschungsgebietes Geotechnik, Nr. 38)*.

[53] Fierenkothen, C. and Pulsfort, M. (2019). Investigations on fresh concrete flow mechanisms in bored piles based on cfd simulations.

[54] Franci, A. and Zhang, X. (2018). 3d numerical simulation of free-surface bingham fluids interacting with structures using the pfem. *Journal of Non-Newtonian Fluid Mechanics*, 259:1–15.

[55] Gao, J. and Fourie, A. (2015). Spread is better: An investigation of the mini-slump test. *Minerals Engineering*, 71:120–132.

[56] Geuzaine, C. and Remacle, J.-F. (2009). Gmsh: A 3-d finite element mesh generator with built-in pre-and post-processing facilities. *International journal for numerical methods in engineering*, 79(11):1309–1331.

[57] Graf, O. (1933). Experiments of the behaviour of Reinforcement in Concrete of Various Compositions. *Deutscher Ausschuss für Eisenbeton*, 71:37–60.

[58] Gram, A. (2009). *Numerical Modelling of Self-Compacting Concrete Flow: Discrete and Continuous Approach*. PhD thesis, US-AB.

[59] Gram, A. and Silfwerbrand, J. (2011). Numerical simulation of fresh SCC flow: applications. *Materials and Structures*, 44(4):805–813.

[60] Gram, A., Silfwerbrand, J., and Lagerblad, B. (2014). Obtaining rheological parameters from flow test — Analytical, computational and lab test approach. *Cement and Concrete Research*, 63:29–34.

[61] Greenshields, C. J. (2015). Openfoam user guide. *OpenFOAM Foundation Ltd, version*, 3(1):47.

[62] Guilkey, J., Harman, T., Xia, A., Kashiwa, B., and McMurtry, P. (2003). An Eulerian-Lagrangian approach for large deformation fluid structure interaction problems, Part 1: algorithm development. *Advances in Fluid Mechanics*, 36:143–156.

[63] Herschel, W. H. and Bulkley, R. (1926). Konsistenzmessungen von gummi-benzollösungen. *Kolloid-Zeitschrift*, 39(4):291–300.

[64] Hirt, C. W. and Nichols, B. D. (1981). Volume of fluid (vof) method for the dynamics of free boundaries. *Journal of computational physics*, 39(1):201–225.

[65] Hosseinpoor, M., Khayat, K. H., and Yahia, A. (2017). Numerical simulation of self-consolidating concrete flow as a heterogeneous material in L-Box set-up: Effect of rheological parameters on flow performance. *Cement and Concrete Composites*, 83:290–307.

[66] ICE (2017). *Specification for piling and embedded retaining walls / Institution of Civil Engineers.* Third edit edition.

[67] Interim, S. C. C. (2003). *Interim Guidelines for the Use of Self-Consolidating Concrete in Precast/Prestressed Concrete Institute Member Plants*. Precast/Prestressed Concrete Institute (PCI).

[68] Issa, R. I. (1986). Solution of the implicitly discretised fluid flow equations by operator-splitting. *Journal of computational physics*, 62(1):40–65.

[69] Jasak, H. (1996). Error analysis and estimation for the finite volume method with applications to fluid flows.

[70] Jeyaraj, J. A. (2018). Numerical modeling of concrete flow in drilled shaft.

[71] Koehler, E. P. and Fowler, D. W. (2004a). Development of a portable rheometer for fresh portland cement concrete. Technical report.

[72] Koehler, E. P. and Fowler, D. W. (2004b). Development of a portable rheometer for fresh portland cement concrete. Technical report, International Center for Aggregates Research.

[73] Koehler, E. P., Fowler, D. W., Ferraris, C. F., and Amziane, S. (2005). A new, portable rheometer for fresh self-consolidating concrete. *ACI SPECIAL PUBLICATIONS*, 233:97.

[74] Kraenkel, T. and Gehlen, C. (2018). Rheology and Workability Testing of Deep Foundation Concrete in Europe and the US. Research Report No. 20-F-0107. *Chair of Materials Science and Testing, Centre for Building Materials, Technical University of Munich*.

[75] Kumar, K., Salmond, J., Kularathna, S., Wilkes, C., Tjung, E., Biscontin, G., and Soga, K. (2019). Scalable and modular material point method for large-scale simulations.

[76] Larisch, D. (2019). Concrete defects in bored piles as a result of insufficient applications of chemical admixtures. In *The NZ Concrete Industry Conference*.

[77] Larsen, B. E., Fuhrman, D. R., and Roenby, J. (2019). Performance of interfoam on the simulation of progressive waves. *Coastal Engineering Journal*, 61(3):380–400.

[78] Lecompte, T. and Perrot, A. (2017). Non-linear modeling of yield stress increase due to scc structural build-up at rest. *Cement and Concrete Research*, 92:92–97.

[79] Long, W., Khayat, K., and Xing, F. (2010). Repeatability of workability test methods of self-consolidating concrete. *Advanced Materials Research*, 168-170:1981–1986.

[80] Love, E. and Sulsky, D. L. (2006). An unconditionally stable, energy–momentum consistent implementation of the material-point method. *Computer Methods in Applied Mechanics and Engineering*, 195(33):3903–3925.

[81] Mechtcherine, V., Gram, A., Krenzer, K., Schwabe, J.-H., Shyshko, S., and Roussel, N. (2014). Simulation of fresh concrete flow using discrete element method (dem): theory and applications. *Materials and Structures*, 47(4):615–630.

[82] Moresi, L., Dufour, F., and Muhlhaus, H. (2003). A Lagrangian integration point finite element method for large deformation modeling of viscoelastic geomaterials. *Journal of Computational Physics*, 184(2):476–497.

[83] Morgan, G. C. (2013a). *Application of the interFoam VOF code to coastal wave/structure interaction*. PhD thesis, University of Bath.

[84] Morgan, G. C. (2013b). *Application of the interFoam VOF code to coastal wave/structure interaction*. PhD thesis, University of Bath.

[85] Mouret, M., Escadeillas, G., and Bascoul, A. (2008). Metrological significance of the column test in the assessment of the static segregation of self-compacting concrete in the fresh state. *Materials and Structures*, 41(4):663–679.

[86] Mullins, G., Ashmawy, A. K., Anderson, B., Deese, G., Garbin, E., Johnson, K., Lowry, S., Stokes, M., Wagner, R. V., and Winters, D. (2005). Factors affecting anomaly formation in drilled shafts.

[87] Nguyen, T. L. H., Roussel, N., and Coussot, P. (2006). Correlation between L-box test and rheological parameters of a homogeneous yield stress fluid. *Cement and Concrete Research*, 36(10):1789–1796.

[88] Nielsson, I. and Wallevik, O. H. (2003). Rheological evaluation of some empirical test methodspreliminary results. In *Third international RILEM symposium, RILEM Pub. PRO*, volume 33, pages 59–68.

[89] Pantev, I. (2016). Contact modelling in the Material Point Method.

[90] Papanastasiou, T. C. (1987). Flows of materials with yield. *Journal of Rheology*, 31(5):385–404.

[91] Papo, A. (1988). The thixotropic behavior of white portland cement pastes. *Cement and Concrete Research*, 18(4):595–603.

[92] Pruijn, N. (2016). The improvement of the material point method by increasing efficiency and accuracy.

[93] Qian, Y. and Kawashima, S. (2018). Distinguishing dynamic and static yield stress of fresh cement mortars through thixotropy. *Cement and Concrete Composites*, 86:288–296.

[94] Reddy, J. N. (2007). *An introduction to continuum mechanics*. Cambridge university press.

[95] Rohe, A. and Liang, D. (2017). Modelling large deformation and soil–water–structure interaction with material point method: Briefing on mpm2017 conference. *Journal of Hydrodynamics, Ser. B*, 29(3):393–396.

[96] Roussel, N. (2006). A thixotropy model for fresh fluid concretes: Theory, validation and applications. *Cement and Concrete Research*, 36(10):1797–1806.

[97] Roussel, N. (2007). Rheology of fresh concrete: from measurements to predictions of casting processes. *Materials and Structures*, 40(10):1001–1012.

[98] Roussel, N. (2011). *Understanding the rheology of concrete*. Elsevier.

[99] Roussel, N. and Coussot, P. (2005). Fifty-cent rheometer for yield stress measurements:From slump to spreading flow. *Journal of Rheology*, 49(3):705–718.

[100] Roussel, N., Geiker, M. R., Dufour, F., Thrane, L. N., and Szabo, P. (2007). Computational modeling of concrete flow: general overview. *Cement and Concrete research*, 37(9):1298–1307.

[101] Roussel, N. and Gram, A. (2014). Simulation of fresh concrete flow. *RILEM State-of-the-Art Reports*, 15.

[102] Roussel, N., Gram, A., Cremonesi, M., Ferrara, L., Krenzer, K., Mechtcherine, V., Shyshko, S., Skocec, J., Spangenberg, J., Svec, O., and Others (2016). Numerical simulations of concrete flow: a benchmark comparison. *Cement and Concrete Research*, 79:265–271.

[103] Roussel, N., Ovarlez, G., Garrault, S., and Brumaud, C. (2012). The origins of thixotropy of fresh cement pastes. *Cement and Concrete Research*, 42(1):148–157.

[104] Roussel, N., Spangenberg, J., Wallevik, J., and Wolfs, R. (2020). Numerical simulations of concrete processing: from standard formative casting to additive manufacturing. *Cement and Concrete Research*, 135:106075.

[105] Saak, A. W., Jennings, H. M., and Shah, S. P. (2004). A generalized approach for the determination of yield stress by slump and slump flow. *Cement and concrete research*, 34(3):363–371.

[106] Sadeghirad, A., Brannon, R. M., and Burghardt, J. (2011). A convected particle domain interpolation technique to extend applicability of the material point method for problems involving massive deformations. *International Journal for numerical methods in Engineering*, 86(12):1435–1456.

[107] Schaer, N., Vazquez, J., Dufresne, M., Isenmann, G., and Wertel, J. (2018). On the determination of the yield surface within the flow of yield stress fluids using computational fluid dynamics. *arXiv preprint arXiv:1808.00913*.

[108] Shmeleva, I. (2018). Flow of tremie concrete in piles and excavation walls. Master's thesis, University of Cambridge.

[109] Soga, K., Alonso, E., Yerro, A., Kumar, K., and Bandara, S. (2015). Trends in large-deformation analysis of landslide mass movements with particular emphasis on the material point method. *Géotechnique*, 66(3):248–273.

[110] Soundararajan, K. K. (2015). *Multi-scale multiphase modelling of granular flows*. PhD thesis, University of Cambridge.

[111] Sulsky, D., Chen, Z., and Schreyer, H. L. (1994). A particle method for history-dependent materials. *Computer methods in applied mechanics and engineering*, 118(1-2):179–196.

[112] Sulsky, D., Zhou, S.-J., and Schreyer, H. L. (1995). Application of a particle-in-cell method to solid mechanics. *Computer Physics Communications*, 87(1):236–252.

[113] Tan, Y., Cao, G., Zhang, H., Wang, J., Deng, R., Xiao, X., and Wu, B. (2015). Study on the Thixotropy of the Fresh Concrete Using DEM. *Procedia Engineering*, 102:1944–1950.

[114] Tanigawa, Y. and Mori, H. (1989). Analytical study on deformation of fresh concrete. *Journal of Engineering Mechanics*, 115(3):493–508.

[115] Tattersall, G. H. (1991). *Workability and quality control of concrete.* F.N.Spon, London.

[116] Tattersall, G. H. and Banfill, P. F. G. (1983). *The rheology of fresh concrete.* Pitman, London.

[117] Tattersall, G. H. and Bloomer, S. J. (1979). Further development of the two-point test for workability and extension of its range. *Magazine of concrete research*, 31(109):202–210.

[118] Thorp, A., Wilkes, C., Nicholson, D., and Bryan, M. (2018). Recent Experience with Tremie Concrete Properties and Testing. *Proceeding of the 2018 DFI-EFFC International Conference on Deep Foundations and Ground Improvement, Rome, Italy*.

[119] Thrane, L. N., Szabo, P., Geiker, M., Glavind, M., and Stang, H. (2004). Simulation of the test method "l-box" for self-compacting concrete. *Annual Transactions of the NORDIC rheology society*, 12(1):47–54.

[120] Tichko, S., Schutter, G. D., Troch, P., Vierendeels, J., Verhoeven, R., Lesage, K., and Cauberg, N. (2015). Influence of the viscosity of self-compacting concrete and the presence of rebars on the formwork pressure while filling bottom-up. *Engineering Structures*, 101:698–714.

[121] Tichko, Serge (2016). *Hydrodynamic modelling of the flow of self-compacting concrete in formworks*. PhD thesis, Ghent University.

[122] Tregger, N., Gregori, A., Ferrara, L., and Shah, S. (2012). Correlating dynamic segregation of self-consolidating concrete to the slump-flow test. *Construction and Building Materials*, 28(1):499–505.

[123] Turgut, P., Turk, K., and Bakirci, H. (2012). Segregation control of SCC with a modified L-box apparatus. *Magazine of Concrete Research*, 64(8):707–716.

[124] Vakhrushev, A., Wu, M., Ludwig, A., Nitzl, G., Tang, Y., and Hackl, G. (2014). Experimental verification of a 3-phase continuous casting simulation using a w ater model. In *Proceedings 8th ECCC Conference, Graz*.

[125] Vasilic, K., Gram, A., and Wallevik, J. E. (2019). Numerical simulation of fresh concrete flow: insight and challenges. *RILEM Technical Letters*, 4:57–66.

[126] Vasilic, K., Schmidt, W., Kühne, H.-C., Haamkens, F., Mechtcherine, V., and Roussel, N. (2016). Flow of fresh concrete through reinforced elements: experimental validation of the porous analogy numerical method. *Cement and Concrete Research*, 88:1–6.

[127] Vosoughi, F., Rakhshandehroo, G., Nikoo, M. R., and Sadegh, M. (2020). Experimental study and numerical verification of silted-up dam break. *Journal of Hydrology*, page 125267.

[128] Wallevik, J. E. (2006). Relationship between the Bingham parameters and slump. *Cement and Concrete Research*, 36(7):1214–1221.

[129] Wallevik, O. H., Feys, D., Wallevik, J. E., and Khayat, K. H. (2015). Avoiding inaccurate interpretations of rheological measurements for cement-based materials. *Cement and Concrete Research*, 78:100–109.

[130] Wallstedt, P. C. and Guilkey, J. (2008). An evaluation of explicit time integration schemes for use with the generalized interpolation material point method. *Journal of Computational Physics*, 227(22):9628–9642.

[131] Wang, B., Vardon, P. J., Hicks, M. A., and Chen, Z. (2016). Development of an implicit material point method for geotechnical applications. *Computers and Geotechnics*, 71:159–167.

[132] Weller, H. G., Tabor, G., Jasak, H., and Fureby, C. (1998). A tensorial approach to computational continuum mechanics using object-oriented techniques. *Computers in physics*, 12(6):620–631.

[133] Zhang, X., Chen, Z., and Liu, Y. (2016). *The Material Point Method: A Continuum-based Particle Method for Extreme Loading Cases*. Academic Press.

[134] Zhao, X. and Liang, D. (2016). Mpm modelling of seepage flow through embankments.

[135] Zienkiewicz, O. C. and Taylor, R. L. (2005). *The finite element method for solid and structural mechanics*. Elsevier.